SACRED HEART COLLEGE, CHALAKUDY

(AFFILIATED TO UNIVERSITY OF CALICUT)

THRISSUR, KERALA - 680307

AQAR 2021-22

CRITERION III

3.3.2 - Number of research papers per teachers in the Journals notified on UGC website during the year



Submitted to

National Assessment and Accreditation Council

Certificate No: PUB.2021/UPJOZ/919

UTTAR PRADESH JOURNAL OF ZOOLOGY

Certificate of Publication

Manuscript Title: LIFE-TABLE PARAMETERS OF SPIDER MITE Tetranychus ludeni Zacher (ACARI: TETRANYCHIDAE) ON Amaranthus tricolor L.

Authored by:

K. P. BETTY AND SANGEETHA G. KAIMAL

Published in:
2021 - Volume 42 [Issue 14]
Date of Publication: 24-Jun-2021
Certificate validation link: https://mbimph.com/index.php/UPJOZ/article/view/2278

Sarmistha Halder
Managing Editor

Reg. Offices:
ASIA: Tarakeswar, Hooghly, PIN-712410, West Bengal, India
EUROPE: 83A Princes St, Edinburgh EH2 2ER, UK

UTTAR PRADESH JOURNAL OF ZOOLOGY

42(14): 96-102, 2021
ISSN: 0256-971X (P)



LIFE-TABLE PARAMETERS OF SPIDER MITE *Tetranychus ludeni* Zacher (ACARI: TETRANYCHIDAE) ON *Amaranthus tricolor* L.

K. P. BETTY[1] AND SANGEETHA G. KAIMAL[2*]

[1]Department of Botany, Sacred Heart College, Chalakudy, Kerala-680 307, India.
[2]Department of Zoology, Providence Women's College, Calicut, Kerala-673 009, India.

AUTHORS' CONTRIBUTIONS

This work was carried out in collaboration between both authors. Both authors read and approved the final manuscript.

Article Information

Editor(s):
(1) Dr. Telat Yanik, Professor, Atatürk University, Turkey.
Reviewers:
(1) Mirna Dwirastina, Indonesia.
(2) Claudia-Maria Simonescu, University Politehnica of Bucharest, Romania.
(3) Liang-ze-nan Wang, Hohai University, P. R. China.

Received: 03 May 2021
Accepted: 09 July 2021
Published: 13 July 2021

Original Research Article

ABSTRACT

Studies on the life table parameters of the spider mite, *Tetranychus ludeni* Zacher infesting *Amaranthus tricolor* was initiated in the laboratory following detached leaf culture method at 30 ± 5°C and 70 ± 2% RH. The respective durations recorded for pre-oviposition period, oviposition period and post-oviposition period were 0.75 ± 2, 10.5 ± 0.8 and 0.75 ± 2 days respectively. The total number of eggs laid by an adult female averaged 91.65 ± 3.9 eggs. Life span was recorded to be 11.75 ± 0.7 days. Durations of both sexual and parthenogenetic reproduction were 10.04 ± 0.28 days and 9.65 ± 0.20 days respectively. Shorter duration of development was observed for parthenogenetic development in comparison to that of sexual reproduction. Male:female sex ratio was recorded to be 1-2: 10. A cognitive aspect that reflected was the addition of a new host plant to the so far enlisted hosts for the mite, *T. ludeni*.

Keywords: *Amaranthus tricolor*; spider mite; *T. ludeni*; moulting; longevity and reproduction.

1. INTRODUCTION

The tetranychid mite (spider mite) *Tetranychus ludeni* is a dreadful pest owing to their ubiquitous presence and destructive potentials to a wide range of economically important plants [1-4]. As invasive species, they inflict deleterious effects on host tissues because of their microscopic size, cryptic behaviour, high fecundity, extremely short lifecycle, polyphagous nature and pesticide resistance crops [5,6,1,3,7,8]. This astounding ability of *T. ludeni* to colonize host plants to replenish all the available

**Corresponding author: Email: drsangeethakaimal@gmail.com, sangeethakaimal@gmail.com;*

nutrients, inflict internal injury, stippling, bronzing and chlorosis, cause photosynthetic decline, languish stomatal conductance and reduce transpiration rates has led to considerable loss to agriculturists. Apart from direct damages, *T. ludeni* is known to act as vectors of plant viral diseases *viz.,* (DEMV) [9].

The current host plant of *T. ludeni, Amaranthus tricolor* L. (Amaranthus, collectively known as amaranth), is a cosmopolitan genus of rapidly-growing annual herbs noted for its brilliantly coloured foliage, variegated in shades of red, green, or yellow. Although several species are often considered as weeds, amaranths are valued world-wide as leafy vegetables and ornamentals. The red spinach, *A. tricolor* belonging to family Amaranthaceae is an annual, broadleaved, erect herb, growing up to 1.25m high and is cultivated in Asia for its edible leaves and seed. The simple (often purplish) leaves of spinach are used either raw or in its steamed form in the preparation of salads, soups and stews. The leaves are rich in proteins (3.5%), carbohydrates (6.6%), minerals (calcium, iron, magnesium, phosphorus, potassium, zinc, copper and manganese) and vitamins. The leaves owing to their medicinal value are also used against external inflammation, diuretics (treatment for bladder distress) and to control haemorrhage following abortion. The whole plant is known for its astringent property and a decoction of old plants when taken internally improves vision and strengthens the liver. Leaves of *A. tricolor* showed signs of heavy infestation of the spider mite, *T. ludeni* and therefore the plant was duly considered for regular collection for biological studies.

The current paper focuses therefore on the developmental aspects of *T. ludeni* on *A. tricolor* as a preliminary step to plan intervention tools for IPM for *T. ludeni* control. Selection of *A. tricolor* as the host plant was done owing to the heavy intensity colonization and high degree of damage induced by *T. ludeni* as well as the uniform presence of the plant throughout the study area coupled with their supreme economic status to mankind. The meticulous planning of a proper IPM strategy demands a thorough knowledge of the biology, ecology and behavior of the mite under consideration.

2. MATERIALS AND METHODS

Studies were initiated during the months of September - May in the Acarology division, University of Calicut, Kerala. Rearing of the spider mite, *T. ludeni* was done following detached leaf culture method [10]. Expanded leaves at 2 months of age excised from *A. tricolor* grown in green houses were placed with their adaxial surface facing upwards on moist cotton bed kept in petridishes. When the leaves showed signs of loss of vitality, they were replaced with fresh ones usually after 2 to 3 days interval. Adult *T. ludeni* females (approx. 25) were transferred to the petridishes containing fresh host leaves immediately after collection from the field. The colonies were maintained in the laboratory under standard conditions in an environmental growth chamber set at 30 ± 5°C and 70 ± 2% RH. Studies on sexual development were done by introducing few males in each of the culture set along with females. Observations on the different aspects *viz.,* oviposition, incubation, hatching, duration of developmental stages, quiscence and moulting was done using Magnus stereozoom trinocular research microscope at 6hr time intervals. The results were statistically analysed, tabulated and presented as mean ± SEM. Identification of the species was done by running appropriate taxonomic keys and confirmation of species was done based on the morphological structure of the male aedeagus, which is the diagnostic feature for species level identification [11,5].

3. RESULTS

3.1 Oviposition

T. ludeni females showed preference to the adaxial leaf surface. No site-specific selection was noticed in the case of oviposition. Prior to egg deposition, adult females constructed webbing from silk threads released from a pair of glands near their mouth. Egg deposition followed a random pattern and were often seen glued over the surface of the webbing. Freshly laid eggs were spherical, transparent and colouless. They turned pale yellow the following day and later to orange on the final day of oviposition. The larval gnathosoma, eye spots and legs could be easily perceived through the egg case few minutes prior to the intitiation of the hatching process. The durations of pre-oviposition, oviposition and post-oviposition periods of *T. ludeni* were recorded to be 0.75 ± 2 days, 10.5 ± 0.8 days and 0.75 ± 2 days respectively on *A. tricolor* (Table 1).

Table 1. Duration (in days) of pre-oviposition, oviposition and post-oviposition periods of *T. ludeni* on *A. tricolor*

Pre-oviposition	Oviposition	Post-oviposition
0.75 ± 2	10.5 ± 0.8	0.75 ± 2

n = 35

3.2 Fecundity and Longevity

The total number of eggs laid by adult *T. ludeni* during its reproductive phase was noted minimum on the firat and second days of oviposition. However, fecundity attained peak on the sixth day following which a slow but steady decline was obseerved from the seventh day to the least on the last day of oviposition. The peak daily egg production on the sixth day was 20.9 ± 0.32 eggs and the least number was 23.2 ± 0.17 eggs on the final ovipositing day. Fecundity per female of *T. ludeni* on *A. tricolor* averaged 91.65 ± 3.9 eggs. Further, it was also observed that the mated females exceeded in their fecundity levels in comparison to the fecundity rate as shown by the virgin females (Table 2). The duration of life span of *T. ludeni* averaged 11.75 ± 0.7 days on *A. tricolor*. The longevity of mated recorded less than virgin females *viz.,* 11.2 ± 0.01 days and 12.75 ± 0.2 days respectively (Table 3).

3.3 Hatching

Hatching process was initiated by the appearance of a slit near the apical margin of the egg along with an increase in the size at the equatorial region. The slit further deepened as the furrow laterally moved to meet mid ventrally. The wriggling movements of the emerging larva further aided the process and the egg cases after hatching was found to separate as two distinct halves. The entire sequence of events culminated in 10 - 12 minutes duration. Range of hatchability of eggs was 92%.

3.4 Duration of Developmental Stages (Table 3)

3.4.1 Incubation period

The period between egg laying and hatching of *T. ludeni* was observed to be 3.4 ± 0.02 days on *A. tricolor*. During this period significant changes were noticed in the shape and colour of the eggs ranging from transparent nature to orangish tinge.

3.4.2 Larval period

Larval period extended from the emergence of larva from the egg to the transformation of inactive quiescent stage. The larva is the smallest life stage, creamy white coloured, with red prominent eye spots and 3 pairs of legs. The larva soon after emergence remained motionless for around 10 minutes before it initiated feeding. The larva with its piercing mouth parts sucked the leaf sap and the feeding process was evident from the rotational movement of the leaf sap in the abdomen of the larva. A change to greenish yellow colour was also observed by the end of the active larval life. The duration recorded was 1.0 ± 0.03 day. Soon after the active life of larva ceased, it stopped feeding and entered into an inactive stage or the first quiescence. This followed moulting and emergence of the first nymphal stage called protonymph.

3.4.3 Protonymphal period

The first stage nymph called protonymph showed increased size than the larval stage and had 4 pairs of legs. Soon after emergence, the body was pale yellow with green dots on its dorsolateral region. After a few minutes of inactivity, the protonymph initiated feeding, the pattern of which was similar to that of the larva. The protonymphal active period lasted for 1.1 ± 0.01 days. This followed the beginning of the second quiescent phase and the subsequent moulting into the deutonymphal stage.

3.4.4 Deutonymphal period

The quiescent protonmphal stage culminated with the emergence of the last instar nymph or the deutonymph. Deutonymphal stage showed great similarity with the adult and hence marked sexual dimorphism could be perceived at this stage. It is larger in size than the protonymph and the feeding activity began 10 minutes after moulting was completed. The deutonymphal period on *A. tricolor* averaged 1.5 ± 0.02 days. AT the end of deutonymphal active life, third quiescence and moulting process into the adult stage followed.

3.5 Adult Stages

Adults of *T. ludeni* could easily be distinguished owing to marked morphological differences. Males appeared to be lesser in number, pale yellow in colour, small sized and spindle shaped with tapering abdomen. They were found gregariously moving faster than the large sized females who were red coloured and with rounded abdomen. The males emerged earlier than females and were found guarding the female quiescent deutonymph to mate as soon as the deutonymph moults into the adult. The males had no role other than reproduction and hence were found to mate multiple times with different females.

Table 2. Fecundity and rate of daily egg production of *I. ludeni* on *A. tricolor*

Number of eggs laid on different days of oviposition										Total number of eggs laid
1	2	3	4	5	6	7	8	9	10	
5.0±0.1	9.2±0.31	11.8±0.2	15.2±0.5	17.6±0.1	20.9±0.3	18.3±0.9	12.2±0.4	8.2±0.5	3.2±0.17	98.2 ± 5.5 Mated female
3.2±0.2	5.1±0.22	8.3±0.42	12.9±0.7	14.2±0.5	17.5±0.3	10.8±0.9	6.6±0.55	2.2±0.4	1.0±0.05	85.1 ± 2.2 Unmated female
Mean ± SEM										91.65 ± 3.9

n = 35

Table 3. Duration (in days) of development and longevity of *I. ludeni* on *A. tricolor*

Egg	Larva	1st Quiescence	Proto-nymph	2nd Quiescence	Deuto-nymph	3rd Quiescence	Total duration	Longevity
3.4±0.02	1±0.03	0.75±0.05	1.1±0.01	1±0	1.5±0.02	1±0	9.75±0.08	11.75 ± 0.7
3.01±0.06	1.08±0.03	0.71±0.04	1.10±0.02	1±0	1.75±0.05	1±0	9.65±0.20 Parthenogenesis	12.75 ± 0.2 Unmated
3.13±0.05	1.12±0.02	0.78±0.05	1.26±0.08	1±0	1.75±0.08	1±0	10.04±0.28 Sexual	11.2 ± 0.01 Mated

n = 35

3.6 Quiescent Periods

Quiescent period is a period of zero activity in the life cycle of *T. ludeni*. The mite showed three stages of quiescence, one at the end of active life of each developing stage. Quiescence is marked by the appearance of a covering over the body surface which appeared opaque in the initial stage and later on turned shiny just few minutes prior to moulting. During this period, *T. ludeni* folded its third pair of legs under the hysterosoma and the first two pairs were projected forwards. A unique feature of the tendency of aggregation was exhibited by *T. ludeni* during all the three quiescent periods. The active stages prior to entering quiescence opted for a secluded safe site preferably near the crevices of the mid rib on the foliage and in the shelter of the webbing. They then moved in close proximity and settled close to each other. As more larval and nymphal quiescent stages joined from different directions the colony of quiescent individuals acquired a circular shape. The durations of the 3 quiescent stages of *T. ludeni* were recorded to be 0.75 $\pm$ 0.05, 1.00 $\pm$ 0 and 1.00 $\pm$ 0 day respectively.

3.7 Moulting

Moulting is the emergence of the subsequent life stage from the preceding life stage with an inactive stage of transition or quiescence in between. Aggregation as observed in *T. ludeni* culminated with moulting. A split that appeared on the mid-dorsal region extended either side to meet mid-ventrally. The active movements of the forelimbs of the emerging stage tampered the posterior half of the mouting skin. The entire process took an average time of 20 minutes for completion. However, the anterior part of the exuviae remained inatact due to the backward movement of the mite during emergence. Scattered white exuviae could be seen on the leaf surface in enormous numbers.

3.8 Mating

Sexual reproduction was done by copulation where the males inserted its aedeagus to the vagina of the female by bending its hysterosoma over that of the female. Mating was completed in 10 minutes and soon after the process the males moved away in search of new adult females.

3.9 Total Duration of Development

Developmental stages followed the same pattern as in other Tetranychid representatives. They showed sexual and parthenogenetic modes of reproduction. The sequence of events in both kinds of reproduction was identical. However, parthenogenesis yielded only males while sexual reproduction resulted in both sexes in the ratio of 1-2 male:10 females. The average durations of development of were 9.75 $\pm$ 0.08 days and that of parthenogenesis versus sexual reproduction were 10.04 $\pm$ 0.28 and 9.65 $\pm$ 0.20 days. Shorter duration of development was observed in parthenogenesis compared to that of sexual reproduction.

4. DISCUSSION

Though the pattern of development and sequence of events matched other Tetranychid mites, *T. ludeni* exhibited a unique behavior of the phenomenon called aggregation. This behavior throws light on the unmatched cohesive nature of the colony unlike other spider mites who prefer to enter quiescence solitarily. [12,3,13,14]. Tetranychid mites show a general preference of depositing eggs close to the midrib or major veins of the host leaves [15,7]. However, the spider mite *T. ludeni* had no such ovipositional site preference [14]. The reason for the ovipositional pattern of laying eggs randomly could be the tough nature of the silken web secreted by *T. ludeni* that provided adequate protection to the delicate eggs and the life stages.

The pre-oviposition and oviposition periods of *T. ludeni* recorded by Puttaswamy and Channa Basavanna [16] on brinjal leaves were 0.98 day and 10.85 days. This is almost in concordance with the present results. On the contrary, the post-oviposition periods reported by the authors were three times greater up to 2.4 days. The same authors [17,18] observed the pre-oviposition, oviposition and post-oviposition periods at 19.3°C - 28.4°C and 53% - 88% RH as 1.54 days, 12.75 days and 3.61 days respectively. In the current study, the rate of oviposition in *T. ludeni* attained the highest record on the 6th day. However, oviposition rate reached peak earlier on the 4th day in *T. evansi* [19], later in the 7th day in *T. urticae* [20] and 9th day in *T. ludeni* [21]. Life span of mated females was found lower than that of unmated females. This highlighted negative implication of copulation on the life span of the mite *T. ludeni*. It was also influenced by the rate of daily fecundity [3,13]. Greater the rate of oviposition, lesser was the longevity of females as recorded in the current investigation.

The process of hatching and the formation of slit closely resembled the pattern in *T. neocaledonicus* [14,7]. Unlike other Tetranychid mites, fluid expulsion from the egg was observed at the time of hatching in *T. ludeni*. Moulting and mating process of *T. ludeni* shared similarities with many other spider

mites as reported by several authors [11,1]. *T. ludeni* males showed great preference for unmated females who were more gregarious and were stationed on the foliage for extended periods than the mated females. This enhanced the chances for more copulation opportunities. *T. ludeni* copulated multiple times with mature females unlike many spider mites where single mating was recorded. A radical behaviual change from this normal nature was recorded in *T. ludeni* wherein the same female engaged in multiple mating with different males [21,12,22].

The occurance of arrhenotoky has been observed in several tetranychid mite species [14,7]. Such dual reproductive tendency is a means to increase the male population that is otherwise always less in the field. The sequence of processes however matches in the two kind of mechanisms. All the progeny were found to be males in the case of parthenogenetic development while in the sexual reproduction both males and females were produced with a sex ratio of 2 males:10 females. The total durations of development of *T. ludeni* as recorded by Mallik and ChannaBasavanna, 1983 (22.2 days) seemed contrary while that observed by Singh et al., [23] (10.16 days) seemed to coincide with the present findings of *T. ludeni* on *A. tricolor*.

A significant observation on the unique pattern of aggregation was noted in *T. ludeni*. This throws light on the ontogeny of *T. ludeni* since it was repeatedly observed at the onset of every quiescent period [24,21,14]. In-depth investigation in anticipated for future research on these lines to have a better understanding of their behavioual pattern under the influence of pheromones.

5. CONCLUSION

Biological studies of *T. ludeni* on *A. tricolor* clearly reflects on the potential of the mite to rise to the status of major pest. The spider mite completed on an average 3-4 generations in the laboratory conditions as well as in the field and build their population well above the threshold level in no time. The deleterious damage caused to the plant is visible to naked eye only at a very later stage of infestation, which is yet another reason for the serious economic loss to growers. Hence control of such harmful pests is the need of the hour particularly for a state like Kerala where agriculture is the major source of income for the majority. A cognitive aspect that elucidated from the present study was the occurrence of the mite on a rich leafy vegetable crop *A. tricolor* as a new host record to the existing list of hosts of *T. ludeni*. Further exploration of the possibility of new host arenas should be necessitated so as to protect the agricultural wealth of our state from being exploited by these dreadful pests.

ACKNOWLEDGEMENTS

The authors are grateful to Dr. N. Ramani, Professor and Former Head, Department of Zoology, University of Calicut for her valuable suggestions and the University of Calicut for financial assistance.

COMPETING INTERESTS

Authors have declared that no competing interests exist.

REFERENCES

1. Gupta SK. Injurious and beneficial mites infesting agri-horticultural crops in India and their management. Nature books India, New Delhi. 2012;362.
2. Binisha KV, Haseena B. Mite fauna associated with major vegetable crops of Thrissur district, Kerala. Entomon. 2013;38(1):47–52.
3. Saritha C, Ramani N. Population Density and Distribution Pattern of Mites Infesting The Invasive Plant, *Bidens sulphurea* cav. International Journal of Science and Research. 2013;4(7):556–559.
4. Lekha C, Kinathi S. Phytophagous mites infesting vegetable crops of Kerala, India, Persian J. Acarol. 2019;(8)1:69–72.
5. Jeppson LR, Keifer HH, Baker EW. Mites injurious to economic plants. University of California Press. 1994;614.
6. Zhang ZQ. Mites of greenhouses, identification, biology and control. CABI Publishing, Wallington UK. 2003;244.
7. Sangeetha GK. Breeding biology of the vegetable mite on Moringa oleifera Lam (ISBN: 978-3-659-78830-7). Lap Lambert Academic Publishing, Beau Bassin 71504, Mauritius. 2019;81.
8. Young MR, Proctor HC, Dewaard JR, Hebert PD. DNA barcodes expose unexpected diversity in Canadian mites. Molecular Ecology. 2019;28(24):5347-5359.
9. Rajagopalan K. First record of spider mite *Tetranychus ludeni Zacher transmitting* Dolichos Enation Mosaic Virus (DEMV). Current Science. 1974;43(15):488-489.
10. Sangeetha GK, Ramani N. Biological studies of *Tetranychus neocaledonicus* Andre (Acari: Tetranychidae) infesting *Moringa oleifera* Lam. Bulletin of Pure and Applied Sciences. 2007;26A(2):51-57.

11. Gupta SK. The Handbook on Plant Mites of India. Zoological Survey of India Calcutta. 1985;507.
12. Sangeetha GK, Ramani N. Biology of *Tetranychus ludeni* Zacher (Acari: Tetranychidae) – A pest of velvet bean. Indian Journal of Fundamental and Applied Sciences. 2011;1(3):1-6.
13. Gotoh T, Moriya D, Nachman G. Development and reproduction of five *Tetranychus species* (Acari: Tetranychidae): do they all have the potential to become major pests? Experimental and Applied Acarology. 2015;66:453–479.
14. Ristyadi D, He ZX, Wang Q. Dynamics of life history traits in Tetranychus ludeni Zacher in response to fluctuating temperatures, Systematic and Applied Acarology. 2019; 24(11):2272–2277.
15. Gotoh T, Saito M, Suzuki A, Nachman G. Effect of constant and variable temperatures on development and reproduction of the two spotted spider mite *Tetranychus urticae* (Acari: Tetranychidae). Systematic and Applied Acarology. 2014;64:465–478.
16. Puttaswamy, Channabasavanna GP. Influence of host plants on the development, fecundity and longevity of *Tetranychus ludeni* Zacher (Acari: Tetranychidae). Indian Journal of Acarology. 1981;5:80-84.
17. Puttaswamy, Channabasavanna GP. Effect of temperature and relative humidity on the development and oviposition of *Tetranychus ludeni* (Acari: Tetranychidae). Indian Journal of Acarology. 1980a;4(1):31-40.
18. Puttaswamy, Channabasavanna GP. Life history of T. ludeni (Acari: Tetranychidae) under field condition. Indian Journal of Acarology. 1980b;4(1):41-48.
19. Qureshi AH, Oatman ER, Fleschner CA. Biology of the spider mite, *Tetranychus evansi* Pritchard and Baker. Annual Entomological Society of America. 1969;62(4):898-903.
20. Shih CT, Poe SL, Cromroy HL. Biology, life table and intrinsic rate of increase of *Tetranychus urticae*. Annual Entomological Society of America. 1976;69:362-364.
21. Oku K, Yano S, Osakabe M, Takafuji A. Mating strategies of *Tetranychus kanzawai* (Acari: Tetranychidae) in relation to mating status of females. Annual Entomological Society of America. 2005;98(4):625-628.
22. Prasad S, Raghuraman M, Singh J. Effect of Temperature and Relative Humidity on the development of Red Spider Mite, *Teteranychus ludeni* Zacher at Varanasi. International Journal of Development Research. 2015;5(4):4021-4024.
23. Singh P, Somchoudhury AK, Mukherjee AB. The influence of natural enemy complex on the population of *Aceria litchii* (Acari: Eriophyidae). In: Progress in Acarology. 1989; 2:361-367.
24. Mallik B, Channabasavanna GP. Life history and life tables of *Tetranychus ludeni* and its predator *Amblyseius longispinosus* (Acari: Tetranychidae; Phytoseiidae). Indian Journal of Acarology. 1983;8:1-12.

© Copyright MB International Media and Publishing House. All rights reserved.

SPECIAL ISSUE

KNOWLEDGE RESONANCE

ISSN : 2231-1629

A HALF YEARLY PEER REVIEWED REASERCH JOURNAL

(Evaluated in the SJIF Journal Masters List Evaluating Process with Impact Factor of 8.072 for Year 2021)

Department of Commerce

Organized

One Day National E-conference on

Corporate Social Responsibility : In India, Amid Covid-19 Pandemic

8th October, 2021



Dr. M. K. Umathe College
Affiliated to R.T.M. Nagpur University, Nagpur

Annasaheb Gundewar College
Affiliated to R.T.M. Nagpur University,Nagpur

Mahatma Gandhi Arts & Commerce College, Parseoni
Affiliated to R.T.M. Nagpur University , Nagpur

Kewalramji Harde Mahavidyalaya
Chamorshi, Affiliated to Gondwana University, Gadchiroli

SPECIAL ISSUE

ISSN : 2231-1629

KNOWLEDGE RESONANCE

A HALF YEARLY PEER REVIEWED REASERCH JOURNAL

(Evaluated in the SJIF Journal Masters List Evaluating Process with Impact Factor of 8.072 for Year 2021)

Department of Commerce

Organized

One Day National E-conference on

Corporate Social Responsibility : In India, Amid Covid-19 Pandemic

8th October, 2021

JOINTLY ORGANIZED BY

Dr. M. K. Umathe College Affiliated to R.T.M. Nagpur University, Nagpur	Annasaheb Gundewar College Affiliated to R.T.M. Nagpur University,Nagpur
Mahatma Gandhi Arts & Commerce College, Parseoni Affiliated to R.T.M. Nagpur University , Nagpur	Kewalramji Harde Mahavidyalaya Chamorshi, Affiliated to Gondwana University, Gadchiroli

Research Journal Publication Committee

Dr. M. K. Umathe College

(Arts, Science & Ramchandra Mokhare College) Nagpur-440022

PLAGIARISM ALERT !

Contributors are advised to adhere to strict academic ethics with respect to acknowledgment of original ideas from others. The editors will not be responsible for any such lapse of the contributor. All submission should be original and must be accompanied by a declaration that it is an original work and has not been published anywhere else. It will be your sole responsibility for such lapses, if any. Neither editor, nor publisher will be responsible for it.

INDEX

1.	**TECH-LOGIC VIEW OF CSR** Mr. Rajesh R Yadav	1
2.	**CORPORATE SOCIAL RESPONSIBILITY: AN ANALYTICAL STUDY OF INDIAN COMPANIES** Dr. Sanjay Dhanvijay* Dr. Vijay R. Bagde** Dr. Sanjay B. Bagde***	4
3.	**THE DYNAMICS OF CORPORATE SOCIAL RESPONSIBILITY IN INDIA VIS-À-VIS PRE AND AMIDST COVID-19 PANDEMIC PERIOD** Ms. Nirmala Daita* Dr. Varsha Thakre**	8
4.	**CORPORATE SOCIAL RESPONSIBILITIES IN COMPANIES ACT 2013** Dr. Shrikant L. Patil	13
5.	**CONTRIBUTION OF CORPORATE SOCIAL RESPONSIBILITY IN COVID -19 PANDEMIC** Dr. Bina Madhukar Moon	16
6.	**A STUDY ON THE CSR INITIATIVE UNDERTAKEN BY CERTAIN INDIAN COMPANIES** Dr. Pratap M. Chauhan.	19
7.	**A STUDY OF INNOVATION MODERN APPROACHES AND ITS INSPIRATION ON STUDENTS' PERFORMANCE OF CLASSROOM TEACHING IN GADCHIROLI CITY** Ganesh Gopalrao Dandekar	22
8.	**CORPORATE SOCIAL RESPOSIBILITY EXCEPTATION: IN INDIA** Dr. Pawan R. Naik	26
9.	**DOMESTIC VIOLENCE AND CORPORATE SOCIAL RESPONSIBILITY** Ms. Kavita Narendra Hedaoo	30
10.	**COMPARATIVE ANALYSIS OF CORPORATE SOCIAL RESPONSIBILTY INITIATIVES IN PUBLIC VS PRIVATE SECTOR** Harshwardhan Bhimrao Lanjewar*, Dr. Vivek V. Nagbhidkar**	34
11.	**EXPEDITION OF CORPORATE SOCIAL RESPONSIBILITY (CSR) DURING COVID-19 IN INDIA** Nijil Jacobi	47
12.	**RESILIENT LEADERSHIP - OPPORTUNITIES AND CHALLENGES FOR LIFE SKILLS** Dr. Sarita Karangutkar	52
13.	**CORPORATE SOCIAL RESPONSIBILITIES OF PROJECT MANAGER OF BUSINESS ADMINISTRATION** Dr.Saurabh Shukla	55
14.	**CSR INITIATIVES IN INDIAN INDUSTRIES, INDIAN BUSINESS, EDUCATION, BANKING AND IT** K. Annapoorneshwari Shetty 1, 2	59
15.	**CONTRIBUTION OF CORPORATE SOCIAL RESPONSIBILITY FUND CONTROLLING COVID-19 PANDEMIC** **A STUDY ON CSR CONTRIBUTION OF BANKING, FINANCE SERVICES AND INSURANCE SECTOR**	64

	Murlidhar Krishnarao Wakode	
16.	**USE OF SINGLE-USE PLASTIC IN THE LIGHT OF ETHICAL THEORIES, STAKEHOLDERS' MANAGEMENT AND FUTURE CORPORATE SOCIAL RESPONSIBILITY TRENDS USING TRIPLE BOTTOM LINE APPROACH** *Dr.Anjali Patkar **Mr.Rahul Mhabde	69
17.	**CORPORATE AND NGO PARTNERSHIP FOR SUCCESSFUL SOCIAL RESPONSIBILITY PROGRAMME IN INDIA** Dr. Satish V. Tewani	79
18.	**INDIA'S JOURNEY TOWARD SUSTAINABLE ENVIRONMENT DEVELOPMENT THROUGH CORPORATE SOCIAL RESPONSIBILITY** Dr. Viraj Pandagle	84
19.	**CORPORATE SOCIAL RESPONSIBILITY** **SUB THEME: FEASIBILITY OF CORPORATE SOCIAL RESPONSIBILITY INITIATIVES IN INDIA IN THE AREAS OF ENVIRONMENT, HEALTH, EDUCATION & HUNGER: BENEFIT & CHALLENGES** Dr. Rajesh G. Walode	87
20.	**CORPORATE SOCIAL RESPONSIBILITIES IN INDIA – ISSUES AND CHALLENGES** Dr. Shrikant L. Patil	91
21.	एकात्मिक बाल विकास सेवा योजनेअंतर्गत कार्यरत अंगणवाडी सेविका व मदतनीसांबद्दलच्या व्यावसायीक सामाजिक जबाबदाऱ्यांचा अभ्यास प्रा. मोरेश्वर भिकाजी शेन्डे	95
22.	व्यावसायिक सामाजिक जबाबदारी **(Corporate Social Responsibility)** प्रा. नरेश दामाजी सोनटक्के	98
23.	व्यावसायिक सामाजिक दायित्वाचे शिक्षण आणि आरोग्य क्षेत्रातील योगदान श्री. दिगंबर भऊरावजी टुले	102
24.	कोवीड 19 चा सामाजिक जीवनावर परिणाम डॉ निता शर्मा	107
25.	भारतातील सामाजीक उत्तरदायित्वाच्या दृष्टिकोनातून पर्यावरणाचा शाश्वत विकास Mahadeo Rambhau Sadawarte	111
26.	भारतीय शक्षणिक क्षेत्रात कॉर्पोरेट सामाजिक जबाबदारीची भूमिका डॉ. घनश्याम बी. बगडे	114
27.	पर्यावरणाचा शाश्वत विकास: एक सामाजिक जबाबदारी डॉ. लिलाधर डी. खरपुरिये	117
28.	भारतीय स्टेट बँकेचे निगमिय सामाजिक जबाबदारी अंतर्गत योगदान डॉ. रुपेश वामनराव खुबाळकर* डॉ. गजानन गोपलराव बाबडे**	121

ISSN 2231-1629
Knowledge Resonance
A Half Yearly National Peer-Reviewed & Indexing with SJIF Impact Factor Research Journal
IMPACT FACTOR 8.072

EXPEDITION OF CORPORATE SOCIAL RESPONSIBILITY (CSR) DURING COVID-19 IN INDIA

Nijil Jacobi
Sacred Heart College, Chalakudy, Kerala

Abstract
Corporate Social Responsibility (CSR) is a method through which an organization consolidates ecological, social and human improvement worries into its arranging and activities to guarantee that its tasks are moral and advantageous for society. CSR in India has customarily been viewed as an altruistic action. Be that as it may, with the initiation of Section 135 in the Companies Act 2013, India turned into the first nation to have legally commanded CSR for determined organizations. The Demonstration requires organizations with a total asset of ₹500 crore or more, or turnover of ₹1,000 crore or more, or a net benefit of ₹5 crore or seriously during the promptly going before monetary year, to burn through 2% of the normal net benefits of the quickly going before three years on CSR exercises. It lists the exercises that can be attempted and the way in which the organizations can embrace CSR projects/programs. In the midst of the COVID-19 outbreak, the Ministry of Corporate Affairs has informed that organizations' consumption to battle the pandemic will be considered substantial under CSR exercises. Assets might be spent on different exercises identified with COVID-19, for example, advancement of medical care including preventive medical care and disinfection, and catastrophe the board.

Keywords: *Company, Corporate Social Responsibility (CSR), COVID-19, Invest India*

Introduction

'CSR is the process by which an organization thinks about and evolves its relationships with stakeholders for the common good, and demonstrates its commitment in this regard by adoption of appropriate business processes and strategies. Thus, CSR is not charity or mere donations CSR is a way of conducting business, by which corporate entitles visibly contribute to the social good. Socially responsible companies do not limit themselves to using resources to engage in activities that increase, only their profits. They use CSR to integrate economic, environmental and social objectives with the company's operations and growth.' (CSR as defined by the Ministry of Corporate Affairs, Government of India).

Corporate Social Responsibility (CSR) doesn't have a generally acknowledged definition; the center of the idea in any case, is organized around the conviction that organization has an awareness of others' expectations towards society and individuals from whom they determine their prosperity. In nations like India, where monetary reconciliation and social consideration are basic powers that drive the majority towards development and improvement CSR has turned into an indispensable and effective piece of corporate scene.

The COVID-19 pandemic has been especially hard on the worldwide economy. There has been a lofty ascent in joblessness this year as the lockdowns and social separating standards have not permitted individuals to go to work, and they don't have the right stuff to work distantly. To make financial recuperation in the COVID-19 followed recently ordinary workplace, the labour force should get what it takes to be more employable.

Discussion

India was the first country in the world to force a legal commitment of CSR for companies meeting certain standards. According to Section 135 of the Companies Act, companies with a total assets of INR 5 Bn ($ 70 Mn) or more, or a yearly turnover of INR 10 Bn ($ 140 Mn) or more, or net profit of INR 50 Mn ($) at least 699,125, to burn through two percent of their normal net profits of three years on CSR. This arrangement makes India the main country in the world that makes both the spending and revealing of CSR commitments compulsory. Besides, the Organizations Act and ensuing alterations have extended and clarified exercises for which the two percent subsidizing can be utilized. The Public authority of India has clarified that CSR spending isn't good cause or simple gifts with no vital benefits. Indeed, there has been a coordinated work to define wide regions (Schedule VII of the Companies Act 2013) under which the subsidizing can be diverted, in this way noticeably and emphatically affecting society. Also, there has been a conscious endeavor to keep the CSR enactment lined up with India's obligation to the United Nations Sustainable

Development Goals (UN-SDGs). Schedule VII of the Companies Act 2013 defines expansive spaces of intercession that are expected to be deciphered generously with the inevitable spotlight being on guaranteeing sustainable development of the country.

A sum of INR 71, 277 Cr have been spent on 1,05,358 CSR projects till Financial Year 2019. The best three spaces getting greatest financing are instruction, wellbeing and provincial turn of events. Another region getting significant subsidizing is natural maintainability. Another intriguing pattern is that significant measures of subsidizing go to higher industrialized states. Since Financial Year 2015, Maharashtra, Karnataka, Gujarat and Tamil Nadu have gotten more than 30% of the absolute CSR spend. This could be for a long time like the organization is hoping to have a positive social effect in their spaces of activity, just as more profound associates with social effect associations working in a similar region. This can likewise be found in information on CSR consumption modes where very nearly 44% of all spending is finished by the actual organizations or by means of trusts/social orders/Segment 8 organizations set-up by them. One more 43 percent is done through different execution accomplices. Notwithstanding, the grouping of expenditure in these states, implies that states, for example, Jharkhand, Bihar, Chattisgarh, Madhya Pradesh and Uttar Pradesh which represent more than 55% of the optimistic areas (states with poor financial pointers), get just 9% of the all-out consumption towards CSR. Indeed, no state, aside from Uttar Pradesh, from the rundown above highlight in the main 10 state beneficiaries. For CSR to be genuinely successful, this awkwardness would need to be adjusted. Contribute India's 'Corporate Social Responsibility Projects Repository' on the India Investment Grid (IIG) is a work toward this path. It is trusted that by giving a stage to all states to list potential CSR projects at a focal level, organizations and their execution accomplices would have the option to survey where their CSR assets would be generally effective across India. Presently, the entryway has over 650+ ventures across eight assorted domains.

CSR and COVID-19 outbreak in India

The India Government announced the novel COVID-19 outbreak in the nation a "notified disaster" to empower state governments to assemble assets from the State Disaster Response Funds (SDRF). Following the notification, the Ministry of Corporate Affairs (MCA) clarified that expenditure of assets for COVID-19 help would be an allowable movement under CSR. Once more, the MCA prompted that the exercises ought to be deciphered generously in order to catch the pith of the exercises allowed under the Timetable. The public authority has likewise set up the 'Prime Minister's Citizen Assistance and Relief in Emergency Situations Fund' (PM CARES) to react to the COVID-19 emergency and give alleviation to those influenced. Further, Schedule VII was altered to incorporate commitments to PM CARES as CSR alongside the current PM's Public Help Asset. Taking advantage of its tremendous organization and connections, Invest India set up a CSR specific help cell to help corporates to channel their CSR subsidizing into different administrative and non-legislative associations just as focal and state-level finances set up for the specific undertaking of COVID-19 relief. To help commitments to alleviation assets across both the middle and states, Invest India made an internet based vault of 30+ alleviation assets just as fostered a pipeline of INR 163 Cr in gifts and CSR commitments from corporates. This empowered corporates and volunteers to find and associate with associations requiring financial or other help in their exercises. Another key enablement work for Invest India's COVID-19 reaction was the assistance of gifts of fundamental supplies, more than 10,86,100 bits of PPEs, basic consideration hardware and different products to cutting edge associations.

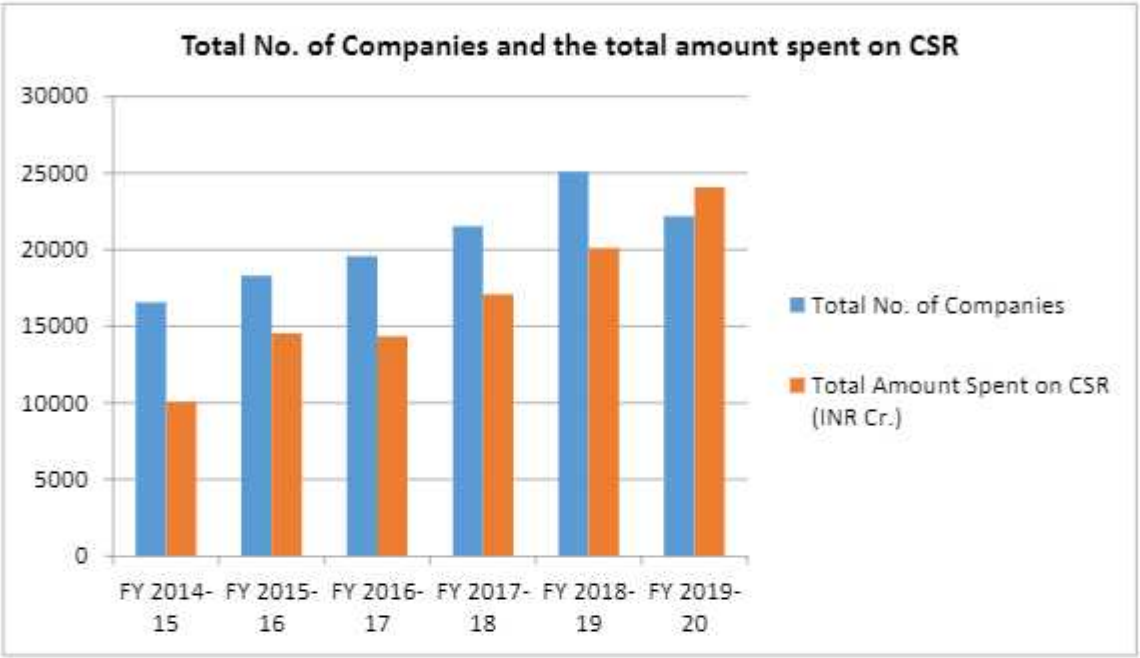
Table 1: Financial Year-wise amount spent on CSR in India

Financial Year	Total No. of Companies	Total Amount Spent on CSR (INR Cr.)	States & UTs Covered	Total No. of CSR Projects	Development Sectors Entered by Companies
FY 2014-15	16548	10066	36	9365	29
FY 2015-16	18292	14517	36	18468	29
FY 2016-17	19552	14344	36	23076	29
FY 2017-18	21515	17079	36	26830	29
FY 2018-19	25093	20099	36	32237	29
FY 2019-20	22155	24063	36	34291	29

Source: National CSR Data Portal, Ministry of Corporate Affairs, Government of India

The above table shows the total amount spent on CSR in India. The total number of companies engaged on CSR goes on increasing across the various financial years in India except FY 2019-20. The total number of companies decreased from 25093 in FY 2018-19 to 22155 in FY 2019-20. Even though the number of companies decreased, the total numbers of CSR projects are very high in FY 2019-20. It is clear that during 2019-20 companies have given more priority to CSR than any other financial years. The total amount spent on CSR in the financial year 2019-20 is the highest than any years. The below given Figure 1 depicts the same.

Figure 1: Total No. of Companies and the total amount spent on CSR



Source: National CSR Data Portal, Ministry of Corporate Affairs, Government of India

Table 2: Top Companies Spent on CSR in India in FY 2019-20

Company Name	Amount (INR Cr.)
RELIANCE INDUSTRIES LIMITED	908.71
TATA CONSULTANCY SERVICES LIMITED	602.00
OIL AND NATURAL GAS CORPORATION LIMITED	582.07
TATA SONS PRIVATE LIMITED	548.83
HDFC BANK LIMITED	535.31
INDIAN OIL CORPORATION LIMITED	518.49
INFOSYS LIMITED	359.94
BHARAT PETROLEUM CORPORATION LIMITED	346.46
POWER GRID CORPORATION OF INDIA LIMITED	346.21
ITC LIMITED	342.24
NTPC LIMITED	304.92
HINDUSTAN ZINC LIMITED	266.93
REC LIMITED	253.64
J. P. MORGAN SERVICES INDIA PRIVATE L...	204.93
NMDC LIMITED	199.99
TATA STEEL LIMITED	183.80
HINDUSTAN PETROLEUM CORPORATION LIMITED	182.24

Source: National CSR Data Portal, Ministry of Corporate Affairs, Government of India

Highlights of the work undertaken by Invest India for COVID-19 related CSR engagements

- ✓ Created a repository of 32 relief funds for companies to access to meet their CSR compliance for the year

- ✓ Assisted in the donation of over 10.86,100+ essential supplies donation from corporates as part of their CSR activities
- ✓ Made 60+ connections for COVID-19 donations
- ✓ Reached out to 289 tech incubators across Indian an effort to channel CSR funds into the developing technology space
- ✓ Developed a pipeline of INR 163 Cr to be channeled to COVID-19 relief funds(state and central level)
- ✓ Received 190 COVID-19 technology solutions approved for CSR funding through national incubators across India

CSR Trends in India in 2021

1. New learning

The COVID-19 changed the elements of nearly everything. Work was slowed down for quite a long time in associations. Notwithstanding, the CSR society proceeded with their tasks yet in a changed manner. The changing trends likewise brought many new learning for the execution organizations. For instance, they figured out how to keep exceeding the networks and aiding them without doing mass social event. Reception of computerized ended up being a major deliverer for some, CSR projects, particularly in the education sector.

2. COVID-19 Vaccination

As the year 2020 drew a weighty CSR center around COVID-19 help gauges, the corporates design COVID-19 immunization for local area and production network laborers under their CSR program.

3. Educational Support

Other than health sector, the educational sector has been profoundly influenced during the COVID-19 pandemic. Education has transformed from off-line to online mode. CSR funds are being used to create a virtual learning environment to the poor who lack such facilities.

4. Livelihood Support

As a huge number of laborers lost their employment because of lockdown and easing back monetary exercises last year, the CSR activities will be giving push on the expertise improvement and occupation arranged preparing project to empower unemployed for new positions.

5. More joint effort with Government

The year 2021 will likewise see a lot more elevated level of joint effort between the corporate world and the public authority offices towards execution of CSR projects.

6. Multiple CRS Projects with Same Objectives

The numerous CSR projects being worked in a similar area and on a similar topic by different companies will create considerable impact in the economy and the society.

7. Bottom-Up Approach

The CSR projects at ground level will have significantly more understanding this time on execution of the undertaking on the ground level. Their experience of dealing with undertakings and method of making effect will get voice in the CSR project arranging and asset distribution.

8. More usage of CSR reserves

Usage of CSR reserves is probably hiking as corporates are under moral obligation to help networks and individuals in out-of-the-box ways. The business and market restoration will help corporate feelings and their CSR arranging and execution will be among first concerns.

Conclusion

CSR of a company is overseen by the most scintillating minds. A company that is spending a lot of its supports needs to consistently guarantee that their cash is spent well, out of power of propensity. To accomplish this, it is executed by scholarly and experienced individuals. Hence, it has an enormous obligation and extension for what's to come. While India is developing at a quick speed, it isn't doing very well in the field of research. Interest in research in training, innovation, medication, space innovation, strategy definition, etc is needed to support native answers for native issues. CSR can turn into a reason for transformation in the field of research. India experiences the issue of mind channel. CSR can possibly keep that from occurring. The year 2020 showed us an alternate feature of life. It caused us to acknowledge how badly pre-arranged we were to confront a catastrophe, regardless of that, how we arose a victor by adjusting to the new and changed conditions. Life after COVID-19 is referred to as 'new-normal' considering the way that it would be for all intents and purposes outlandish for individuals to return to the predictability of the time before the pandemic. 2020 likewise disturbed the CSR space in a significant manner. The greater part of the organizations spent most of their CSR assets towards COVID-19 help in 2020. This removed the funds and consideration from numerous different causes and objectives regarding tending

to them. As the world moves towards the recuperation stage, the organizations are equipping with new plans and objectives for their CSR drives.

Reference

1. Dezan Shira & Associates, Corporate Social Responsibility in India, India Briefing, March 23, 2020 https://www.india-briefing.com/news/corporate-social-responsibility-india-5511.html/
2. Hency Thacker, what is CSR? The CSR Journal, April 7, 2020 https://thecsrjournal.in/what-is-csr-corporate-social-responsibility/
3. Hency Thacker, 'Top CSR Trends to Expect in 2021', The CSR Journal, January 1, 2021, https://thecsrjournal.in/top-csr-trends-to-expect-in-2021/
4. Kasmin Fernandes and Hency Thacker, Top 100 companies in India for CSR in 2020, The CSR Journal, November 3, 2020, https://thecsrjournal.in/top-indian-companies-for-csr-in-2020/
5. Ministry of Corporate Affairs, Government of India, Empowering Business - Protecting Investors, https://www.mca.gov.in/MinistryV2/faq+on+csr+cell.html
6. National CSR Data Portal, Ministry of Corporate Affairs, Government of India, https://www.csr.gov.in/
7. Rakesh Nangia, A closer look at CSR law, The Hindu – Business Line, February 21, 2021 https://www.thehindubusinessline.com/business-laws/a-closer-look-at-csr law/article33897046.ece
8. Shiv Nath Sinha, Corporate Social Responsibility in India, Economic & Political Weekly, ISSN (Print) - 0012-9976 | ISSN (Online) - 2349-8846, Vol. 56, Issue No. 26-27, 26 Jun, 2021 https://www.epw.in/journal/2021/26-27/special-articles/corporate-social-responsibility-india.html
9. Shweta Singh, '8 CSR trends to dominate in 2021', The CSR Universe, Jan 17, 2021 https://thecsruniverse.com/articles/8-csr-trends-to-dominate-in-2021
10. Sidharth Choudhary, Vasundhara Singh, Anusha Bhagat, Shawn Bhalla and Shubhangi Thakur 'The changing landscape of CSR in India during COVID-19', September 03, 2020, https://www.investindia.gov.in/siru/changing-landscape-csr-india-during-covid-19

Editorial Board

CHIEF EDITORS

Dr. D. V. Naik
Principal
Dr. M.K. Umathe College
Nagpur

Dr. Gajanan Patil
Principal
Annasaheb Gundewar College
Nagpur

Dr. L. B. Jadhav
Off. Principal
Mahatma Gandhi Art & Commerce
College, Parseoni, Nagpur

Dr. H. P. Banpurkar
Principal
Kewalramji Harde Mahavidyalaya
Chamorshi , Gadchiroli

EDITORS

Dr. Rajendra Selukar
Head of Department, Commerce
Dr. M.K. Umathe College,
Nagpur

Dr. Varsha Thakre
Head of Department, Commerce
Annasaheb Gundewar College
Nagpur

Prof. Mahesh G. Chonde
Head of Department, Commerce
Mahatma Gandhi Art & Commerce
College, Parseoni, Nagpur

Dr. Pawan R. Naik
Head of Department, Commerce
Kewalramji Harde Mahavidyalaya
Chamorshi , Gadchiroli

ASSOCIATE EDITORS

Prof. Harshwardhan Lanjewar
Assistant Professor
Dr. M.K. Umathe College,
Nagpur

Prof. M. K. Wakode
Assistant Professor
Annasaheb Gundewar College
Nagpur

Dr. R.D. Kabhe
Associate Professor
Mahatma Gandhi Art & Commerce
College, Parseoni, Nagpur

Prof. G.G. Dandekar
Assistant Professor
Kewalramji Harde Mahavidyalaya
Chamorshi , Gadchiroli

The Editors or Publisher do not assume responsibility for the opinions expressed by the authors of the papers

Published by
Research Journal Publication Committee
Dr. M. K. Umathe College
(Arts, Science & Ramchandrarao Mokhare Commerce College)
Lokseva Nagar, Bhamti, Ring Road, Nagpur-440022.
Phone No. 0712-2227062, 09421537123, **Email Id:** knowledgeresonancengp@gmail.com
Website- http://knowledgeresonance.com

Printed by
Dinesh Graphic
Shop No.3, 54-G, Vishnu Apartment, Trimurti Nagar, Nagpur-440 022 **M.** 9422119631

AKSHAR WANGMAY

International Peer Reviewed Journal

UGC CARE LISTED JOURNAL
October – 2021
Issue-IV, Volume-III

Chief Editor

Dr. Nanasaheb Suryawanshi

PRATIK PRAKASHAN, 'PRANAV, RUKMENAGAR, THODGA ROAD AHMEDPUR,
DIST. LATUR, -433515, MAHARASHTRA

Editorial Board

Dr. Mahendra S. Kadam
Dr. Netaji B. Kokate
Dr. Balasaheb V. Das
Mr. Zakirhusen B. Mulani

The Editors shall not be responsible for originality and thought expressed in the papers. The author shall be solely held responsible for the originality and thoughts expressed in their papers.

© All rights reserved with the Editors **Price: Rs.1000**

Living Life to the Fullest: Towards an Understanding of Disabled Children's Childhood Studies

Ms. Noble A. Pallath
Assistant Professor,Department of English, Sacred Heart College, Chalakudy
phd2020kreupasanam@gmail.com

"We live in a world of norms. Each of us endeavours to be normal or else deliberately tries to avoid [illegible] state. We consider what the average person does, thinks, earns or consumes…There is probably no area of contemporary life in which some idea of a norm, mean, or average has not been calculated…To understand the disabled body, one must return to the concept of the norm, the normal body. So much of writing about disability has focused on the disabled person as the object of study… I would like to focus not so much on the construction of disability as on the construction of normalcy. I do this because the "problem" is not the person with disabilities; the problem is the way that normalcy is constructed to create the "problem" of the disabledperson."

Lennard J. Davis' *the Disability Studies Reader*

Disability Studies being a burgeoning and developing field of academic inquiry, has received worldwide attention across associations of disabled people and their associates. It has now become an action orientated praxis. Research reveals that more attention is paid to disabled children's everyday interests and their concerns. Contemporaneously, this statement reveals that disabled children's everyday desires, wishes, interests and their concerns are taken into serious consideration. More lively and collective constructions of childhood, movements and campaigns around children's rights have gained much speed and momentum. The daily lives of disabled children are monitored by a galaxy of adults and a host of professionals which include teachers, social workers, doctors and other allied health professionals. The lives of disabled children are in a way surveilled by this team of competent workforce. In fact, the world of disabled children are scrutinized by grown-ups more than any other group of children.

Despite the heed being paid to the problems of the disabled children and their upliftment, the disabling society is replete with negative practices and stereotypes concerning them. The idea of normal development and the associated services disabled children receive always surfaces when the focus of the critical inquiry is targeted onto disabled children. Hence, a rights discourse also tends to be normative. This paper is an exploratory endeavour to dispel the unconstructive practices and typecasts that persist in the lives of disabled children and in doing so, ventures forth to embrace their lives and to focus on the hopes, needs, dreams, wishes and aspirations of disabled children, young people, their families and other allies and associates.

The current study aims to bring together theories of disability and childhood and how the disabled children are in need of professional intervention to make their life more meaningful and productive. The theories of disability and childhood have always projected a deficit view of disabled children in need of specialized interference. Disabled children's lives have been marginalized within childhood studies. Childhood Studies an adult-centric area of study, has always under-theorised the lives of disabled children. Disabled children are often depicted as being dependent, inactive, and their rights are interpreted as being totally absent and affixed. The highlight is always on their impairments, vulnerabilities and deformities. The focus on disabled children as people with childhood in a social context has been preoccupied with negative images. Disabled children are often defined against the norms of child development. Their voices have often been excluded and the emphasis is placed on the perspectives of parents, young people and professionals.

The study of disabled children's lives is often made from the perspective of a medical or individual model of disability. The medical model approach, widely critiqued in it, conceptualizes disability as a medical problem for individuals. With the initiation of social oppression models of disability, a shift in focus away from the individuals' bodies and minds to viewing disability as a form of social oppression has become increasingly evident. The social oppression models of disability are concerned with disability as social oppression. It sparsely and rarely provides an adequate and sufficient illustrative framework for the experiences of the disabled children. It looks at the ways in which disabled people are subjected to everyday exclusion and discrimination because of disablism.

In fact, disabled people are not disabled by their bodily impairments and limitations but by the attitudes and outlooks of a disabling society. However, in certain parts of the world, the disabled people are expected to live culturally normative lives. With concepts like inclusion, assimilation, acceptance, accommodation and tolerance gaining momentum in today's contemporary global scenario, the systemic cultural and attitudinal barriers that ostracize disabled people are annulled and negated and how these crippling practices might be exposed and removed are also taken into serious consideration. The need for

inclusion and an attention to the voices of disabled children continue to dominate in today's floor of intellectual discussions. Thinking from the standpoint of the disabled children, more focus should be given to their perspectives, their roles in contesting their day by day lives, and to examine the environments, affiliations, and structures which formed their understandings and experiences.

The rise and emergence of Disabled Children's Childhood Studies, as a new area of study, is a vital step taken in the right direction to tackle this grave problem of stigmatization. Disabled Children's Childhood Studies, of international origin with its roots at UK, is a developing field. It draws heavily upon both disability studies and childhood studies. It challenges all sorts of everyday exclusionary practices because of disablism and opens with a positive view of disabled children's childhood. This branch of study seeks to re-orientate research inquiry, moving away from 'deficits and lacks,' to focus, instead, on their 'hopes, dreams and aspirations' of disabled children. Disabled Children's Childhood Studies seeks to do something different. It ventures to look at the standpoints of disabled children themselves. The focus is on the positive contributions of disabled children in their everyday worlds. Its attempt is to erase the negative images of disabled children as promoted by the dominant forces of the social world.

Disabled Children's Childhood Studies places the stress on revisiting and revamping off-putting assumptions and pre-suppositions on the lives of disabled children and so to promote all children's potential. It also offers exciting opportunities to re-orientate, reshape and refashion norms that dominate children's lives. It values the contributions of disability studies and childhood studies to disabled children and young people's lives. It is an attempt to re-energise and revitalize deliberations and discourses and destabilizes professionalization, medicalization and pathologization which continue to regulate disabled children's everyday lives. It puts forth an ethical research design that prioritizes the voices and experiences of disabled children at the heart of the inquiry. Thus, Disabled Children's Childhood Studies, as a field of inquiry, argues for a reorientation of research with disabled children. Re-orientating research to the voices and concerns of disabled children, is a shift away from generic claims related to disabled children and professionals' concerns about issues of impairment and vulnerability to inclusion of disabled children's and young people's experiences. The branch also questions the ethicality of research by foregrounding nonspecific claims about the lives of all children and yet excluding disabled children.

Disabled Children's Childhood Studies reflects disabled children's concerns and instead of posing questions like 'What is wrong with you?' it foregrounds, fundamentally ethical questions like 'What is wrong with society?' and all the more, it hits at 'What needs to change?' The relevance of this field of inquiry lies in the fact that apart from involving disabled children in research, the basic query is inevitably linked with what is constructed as the 'problem' to be researched upon. It places a special emphasis on the expertise and insights of the disabled children and their families. It completely negates pejorative practices of objectifying disabled children and nullifies all sorts of exercises in exploitation. It refutes many a deliberate attempt to invalidate their existence. The distinctness of this field of study lies in the fact that it reflects the centrality of disabled children's voices in disability studies.

Disabled Children's Childhood Studies with its focus on the experiences of the disabled children aims to challenge, recognize, investigate and change ableism. It comes down as a gentle reminder to the othering practices enabled by ableism. It identifies and changes a negative culture generated as part of ableism and targets to develop a positive all-inclusive culture. It advocates undertaking social action, participation and recreation in bringing about a positive change in the way societal forces look forward to disabled children. In essence, the voices and concerns of the child are at the heart of Disabled Children's Childhood Studies. At the same time, the voices of the family members and others who care for disabled children also play an instrumental role in Disabled Children's Childhood Studies. This paradigm shift promoted by Disabled Children's Childhood Studies is in the re-positioning of emotion in research. The historic preoccupation with normalization is challenged to the core. Alteration of this imposing paradigm of emotion begins with an aspiration for disabled children and young people and rages against normalcy. This kind of transformative research reimagines possible future for disabled children and young people.

The lived experiences of disabled children and parents, when given due stress, serve to dispel the notion of the norm and disapprove the tragedy dynamic of disablism. Disabled Children's Childhood Studies' shift away from the life-limiting, alienating, normalizing, life-threatening and segregating practices represented by medicalised and psychologised accounts of disabled children's lives, involves re-orientation of research so that disabled children and their associates can live life to the fullest. Living life to the fullest, a recently conceived and developed research project within the burgeoning field of Disabled Children's Childhood Studies, envisions new understandings of the hopes, dreams, desires and aspirations of disabled children and young people with short lives. In living life to the fullest, rather than an aporetic situation, disability becomes esteemed, lively and future facing through shared responsibility, collectivity and co-productive

research which aim to stimulate social change. The hitherto unattended lives, concerns and experien
disabled children and their families acquire an enhanced and added significance in the political, e
intellectual, emotional and institutional domains of knowledge made possible through the newly em
and surfacing field of epistemology so called as Disabled Children's Childhood Studies.

Works Cited

1. Barker, Clare et. al. eds. *The Cambridge Companion to Literature and Disability*. Cambridge
    a. UP, 2018.
2. Barnes, C. et. al. *Disability: Key Concepts*. Polity Press, 2003.
3. Barton, L. ed. *Disablity, Politics and the Struggle for Change*. David Fulton, 2001.
4. Davis, Lennard J. ed. *The Disablity Studies Reader*. Routledge, 2017.
5. Foss, Chris et. al. eds. *Disability in Comic Books and Graphic Narratives*. Palgrave Macmillan,
    a. 2016.
6. Goodley, Dan. *Disability Studies: An Interdisciplinary Introduction*. Sage, 2011.
7. ---. Disability Studies: *Theorising Disablism and Ableism*. Routledge, 2014.
8. Shakespeare, T. *Disablity, Rights and Wrongs*. Routledge, 2013.
9. Stiker, Henri Jacques. *A History of Disablity*. University of Michigan P, 2000.
10. Thomas, Gareth M. et al. eds. *Disability, Normalcy and the Everyday*. Routledge, 2018.

ISSN : 2455-4219
(UGC-Care Listed)

आलोचन दृष्टि

Aalochan Drishti

An International Peer Reviewed Refereed Research Journal of Humanities

A Special Issue on Contemporary Thought

Year - 06 **Volume - 25** **December, 2021**

प्रधान-संपादक
डॉ० सुनील कुमार मानस

संपादक
डॉ० योगेश कुमार तिवारी

प्रबंध-संपादक
श्री सुधीर कुमार तिवारी

© **प्रकाशक :**
संपादकीय / प्रकाशकीय पता :–
सृजनश्री न्यास
आजाद नगर, बिन्दकी, जनपद–फतेहपुर,
उ0प्र0–212635
ई–मेल : aalochan.p@gmail.com

मुद्रण :– जय ग्राफिक्स एण्ड कान्सट्रक्सन,
आई0टी0आई0 रोड़, फतेहपुर–212601।

सदस्यता शुल्क	एक अंक	वार्षिक	आजीवन
व्यक्तिगत	300	1200	10,000
संस्थागत	400	1500	15,000

Mapping the Art and Landscape of Literary Research

Ms. Noble A. Paliath*

Abstract

Literary Research or Literature Research, an expansive and extensive branch of inquiry in itself, is indicative of the discourses based on existing bits of info and addition of further epistemological units of info for future research in that field. English studies signify the production, interpretation, evaluation and consumption of texts created in English. It encompasses an open range of multi-disciplinary modes of communication. The current research article is a collection of different blocks of info based on the much familiar and less commonly explored wide choice of research methods deployed by many a research scholar in English studies. These research methods include textual analysis, discourse analysis, visual methodologies, auto/biographical methods, archival methods, interviewing, ethnographic methods, oral history, creative writing, quantitative analysis and ICT methods. All the afore-mentioned and suggested research methods may have plus and minus points, but have generally come down all these years as discrete and must-try types contributing productively to the successful accomplishment of the initiated research action. The multi-disciplinary nature of research methods applied by aspiring academicians belonging to the Arts and Humanities stream community stresses the need for professionals of various specializations who are increasingly being sought after in today's employment scenario. It also blurs the boundaries between diverse academic disciplines thereby ensuring profound and multifarious research inquiries.

Key Words: Literary Research, epistemological, English studies, textual analysis, discourse analysis, visual methodologies, archival methods, ethnographic methods, ICT methods, multi-disciplinary, Arts and Humanities, specializations, scenario

The concept of research methods was not widely and broadly deliberated and discussed in English studies in the olden times. What was research methods associated with English studies was a remote concept at least even during the 1980s. The only outlets available to research in English studies were a brief introduction to the vagaries and whimsies of the library. The whole process of conducting research in English studies was unknown owing to a lack of specific guidelines regarding the same. In other words, there was a marked non-visibility and continued absence of writing on research methods in certain humanities subjects including English. Historically, not much attention was paid to the issue of research training methods. Neither have a few disciplines like the Arts and Humanities made it a subject matter of serious and in-depth contemplation. Little sense was given to the knowledge about the process of conducting research in the Arts and Humanities branches and also on how you did might influence the outcome.

The above-mentioned systemic absence of research methods in certain humanities subjects including English fuelled the urgent need for lively, useful and enriching academic discussions and

* Assistant Professor Department of English Sacred Heart College, Chalakudy, Thrissur, Kerala, India

supportive inputs in this regard. This realization triggered off many intensive and productive discussions about integrated research methods in the Humanities and Social Sciences. However, with more and more attention paid to research methods in the Humanities and Social Sciences, research training in these fields of academic disciplines is ever on the move and is undergoing significant changes. During the second half of the 1990s, when the problem of research training was seriously thought of, many converged on the idea that research methods were what you asked other people to deliver to your students mainly in the form of a basic library intro and basic computing skills.

The commonsensical tradition that was much in vogue upheld the idea that research methods and skills were divorced from the academic inquiry into the subject and that it was their---both librarians' and computer technicians'---job to deliver any relevant training. At the same time, many active researchers associated with the Arts and Humanities wing employ and make use of many a research method to produce their distinct and unique academic contributions to the field of research. Nevertheless, they have remained non-articulate and mute about what is the modus operandi implemented by them so as to achieve the desired outcome. A series of responses to and corresponding views advocating research methods in English or be it any subject belonging to Arts and Humanities stream for that matter, are that research methods cannot be taught but are picked up by doing research. Such a view is clearly suggestive and reflective of the research environment that places stress and emphasis on learning by doing.In essence, research methods are something that gradually evolve and take shape in the due course of research. This kind of an observation suggests the marked absence of a significant history in lack of providing and discussing research training methods to be made use of in the Arts and Humanities research areas. However, a point to be noted is that unlike research degrees in the Social Sciences, PhDs in English do not require a methodology section but are carefully and deliberately incorporated for the sake of fulfilling and filling up different subheads that constitute a research proposal. This situation underwent a dramatic and paradigm shift with the turn of the century. Rejuvenation happened in the field of Arts and Humanities research methods with the publication of a timely report on *Postgraduate Training in Research Methods: Current Practice and Future Needs in English* (2003).However, further resurgence of innovations in these fields of study came to be conceived of as part of the initiatives of AHRB (Arts and Humanities Research Board) that acknowledged, identified and necessitated the need to nurture research cultures and encourage best practices in research training. It also foregrounded the immediate and instant need for advocating research methods as part of research training; also as a part of undertaking their research. Such an initiative spearheaded by AHRB conceived of a meta-discourse that is made eligible to communicate knowledgeably in the subject chosen and also explicitly and necessarily answers questions like how we do, what we do and why we do as part of learning about research methods. The board also promotes the view that training in research skills and techniques is an important step taken by research scholars; is the key element in the development of a research student.Thus, the notion much currently in vogue is the requirement to integrate and encapsulate proper research training in Arts and Humanities stream. A further noticeable fact is that humanities research in general and English studies in particular require and demand different kinds of research skills. A common method of instruction in this context, proves false, mismatching and ineffective. There is a limit to what you can teach in a group and combined way. The specific skills that are needed by an individual are so particular. The skills each individual acquire are part of the actual research work. It is impossible to separate skills from actual research work. Both are inseparable entities as a lot of those skills are learnt on the job; while carrying out the actual research work.As such, taking into grave consideration the nature

of research in Arts and Humanities sector, no common ways, methods, techniques and tools of what research training courses should deliver are prescribed. It points to a definitive and particular view of research; a responsive model of research. It identifies and responds to individual needs as they arise from a specific research project. What research methods are relevant to that particular project are the only ones needed to be acquired by the one doing the research concerned. Most of the scholars, for the rest of their life, will utilize only those research methods they acquired to complete their research endeavour. However, research methods training beyond the needs of a particular project, broadens a researcher's research skills and knowledge base and may be kept preserved for future needs. The idea that research students should only be taught those research methods that have direct relevance to their research work is necessarily a bone of contention. Contrastingly, understanding research methods more broadly is all about opening up the possibilities of different kinds of innovative and divergent research. It also gives researchers a wide array of choices regarding what kinds of research are to be done both in the near and far future. A sound knowledge regarding the expansive range of research methods, enables researchers to think in many ways about doing research. The present article focuses on the research methods that may be adopted by those aspiring researchers in the field of English studies. Conventionally, research carried out in the field of English studies was construed in the end as all about reading about text; it is a case of knowing your texts. This kind of a unified perception sustains the idea that the domain of English studies research is limited to text-based research and textual analysis but later with more and more studies carried out in the field proved that English studies meant much more than textual analysis; it means much more than the interaction between text and readers. The current research article is an exploratory attempt to understand and unveil a diverse range of new and different, tried and met-with-success research methods in English and also ways of conducting research in English studies. The article may also be interpreted as an examination of different research methods that might be implemented in English studies. The research methods thus not only become a tool for research but also help shape both the research and its results.

Research skills, methods and methodologies are interdependent and are helpful and useful in understanding different aspects of the research process and are also equally important and mandatory for the successful completion of a perfectly valid research project. These three together--research skills, methods and methodologies---will alone gauge and determine the focus and outcome of a research project. Research skills are techniques used for handling material. The skill sets include dissertation skills (how to construct, frame and structure sentences in a piece of writing), IT skills (use of advance computer technologies in addition to many other uses), skills in libraries (search for various info), bibliographical skills (sources used as the basis for research), editorial skills (the ability to edit and proofread written pieces of info) and professional skills (how to make effective paper presentations in the venue of academic deliberations). Research methods tell us how to carry out our research work. The choice of methods from out of the existing possible ones depends on the kind of research one wants to conduct. Research methodologies signify the perspectives the researchers may bring in to support their field of inquiry. Many a critical perspective and readings of varied literary texts are possible because different people bring different perspectives to bear on their analyses of a given text. Moreover, deciding on a particular research project to a significant extent, is deciding on the specific research skills, methods and methodologies apposite to conduct that research. However, one should not be oblivious of the fact that to accomplish the research activity successfully, all researchers require more than one research skill or method; they should employ a combo of many a method.

Of the umpteen research skills, methods and methodologies, this present article would like to add a word more about research methods in English studies in particular. Archival methods are effective ways of carrying out research in English studies. They suggest the nature of archives, why archives are established, the incompleteness of archives and the endless search for lost objects within these; also, chances of consulting other archival sources for getting the info complete in itself. Auto/biographical research methods provide a brief historical overview of changes in autobiographical writing and also the idea of the subject as individual, as part of a collective, in different kinds of auto/biographical writing. Oral history is an uncommon, not much explored and not much discussed method in English studies but such historical methods engaging the workings of personal memory, narrative, culture and transmission can make easy our comprehension of events and experiences including those of the social, cultural and literary levels.Discourse analysis may be used as a method for exploring visual signs; shows how images construct specific views of the world. It may also be used as a method for textual interpretations. Discourse analysis may be used as a method for researching both written and oral language as it is actually used, as it references a theory of language. It is concerned with analysing patterns in language use in order to unearth the workings of ideology. Computer-aided discourse analysis with the help of relevant software is also tried out by an increasingly number of researchers within English studies. It signalled a new wave of change under the banner of IT revolution in English studies. Creative writing as a research method is an important element within English departments as it aids the generation, invention, discovery and creation of different insightful ideas. With the proliferation of the field of creative arts and other arenas like music, dance, film, fine arts, video and digital works, the popularity of creative writing as a research method is ever on the increase. Creative writing constitutes an effective research method as it explores the ways in which writing skills may be used as a means of materializing varied subject matters. It is also a kind of research one makes into the nature of literary form and language. In other words, creative writing, may be considered as a metanarrative about the whole research process.

Although visual signs are part and parcel of our cultural world, visual methods are also not much discussed in English studies. These methods, with the genre and format of graphic narratives as typical examples, produce a rich visual world that forms an integral aspect of literature. Semiology and discourse analysis, as approaches, also help researchers in further decoding the complexity of visual signs. These kinds of approaches invite attention to diverse aspects of visual images and thus suggest new avenues of research for English studies. It is to be noted that visual images do not only accompany texts, but texts too accompany visual images as in case of captions to photographs, textual accompaniments to images in books and so on. This interplay between text and image is an area of research that deserve yet another focus of attention in English studies research. Textual analysis method is all about close readings of cultural artefacts. A background research into the context of the cultural artefacts under scrutiny, the context of its production, its thematic concern and its consumption are given due focus and emphasis in this method. The process of meaning-making which is differently understood in different historical eras and by different historians is also a key factor in undertaking textual analyses. Interviewing is also an effective research method in English studies research. However, it requires a series of practical skills, a fair understanding of the different kinds of interview one might conduct, all possible ways of conducting interviews et cetera are also explored by researchers. Interview cannot be labelled as a stand-alone method as it often combines with other research methods and forms a central plank of many a research process. Ethnographic research methods inform a variety of literary outpourings that might be analyzed in the context of English studies. These methods may be

extended to cultural and social practices, especially in the field of travel writing or travelogues wherein participant observations play a key role in producing travel accounts. Also, audience research in the theatre, film and at performing sites such as literature festivals might be conducted using ethnographic methods. Quantitative methods of research in the study of literature, especially in the form of words (subjective) and numbers (objective), form interpretive tools and serve as a means of conveying sets of valuable info. Specifically, statistical methods are highly useful for displaying info about texts, audiences' production and consumption of texts and so on. ICT as a research method in English studies is a recently emergent phenomenon. Nevertheless, it is carried out by specialist researchers associated with the fields of textual analysis and linguistics. With the scientific strides and advancements in the field of technology and advent of more and more computer software and hardware, enhanced opportunities for researchers in literary studies are ensured to work on literary and other texts. This kind of research method discusses various ways in which ICT has been used to store and analyze literary texts. How computers as a medium changed our relations to texts, issues involved in creating digital archives of manuscript sources, literature digitization projects and the possibilities of collaborative research are also possible areas of exploration while pursuing ICT as a research method.

The current article may be considered as an attempt to engage and showcase different research methods in English studies that are relevant to be pursued by research students, researchers and research methods teachers in this era of accentuated and heightened research activities. This kind of analysis, non-conclusive in itself, underscores the fact that in addition to the above mentioned research methods; there are also other possible and viable areas of research practices yet to be explored by the research aspirants. A detailed critical scrutiny of the above enlisted research methods in English studies, may tend one to evolve a critical stance that all these methods aid a kind of scientisation of humanities and are inappropriate to be pursued by the humanities community itself. But instead of thinking of stringent research methods exclusively to be followed by those pursuing humanities disciplines only, let research activities be more and more dialogic and collaborative across disciplines. This kind of an accommodative approach, that blurs the boundaries and distinctions between different fields of study, may encourage researchers to think divergently about the kinds of research across a range of disciplinary backgrounds they might engage in.

References :-

1. Cauvery, R. et al. Research Methodology. S. Chand and Compamy Pvt. Ltd., 2010.
2. Dhingra, Manish. et al. Research Methodology. Enkay Publishing House, 2012.
3. Griffin, Gabriele. editor. Research Methods for English Studies. Rawat Publications, a.2007.
4. Gupta, Mukul. et al. Research Methodology. PHI Learning Pvt. Ltd., 2011.
5. Kothari, C. R., et al. Research Methodology: Methods and Techniques. Second Revised a Edition. New Age International Publishers, 2010.
6. Sadie, William. Postgraduate Training in Research Methods: Current Practice and a Future Needs in English. English Subject Centre, 2003.
7. Sam Daniel, P. et al. Research Methodology. Kalpaz Publications, 2007.
8. Singh, Abhilasha. et al. Research Methodology: Tools, Techniques and Methods. Axis. a. Books (P) Ltd. Production, 2013.
9. Srivastava, Raju. Research Methodology in English Studies. Sublime Publications, 2013.
10. Vijayalakshmi, G. et al. Research Methods: Tips and Techniques. MJP Publishers, 2009.
11. Walliman, Nicholas. Your Research Project: Designing and Planning Your Work. Third a. Edition. Sage, 2011.

Received: 3 February 2021 | Revised: 24 April 2021 | Accepted: 12 May 2021

DOI: 10.1002/jmr.2916

RESEARCH ARTICLE

Journal of Molecular Recognition WILEY

Spectroscopic, density functional theoretical study, molecular docking, and *in vitro* studies based on anticancer activity studies against A_{549} lung cancer cell line of diphenylhydantoin adsorbed on AuNPs surface

V. Shyni[1] | D. R. Leenaraj[2] | Reena Ittyachan[3] | Lynnette Joseph[1] | D. Sajan[1]

[1]Centre for Advanced Functional Materials, Department of Physics, Bishop Moore College, Mavelikara, Kerala, India

[2]Department of Physics, Mar Ivanios College, Thiruvananthapuram, Kerala, India

[3]Department of Physics, Sacred Heart College, Chalakudy, Kerala, India

Correspondence
Lynnette Joseph, Centre for Advanced Functional Materials, Department of Physics, Bishop Moore College, Mavelikara, Kerala 690110, India.
Email: lynnettejohn@gmail.com

Funding Information
DST FIST, Grant/Award Number: SR/FST/College-182/2013, November 2013 & FIST No.3

Abstract

The optimized geometry, FT-Raman, FT-IR, surface-enhanced Raman scattering, UV-Vis spectra, frontier molecular orbital analysis, molecular electrostatic potential analysis, and local and global reactivity descriptors of diphenylhydantoin (DPH) and diphenylhydantoin@AuNPs (DPHA) molecule have been investigated with the help of density functional theory method (B3LYP/6-31++G [d,p] together with LANL2DZ) and was compared and analyzed with the corresponding experimental data in order to identify their structural and bonding features responsible for their bioactivity. *In-silico* (molecular docking) biological activity screening of the molecules together with the *in-vitro* (SERS and MTT assay) analysis confirms the anticancer activity of DPH and DPHA molecules. The results of the structure-activity studies and bioactivity studies signify that the DPHA molecule is more active than the DPH molecule against lung cancer.

KEYWORDS
conjugation, Fukui, ICT, molecular docking, MTT assay, SERS

1 | INTRODUCTION

Hydantoin fascinated a lot of attention as it provides four derivatization positions including two hydrogen bond acceptors and two hydrogen bond donors, which are considered a valuable privileged scaffold in drug discovery.[1] The uniqueness of the hydantoin ring is that it gives a combined effect of both imides and carbonyl groups. In particular, hydantoin, which has a fifth-place replacement carbon atom, has more pharmaceutical effect.[2-4] In the absence of a functional group, the biphenyl ring has a neutral molecular effect.[5] Replacement of the hydrogen atoms with a biphenyl ring in the fifth position of the hydantoin ring (DPH) gives planarity to the ring and significantly enhances its optical brightener and pharmaceutical properties.[6,67] Moreover, biological activity such as anticonvulsant,[7,8] epilepsy,[9,10] and antidiuretic[11] has also been reported in such molecules. The inherent pharmacological significance of the DPH molecule and the biocompatibility of refractory metals[12] guided researchers to combine the two on the same platform.[13-16] The different photochemical properties (low cytotoxicity, ease of synthesis, and biophysically compatible fabrication)[17] make AuNPs superior to other metal nanoparticles in terms of performance and attract the attention of researchers. This paved way for us to study of the combination of DPH molecule and the AuNPs and to investigate its enhancement in potential activity. Literature survey shows that, although studies on the electronic structure, spectroscopic, and cancer functions of the DPH and DPHA molecules have been conducted,[18-21] no in-depth studies have been conducted. Spectroscopic and quantum chemical investigations of the vibrational spectra for the DPH and DPHA molecule and its derivatives were also peripherally studied.[13,22,23] Study of the relationship between the structure–property and the stability of the system before and after adsorption of Au NPs (DPH and

 © 2021 John Wiley & Sons Ltd.

diphenylhydantoin@AU NPs (DPHA), respectively) in a comprehensive manner, using spectroscopic techniques combined with DFT computations as well as in vitro and in silico analyses, which throws light on the potential of DPHA for targeted drug delivery and photothermal therapy, has not yet reported. In the present study, the probable reactive sites are made out from the molecular electrostatic potential (MEP) surface analysis and the molecular reactivity of DPH and DPHA through global and local reactivity descriptors derived from the density functional theory (DFT). The molecular docking analysis was also carried out to perceive the inhibitory nature of DPH molecule against cancer proteins. Surface-e Raman scattering (SERS) study of DPHA was performed to study the intramolecular charge transfer mechanism between Au NPs and DPH and has been theoretically investigated by density functional theory (DFT) calculations. Further, SERS mapping has been used for the recognition of cancer cells with DPHA, and the destruction of cancer cells has been studied by MTT assay.

2 | METHODS

2.1 | Preparation of gold colloids, cell culture, and protocol used for MTT assay

Diphenylhydantoin (99%), gold (III) chloride trihydrate (99.99%), and trisodium citrate (99%) were purchased from Sigma-Aldrich and used without further purification. Double distilled water was used throughout the experiments. The procedure for preparation of gold colloids, the cell culture of human lung cancer cell lines A_{549}, and the protocol used for MTT assay are detailed in our earlier report.[24]

2.2 | Instrumentation

The FT-IR spectrum of DPH molecule was recorded in the region 4000-400 cm^{-1} using a PerkinElmer Spectrum One FT-IR Spectrometer in the KBr matrix, and the interferogram was collected at an optical resolution of 1 cm^{-1}. The FT-Raman spectrum of the DPH molecule was recorded using 1064 nm line of Nd:YAG laser as excitation wavelength and an output of 150 mW, in the region 3500 to 50 cm^{-1} on a BRUKER RFS 27: Standalone FT-Raman spectrometer using the powdered form of the sample. The spectral resolution after apodization was 2 cm^{-1}. The absorption spectra of the DPH and DPHA were recorded in DMSO as a solvent using PerkinElmer lambda 950 UV-VIS-NIR in the region 200-800 nm. Particle size measurements were performed on a high-resolution transmission electron microscopy (Tecnai T30 G2 S-Twin, FEI Company). Samples for TEM characterization were prepared by placing a drop of gold colloidal solution on a carbon-coated copper grid and dried under an IR lamp. SERS experiments were carried out by incubating DPH with citrate-stabilized spherical Au NPs (Au NPs; 40 nm) as a SERS substrate, and the spectra were recorded by a WI-Tec Raman microscope (633 nm excitation wavelength, 7 mW power laser) in the range 200-3000 cm^{-1} with 2 cm^{-1} resolution and an integration time of 0.5 and 20, accumulations. A_{549} lung cancer cells were cultured in a four-well chamber slide, and 100 μL (9:1, Au NPs/ DPH) of DPHA was added to the wells separately and was incubated at 37°C. SERS spectra were recorded after 30 minutes. SERS mapping has been performed using two cells by confocal Raman microscopy using 0.5 as integration time, 150 × 150 as points per line, and 50 × 50 μm mapping area along with X and Y directions. The excitation and emission spectra were documented on a SPEX Fluorolog F112X spectrofluorimeter.

2.3 | Computational details

Equilibrium geometry and harmonic vibrational wavenumbers were calculated using the pure DFT models using the Gaussian'09 suite software package[25] which provides a good compromise between computational time and accuracy as well as excellent agreement with experimental results. The combined use of Hartree-Fock and Becke exact exchange functionals[26] with the Lee-Yang-Parr correlation (LYP)[27] hybrid functional with the standard basis set 6-31++G (d,p) and the electron core potential basis set LANL2DZ[28] were used for the DPH and DPHA molecule calculations, respectively. The detailed computation about quantum chemical insight (geometry optimization, vibrational wave number calculation on the basis of the potential energy distribution [PED], natural bond orbital [NBO] analyses) and in silico studies (docking) is detailed in our earlier report.[24]

3 | RESULTS AND DISCUSSION

3.1 | Structural description

The stable structure of the bioactive conformer of DPH and DPHA molecules along with their atom numbering scheme is shown in Figure 1A and B. The most important structural parameters of the stable conformers of both molecules are summarized in Table 1. The calculated structural parameters (gas phase) are compared with reported (solid phase) crystallographic data (CCDC No: 1811138).[29] The comparison of theoretical and experimental geometrical parameters using linear regression coefficient (R^2) calculations is graphically represented in Figure 2. The R^2 shows the reliability of theoretical calculation, however, a little bit deviation is observed. Stabilized conformation of DPH and DPHA shows that the phenyl rings are *cis* oriented, and the hydantoin ring is in *trans* orientation relative to the phenyl rings. Moreover, the molecules adopted *anticlinal* conformation (Y-shaped conformation). The values of connected exocyclic angles between phenyl and hydantoin rings are 112.56° (C_3-C_{12}-N_{13}), 112.62° (C_3-C_{12}-C_{21}), and 112.50° (C_{16}-C_{12}-C_{21}) in DPH.

In Ph1, the calculated bond lengths of C_1-H_7, C_2-H_8, C_4-H_9, C_5-H_{10}, and C_6-H_{11} are 1.0842, 1.0827, 1.0829, 1.0842, and 1.0842, respectively. Here, it shows that there is a slight asymmetry in the

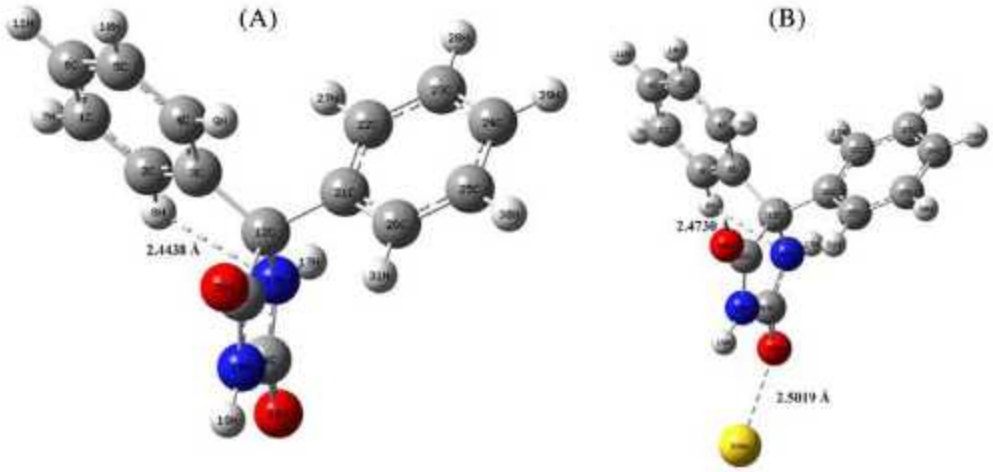


FIGURE 1 Optimized structure of (A) DPH with 6-31++G (d,p) basis set and (B) DPHA with LANL2DZ basis set using B3LYP functional

TABLE 1 Optimized geometrical parameters of the DPH and DPHA molecule along with corresponding experimental data obtained by XRD

Bond length (Å)				Bond Angle (˚)				Torsional Angle (°)			
	DFT				DFT				DFT		
Parameter	DPH	DPHA	[a]Exp.	Parameter	DPH	DPHA	[a]Exp.	Parameter	DPH	DPHA	[a]Exp.
C_3-C_4	1.4007	1.4118	1.389	C_2-C_3-C_4	119.15	119.37	118.02	C_3-C_{12}-N_{13}-H_{17}	87.49	75.06	62.61
C_1-H_7	1.0842	1.0872	0.929	C_3-C_{12}-N_{13}	112.56	112.24	112.42	C_3-C_{12}-N_{13}-C_{14}	−119.94	−113.93	−117.39
C_2-H_8	1.0827	1.0860	0.930	C_{12}-N_{13}-C_{14}	113.79	114.02	113.65	C_{12}-N_{13}-C_{14}-N_{15}	7.12	1.17	3.42
C_4-H_9	1.0829	1.0862	0.930	N_{13}-C_{14}-N_{15}	105.55	106.52	107.27	N_{13}-C_{14}-N_{15}-C_{16}	−6.41	−2.58	−2.53
C_5-H_{10}	1.0842	1.0871	0.930	C_{14}-N_{15}-C_{16}	113.66	112.88	111.99	C_{14}-N_{15}-C_{16}-C_{17}	3.26	2.85	0.73
C_6-H_{11}	1.0842	1.0872	0.930	N_{15}-C_{16}-C_{12}	106.03	106.39	107.01	C_{16}-C_{12}-N_{13}-C_{14}	−5.09	0.46	−2.83
N_{13}-C_{14}	1.3711	1.3689	1.333	C_{16}-C_{12}-N_{13}	100.49	100.12	99.97	H_{17}-N_{13}-C_{14} − O_{18}	−19.63	−7.46	3.25
C_{14}-N_{15}	1.4079	1.4068	1.394	C_{16}-C_{12}-C_{21}	112.50	113.01	113.02	O_{18} − C_{14}-N_{15}-H_{19}	−3.04	−1.89	−2.44
C_{14}-N_{13}	1.3711	1.3689	1.367	C_3-C_{12}-C_{21}	112.62	112.88	112.18	H_{19}-N_{15}-C_{16} − O_{20}	−0.31	1.32	0.23
C_{14}-N_{15}	1.4079	1.4068	1.456	C_{21}-C_{22}-C_{23}	120.69	120.58	120.90	O_{20} − C_{16}-C_{12}-C_{21}	64.54	61.93	64.76
C_{21}-C_{22}	1.4004	1.4133	1.372	C_{22}-C_{23}-C_{24}	120.13	120.07	120.62	O_{20} − C_{16}-C_{12}-C_3	−60.50	−63.71	−60.10
C_{14} = O_{18}	1.2071	1.2551	1.218	N_{13}-C_{14}-O_{18}	128.60	127.11	124.86	H_{17}-N_{13}-C_{14}-O_{18}	−19.63	−7.46	−5.76
H_8···N_{13}	2.4438	2.4730	2.482	C_{23}-C_{24}-C_{25}	119.55	119.57	118.52	H_{19}-N_{15}-C_{14}-O_{18}	−3.04	−1.89	−0.34
O_{18}···Au_{32}	-	2.5019	-	C_{14} O_{18}···Au_{32}	-	126.66	-	N_{15}-C_{14}-N_{13}-H_{17}	160.63	178.28	178.80

[a]Taken from Ref [34].

C–H bond lengths. That is the C_2-H_8 bond and C_4-H_9 is slightly shorter than the other three. The shortening of C_2-H_8 bond may be due to the C–H···N intramolecular hydrogen bonding between C_2-H_8 in Ph1 and hydantoin N_{13} (C_2-H_8···N_{13}). The distance of H_8···N_{13} is significantly shorter than the van der Waals separation between nitrogen and hydrogen atom; 2.4438 Å for DPH and 2.4730 Å for DPHA. In the case of DPHA, the strength of the hydrogen bonding can be seen to be very low compared to DPHA. The corresponding bond angle of C_2-H_8···N_{13} is 99.93° and 99.37° for DPH and DPHA, respectively. It can be seen that the exocyclic torsion angle around the C_{14}-N_{13} bond has changed due to this intramolecular hydrogen bonding. The associated torsional angles, O_{18} = C_{14}-N_{15}-H_{19} and H_{17}-N_{13}-C_{14} = O_{18} in DPH are −0.31°, −3.04° and − 19.63°, respectively and the torsional angles, H_{19}-N_{15}-C_{16} = O_{20}, O_{18} = C_{14}-N_{15}-H_{19}, and H_{17}-N_{13}-C_{14} = O_{18} in DPHA are 1.32°, −1.89°, and − 7.46°, respectively.

The N_{13}-C_{14} and C_{14}-N_{15} bond lengths in DPHA molecule (N_{13}-C_{14} = 1.3689 Å and C_{14}-N_{15} = 1.4068 Å) are significantly shorter than the N_{13}-C_{14} and C_{14}-N_{15} bond lengths in the DPH molecule (N_{13}-C_{14} = 1.3711 Å and C_{14}-N_{15} = 1.4079 Å). This discrepancy is due to the conjugation of electrons of the AuNPs and carbonyl bond, allowing the electrons to smear out along the C-N bond. Similarly, the length of the carbonyl group involved in conjugation is seen to be longer. The increase of the C-C bond length in the phenyl rings proves that this conjugative interaction is responsible for the intramolecular charge transfer (ICT) toward the Ph1 and Ph2. It can

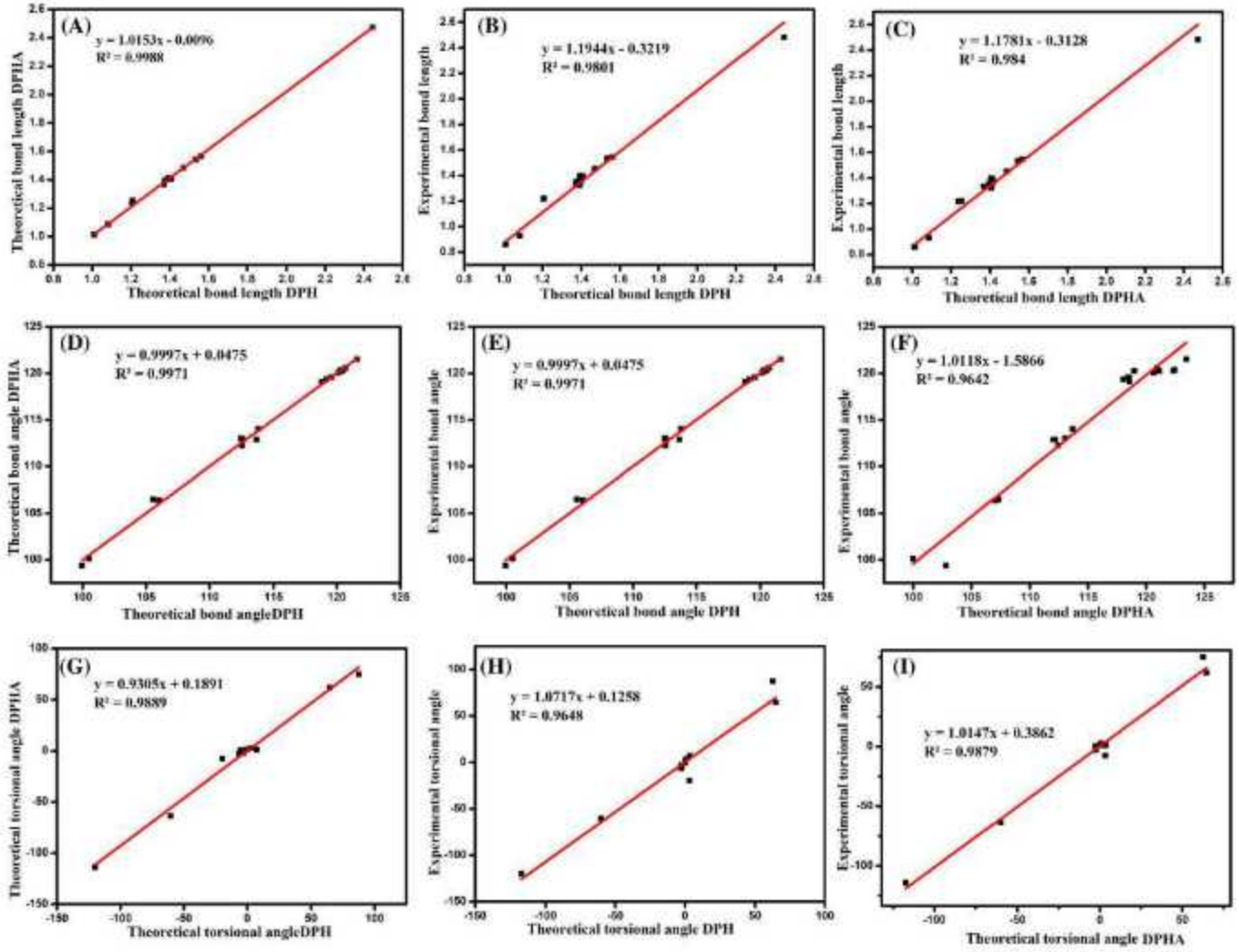


FIGURE 2 Linear regression coefficient (R^2) of bond length (A) theoretical DPH and DPHA (B) Experimental and theoretical DPH (C) Experimental and theoretical DPHA, Bond angle of (D) theoretical DPH and DPHA (E) Experimental and theoretical DPH (F) Experimental and theoretical DPHA, Torsional angle (G) theoretical DPH and DPHA (H) Experimental and theoretical DPH (I) Experimental and theoretical DPHA

be seen that the comparatively longest bond distances are of C_3-C_4 and C_{21}-C_{22} which are situated at the junction of the Ph1, Ph2, and hydantoin rings (Table 1), than any other C—C bond length in optimized structure. Consequences of this ICT are the shrinking of the endocyclic angles centered at C_3 and C_{21} which are 119.37° (C_2-C_3-C_4) and 119.12° (C_{22}-C_{21}-C_{26}), respectively (for DPHA). In DPH molecule, the shrinking of the endocyclic angles centered at C_3 and C_{21} are 119.15° and 118.82°, respectively. The lengthening of bond length $C_{14} = O_{18}$ (1.26 Å) in the DPHA molecule than DPH (1.21 Å) is due to the hydrogen bonding between DPH and AuNPs (C_{14}-O_{18}···Au_{32}). The bond angle H_{17}-N_{13}-$C_{14} = O_{18}$ is increased and H_{19}-N_{15}-$C_{14} = O_{18}$ is decreased. This evidence that charge transfer occurs between the DPH molecule and AuNPs through $C_{14} — O_{18}$. In short, each part of the DPH and DPHA molecule is balanced by conjugative as well as ICT interactions leading to molecular stability. Nevertheless, these interactions are more pronounced in DPHA than DPH.

3.2 | NBO analysis

3.2.1 | Donor–acceptor interactions

The NBO evaluation offers second-order perturbative estimates of exact donor–acceptor interactions in the NBO basis which are expressed in kcal/mol and symbolize the stabilizing effect owing to the interaction between filled Lewis and empty non-Lewis-type NBOs. The major interactions of DPH and DPHA in terms of higher E (2) values are listed in Table 2. NBO data show that the conjugative interactions in the DPHA molecule are n_1 (N_{13}) → $\pi^*(C_{14} = O_{18})$, $n_1(N_{15}) \rightarrow \pi^*(C_{14} - O_{18})/\pi^*(C_{16} = O_{20})$, $n_2(O_{18}) \rightarrow \sigma^*(N_{13}\text{-}C_{14})/\sigma^*(C_{14}\text{-}N_{15})$, $n_2(O_{20}) \rightarrow \sigma^*(C_{12}\text{-}C_{16})/\sigma^*(N_{15}\text{-}C_{16})$ with stabilization energy equal to 52.05 46.25, 56.30, 24.72, 28.37, 23.14, and 27.20 kcal/mol, respectively. The same donations in the DPH molecule change to 36.77, 30.23, 28.81, 10.25, 10.99, 10.53, and 12.82 kcal/mol, in the same order. The two vicinal orbitals like π and π^* strongly overlap, and

TABLE 2 Selective donor–acceptor hyperconjugative interactions of DPH and DPHA

	Donor (i)		Acceptor (j)				
	NBO	Occupancy	NBO	Occupancy	E(2)[a] kcal/mol	E(j)-E(i)[b] (a.u.)	F(i,j)[c] (a.u.)
DPH	$\pi(C_1\text{-}C_6)$	1.97961	$\pi^*(C_2\text{-}C_3)$	0.02402	11.10	0.28	0.068
	$\pi(C_1\text{-}C_6)$	1.97961	$\pi^*(C_4\text{-}C_5)$	0.01555	10.56	0.29	0.067
	$\pi(C_2\text{-}C_3)$	1.67512	$\pi^*(C_1\text{-}C_6)$	0.01627	10.85	0.29	0.067
	$\pi(C_2\text{-}C_3)$	1.67512	$\pi^*(C_4\text{-}C_5)$	0.01555	10.31	0.29	0.067
	$\pi(C_4\text{-}C_5)$	1.66000	$\pi^*(C_1\text{-}C_6)$	0.01627	10.96	0.28	0.068
	$\pi(C_4\text{-}C_5)$	1.66000	$\pi^*(C_2\text{-}C_3)$	0.02402	11.55	0.28	0.069
	$\pi(C_{21}\text{-}C_{26})$	1.97245	$\pi^*(C_{22}\text{-}C_{23})$	0.01532	10.45	0.28	0.068
	$\pi(C_{21}\text{-}C_{26})$	1.97245	$\pi^*(C_{24}\text{-}C_{25})$	0.01605	10.45	0.29	0.067
	$\pi(C_{22}\text{-}C_{23})$	1.97723	$\pi^*(C_{21}\text{-}C_{26})$	0.02404	11.37	0.29	0.069
	$\pi(C_{22}\text{-}C_{23})$	1.97723	$\pi^*(C_{24}\text{-}C_{25})$	0.01605	10.64	0.28	0.067
	$\pi(C_{24}\text{-}C_{25})$	1.97960	$\pi^*(C_{21}\text{-}C_{26})$	0.02404	11.50	0.28	0.069
	$\pi(C_{24}\text{-}C_{25})$	1.97960	$\pi^*(C_{22}\text{-}C_{23})$	0.01532	10.77	0.28	0.068
	$n_1(N_{13})$	1.75258	$\pi^*(C_{14}=O_{18})$	0.01309	36.77	0.29	0.113
	$n_1(N_{15})$	1.65397	$\pi^*(C_{14}=O_{18})$	0.01309	30.23	0.29	0.104
	$n_1(N_{15})$	1.65397	$\pi^*(C_{16}=O_{20})$	0.01043	28.81	0.29	0.117
	$n_2(O_{18})$	1.97852	$\sigma^*(N_{13}\text{-}C_{14})$	0.07659	10.25	0.69	0.120
	$n_2(O_{18})$	1.97852	$\sigma^*(C_{14}\text{-}N_{15})$	0.09152	10.99	0.64	0.122
	$n_2(O_{20})$	1.84231	$\sigma^*(C_{12}\text{-}C_{16})$	0.09374	10.53	0.58	0.105
	$n_2(O_{20})$	1.84231	$\sigma^*(N_{15}\text{-}C_{16})$	0.07963	12.82	0.70	0.126
DPHA	$\pi(C_1\text{-}C_6)$	0.99060	$\pi^*(C_2\text{-}C_3)$	0.01295	20.50	0.28	0.070
	$\pi(C_1\text{-}C_6)$	0.99060	$\pi^*(C_4\text{-}C_5)$	0.00766	19.46	0.28	0.069
	$\pi(C_2\text{-}C_3)$	0.98599	$\pi^*(C_1\text{-}C_6)$	0.00809	19.35	0.28	0.070
	$\pi(C_2\text{-}C_3)$	0.98599	$\pi^*(C_4\text{-}C_5)$	0.00766	19.37	0.28	0.069
	$\pi(C_4\text{-}C_5)$	0.98853	$\pi^*(C_1\text{-}C_6)$	0.00809	20.49	0.28	0.070
	$\pi(C_4\text{-}C_5)$	0.98853	$\pi^*(C_2\text{-}C_3)$	0.01295	20.87	0.27	0.071
	$\pi(C_{21}\text{-}C_{26})$	0.98619	$\pi^*(C_{22}\text{-}C_{23})$	0.00753	20.08	0.29	0.069
	$\pi(C_{21}\text{-}C_{26})$	0.98619	$\pi^*(C_{24}\text{-}C_{25})$	0.00801	19.56	0.29	0.069
	$\pi(C_{22}\text{-}C_{23})$	0.98864	$\pi^*(C_{21}\text{-}C_{26})$	0.01296	20.66	0.27	0.071
	$\pi(C_{22}\text{-}C_{23})$	0.98864	$\pi^*(C_{24}\text{-}C_{25})$	0.00801	19.92	0.28	0.070
	$\pi(C_{24}\text{-}C_{25})$	0.99058	$\pi^*(C_{21}\text{-}C_{26})$	0.01296	20.83	0.27	0.071
	$\pi(C_{24}\text{-}C_{25})$	0.99058	$\pi^*(C_{22}\text{-}C_{23})$	0.00753	20.34	0.28	0.070
	$n_1(N_{13})$	0.85858	$\sigma^*(C_{14}=O_{18})$	0.20271	52.05	0.24	0.121
	$n_1(N_{15})$	0.82297	$\pi^*(C_{14}=O_{18})$	0.00732	46.25	0.24	0.110
	$n_1(N_{15})$	0.82297	$\pi^*(C_{16}=O_{20})$	0.00572	56.30	0.26	0.113
	$n_2(O_{18})$	0.97746	$\sigma^*(N_{13}\text{-}C_{14})$	0.03174	24.72	0.69	0.108
	$n_2(O_{18})$	0.97746	$\sigma^*(C_{14}\text{-}N_{15})$	0.03689	28.37	0.63	0.106
	$n_2(O_{20})$	0.98669	$\sigma^*(C_{12}\text{-}C_{16})$	0.04643	23.14	0.56	0.098
	$n_2(O_{20})$	0.98669	$\sigma^*(N_{15}\text{-}C_{16})$	0.04058	27.20	0.64	0.116
	$n_6(Au_{32})$	0.00136	$\pi^*(C_{14}=O_{18})$	0.20271	29.25	0.65	0.040

[a]E(2) is the energy of orbital interactions.
[b]E(j)-E(i) is the energy difference between donor and acceptor i and j NBO orbitals.
[c]F(i,j) is the Fock matrix element between i and j NBO orbitals.

the resulting ICT interaction has important consequences for structure and reactivity of the molecules. In both molecules, almost similar ICT interactions were noticed. The stabilization energy of these interactions shows that DPHA has comparatively higher value. The very important interactions among them are the electron donation of C-C orbitals to the neighboring antibonding C-C orbital's in the Ph1

and Ph2 ring [$\pi(C_1\text{-}C_6) \rightarrow \pi^*(C_2\text{-}C_3)/\ \pi^*(C_4\text{-}C_5)$, $\pi(C_2\text{-}C_3) \rightarrow \pi^*(C_1\text{-}C_6)/\ \pi^*(C_4\text{-}C_5)$, $\pi(C_4\text{-}C_5) \rightarrow \pi^*(C_1\text{-}C_6)/\ \pi^*(C_2\text{-}C_3)$, $\pi(C_{21}\text{-}C_{26}) \rightarrow \pi^*(C_{22}\text{-}C_{23})/\ \pi^*(C_{24}\text{-}C_{25})$, $\pi(C_{22}\text{-}C_{23}) \rightarrow \pi^*(C_{21}\text{-}C_{26})/\ \pi^*(C_{24}\text{-}C_{25})$, $\pi(C_{24}\text{-}C_{25}) \rightarrow \pi^*(C_{21}\text{-}C_{26})/\ \pi^*(C_{22}\text{-}C_{23})$], which clearly manifests the evidences for the elongation and weakening of the C-C bonds in the two phenyl rings. Another charge transfer interaction from n_6 (Au_{32}) to $\sigma^*(C_{14} = O_{18})$ with stabilization energy of 29.25 kcal/mol stabilization energy was predicted in DPHA molecule. In short, the NBO results show that the conjugative and ICT interactions are dominant in DPHA molecule.

3.2.2 | Natural population analysis

The population analysis is a mathematical way of partitioning the wave function of electron density within the molecule.[30] Natural population analysis of DPH and DPHA molecule is shown in Figure S1. All carbon atoms except C_{14} and C_{16} in DPH and C_3, C_{12}, C_{14}, C_{16}, and C_{21} in DPHA exhibit a negative charge. The C_{14} and C_{16} carbon atoms show high positive charge in the DPH molecule. However, when AuNPs were adsorbed into the DPH molecule, the positive charge of both atoms decreased. This may be due to the electron-withdrawing nature of electronegative atoms (oxygen) bonded with the carbon atom. The positive charge of the C_{14} atom decreased more than that on C_{16}, and it may be due to the ICT between AU NPs and DPH molecule. When AuNPs are adsorbed by the DPH molecule, the charges on skeletal carbon atoms C_3, C_{12}, and C_{21} are converted from negative to positive which confirms ICT and the consequent variation in C—C bond length and bond angle. All hydrogen atoms show positive charge, among them H_{17} (0.349) and H_{19} (0.386) show more positive charges and are due to the electron-withdrawing nature of the nitrogen atom attached to them. In addition, after adsorptions of the electronegative AuNPs to the DPH molecule, AuNPs become positively charge revealing that the charge is delocalized.

3.3 | Frontier molecular orbital analysis and electronic spectra

Frontier molecular orbitals (FMOs) energies, energy gap, and excitation energies have an influence on the stability of a molecule. Also, it interprets the chemical and biological reactivity of the molecules. Frontier molecular orbital isosurface plots of the DPH and DPHA molecule are shown in Figure 3B and C, respectively. In the HOMO of the DPH molecule, the electron distribution is scattered over ph 1 than at ph 2, resulting in −6.52 eV of energy. On the other hand, the HOMO of the DPHA molecule is spread over the hydantoin ring and ph 2 resulting in −5.32 eV energy. The LUMO map of the DPH molecule demonstrates the distribution of electrons equally at ph 1 and ph 2 with energy of −2.02 eV. The LUMO map of the DPHA molecule shows that there is an electronic distribution in the phenyl ring moieties with energy of −3.79 eV. The well-overlapped HOMO and LUMO frontier orbitals on all σ-electron hyperconjugated bonds (skeletal $C_3\text{-}C_{12}\text{-}C_{21}$) have occurred more in DPHA than DPH molecule which benefits the strong HOMO→LUMO transition in DPHA molecule. The DPH molecule adsorbed on AuNPs (DPHA) almost maintains the HOMO distribution unchanged but affects the LUMO distribution more, which leads to the decrement in the energy gap value. The band gap energy of the DPH molecule is reduced from 4.50 eV to 1.53 eV as Au NPs are attached to DPH. So, electron movement between these orbitals is easily facilitated in DPHA, thereby increasing the molecular electrical transport properties and photostability. As photostability increases, its drug stability also increases. Also, the lowering of the energy gap is promoted through the interaction between a lone pair electron in the AuNPs and π-electron conjugation in the ring system.[31,32] Thus, it may be concluded that the high value of HOMO and the narrow energy gap for DPHA are manifested in its high reactivity with low kinetic stability when compared to DPH.

The global chemical reactivity descriptors like ionization potential (A), electron affinity (I), electronegativity (χ), chemical potential (μ), electrophilicity index (ω), chemical hardness (η), and softness (S) are based on HOMO-LUMO energy values. These chemical descriptors were defined by Koopman's theorem[33] expressed by the relations, $I = -E_{HOMO}$, $A = -E_{LUMO}$, $\eta = \frac{(I-A)}{2}$, $S = \frac{1}{\eta}$, $\mu = \frac{-(I+A)}{2}$, $\chi = \frac{(I+A)}{2}$, $\omega = \frac{\mu^2}{2\eta}$. The calculated values of I, A, χ, μ, η, S, and ω are 6.13 eV, 1.63 eV, 3.88 eV, 3.88 eV, 2.25 eV, 0.44 $(eV)^{-1}$, and 3.35 eV, respectively, for DPH molecule. And for DPHA molecule, the calculated values of I, A, χ, μ, η, S, and ω are 3.66 eV, 2.13 eV, 2.89 eV, 2.89 eV, 0.77 eV, 1.31 $(eV)^{-1}$, and 5.48 eV, respectively. The chemical hardness of the DPH molecule is higher than that of the DPHA molecule. This shows that the DPHA molecule has more electronegativity and chemical stability than the DPH molecule. Also, the electrophilicity index of the DPHA molecule is higher than the DPH molecule which causes the energy lowering due to electron flow between the donor and acceptor. The values of the global chemical reactivity descriptors disclose that the DPHA molecule is more reactive than the DPH molecule.

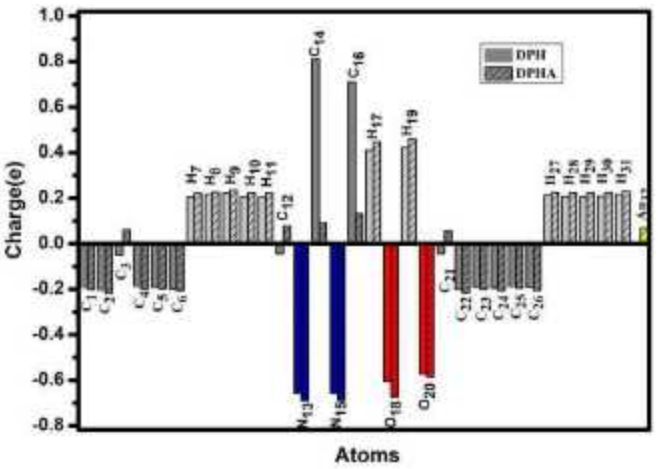


FIGURE 3 (A) Electronic transitions of simulated and observed UV–vis spectra of DPH and DPHA molecule, (B) graphical representation of frontier molecular orbital of DPH molecule, and (C) graphical representation of frontier molecular orbital of DPHA molecule

The electron density–based local reactivity descriptors such as Fukui functions (f_k^+,f_k^-,f_k^0), local softness (S_k^+, S_k^-, S_k^0), and local electrophilicity indices (ω_k^+, ω_k^-, ω_k^0) were calculated for the DPH and DPHA molecules using Mulliken population analysis to predict the possible electrophilic and nucleophilic reactive site of the molecule.[34,35] From the observation (Table S2), it is evident that the most susceptible site to electrophilic attack and the nucleophilic attack is located on the O_{18}, N_{15}, and the C_{14} atoms in the hydantoin ring, respectively, for both molecules. Therefore, the above result confirmed that the most reactive sites is located on C_{14}, and free radical attacks are more probable on oxygen (O_{18}) in the hydantoin ring. In a free radical attack, the nitrogen (N_{15}) atom of the hydantoin ring is almost similar to the oxygen (O_{18}) atom in the hydantoin ring. The reactive sites of DPH are similar to that of DPHA molecules but the corresponding intensities being higher in the DPHA molecule. Free radicals occur when atoms or molecules gain or lose electrons, meaning that adsorption of AuNPs in the DPH molecule facilitates the flow of electrons, *that is*, ICT. Literature review [36] shows that free radicals are volatile molecules that destroy cancer cells in the body, meaning that the DPHA molecule can further destroy cancer cells. The results of frontier molecular orbitals energy gap, global, and local reactive descriptors reveal that the DPHA molecule shows higher cancer activity than the DPH molecule. The molecular electrostatic potential (MEP) also predicts reactive sites for electrophilic or nucleophilic attack. It gives the 3D conformation of the Fukui function. In Figure 4A and B, it is evident that electronegative oxygen and nitrogen in DPH and Au NPs in DPHA show negative potential, while nucleophilic reactive hydrogen atoms show positive potential. This gives information for the region from where the compound can have intramolecular interaction.

The theoretical and experimental absorption wavelengths of DPH and DPHA are compared and are tabulated in Table 3, and the corresponding transition energies are sketched in Figure 3A. As can be seen from Table 3 and Figure 3A, there is a well agreement between the theoretical and experimental λ_{max} for both DPH and DPHA molecules. The calculated electronic transition for the DPH molecule was obtained at 246 nm, and the corresponding electronic transition was observed at 250 nm, which is assigned to the $\pi \rightarrow \pi^*$ transitions in the molecule.[37] The $\pi \rightarrow \pi^*$ transitions indicate the presence of conjugation interactions in the hydantoin ring. Also, the calculated electronic transition for the DPHA molecule was obtained at 664 nm, and the corresponding electronic transition was observed at 656 nm, which is assigned to the $n \rightarrow \sigma^*$ transitions.[38] This $n \rightarrow \sigma^*$ transitions arise due to the electronic transitions from a lone pair of electrons present in the electronegative atoms to σ electrons in the molecule. The optical band gap was obtained from Tauc's equation[39] [$\alpha h\nu = A\ (h\nu\text{-}E_g)^n$] and graphical plot (Figure 5). The energy required for the exciting electron from $\pi \rightarrow \pi^*$ transition state for the DPH and DPHA is 4.356 eV (Figure 5A) and 1.902 eV (Figure 5B), respectively, and it matches with the frontier molecular orbital energy gap. All of the above optical studies reveal that DPHA possesses good optical behavior and has enhanced bioactivity than DPH.

3.4 | FT-IR and FT-Raman spectral analysis

Vibration spectral analysis of molecules can provide in-depth knowledge of the relationship between molecular structure and bioactivity; therefore, a theoretical and experimental analysis of the DPH was performed. The experimental and simulated wavenumbers using hybrid B3LYP with the combination of LANL2DZ basis set along with their possible assignments along with their potential energy distribution (PED) are depicted in Table 4. The combined observed and simulated IR and Raman spectra of DPH are shown in Figures 6 and 7, respectively.

3.5 | Hydantoin ring vibrations

The DPH molecule has an aromatic five-substituted hydantoin derivative, which has two NH and two C=O moieties. Both functional groups have made their own contributions in modes of vibration.

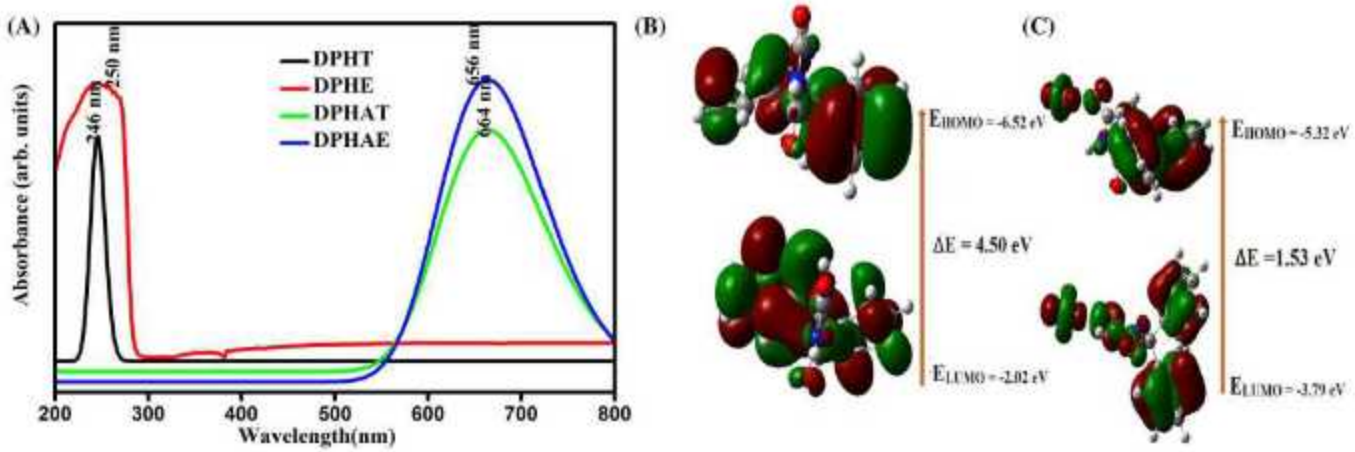


FIGURE 4 Molecular electrostatic potential plots of (A) DPH with 6-31++G (d,p) basis set and (B) DPHA with LANL2DZ basis set using B3LYP functional

TABLE 3 Experimental absorptions (λ_{max}Expt), calculated absorptions (λ_{max}calc.), energy (E), and oscillator strength (f) of the DPH and DPHA molecule using TD-DFT method at the B3LYP/6-311++G(d,p) and B3LYP/LANL2DZ level of basis set

Molecules	Excitation	CI expansion co-efficient	λ_{max}calc. (nm)	λ_{max}Expt. (nm)	E (eV)	(f)	Contribution of orbital	Bands
DPH (HOMO→64 and LUMO→67)	Excited state1 62 → 67 62 → 71 65 → 67 66 → 67 66 → 69 66 → 71	Singlet A −0.31457 0.14337 0.35887 0.38127 0.13415 −0.12667	246	250	5.1204	0.0409	π → π*	R-Bands (German: Radikalartig)
	Excited State 2 64 → 68 65 → 67 65 → 68 65 → 71 66 → 67 66 → 70	Singlet A 0.13459 −0.33124 0.10356 −0.1058 0.39305 −0.15123			5.1204	0.0101	π → π *	R-Bands (German: Radikalartig)
	Excited State 3 63 → 68 64 → 67 64 → 69 65 → 69 66 → 68 66 → 70	Singlet A −0.24566 0.2419 −0.19545 0.14892 −0.13369 0.25873			5.2457	0.0010	π → π *	R-Bands (German: Radikalartig)
DPHA (HOMO→75B and LUMO→76B)	Excited State1 75B — 76B	2.003-A 0.98837	664	636	1.8648	0.0040	n — σ*	R-Bands (German: Radikalartig)
	Excited State 2 71B → 76B 72B → 76B 73B → 76B 74B — 76B	2.003-A 0.75401 0.1513 −0.44602 −0.44993			1.9893	0.0000	n → σ*	R-Bands (German: Radikalartig)
	Excited State 3 70B — 76B 71B — 76B 72B — 76B	2.003-A 0.3363 −0.13057 0.92224			1.9952	0.0001	n → σ*	R-Bands (German: Radikalartig)

Abbreviations: Expt.—Experimental UV-visible absorption wavelength, calc.—calculated UV-visible absorption wavelength, CI—configuration interaction expansion coefficient.

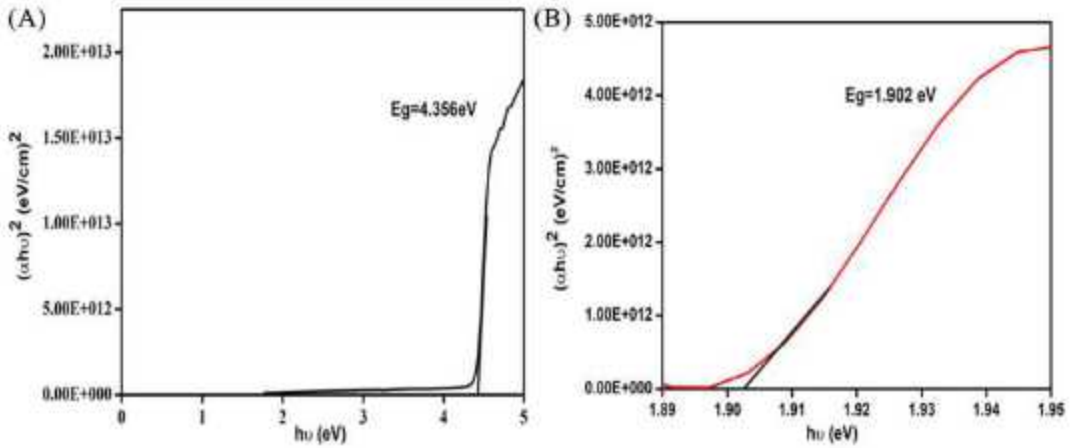


FIGURE 5 Tauc's plot of (A) DPH molecule and (B) DPHA molecule

TABLE 4 Vibrational assignments for the DPH molecule

Unscaled wavenumber	Scaled wavenumber	Experimental		Assignments with PED%
		IR	Raman	
3635	3519	3475(vw)		ν NH (100) hyn
3634	3518	3271(vs)	3266(vw)	ν NH (98) hyn
3199	3096	3208(vs)		^{2}ν CH (100) ph 1
3197	3095	3197(vs)	3174(vw)	^{2}ν CH (100) ph 2
3175	3073	3072(m)	3071(vs)	^{7b}ν CH (96) ph 1
3172	3070	3068(s)		^{7b}ν CH (98) ph 2
3165	3064	2797(w)		^{13}ν CH (97) ph 1(36) ph 2
3164	3063	2709(w)		^{13}ν CH (92) ph 2(42) ph (19)
1845	1786	1772(vs)	1790(vs)	ν C=O (98) hyn
1810	1752	1722(vs)	1757(S)	ν C O (95) hyn
1642	1589	1598(w)	1602(m)	^{8b}ν CC (98) ph 2(53) ph 1
1639	1586		1586(S)	^{8a}ν CC (96) ph 1(53) ^{8b}ν CC ph 2(33)
1526	1477	1493(w)	1497(S)	^{19a}ν CC ph 2 (63)
1523	1474	1450(m)		^{19a}ν CC ph 1 (58)
1478	1431	1448(s)		^{19b}ν CC ph 2 (62), ^{19b}ν CC ph 1 (25)
1476	1429		1403(w)	^{3}δ (CH) Ph1 (69), ^{3}δ (CH) Ph2 (49)
1398	1354		1362(m)	δ (NH)hyn (82)
1377	1333		1343(w)	δ (NH) hyn (85)
1329	1286	1285(w)		^{14}ν CC ph 2 (62), ^{14}ν CC ph 1 (20)
1321	1279	1234(s)		^{14}ν CC ph 2 (68), ^{14}ν CC ph 1 (23)
1230	1191	1194(s)	1197(s)	ν CN (70) ν CC (26) hyn
1214	1175	1188(m)		^{15}δ (CH) (65) ph 2
1199	1160		1160(s)	^{9b}δ (CH) (56) ph 1, δ (NH) (24) hyn
1183	1145	1117(w)	1121(m)	^{15}δ (CH) (42) ph 2
1118	1082		1103(m)	^{18a}δ (CH) (42) ph 2, ^{18b}δ (CH) (23) ph 1, δ (NH) (32) hyn
1110	1074	1071(w)	1100(m)	^{18b}δ (CH) (22) ph 2
1083	1048		1034(vs)	ν CN (52) hyn, ^{18b}δ (CH) (26) ph 1
1051	1017	1015(w)	1017(m)	^{18a}δ (CH) (82) ph 1
1018	986		1006(w)	^{12}δ CCC (72) ph 2
1017	984	983(w)	985(vs)	^{12}δ CCC (72) ph 1
981	950	936(w)	940(w)	ν CCN (76) hyn, ^{17b}γ CH (18) ph 1
948	918	910(w)	918(vw)	γ CC O (40) hyn
859	832		845(m)	^{10a}γ CH (73) ph 1
855	827		789(s)	^{10a}γ CH (73) ph 2
793	790	785(s)	785(s)	^{10b}γ CH (73) ph 1
780	775		771(m)	^{10b}γ CH (73) ph 2
760	768	768(s)	765(s)	^{17b}γ CH (63) ph 2
755	755	746(s)	748(w)	^{17b}γ CH (63) ph 1
745	721	724(s)	726(vw)	γ CNH (65), ^{11}γ CH (23) ph 2
712	690	697(s)		^{11}γ CH (84) ph 1
711	688		689(s)	^{11}γ CH (70) ph 2
692	670	653(s)	657(s)	^{6a}γ CCC (70) ph 2, ^{6b}γ CCC (24) ph 1
653	632	642(s)	649(w)	γ NHC=O (69) hyn
635	615		643(w)	^{6b}δ CCC (49) ph 2, τ CNCN (28) hyn,
633	612		619(m)	^{6b1}δ CCC (49) ph 1,

(Continues)

TABLE 4 (Continued)

Unscaled wavenumber	Scaled wavenumber	Experimental		Assignments with PED%
		IR	Raman	
616	597	597(w)		γ CCNH (68) hyn
533	516	519(w)	518(vw)	γ CCNH (56) hyn, ^{16b}bγ CCC (28) ph 2
500	484	496(w)		^{16b}bγ CCC (40) ph 1, ^{16b}bγ CCC (35) ph 2
454	439		431(vw)	γ C-C—O(29) hyn
347	336		354(w)	τ CCNH (22) hyn
307	298		287(s)	τ CC—O (22) hyn
273	264		251(s)	τ C-Ph1(32), τ C-Ph2(39)
146	141		164(vw)	γ NH (52), γ C=O (89) hyn
131	126		102(s)	γ NH (75), γ C=O (65) hyn
102	99		99	BF ph 1,ph 1
68	66		73(w)	BF ph 1,ph 2
52	51		58(vw)	BF hyn,ph 2

Abbreviations: ν—streching, δ—in-plane bending, γ—out-of-plane bending, τ—torsion, BF—butterfly mode, hyn—hydantoin ring, ph 1—phenyl ring 1, ph 2—phenyl ring 2.

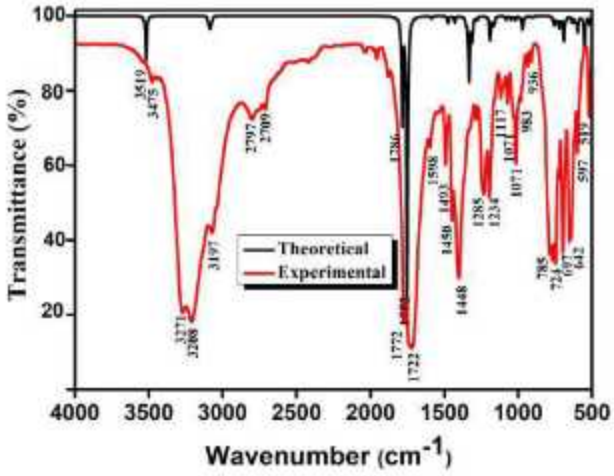


FIGURE 6 Comparison of observed and simulated FT-IR spectra of DPH molecule

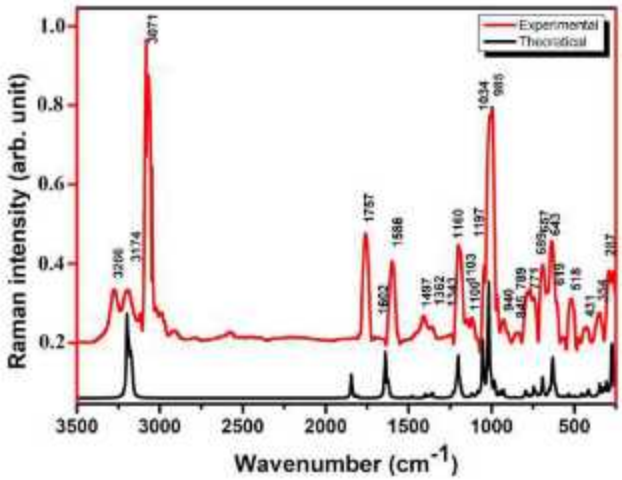


FIGURE 7 Comparison of observed and simulated FT-Raman spectra of DPH molecule

These contributions make the hydantoin ring a good electron donor in the DPH molecule. In hydantoin, the NH stretching mode is usually expected at 3500-3200 cm^{-1}.[40,41] NH stretching is assigned for DPH at 3475 and 3271 cm^{-1} as broad and intense bands in IR and a very weak band in Raman at 3266 cm^{-1}. This broadness of NH stretching wavenumber is probably due to the inter- and intramolecular hydrogen bonding interaction, as well as the existence of C—H···N intermolecular hydrogen bonding. The aromatic C=O stretching mode is habitually anticipated at 1775-1650 cm^{-1}.[40,41] The calculated aromatic C=O stretching vibrational modes of the DPH molecule were obtained at 1786 and 1752 cm^{-1}. The observed very strong peaks at 1772 and 1722 cm^{-1} in the IR spectrum and 1790 and 1757 cm^{-1} strong bands in Raman were assigned to the ring C=O stretching vibrations of the molecule. The intensity of the C=O band shows that the size of the hydantoin ring is small.[42] The red-shift of $C_{14} = O_{18}$ stretching mode may be due to the inductive pull of the electron density in the hydantoin ring. This tends to decrease the double-bond character of the $C_{14} = O_{18}$ carbonyl bond. In addition, the charge is higher in the O_{18} as evidenced by natural population analysis and stabilized geometry. The ring C—C and C—N stretching vibrations of the heteroaromatic moiety like hydantoin are expected in the region 1625 to 1100 cm^{-1}.[41] In DPH molecule, this mode is simultaneously observed in IR at 1194 cm^{-1} and in Raman at 1197 cm^{-1}. The CC and CN stretching modes are observed at 936 (IR), 940 (Raman), and 1034 (Raman) cm^{-1}, respectively, which is an evidence for the charge-transfer interaction. The down-shifting and enhanced intensity of CC

and CN stretching wavenumber are due to the ICT interaction between the phenyl and hydantoin rings through the CC skeleton.[43] The observed stretching wavenumbers are in good agreement with the PED results.

The NH in-plane and out-of-plane bending vibration bands in hydantoin ring are normally expected in the region 1650-1550 cm^{-1} and 720-520 cm^{-1}, respectively.[40,41] The NH in-plane bending mode is observed at 1103 cm^{-1} and (1362, 1343, and 1160 cm^{-1}) in Raman and IR spectra, respectively. The out-of-plane bending mode is observed at 518 cm^{-1} and 519 cm^{-1} in Raman and IR, respectively. From the literature, the vibrational band corresponding to the CCC=O out-of-plane bending modes is reported at 500-450 cm^{-1}.[41] The out-of-plane bending mode is observed in Raman at 431 cm^{-1}. The experimental wavenumber are nearly lower than that of the calculated wavenumber (for isolated molecules) due to intermolecular dipole–dipole interaction in the crystals.

3.6 | Biphenyl ring vibrations

The various vibrations of the substituted phenyl rings were comprehensively studied according to Wilson's numbering convention.[41,44] In the DPH molecules, the fifth position in the hydantoin is replaced with the phenyl groups. The allowed CH stretching modes of phenyl rings are 7b, 2, and 13 falling in the region at 3100-3000 cm^{-1}.[45,46] In DPH, the ring mode 2 of ph 1 and ph 2 are observed at 3208 cm^{-1} and 3197 cm^{-1}, respectively, with PED 100% in IR. Modes 7b are observed at 3072 cm^{-1} and 3068 cm^{-1} in IR for ph 1 and ph 2, and at 3071 and 3074 cm^{-1}, respectively, in Raman. The IR bands observed at 2797 and 2709 cm^{-1} at ph 1 and ph 2, respectively, correspond to mode 2. Blue-shifting of CH stretching wavenumbers in phenyl ring is due to the charge delocalization.

The allowed tangential CC stretching modes are 8a, 8b, 19a, 19b, and 14 for the biphenyl derivatives.[47,48] The degenerate vibrational pairs 8a and 8b are expected in the region 1570-1628 cm^{-1} and 1552-1605 cm^{-1}, respectively.[51] The observed strong band in Raman at 1586 cm^{-1} is assigned to the CC stretching mode 8a of ph 1. Mode 8b of ph 1 and ph 2 are observed as a weak IR band at 1598 cm^{-1} and medium Raman band at 1602 cm^{-1}. Ring mode 19a is anticipated in the 1460-1530 cm^{-1} region and 19b in the 1370-1470 cm^{-1} region.[47] Mode 19a of ph 1 and ph 2 is observed at 1450 cm^{-1} and 1493 cm^{-1} in IR. 19a mode's Raman band is observed at 1497 cm^{-1} in the ph 2 ring. Mode 19b of ph 1 and ph 2 is observed as a strong IR band at 1448 cm^{-1}. The CC stretching mode 14 is normally expected in the region 1290-1330 cm^{-1} [47] which has been observed in IR at 1285 and 1234 cm^{-1} for ph 1 and ph 2 rings. The simultaneous activation of CC stretching modes 8a, 8b, 19a, and 19b provides the evidence for the ICT interaction.

The normal modes 3, 9b, 15, 18a, and 18b are classified as CH in-plane bending vibrations which are expected in the regions 1260-1313 cm^{-1}, 1156-1168 cm^{-1}, 1140-1170 cm^{-1}, 1004-1022 cm^{-1}, and 1100-1128 cm^{-1}, respectively.[44,49] Mode 3 is observed as a strong IR band at 1402 cm^{-1} and a weak Raman band at 1403 cm^{-1}, respectively, for both ph 1 and ph 2. Mode 9b is observed as a medium band in Raman at 1160 cm^{-1} in ph 1 ring. The observed medium and weak IR band at 1188 and 1117 cm^{-1} and very strong Raman band at 1121 cm^{-1} are assigned to mode 15 of Ph2. Mode 18a is observed as a weak IR band at 1015 cm^{-1} and medium Raman band at 1017 cm^{-1} in ph 1 ring. The observed weak IR band at 1071 cm^{-1} and strong Raman bands at 1103, 1100, 1121, and 1034 cm^{-1} are assigned to mode 18b. The in-plane bending modes 3, 9b, 15, 18a, and 18b of ph 1 and ph 2 have found to be simultaneously active in both IR and Raman spectra because of the symmetry lowering of the molecule. Furthermore, such deformation changes the bond length between the carbon atoms, which build the charge transfer axis, and the polarizability of such a π-conjugated system. The complete vibrational assignments of DPH molecule are given in Table 4.

3.7 | SERS spectral analysis

The absorption spectra of AuNPs are affected by the shape and size of the nanoparticles. UV–Vis spectra of the Au NP colloids are presented in Figure 8A. The gold colloids were wine red (Figure 8C) in color and had absorption maxima at 529 nm. The nanostructure and morphology of gold colloids analyzed by transmission electron microscope (TEM) are shown in Figure 8B. The average particle size of the gold colloids is about 40 nm. After chemical interactions between DPH and AuNPs, the SERS spectral analysis of the DPHA molecule was performed based on three different concentrations. The observed and simulated Raman spectra were compared with the observed and simulated SERS spectra (Figure 9) and found that the experimental spectra fit well with the theoretical spectra (Table 5). The strong 431 and 354 cm^{-1} bands shifted to 439 and 360 cm^{-1}, which may be attributed to sensitivity to the adsorption of DPH. Also, a few of the bands associated with the adsorption to the gold surface have shifted perceptibly. This indicates a strong interaction between the DPH molecule and the AuNPs. Intense bands at 249 cm^{-1} and shoulder bands at 229 cm^{-1} were observed, showing the adsorption reaction of the AuNPs.[50] These bands interacted with the oxygen atom (O_{1a}) and nitrogen atom (N_{1s}) in the hydantoin ring, respectively, thereby achieving a kinetically favorable interaction. This interaction is also favored by the inductive effect imposed by the C=O in the hydantoin ring on the metal. The other interaction is possible via the nitrogen of the hydantoin ring. This interaction may be arising from the charge transfer between the low electronegative oxygen and nitrogen atoms with the metal, the nitrogen attachment being kinetically favored through the shoulder band.

The most significant feature of the SERS spectrum is the emergence of a strong observed band at 1739 cm^{-1} and a simulated band at 1746 cm^{-1} assigned to the C—O stretching, which was expected in the region 1700-1860 cm^{-1}.[51] Also, the C—O stretching band of the carbonyl group in the hydantoin ring has a remarkable redshift (17 cm^{-1}) in the SERS spectrum compared with the normal Raman spectrum. This enhancement and shifting in the intensity of the C=O stretching vibration suggest that the C=O group is directly involved in

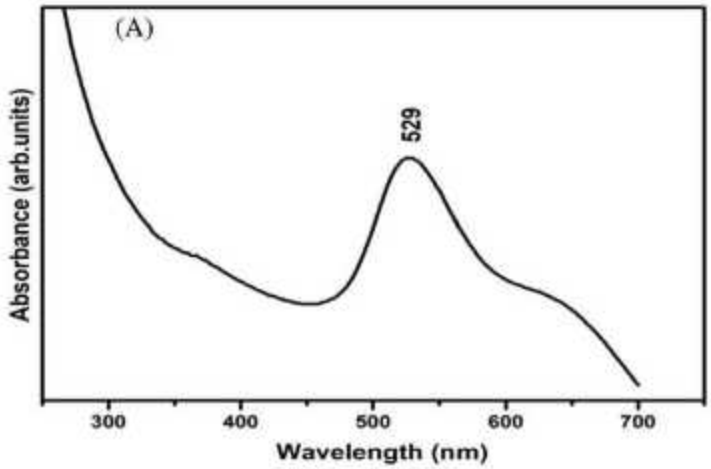


FIGURE 8 Nanostructure and morphology of gold colloids: (A) UV–Vis spectra of the Au NP, (B) transmission electron microscope (TEM) Image, and (C) wine red color of gold colloids

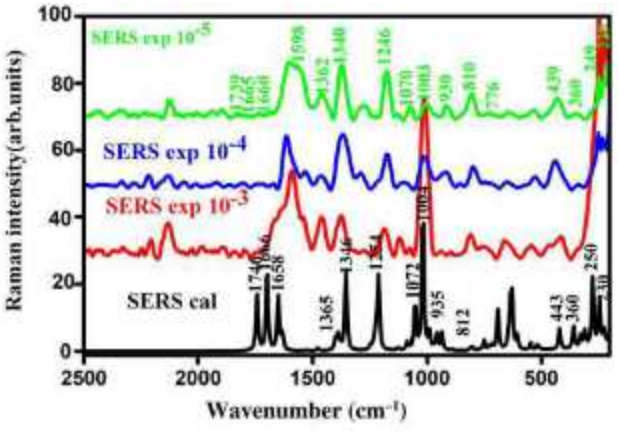


FIGURE 9 SERS of DPHA at three different concentrations (10^{-3}, 10^{-4}, and 10^{-5} M) and calculated SERS spectra

the interaction with the gold surface. Natural population analysis as well as the analysis of stabilized parameters of the DPHA molecule supports the existence of more negative charge on O_{18} atom. This confirms the direct binding of the molecule to the gold surface, forming a stable DPH-AuNPs (DPHA). The C–N stretching vibrations of the heteroaromatic moiety are expected in the region 1625 to 1100 cm^{-1}, [52] and the band is observed at 1246 cm^{-1}, which has been red-shifted compared with the normal Raman. This is due to the localized lone pair electron in the amine group that is delocalized to ring on account of the interaction of the NH in the hydantoin ring with the metal surface. From the literature, the vibrational band for the C–N in-plane and out-of-plane bending modes is reported at 1660-776 cm^{-1} and 1550-1650 cm^{-1}, respectively.[68] It was found that the CN out-of-plane bending and in-plane bending modes appear at 776 and 1598 cm^{-1}, respectively, with enhanced intensity. The enhancement in various in-plane and out-of-plane bending of CN in hydantoin ring vibrations suggests that the hydantoin ring is in a nearly tilted orientation over the gold surface. Also, $C_{14} = O_{18}$ stretching mode is enhanced and shifted from the normal frequency showing that the DPH molecule is very close to gold surface.

The various normal vibrations of the monosubstituted phenyl rings are assigned according to Wilson's numbering convention.[44] The degenerate C–C stretching mode 8 splits into 8a and 8b vibrational bands and is expected in the region 1570-1628 cm^{-1} and 1552-1605 cm^{-1}, respectively.[44,47] Although the degenerate C–C stretching modes 8a and 8b of the monosubstituted phenyl rings are insensitive to the substituents, the intensity of the 8a mode increases with the enhancement of the conjugation with the hydantoin. 8a mode is observed as a strong Raman band at 1598 cm^{-1} in ph 1 and ph 2. Also, the medium intensity band observed at 1665 cm^{-1} for ph 2 and 1660 cm^{-1} for ph 1 in Raman has been assigned to 8a. The enhanced intensity clearly demonstrates the delocalization of electrons in the ring system. The normal modes 3, 15, 18a, and 18b are classified as CH in-plane bending vibrations, which are expected in the regions 1260-1313 cm^{-1}, 1140-1170 cm^{-1}, 1004-1022 cm^{-1}, and 1100-1128 cm^{-1}, respectively.[44,69] In ph 1, the four C–H in-plane bending modes appear in Raman viz. the enhanced in-plane bending bands at 1362, 1160, 1110, and 1070 cm^{-1} of modes 3,15, 18a, and 18b, respectively. Also, in the ph 2 ring, C–H in-plane bending bands are observed at 1340, 1170, and 1110 cm^{-1} corresponding to modes 3, 15, and 18b, respectively. The increase in intensity is due to the polar ring substituents present in the phenyl ring and adsorption of AuNPs which alters the intensity of C–H stretching and bending modes. The complete vibrational assignments of DPH molecule are given in Table 5.

3.8 | *In-silico* biological activity screening

Molecular docking is widely used for *in-silico* biological activity screening. With the aim to investigate the preferred binding orientation, affinity, and activity of drug molecules and their protein targets, a molecular modeling study was performed using AutoDock Tools for docking. Lung cancer (PDB ID:2ITO),[53] skin cancer (PDB ID:2VCJ),[54] brain cancer (PDB ID:1QH4),[55] and gastric cancer (PDB ID:1BJ7)[56] proteins of different receptors were selected from the Protein Data Bank (PDB) to dock to DPH and DPHA molecules to locate the active

TABLE 5 Selected theoretical and experimental SERS spectral bands of the DPHA molecule with 10^{-3} M, 10^{-4} M, and 10^{-5} M concentrations

FT-Raman		SERS				
Theoretical wavenumber (cm^{-1})	Experimental wavenumber (cm^{-1})	Experimental wavenumber (cm^{-1})			Theoretical wavenumber (cm^{-1})	Assignments with PED(%)
		10^{-3} M	10^{-4} M	10^{-5} M		
1752	1722	1739	1739	1739	1746	ν C O hyn (100)
1589	1602	1665	1665	1665	1666	^{8b}ν CC ph 2 (85)
1586	1586	1660	1660	1660	1658	^{8b}ν CC ph 1 (92)
1589	1602	1598	1598	1598	1610	^{8a}ν CC ph 2 (85), ^{8a}ν CC ph 1 (45), δCN (32) hyn
1354	1362	1362	1362	1362	1365	^{3}δ CH ph 1 (83)
1333	1343	1340	1340	1340	1346	^{3}δ CH ph 2 (90)
1191	1197	1246	1246	1246	1254	ν CN hyn (85)
1181	1179	1170	1170	1170	1175	^{15}δ CH ph 2 (96)
1171	1169	1159	1159	1159	1160	^{15}δ CH ph 1 (90)
1082	1103	1110	1110	1110	1113	^{18b}δ CH (85) ph 2, ^{18a}δ CH (45) ph 1
1074	1100	1070	1070	1070	1072	^{18a}δ CH (85) ph 1
1010	1017	1003	1003	1003	1004	^{12}δ CCC ph 1 (86)
986	1006	930	930	930	935	^{12}δ CCC ph 2 (82)
832	845	810	810	810	812	^{10b}γ CH ph 2 (64)
775	771	776	776	776	779	γ NH(45), γ CN (65) hyn
439	431	439	439	439	443	γ CC=O(29) hyn
336	354	360	360	360	360	τ CCNH (22) hyn
		249	249	249	250	ν Au-O (85)
		229	229	229	230	ν Au-N (90)

Abbreviations: ν—Streching,δ—inplane bending, γ—out-of-plane bending, hyn—hydantoin, ph 1—phenylring 1, ph 2—phenyl ring 2.

site. The ligand PDB file was generated from the optimized molecular structure of the DPH and DPHA molecules. The AutoDockTools graphical user interface was used to remove the ligand and water molecules present in the target proteins, which were also used to add the polar hydrogen bond and Geisteger charges in the target proteins. The Lamarckian Genetic Algorithm (LGA) was used for molecular docking calculations.[24] The docking parameters such as binding energy, inhibition constant, and intermolecular energy of the molecule with respect to the targeted proteins were calculated. The energy released due to the bond formation or, rather, interaction of the ligand and protein is expressed in terms of binding energy. The binding energies for the DPH molecule with 2VCJ, 1QH4, 2ITO, and 1BJ7 were calculated as −7.8 kcal/mol, −7.4 kcal/mol, −8.0 kcal/mol, and −7.2 kcal/mol, respectively. The binding energies for the DPHA molecule with 2VCJ, 1QH4, 2ITO, and 1BJ7 were calculated as −7.6 kcal/mol, −6.4 kcal/mol, −8.6 kcal/mol, and − 6.1 kcal/mol, respectively. Analysis of the binding free energy shows that the protein 2ITO had low binding free energy in the DPH and DPHA molecules. Furthermore, comparison of DPH (−8.0 kcal/mol) and DPHA (−8.6 kcal/mol) molecules show that the DPHA molecule has less binding free energy. Inhibition constant is an indication of how potent an inhibitor is. The inhibition constant for DPH molecule for 2VCJ, 1QH4, 2ITO, and 1BJ7 are calculated to be 146.98 mM, 125.70 mM, 2.74 mM, and 2.91 mM, respectively while that for the DPHA molecule are calculated to be 120.98 mM, 115.70 mM, 2.05 mM, and 2.15 mM, respectively. The inhibition constant is directly proportional to the binding free energy. The protein 2ITO has low inhibition constant in both DPH (2.74 mM) and DPHA (2.05 mM) molecule. While comparing DPH and DPHA molecule, the latter shows low inhibition constant with 2ITO protein. These results strengthen the binding free energy results. Hence, it is clear that that small quantity of DPHA molecule is sufficient to prevent the lung cancer. The intermolecular energy was estimated for the combination of the ligand and the protein in their bound conformation. The intermolecular energy for the DPH molecule with 2VCJ, 1QH4, 2ITO, and 1BJ7 was calculated as −5.86 kcal/mol, −4.09 kcal/mol, −4.06 kcal/mol, and − 7.35 kcal/mol, respectively. And the intermolecular energy for the DPHA molecule 2VCJ, 1QH4, 2ITO, and 1BJ7 was calculated as −5.68 kcal/mol, −4.04 kcal/mol, −4.03 kcal/mol, and − 6.85 kcal/mol, respectively. The intermolecular energy is high in 2ITO-DPH (−4.06 kcal/mol) and 2ITO-DPHA (−4.03 kcal/mol) protein ligand combination. However, the 2ITO-DPHA protein–ligand combination shows more intermolecular energy confirming that the 2ITO-DPHA protein–ligand combination is superior to other combinations. The 2ITO proteins show low binding free energy and inhibition constant but high intermolecular energy for both the DPH and DPHA molecule. Also, the number of hydrogen

bonds between 2ITO and the molecule is more (Figure 11). The binding affinity of the ligand to targeted proteins exhibited the following order 2ITO > 2VCJ > 1QH4 > 1BJ7. These results reveal that the 2ITO receptor shows more activity than other receptors toward the DPH and DPHA molecules. These results confirm that the DPH and DPHA molecule show more activity toward lung cancer proteins. The hydrogen bond between the DPH molecule and the receptors 2VCJ, 1QH4, 2ITO, and 1BJ7 are (GLN A: 184, LEU A:76, MET A:195, ASP 179), (LEU A:66, GUA:68, TYR A:83 and PHE A82), (LEU A:862, ALA A:864, VAL A:834, ARG A:889, and LYS A:860), and (ASN A:31, LYS A:58, LEU A:152, MET A:98, and ALA A:55), respectively. The hydrogen bonds between the DPHA molecule and the receptors 2VCJ, 1QH4, 2ITO, and 1BJ7 are (VAL A:62, META:43, ARG A:23, ASN A:56), (GLYA96, ILEA91), (GLYA76, VALA66, LEU76, ASN 31, LYS 58), and (CYSA53, ARGA117), respectively. Hydrogen bonding between DPH and DPHA molecule and amino acids of proteins is shown in Figure 10 and tabulated in Table 6. The hydrogen bonding confirms that the DPH and DPHA molecules can act as a good inhibitor against lung cancer. Also, binding free energy, inhibition constant, intermolecular energy, and hydrogen bonding confirm that the DPHA molecule has shown more activity than the DPH molecule against lung cancer.

3.9 | Recognition of human lung cancer cells—in vitro analysis

In vitro analysis of lung cancer cells was done using SERS and MTT assay for examining mutations and the cytotoxic effect of DPH and DPHA. For SERS study inside the cell, the DPHA molecule was up taken to the cell, which was distributed in the cytoplasmic area within 2 hours. The absorption peak was observed at 455 nm (Figure 11A). Normally cytoplasmic peak appears at 300-700 nm.[57] After 3 hours, this absorption peak disappeared showing that the DPHA molecule slowly migrated into the nucleus. After 4 hours, with no cytoplasmic fluorescence that rationalizes the SERS studies, nuclear accumulation was observed. The results obtained were compared with other similar studies reported in the literature and are shown in Table 7. The vibration of the phosphodioxy group in the cell line produces a strong Raman intensity at 1091 cm^{-1}, which confirms changes in nucleic acid. [58,59] Raman intensity corresponding to nucleotides is identified at 771 cm^{-1} (thymine, cytosine, and uracil), 1305 cm^{-1}(thymine, guanine, and adenine), and 1576 cm^{-1} (guanine and adenine).[60] The 771 cm^{-1} intensity confirms the mixing of DNA and RNA.[61] The presence of nucleic acids inside the cell line was detected by the spectral line observed at 826 cm^{-1} which is the vibration of the sugar-phosphate o-p-o backbone. The sugar-phosphate backbone forms the structural framework of nucleic acids, including DNA and RNA. A reduction in the relative intensity of the lipid band at 1423 cm^{-1} indicates the decrease of lipid-to-protein ratio. [62] The above assignments show biochemical changes in the nucleus and indicate[63] that DPHA interacts with apoptotic (cancer) cell. This will enable label-free monitoring and could further potentiate the therapeutic utility. SERS spectrum obtained from DPHA within the lung cancer cell is associated with proteins, nucleic acids, lipids, and carbohydrates which are identified, and assignments are plotted in Figure 11B and Table 7.

The cellular internalization was explored by Raman imaging analysis. For that, bright field (Figure 12A) and Raman mapping for DPHA localization were observed within 1 hour and 3 hours of incubation of DPHA in A_{549} cells. Raman spectral and imaging analysis from A_{549} cells showed that the intensity of Raman band got enhanced. Raman imaging and complementary spectral analysis of DPHA demonstrated time-dependent localization due to early distribution of the cytoplasm and subsequent migration to the nucleus. From the Raman images, it is clear that DPHA has entered into A_{549} lung cancer cells. 2D SERS mapping (Figure 12C) was used to track the spatial and temporal progress of the uptake of nanoparticles in cancer cells at various time

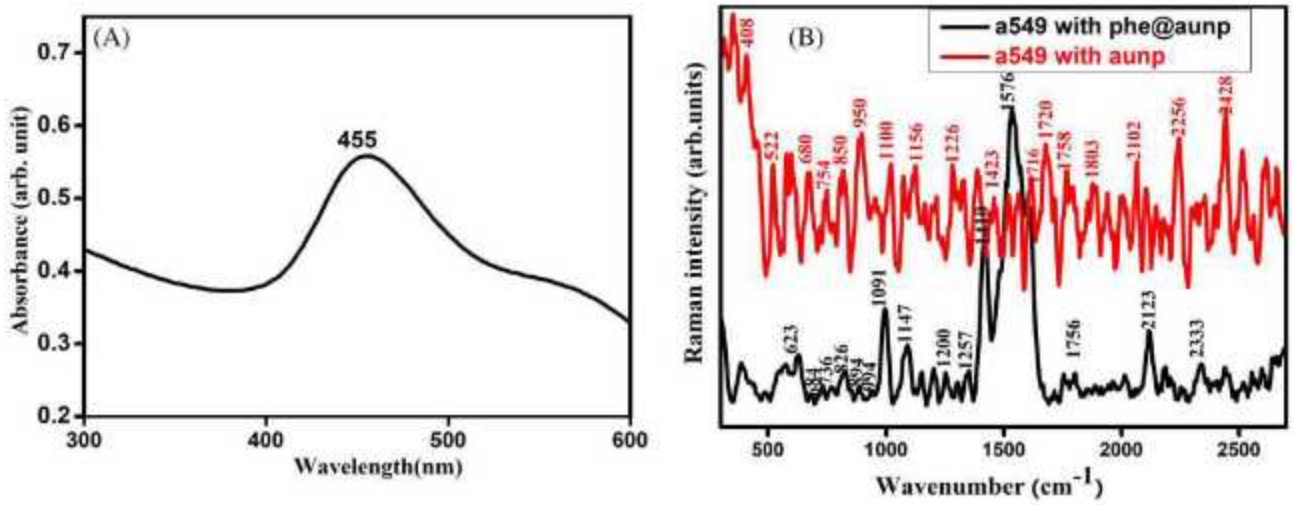


FIGURE 11 (A) UV-Vis spectra of DPHA molecule inside A_{549} lung cancer cell line and (B) SERS spectra analysis of DPHA and AuNP inside A_{549} lung cancer cell line

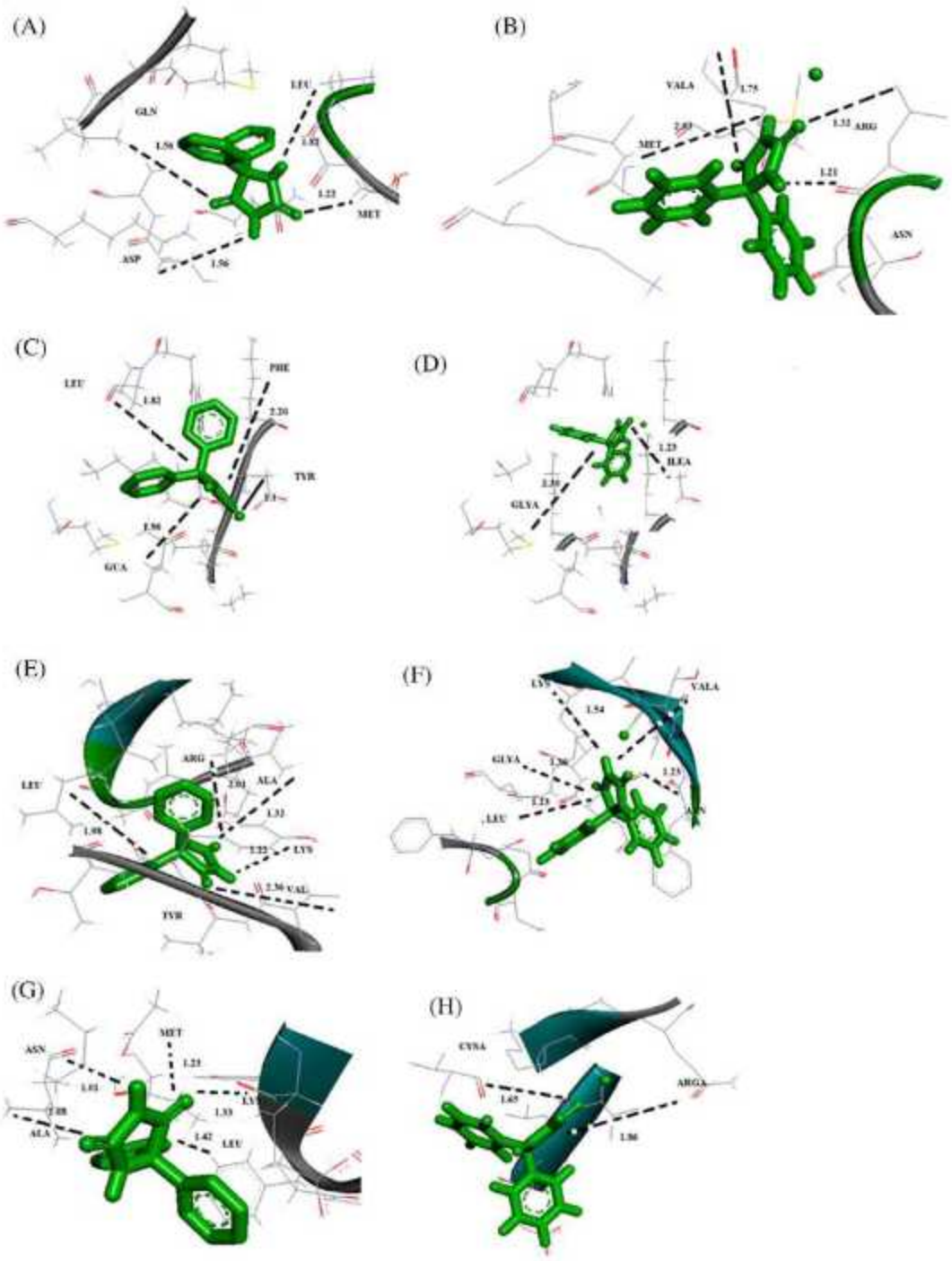


FIGURE 10 Pictorial representation of possible binding sites of DPH and DPHA molecules with the target proteins (A) 2VCJ-DPH, (B) 2VCJ-DPHA, (C) 1QH4-DPH, (D) 1QH4-DPHA, (E) 2ITO-DPH, (F) 2ITO-DPHA, (G) 1BJ7-DPH, and (H) 1BJ7-DPH

points.[64] Also SERS maps were constructed to show drug internalization. The white light image of such an apoptotic A_{549} lung cancer cell is shown in Figure 12A. From Figure 12D, it is seen that the cell has a size of 10 μm and is much smaller than the control cell showing that the cells are apoptotic. This was further confirmed through the MTT viability assay.[65,66] MTT assay has been done in three concentrations of DPH and DPHA molecules. DPH and DPHA show cytotoxic effect, with more cytotoxicity in 1000 μM. The DPHA molecule shows more cytotoxicity effect than DPH molecule. But there is no cytotoxic effect for Au NPs alone. The above results show that Au NPs aids cellular uptake of the drug of interest and allow targeted drug delivery. The comparative results are delineated in Table 8 and Figure 12E. The above results show that DPHA interacts with apoptotic cell (MTT assay) and can be used for effective monitoring through SERS, which enable label-free monitoring and can further potentiate the therapeutic utility.

TABLE 6 Docking results of the DPH and DPHA molecule with the different cancer proteins

Protein Code	Free energy of binding (kcal/mol)		Inhibition Constant, (K_i) (mM)		No. of hydrogen bonds		Bonded protein residues and hydrogen bonds (Å)	
	DPH	DPHA	DPH	DPHA	DPH	DPHA	DPH	DPHA
2VCJ	−7.8	−7.6	146.98	120.98	4	2	GLN A: 184···O_{20}(1.56) LEU A:76···N_{12}(1.86) MET A:195···O_{18} (1.22) ASP 179···N_{15} (2.20)	VAL A:62···O_{20}(1.75) META:43···N_{15}(2.03) ARG A:23···O_{18}(1.32) ASN A:56···N_{12}(1.21)
1QH4	−7.4	−6.4	125.70	115.70	4	2	LEU A;66···C_{12}(1.82) GUA:68···O_{18}(1.96) TYR A:83···O_{20}(1.10) PHE A82···N_{15}(2.20)	GLY:A96···O_{20}(2.30) ILE:A91···O_{18}(1.23)
2ITO	−8.0	−8.6	2.74	2.05	5	5	LEU A:862···C_2(1.98) ALA A:864···O_{18}(1.32) VAL A:834···O_{20}(2.36) ARG A:889···O_{18}(2.01) LYS A:860···N_{12}(1.22)	GLYA76···O_{18}(1.36) VALA66···N_{12}(1.68) LEU76···O_{18}(1.23) ASN 31···O_{20}(1.23) LYS 58···N_{12}(1.54)
1BJ7	−7.2	−6.1	2.91	2.15	5	5	ASN A:31...N15(1.01) LYS A:58...O20(1.33) LEU A:152...N12(1.42) MET A:98...O20 (1.23) ALA A:55...O18(1.68)	CYS:A53···O_{18}(1.65) ARG:A17···O_{20}(1.86)

TABLE 7 Major assignments for Surface Enhanced Raman bands of the DPHA molecule in the lung cancer cell line A_{549}

Raman band	Nucleic acid	Proteins	Carbohydrates	Lipids
623		Phe (C-C twist)		
684	TG	Met, Cys (C-S str.)		
736	T (ring br.)			
749		Trp (ring br.)		
771	T, U, C (ring br.,RNA)			
826	O-P-O (asym.str.)	Tyr (ring br.)		
894		Lys (C-C,C-N str.)		
994		β-helix, C-C str.		=CH bend
1091	PO_2 str.	nar. (C-C str.)	C-O, C-C str.	Chain C-C str.
1147		C-C / C-N str.	C-C str.	
1200	A,T	amide III Phe, Trp (C-CJls str.)		
1257	T,A	Amide III, α- and β-helix structures		−CH bend
1305	T,A,G			
1423	G,A	CH_2def, collagen	CH_2def	CH_2def, hospholipids
1537		Amide II (CN str.)		
1576	G,A	Trp, (C=C ring str.)		
1716	T G,C (ring br.)	Amide I		C–C str.
1756				C–O ester str.

Abbreviations: T—thymine; G—guanine; A—adenine; U—uracil; C—cytosine; Phe—phenylalanine; Tyr—tyrosine; Met—methionine; Cys—cystine; Trp—tryptophan; Lys—lysine; str—stretch; def—deformation; PO_2—phosphodioxy; nar—unspecified nonaromatic side chains; br—breathing mode; sym—symmetric; asym—asymmetric; bk—backbone.

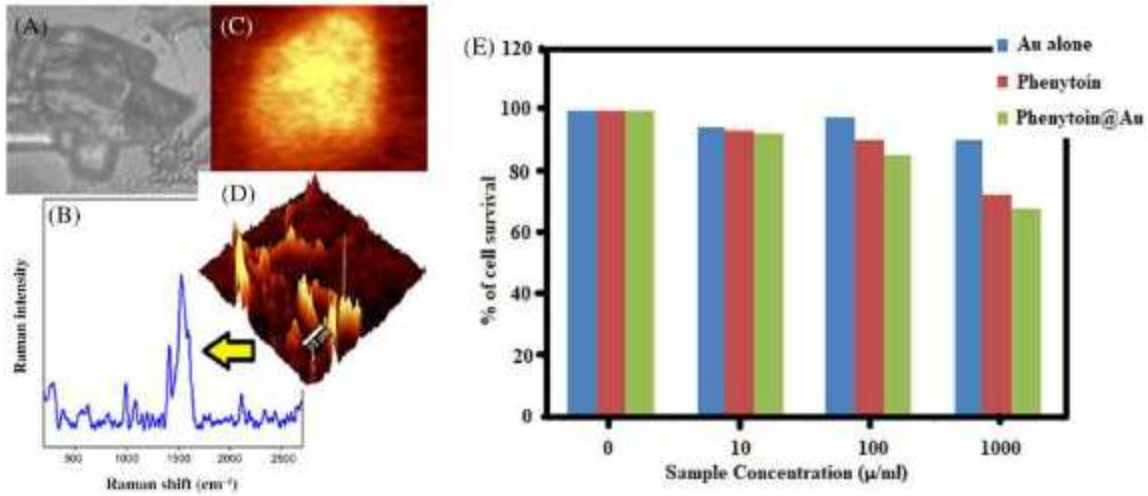


FIGURE 12 Raman imaging of the DPHA molecule in the A_{549} cell line: (A) bright field images, (B) spectrum, (C) 2D image, (D) 3D image, and (E) 3D graphical representation of cytotoxic effect

TABLE 8 Information about cytotoxic effect of the DPH and DPHA molecule and AuNPs in the A_{549} lung cancer cell line

Concentration (μg/mL)	AuNPs	DPH	DPHA
0	100	100	100
10	94.45	93.4333	92.24
100	97.73	90.5	85.6
1000	90.55	72.2	67.73

3.10 | Conclusion

Quantum chemical calculations and vibrational spectral studies have been performed on DPH and DPHA molecules to identify the structural and bonding features responsible for their bioactivity. The geometry of the DPH and DPHA molecules was optimized, using the hybrid DFT method B3LYP with 6-31++G (d,p) and LANL2DZ basis set, respectively, which shows that the phenyl rings are *cis* oriented, and the hydantoin ring is in *trans* orientation relative to the phenyl rings. The theoretical results were compared with the experimental observations, and results show that the molecules are in an anticlinical conformation, strongly affected by the conjugation effect. The *trans*-oriented hydantoin ring and AuNPs play an important role in enhancing the conjugation of the system as well as its selectivity. The observed intense bands at 249 cm^{-1} and shoulder bands at 229 cm^{-1} in the SERS spectrum manifest that the interaction between the AuNPs and the DPH molecule is through oxygen atom (O_{18}) and the nitrogen atom (N_{15}) in the hydantoin ring. The CN in-plane and out-of-plane bending mode and enhanced as well as shifted C=O stretching mode in the SERS spectrum confirmed the above result and predicted a nearly tilted orientation of the DPH molecule over the gold surface. The analysis of strength of the C—H···N intramolecular hydrogen bonding between C_2-H_8 in Ph1 and hydantoin, as well as the variation in CN, C=O, and CC bond lengths, confirms the conjugation of bonds, and hence the intramolecular charge transfer between Ph1 and Ph2 rings. The stabilization energy confirmed that hyperconjugative interactions are stronger in DPHA molecule than the DPH molecule. The CC and CN stretching wavenumber is down-shifted and enhanced in the vibrational spectrum, indicating the ICT interaction between the phenyl and hydantoin rings through the CC skeleton. The natural population analysis on the skeletal carbon atoms C_{12}, C_3, and C_{21} before and after adsorption of AuNPs confirmed the enhanced ICT due to AuNP adsorption. In addition, after adsorption of the electronegative AuNPs to the DPH molecule, the former become positively charged revealing the delocalization of charge. This delocalization has been evidenced in the well-overlapped HOMO and LUMO frontier orbitals on all σ-electron hyperconjugated bonds (skeletal C_3-C_{12}-C_{21}), the overlap being greater in DPHA than DPH molecule which benefits the strong HOMO→LUMO transition in DPHA molecule. So, electron movement between these orbitals is easily facilitated in DPHA, thereby increasing the molecular electrical transport properties and photostability. The global and local reactive descriptor of the DPH and DPHA molecule shows that the DPHA molecule has higher anticancer activity than the DPH molecule. The binding free energy, inhibition constant, intermolecular energy, and hydrogen bonding between the ligand and protein signify that the DPHA molecule is more active than the DPH molecule against lung cancer. These results were further confirmed by MTT assay and SERS mapping analysis.

ACKNOWLEDGEMENTS

The author (SV) acknowledges Department of Physics, Mar Ivanios College, Thiruvananthapuram, Kerala, for the computational facility using the Gaussian 09. DS also acknowledge the DST-FIST program (SR/FST/College-182/2013, November 2013 & FIST No.393 dated September 25, 2014) to the Bishop Moore College.

CONFLICT OF INTEREST

The authors declare that they have no known competing financial interests or personal relationships that could have appeared to influence the work reported in this paper.

CREDIT AUTHORSHIP CONTRIBUTION STATEMENT

S.V: Conceptualization, methodology, writing—original draft, L.D.R: conceptualization, methodology, R.I: data curation, L.J: writing—review and editing, supervision, and D.S: conceptualization, writing—original draft, funding acquisition, and validation.

DATA AVAILABILITY STATEMENT

The data that support the findings of this study are available from the corresponding author upon reasonable request.

ORCID

Lynnette Joseph https://orcid.org/0000-0003-4528-680X

REFERENCES

1. Ildiz GO, Nunes CM, Fausto R. Matrix isolation infrared spectra and photochemistry of hydantoin. *J Phys Chem A*. 2013;5(2):726-734.
2. Paterson LO. Halogenated hydantoins. U.S. Patent No. 2,779,764. 29 Jan. 1957.
3. Bogoch S, Dreyfus J. *The Broad Range of Use of Diphenylhydantoin*. New York: Dreyfus Medical Foundation; 1970.
4. Perry JK, Newmark ME. Hemodialysis in the treatment of psoriasis. *Ann Intern Med*. 1979;91(2):207-218.
5. Jain ZJ, Gide PS, Kankate RS. Biphenyls and their derivatives as synthetically and pharmacologically important aromatic structural moieties. *Arab J Chem*. 2017;10:S2051-S2066. https://doi.org/10.1016/j.arabjc.2013.07.035.
6. Johansson MP, Olsen J. Torsional barriers and equilibrium angle of biphenyl: reconciling theory with experiment. *J Chem Theory Comput*. 2008;4(9):1460-1471.
7. Craig S. Phenytoin poisoning. *Neurocrit Care*. 2005;3(2):161-170.
8. Yaari Y, Selzer ME, Pincus JH. Phenytoin: mechanisms of its anticonvulsant action. *Ann Neurol*. 1986;20(2):171-184.
9. Richens A. Clin of phenytoin. *Clinical*. 1979;4(3):153-169.
10. Lopez T, Quintana P, Ascencio J, Gonzalez RD. The determination of dielectric constants of mixtures used in the treatment of epilepsy and the encapsulation of phenytoin in a titania matrix. *Colloids SurfA Physicochem Eng asp*. 2007;300(1–2):99-105.
11. Tanay A. Long-term treatment of the syndrome of inappropriate antidiuretic hormone secretion with phenytoin. *Ann. Intern Med*. 1979;90(1):50.
12. Matsuno H. Biocompatibility and osteogenesis of refractory metal implants, titanium, hafnium, niobium, tantalum and rhenium. *Biomaterials*. 2001;22(11):1253-1262.
13. Trisovic NP, Bozic BD, Lovic JD, et al. Electrochemical characterization of phenytoin and its derivatives on bare gold electrode. *Electrochim Acta Theriol*. 2015;161:378-387.
14. Giunchi A, Rivalta A, Bedoya-Mart´ N, et al. Surface induced phenytoin polymorph. 2. Structure validation by comparing experimental and density functional theory Raman spectra. *Crystal*. 2019;1(4):6067-6073.
15. Lopez T, Quintana P, Ascencio J, Gonzalez RD. The determination of dielectric constants of mixtures used in the treatment of epilepsy and the encapsulation of phenytoin in a titania matrix. *Colloids Surf. A Physicochem. Eng. ASP*. 2007;30(1–2):99-105.
16. Braun DE, Rivalta A, Giunchi A, et al. Surface induced phenytoin polymorph. 1. Full structure solution by combining grazing incidence X-ray diffraction and crystal structure prediction. *J Am Chem Soc*. 2019;57(1):6058-6066.
17. Dykman LA, Khlebtsov NG. Gold nanoparticles in biology and medicine: recent advances and prospects. *Acta Naturae*. 2011;3(2):34-55.
18. Yogeeswari P, Sriram D, Thirumurugan R, et al. Discovery of N-(2,6-Dimethylphenyl)-substituted Semicarbazones as anticonvulsants: hybrid Pharmacophore-based design. *J Med Chem*. 2015;48:6202-6211.
19. Thenmozhiyal JC, Wong PTH, Chui WK. Anticonvulsant activity of phenylmethylene hydantoins: a structure-activity relationship study. *J Med Chem*. 2004;47(6):1527-1535.
20. Camerman A, Camerman N. The stereochemical basis of anticonvulsant drug action. I. the crystal structure of diphenylhydantoin, a non-centrosymmetric structure soluted by centric symbolic addition. *Acta Cryst*. 1971;27(11):2205-2211.
21. Wong MG, Defina JA, Andrews PR. Conformational analysis of clinically active anticonvulsant drugs. *J Med Chem*. 1986;29(4):562-572.
22. Guerrab W, Lgaz H, Kansiz S, et al. Synthesis of a novel phenytoin derivative: crystal structure Hirshfeld surface analysis and DFT calculations. *J Mol Struct*. 2020;1205:127630.
23. Luchian R, Vinţeler E, Chiş C, Vasilescu M, Leopold N, Chiş V. Molecular structure of phenytoin: NMR, UV-Vis and quantum chemical calculations. *Croat Chem Acta*. 2015;88(4):511-522.
24. Shyni V, Leenaraj DR, Lynnette Joseph, Sajan D. Investigations of dianhydro-D-glucitol adsorbed on AuNPs surface: in silico and in vitro approach based on anticancer activity studies against A549 lung cancer cell lines. *J Mol Recognit*. 2021;0952-3499:1099-1352.
25. Frisch MJ, Trucks WG, Schlegel HB, et al. *Gaussian 09, Revision A.02*. Wallingford CT: Gaussian, Inc; 2009.
26. Becke AD. Density-functional thermochemistry. III. The role of exact exchange. *Int J Chem Phys*. 1993;98(7):5648-5652.
27. Lee C, Yang W, Parr RG. Development of the Colle-Salvetti correlation-energy formula into a functional of the electron density. *Phys Rev B*. 1988;37(2):785-789.
28. Wadt WR, Hay PJ. Ab initio effective core potentials for molecular calculations potentials for main group elements Na to Bi. *J Chem Phys*. 1985;82(1):284-298.
29. Kalaiarasi C, Sangeetha P, Pavan MS, Kumaradhas P. Crystal structure and theoretical charge density studies of dilantin molecule. *J Mol Struct*. 2018;1170:105-118.
30. Reed AE, Weinstock RB. Weinhold F. Natural population analysis. *J Chem Phys*. 1985;83(2):735-746.
31. Zhaoguang LZ, Zhang JL, Zhang W, et al. Effect of fluorine substitution on naphtha [2,1-b:3,4-b'] bis[1]-benzothiophene-derived semiconductors for transistor application. *Org Electron*. 2016;32:47-53.
32. Zhang M, Guo X, Zhang S, Hou J. Synergistic effect of fluorination on molecular energy level modulation in highly efficient photovoltaic polymers. *Adv Mater*. 2014;26:1118-1123.
33. Calais JL, Parr RG, Yang W. *Density-functional theory of atoms and molecules*. New York: Oxford University Press; 1989.
34. Swager TM, Levine M. HOMO and LUMO Trends in Conjugated Acenes. *Synfacts*. 2009;2009(07):0732-0732. http://dx.doi.org/10.1055/s-0029-1217213.
35. Walker W, Veldman B, Chiechi R, Patil S, Bendikov M, Wudl F. . Anti-aromatic Lowering of the HOMO-LUMO Gap. *Synfacts*. 2009;2009(02):0151-0151. http://dx.doi.org/10.1055/s-0028-1087493.
36. Rao PS, Kalva S, Yerramilli A, Mamidi S. Free radicals and tissue damage: role of antioxidants. *Free Radic Res*. 2011;1(4):2-7.
37. Yadav LDS. *Organic Spectroscopy*. Netherlands: Springer; 2005.
38. Nataraj A, Balachandran V, Karthick T. FT-IR and Raman spectra, DFT and SQMFF calculations for geometrical interpretation and vibrational analysis of 3-nitro-p-toluic acid. *J Mol Struct*. 2012;1022:94-108.
39. Bhatt R, Bhaumik I, Ganesamoorthy S, et al. Urbach tail and bandgap analysis in near stoichiometric LiNbO3 crystals. *Phys Status Solidi*. 2011;209(1):176-180.

40. Pretsch E, Bühlmann P, Badertscher M. *Structure Determination of Organic Compounds*. Berlin Heidelberg: Springer; 2009.
41. Socrates G. *Infrared Characteristic Group Wavenumber*. New York: John Wiley and Sons; 1980.
42. Mukhopadhyay A, Mukherjee M, Pandey P, Samanta AK, Bandyopadhyay B, Chakraborty T. Blue shifting C−H···O hydrogen bonded complexes between chloroform and small cyclic ketones: ring-size effects on stability and spectral shift. *J Phys Chem A*. 2009; 113:3078-3087.
43. Ravikumar C, Joe IH, Jayakumar VS. Charge transfer interactions and nonlinear optical properties of push–pull chromophore benzaldehyde phenylhydrazone: a vibrational approach. *Chem Phys Lett*. 2008;460 (4–6):552-558.
44. Varsanyi G. *Vibrational Spectra of Benzene Derivatives*. NewYork: Academic Press; 1969.
45. Coates J. *Interpretation of Infrared Spectra: a Practical Approach*. New York: John Wiley & Sons Inc.; 2000.
46. Roeges NPG. *A Guide to Complete Interpretation of Infrared Spectra of Organic Structure*. New York: John Wiley & Sons Inc; 1994.
47. Dollish FR, Fateley WG, Bentley F. *Characteristic Raman Frequencies of Organic Compounds*. Chichester: Wiley; 1974.
48. Dollish F, Bentley F. Infrared and Raman spectra of common organic compounds—from the Aldrich library of FT-IR spectra and the Dollish, Fateley and Bentley collection. *The Handbook of Infrared and Raman Characteristic Frequencies of Organic Molecules*. New York, NY: Academic Press; 1991:423-454.
49. Volovsek V, Baranovic G, Colombo L, Durig JR. Vibrational spectra of Para-disubstituted benzophenones. *J Raman Spectrosc*. 1991;22(1): 35-41.
50. Mdluli PS, Sosibo NM, Revaprasadu N, Karamanis P, Leszczynski J. Surface enhanced Raman spectroscopy (SERS) and density functional theory (DFT) study for understanding the regioselective adsorption of pyrrolidinone on the surface of silver and gold colloids. *J Mol Struct*. 2009;935(1–3):32-38.
51. Yang Y, Nogami M, Shi J, Chen H, Ma G, Tang S. Enhancement of third-order optical nonlinearities in 3-dimensional films of dielectric Shell capped au composite nanoparticles. *J Phys Chem B*. 2005;109 (11):4865-4871.
52. Foster JP, Weinhold F. Natural hybrid orbitals. *J Am Chem Soc*. 1980; 102:7211-7218.
53. Yun C-H, Boggon TJ, Li Y. Structures of Lung Cancer-Derived EGFR Mutants and Inhibitor Complexes: Mechanism of Activation and Insights into Differential Inhibitor Sensitivity. *Cancer Cell*. 2007;11(3): 217-227. https://doi.org/10.1016/j.ccr.2006.12.017.
54. Brough PA, Aherne W, Barril K, et al. 4,5-Diarylisoxazole Hsp90 Chaperone Inhibitors: Potential Therapeutic Agents for the Treatment of Cancer. *J. Med. Chem*. 2008;51(2):196-218. http://dx.doi.org/10.1021/jm701018h.
55. Eder M, Schlattner U, Wallimann T, Becker A, Kabsch W, Fritz-Wolf K. Crystal structure of brain-type creatine kinase at 1.41 Å resolution. *Protein Sci*. 2008;8(11):2258-2269. http://dx.doi.org/10.1110/ps.8.11.2258.
56. Rouvinen J. bovine lipocalin allergen bos D2, 1999.
57. Chen Y, Zhang YX, Wu ZF, et al. Biodegradable poly(ethylene glycol)-poly(ε-carprolactone) polymeric micelles with different tailored topological amphiphilies for doxorubicin (DOX) drug delivery. *RSC Adv*. 2016;6(63):58160-58172.
58. Ramya AN, Joseph MM, Maniganda S, Karunakaran V, Sreelekha TT, Maiti KK. Emergence of gold-mesoporous silica hybrid nanotheranostics: Dox-encoded, Folate targeted chemotherapy with modulation of SERS fingerprinting for apoptosis toward tumor eradication. *Small*. 2017;13(31):1700819.
59. Feng X, Moy AJ, Nguyen HTM, et al. Raman active components of skin cancer. *Biomedical Optics Express*. 2017;8(6):2835.
60. Stone N, Stavroulaki P, Kendall C, Birchall M, Barr H. Raman spectroscopy for early detection of laryngeal malignancy: preliminary results. *Laryngoscope*. 2000;110(10):1756-1763.
61. Hester RE. Biological applications of Raman spectroscopy. *FEBS Lett*. 1988;230(1–2):222-222.
62. Dollish FR, Fateley WG, Bentley FF. Characteristic Raman frequencies of organic compounds. *Anal. Chim Acta*. 1975;75(2):492.
63. Narayanan N, Nair LV, Karunakaran V, et al. Investigation of apoptotic events at molecular level Induced by SERS guided targeted theranostic nanoprobe. *Nanoscale*. 2016;8(22):11392-11397.
64. Smith R, Wright KL, Ashton L. Raman spectroscopy: an evolving technique for live cell studies. *Analyst*. 2016;141(12):3590-3600.
65. Mosmann T. Rapid colorimetric assay for cellular growth and survival: application to proliferation and cytotoxicity assays. *J Immunol Methods*. 1983;65:55-63.
66. Flahaut E, Durrieu M, Remy-Zolghadri M, Bareille R, Baquey C. Investigation of the cytotoxicity of CCVD carbon nanotubes towards human umbilical vein endothelial cells. *Carbon*. 2006;44: 1093-1099.
67. Toedt J, Koza D, Van Cleef-Toedt K. *Chemical composition of everyday products*. Westport, Connecticut: Greenwood Press; 2005.
68. Tufan Y, Karacan N, Davies JED. Vibrational spectroscopic investigations of M(Imidazole)2Ni(CN)4·2C6H12 clathrates. *Vib. Spectrosc*. 2000;23(1):51-55. http://dx.doi.org/10.1016/s0924-2031(99)00074-0.
69. Baranović G, Eckert-Maksić M, Golić M, Durig JR. Vibrational spectra. ab initio calculations and normal coordinate analysis for 3-methyl-3-vinylcyclopropene. *J Raman Spectrosc*. 1993;24(1):31-41. http://dx.doi.org/10.1002/jrs.1250240105.

SUPPORTING INFORMATION

Additional supporting information may be found online in the Supporting Information section at the end of this article.

How to cite this article: Shyni V, Leenaraj DR, Ittyachan R, Joseph L, Sajan D. Spectroscopic, density functional theoretical study, molecular docking, and *in vitro* studies based on anticancer activity studies against A_{549} lung cancer cell line of diphenylhydantoin adsorbed on AuNPs surface. *J Mol Recognit*. 2021;1–19. https://doi.org/10.1002/jmr.2916

Received: 6 March 2021 | Accepted: 25 May 2021
DOI: 10.1002/jmr.2920

RESEARCH ARTICLE

Journal of Molecular Recognition WILEY

Anticancer activity of indapamide adsorbed on gold nanoparticles: DFT, in-silico, and in-vitro analysis

V. Shyni[1] | D. R. Leenaraj[2] | Reena Ittyachan[3] | Lynnette Joseph[1] | D. Sajan[1]

[1]Centre for Advanced Functional Materials, Department of Physics, Bishop Moore College, Mavelikara, Kerala, 690110, India

[2]Department of Physics, Mar Ivanios College, Thiruvananthapuram, India

[3]Department of Physics, Sacred Heart College, Thrissur, India

Correspondence
Lynnette Joseph, Centre for Advanced Functional Materials, Department of Physics, Bishop Moore College, Mavelikara, Kerala 690110, India.
Email: lynnettejohn@gmail.com

Funding information
Department of Science and Technology, Ministry of Science and Technology, India

Abstract

The adsorption properties of the lung cancer agent indapamide (IND) on gold nanoparticles (AuNPs), were studied with the help of surface-enhanced Raman scattering techniques. The structure-activity of the IND and INDA molecule has been studied using DFT/B3LYP methodology. NBO analysis reveals that, both the molecules are stabilized by a C—H···O intramolecular hydrogen bonding, apart from the conjugative and intramolecular charge transfer interactions. The analysis of the electron density of frontier molecular orbital analysis gives a comparative idea of the reactivity, the low kinetic stability, and low value of energy gap indicating the electron transport in the molecule and thereby its bioactivity. The molecular electrostatic potential, local and global reactivity indicators predict the reactive site of the molecules. FT-IR, FT-Raman, and surface-enhanced Raman scattering have been investigated and compared with the theoretical prediction. Effective in-silico (molecular docking) biological activity screening of the molecules was checked on lung cancer cells. In-vitro (surface-enhanced Raman scattering techniques and MTT assay) analysis confirms the results from the in-silico analysis. This study promotes the potential of SERS agents for targeted drug delivery and photothermal therapy and the novelty of the IND and INDA molecule against lung cancer activity.

KEYWORDS
conjugation, Fukui, ICT, molecular docking, MTT assay, SERS

1 | INTRODUCTION

The toolbox of medicinal chemists is composed of a fairly small number of privileged building blocks, recurrently found in potent drug molecules; the SO_2NH_2 (sulfamoyl group) moiety is one of them.[1] The primary sulfonamides of the type RSO_2NH_2 constitute an important class of drugs, comprising several types of pharmacological agents possessing antibacterial, antiviral, anticarbonic anhydrase (CA), diuretic, protease inhibitory, cyclooxygenase 2 (COX2) inhibitory, and anticancer activities.[2-11] Inhibitor binding potency depends on the acidity of the sulfonamide group. Therefore, inhibitors with electron-withdrawing groups such as chlorophenyl ring, amide group, indole ring, and methyl group have increased inhibitor potency and inhibitor selectivity.[12,13] Methylindolin,[14] the most active hydrogen carrier, is formed when the biologically active methyl group[15] joins in the second position of the indole ring.[14] When the growth regulator 2-chlorobenzamide[16-20] joins with the sulfamoyl group, it become sulfamoyl chlorobenzamide,[21] the antihypertensive agent. The sulfamoylchlorobenzamide and methylindoline merge in conjunction which is recognized as indapamide [IND]. The IND molecule is an orally active sulphonamide diuretic agent.[21] Apart from the diuretic action IND compound exerts spasmolytic effects on blood vessels, consequently reducing the blood pressure.[22] Sulfonamides represent one of the classical chemo types associated with potent carbonic anhydrase (CA) inhibition.[16] The calcium channel blocker benidipine,[17] lowers the response to sympathetic nerve stimulation.[18] These medicinal properties of the IND molecule were the inspiration to examine its activity against lung cancer owing to the fact that hypertension, edema, pus, cough in lungs are the risk factor in lung cancer patients.[19,20] Also, shortness of breath and respiratory

 © 2021 John Wiley & Sons Ltd.

distress often increase the suffering of advanced-stage lung cancer patients. These symptoms can be triggered by pulmonary hypertension.[23] Therefore, it is important to analyze the anti-lung cancer characterization of the IND molecule for future studies. Researchers are still struggling to gather enough evidence before reaching the final conclusion about the effectiveness of the diuretic drug for lung cancer chemo.[24] From the literal review it has been apprehended that so far no study has been done on the lung cancer activity of indapamide, a diuretic drug. Hence, in this study, the characteristic features of the diuretic drug IND were identified to explore its scope for lung cancer activity.

Vibration spectral studies of molecules provide in-depth knowledge of the relationship between molecular architecture and bioactivity.[25] For this reason, the vibration spectral investigation of IND was carried out based on the Density Functional Theory (DFT). The theoretical studies support the experimental evidence. The gold nanoparticle has excellent bio-compact properties.[26] making it a suitable metal surface for drug distribution. The medicinal importance of IND and the biocompatibility of Au will offer better cancer therapy with fewer side effects. The global and local DFT reactivity descriptors of IND and indapamide@AuNPs (INDA) are useful in predicting the possible reactive sites of the molecular systems and the overall stability of the system respectively. Molecular docking is a powerful computational tool in predicting the binding mode and binding affinity of a ligand with proteins and provides high-quality predictions of ligand conformations. Therefore, here molecular docking study has been used to obtain information about protein-ligand reactions for IND and INDA, with different lung cancer proteins. It is a scaffold for the in-vitro study.

MTT assay, a well-established sensitive and reliable indicator of cellular metabolic activity, was performed for IND and INDA, to evaluate the cell viability. The research extends to the application of SERS technique also for the analysis of lung cancer cells (A549) using gold colloidal nanoparticles. In the present investigation, optimized molecular geometry, frontier molecular orbital (FMOs), molecular electrostatic potential (MEP) surface analysis, natural population analysis (NPA), and natural bond orbital (NBO) analysis of IND and INDA have been studied. Also, the molecular reactivity of IND and INDA through global and local reactivity descriptors is derived from density functional theory. Molecular docking analysis was also carried out to perceive the inhibitory nature of the IND and INDA molecule against lung cancer proteins. Surface-Enhanced Raman Scattering (SERS) study of IND has revealed its orientation on Au NPs and has been theoretically verified by density functional theory calculations. Also, the SERS spectra of INDA have been analyzed by incubating the drug-treated A549 cells, which divulges how INDA interacts with cells. The MTT assay has spelt out the survival and proliferation of cells when IND, INDA, and AU NPs interact with the cell.

2 | MATERIALS AND METHODS

2.1 | Preparation of gold colloids, cell culture, and protocol used for MTT assay

Indapamide (99%), Gold (III) chloride trihydrate (99.99%), and trisodium citrate (99%) were purchased from Sigma-Aldrich and used without further purification. Double distilled water was used throughout the experiments. The procedure for the preparation of gold colloids, the cell culture of human lung cancer cell lines A549, and the protocol used for MTT assay are detailed in our earlier report.[27]

2.2 | Spectroscopic measurements

The FT-IR spectrum of the IND was recorded with Perkin-Elmer Spectrum One FT-IR Spectrometer by using the KBr pellet technique in the wavenumber range 4000 to 400 cm^{-1} with an optical resolution of 1 cm^{-1}. The FT-Raman spectrum was determined in the range from 3500 to 50 cm^{-1} with the spectral resolution of 2 cm^{-1} using BRUKER RFS 27: Standalone FT-Raman Spectrometer; with a 1064 nm Nd: YAG laser source. The absorption spectra of the IND and INDA were recorded in DMSO as a solvent using Perkin Elmer lambda 950 UV-VIS-NIR in the region 200 to 800 nm. Particle size measurements were performed by High-Resolution Transmission electron microscopy (Tecnai T30 G2 S-Twin, FEI Company). Samples for TEM characterization were prepared by placing a drop of gold colloidal solution on a carbon-coated copper grid and dried under an IR lamp. SERS experiments have been carried out by incubating IND with citrate stabilized spherical Au NPs (Au NPs; 40 nm) as a SERS substrate and the spectra were measured by a WI-Tec Raman microscope (WI-Tec, Inc., Germany, alpha 300R). A laser beam was directed to the sample through 20 × objective with 600 g/mm grating and a Peltier cooled CCD detector. Samples were excited with a 633 nm excitation wavelength laser with 7 mW power. Stokes shifted Raman spectra were collected in the range 200 to 3000 cm^{-1} with 2 cm^{-1} resolution and an integration time of 0.5 and 20, accumulations. Prior to every measurement, calibration with a silicon standard (Raman peak cantered at 520 cm^{-1}) was performed. A_{549} Lung cancer cells were cultured in a four-well chamber slide and 100 µL (9:1, Au NPs/ IND) of INDA was added to the wells separately and was incubated at 37°C. SERS spectra were recorded after 30 minutes. After checking the SERS spectra inside the cells, SERS mapping has been performed using two cells by confocal Raman microscopy using 0.5s integration time, 150 × 150 points per line, and 50 × 50 µm mapping area along with X and Y directions. The excitation and emission spectra were documented on a SPEX Fluorolog F112X spectrofluorimeter. The MTT assay was recorded on a TECAN spectrophotometer with a reference reading at 655 nm.

2.3 | Computational details

Density functional theory (DFT) calculations were performed with the Gaussian'09 suite of programs[28] using B3LYP/6-31++G (d,p) together with the LANL2DZ basis set. B3LYP is a hybrid functional combining the Hartree-Fock and Becke exact exchange correlation[29] with the Lee-Yang-Parr correlation functional (LYP).[30] The time-dependent density functional theory (TDDFT) calculations were performed with the long-range corrected functional CAM-B3LYP and 6-31++G (d, p) together with LANL2DZ basis set. The molecule-

metal system structures of gold were optimized using same level of theory (B3LYP)[31] with the electron core potential basis set LANL2DZ developed by Hay and Wadt.[32,33] The detailed computation about quantum chemical insight (geometry optimization, Natural bond orbital (NBO) analyses vibrational wave number calculation on the basis of the potential energy distribution (PED)) and in silico studies (docking) are detailed in our earlier report.[27]

3 | RESULT AND DISCUSSION

3.1 | Structural analysis

The stable structure of IND and INDA molecules was calculated using DFT/B3LYP functional with hybrid 6-311++G (d, p) and LANL2DZ basis sets and are shown in Figure 1A,B. respectively. The optimized geometrical parameters were compared with the reported crystallographic data (CCDC No: 1448939)[34] and are tabulated in Table 1. The comparison of theoretical and experimental geometrical parameters using linear regression coefficient (R^2) calculations is graphically represented in Figure 2. The R^2 values show the reliability of theoretical calculation, howbeit, a little bit deviation is observed. This small deviation is due to the fact that the theoretical calculations are for the molecule in the gaseous phase and the experimental results are due to the molecule in the solid phase. The stabilized conformer shows that the IND consists of both a polar sulfamoyl chlorobenzamide moiety and a lipid-soluble methylindoline moiety. The chlorobenzene ring is planar but when it is connected with sulfamoyl it becomes a chair configuration with the confirmed dihedral angles, that is N_8—S_2—C_{21}—C_{20} and N_8—S_2—C_{21}—C_{23} are 124.1° and 98.2°, respectively. This moiety has bridged to the indole system through almost planar secondary amide. The steric hindrance between H_{31} in the secondary amide and H_{36} in the chlorobenzeneslighty distorts the planarity of the secondary amide. The envelope configuration is exhibited due to the attachment of a unique gauche-conformed methyl group to the indole system. The stabilized conformation of the INDA molecule is almost similar to the IND molecule, with the dihedral angle N_8—S_2—C_{21}—C_{20} and N_8—S_2—C_{21}—C_{23} being 128.2° and 95.6°, respectively. The bond angle of sulfur dioxide is 121.1° and 121.2° for IND and INDA molecules, respectively being slightly greater than the normally adopted bond angle. This is due to the intramolecular hydrogen bonding (C_{20}—H_{36}···O_4) between oxygen (O_4) and chlorophenyl C_{20}—H_{36}. The interesting factor observed in optimized geometry is the discrepancy of CC bond length in indole ring, that is, the lengthening of the C_9—C_{13}, C_9—C_{10}, and C_{10}—C_{11}bonds (1.53 Å, 1.56 Å and, 1.52 Å, respectively) and the shortening of the C_{11}—C_{12}, C_{11}—C_{14}, C_{14}—C_{16}, C_{16}—C_{17}, C_{17}—C_{15}, and C_{15}—C_{12} are 1.41 Å, 1.40 Å, 1.09 Å, 1.41 Å, 1.41 Å, and 1.40 Å, respectively. The inductive electron donor effect of the methyl group is reflected towards the indole ring. The DFT calculation shows that the bond lengths of S_2—O_4 and S_2—O_5 are 1.63 Å and 1.62 Å for the IND molecule and 1.63 Å and 1.67 Å for the INDA molecule, respectively. These are longer than the normal S—O bond length due to the C_{20}—H_{36}···O_4 (Figure 1A,B) intramolecular hydrogen bonding. However, the experimental values of the S_2—O_4 and S_2—O_5 bond lengths are both 1.44 Å. These are shorter than the normal S—O bond length due to intermolecular hydrogen bonding. In addition, another intramolecular hydrogen bonding (C_{22}—H_{37}···O_3) is observed in both IND and INDA molecules in between chlorophenyl and secondary amide. From the experimental and theoretical calculations of the IND and INDA molecules, the bond length of C_9—H_{25} (1.11 Å) is longer than that of other C—H bonds. The reason behind this is the interaction of methyl group with the axial hydrogen at C_9 that is the diaxial interaction. In other words, the lengthening of the bond length of C_9—H_{25} is due to steric interactions between axial substituents. In chlorophenyl, endocyclic bond angle C_{20}—C_{21}—C_{23} (121.1°) is increased and the exocyclic bond angle C_{21}—C_{20}—C_{19} (119.2°) and C_{21}—C_{23}—C_{24} (119.1°) is decreased from the normal bond angle (120°). This is due to the attachment of sulfamoyl group. The experimental values (Table 1) of C—H bond length are decreased, which is overestimated by DFT calculations. This may be due to the electronic effect of the methyl group. The DFT calculations show that the bond length of the C—Cl bond is 1.80 Å in both IND and INDA molecules. The theoretical calculation shows that the bond length increases. which is due to the redistribution of lone pair charges of oxygen and

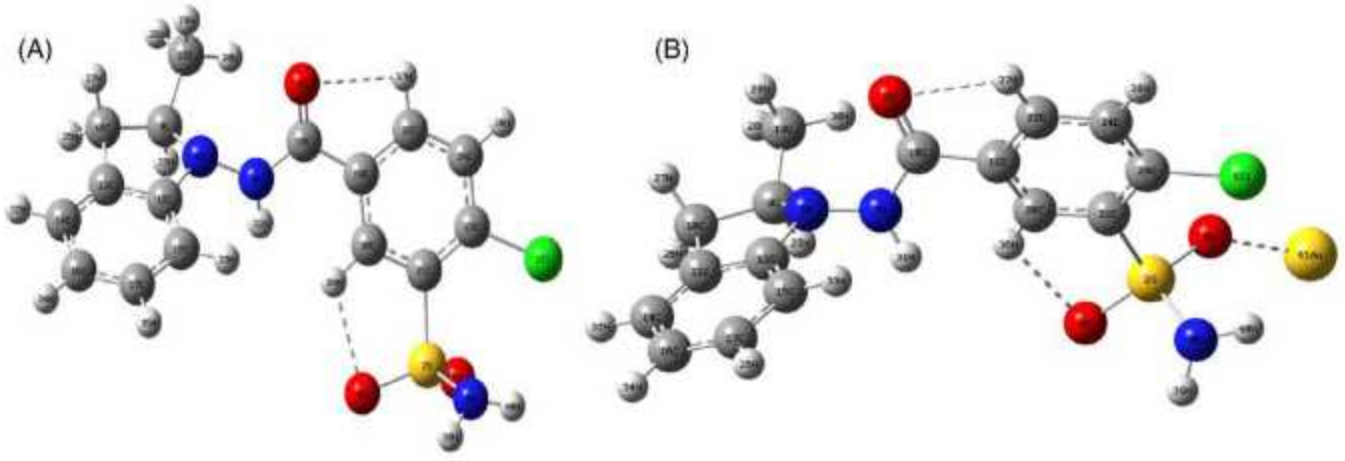


FIGURE 1 Optimized structure of (A) IND and (B) INDA using the B3LYP/6-31++G (d,p) together with the LANL2DZ basis set

TABLE 1 Optimized geometrical parameters of IND and INDA using B3LYP/6-31++G (d,p) together with the LANL2DZ basis set

Bond length (A°)				Bond angle (°)				Dihedral angle (°)			
Parameter	IND	INDA	Exp.[a]	Parameter	IND	INDA	Exp.[a]	Parameter	IND	INDA	Exp.[a]
S_2–C_4	1.63	1.63	1.45	C_4–S_2–C_5	121.5	121.3	121.4	N_8–S_2–C_{21}–C_{20}	−120.1	−117.23	−118
S_2–C_5	1.62	1.67	1.44	C_4–S_2–N_8	105.8	105.6	105.5	N_8–S_2–C_{21}–C_{23}	62.2	64	77.6
S_2–N_8	1.77	1.77	1.68	O_4–S_2–C_{21}	105.4	106.6	108.8	O_4–S_2–N_8–H_{39}	14.1	17.2	18.2
S_2–C_{21}	1.89	1.89	1.77	O_5–S_2–N_8	110.6	109.8	108.2	O_4–S_2–N_8–H_{40}	152.6	154.2	158.5
C_9–H_{25}	1.11	1.11	1.10	O_5–S_2–C_{21}	110.7	110.9	110.1	O_5–S_2–N_8–H_{39}	−118.4	−115.6	117.4
O_3–C_{18}	1.25	1.25	1.23	C_{20}–C_{21}–C_{23}	121.1	121.2	120.2	O_5–S_2–N_8–H_{40}	20.4	22.7	24.1
N_6–N_7	1.40	1.40	1.40	C_{19}–C_{20}–C_{21}	119.2	119.2	120.1	C_{21}–S_2–N_8–H_{39}	124.4	128.6	130.2
N_6–C_9	1.51	1.51	1.48	C_{21}–C_{23}–C_{24}	119.1	119.1	119.3	C_{21}–S_2–N_8–H_{40}	−98.22	−95.15	−98.21
N_6–C_{12}	1.42	1.42	1.42	N_8–S_2–C_{21}	104.4	105.5	102.4	O_5–S_2–C_8–H_{39}	−118.1	122.2	−125.1
N_7–C_{18}	1.39	1.39	1.38	N_7–N_6–C_9	118.2	118.8	117.4	O_5–S_2–C_8–Au_{40}		127.7	
N_7–H_{31}	1.02	1.02	1.01	N_7–N_6–C_{12}	119.6	119.6	114.1	H_{25}–C_9–C_{10}–C_{11}	89.9	90.5	92.8
N_8–H_{39}	1.02	1.02	1.02	C_9–N_6–C_{12}	109.8	109.6	104.1	H_{25}–C_9–C_{10}–H_{26}	−32.8	−32.2	35.2
N_8–H_{40}	1.02	1.02	1.02	N_6–N_7–C_{18}	122.3	122.1	118.4	C_{10}–C_{11}–C_{14}–C_{16}	−177.5	−177.4	−177.2
C_{11}–C_{12}	1.41	1.41	1.40	N_6–N_7–H_{31}	118.2	118.2	116.7	C_{10}–C_{11}–C_{14}–H_{32}	2.6	2.7	2.8
C_{11}–C_{14}	1.40	1.40	1.39	C_{18}–N_7–H_{31}	120.3	120.7	119.7	H_{33}–C_{15}–C_{17}–C_{16}	179.3	178.9	180.6
C_{12}–C_{15}	1.40	1.40	1.39	S_2–N_8–H_{39}	112.3	112.2	111.6	H_{33}–C_{15}–C_{17}–H_{35}	−0.6	−0.8	−0.9
C_{14}–C_{16}	1.42	1.42	1.40	S_2–N_8–H_{40}	114.7	114.6	113.6	C_{18}–C_{19}–C_{20}–C_{21}	−179.1	179.4	−180.2
C_{15}–C_{17}	1.41	1.41	1.40	O_{39}–N_8–H_{40}	118.2	118.8	118.1	C_{18}–C_{19}–C_{20}–H_{36}	−1.0	1.2	1.8
C_{16}–C_{17}	1.41	1.41	1.40	N6–C_9–C_{10}	102.2	102.3	102.1	C_{21}–C_{23}–C_{24}–C_{22}	−0.4	0.3	0.8
O_5···Au_{41}		22.31		N_6–C_9–C_{13}	113.9	112.2	113.1	C_{21}–C_{23}–C_{24}–H_{38}	179.3	−179.6	179.5
O_4···H_{36}	2.30	22.33	2.42	N_6–C_9–H_{25}	108.8	108.1	112.8	C_{12}–C_6–C_9–C_{10}	25.1	24.4	25.7
O_3···H_{37}	2.47	22.49	2.47	N_6–C_{12}–C_{11}	110.6	110.6	109.2	C_{12}–C_6–C_9–C_{13}	148.9	148.2	148.9
C_{13}–H_{28}	1.10	1.10	1.10	N_6–C_{12}–C_{15}	129.8	128.5	128.4	C_{12}–C_6–C_9–H_{25}	−89.8	−90.6	−89.2

[a]Taken from Reference 35.

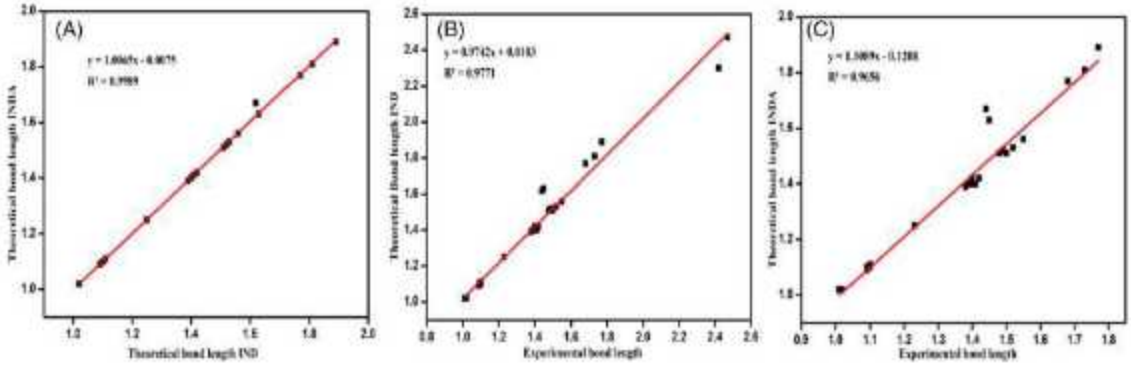


FIGURE 2 Linear regression coefficient (R2). (A) Theoretical IND and INDA bond lengths. (B) Experimental and theoretical IND bond length. (C) Experimental andtheoretical INDA bond lengths

nitrogen in the sulfamoyl group into chlorine in the chlorophenyl ring, and resultantly the chlorophenyl ring is significantly delocalized. The C_{20}–H_{36}···O_4 intramolecular hydrogen bond confirms this interaction. But the experimental value is 1.73 Å. The reduction of C_{20}–H_{36} bond length is due to the intermolecular hydrogen bonding. The skeleton bond length of CS increased in theoretical prediction and decreased in experimental prediction, confirms the interaction between the sulfamoyl group and the chlorophenyl ring.

3.2 | Natural population and natural bond orbital analysis

The variations of structural parameters and vibrational frequency depend on the allocation of charges on every atom in the molecule. Due to the distribution of charges over the atoms, the donor and acceptor pairs are formed and transfer of charges within the molecule takes place which leads to providing effective information about the

TABLE 2 Selective donor-acceptor hyperconjugative interactions of IND and INDA

	Donor (*i*)		Acceptor (*j*)				
Molecules	NBO	Occupancy	NBO	Occupancy	$E(2)^a$ kcal/mol	$E(j) - E(i)^b$ (a.u.)	$F(i,j)^c$ (a.u.)
IND	$\pi(Cl_1-C_{23})$	1.98648	$\pi^*(C_{20}-C_{21})$	0.02136	2.9	1.22	0.053
	$\pi(S_2-O_4)$	1.97484	$\pi^*(S_2-O_5)$	0.16199	3.31	0.88	0.05
	$\pi(S_2-C_{21})$	1.95788	$\pi^*(N_8-H_{39})$	0.00652	0.52	1.07	0.021
	$\pi(S_2-C_{21})$	1.95788	$\pi^*(C_{19}-C_{20})$	0.02425	2.81	1.21	0.052
	$\pi(S_2-C_{21})$	1.95788	$\pi^*(C_{23}-C_{24})$	0.02598	2.61	1.19	0.05
	$\pi(O_3-C_{18})$	1.99167	$\pi^*(N_7-C_{18})$	0.07906	0.81	1.41	22.12
	$\pi(O_3-C_{18})$	1.99167	$\pi^*(N_7-H_{31})$	0.03601	1.35	1.36	6.42
	$\pi(O_3-C_{18})$	1.99167	$\pi^*(C_{19}-C_{20})$	0.02425	1.4	1.52	16.04
	$\sigma(N_6-C_9)$	1.97827	$\sigma^*(C_{13}-H_{28})$	1.98385	5.63	1.16	0.038
	$\sigma(N_6-C_9)$	1.97827	$\sigma^*(C_{13}-H_{29})$	1.98668	2.11	1.37	0.024
	$\sigma(N_6-C_9)$	1.97827	$\sigma^*(C_{13}-H_{30})$	1.98642	1.81	1.91	0.044
	$n1(Cl_1)$	1.99306	$\pi^*(C_{23}-C_{24})$	0.02598	1.35	1.47	0.04
	$n2(Cl_1)$	1.97039	$\pi^*(C_{21}-C_{23})$	0.44314	3.86	0.85	0.051
	$n2(Cl_1)$	1.97039	$\pi^*(C_{23}-C_{24})$	0.02598	3.36	0.85	0.048
	$n3(Cl_1)$	1.92560	$\sigma^*C_{21}-C_{23})$	0.44314	12.31	0.3	0.06
	$n1(O_3)$	1.98034	$\pi^*(C_{18}-C_{19})$	0.06564	2.29	1.09	7.03
	$n2(O_3)$	1.86745	$\pi^*(N_7-C_{18})$	0.07906	23.89	0.67	2.36
	$n1(O_4)$	1.98692	$\pi^*(S_2-O_5)$	0.16199	1.24	0.98	0.032
	$n2(O_4)$	1.85185	$\pi^*(S_2-N_8)$	0.22857	6.92	0.32	0.043
	$n2(O_4)$	1.85185	$\pi^*(S_2-C_{21})$	0.19834	10.23	0.35	0.054
	$n2(O_4)$	1.85185	$\pi^*(C_{20}-H_{36})$	0.01718	1.09	0.71	0.026
	$n3(O_4)$	1.82825	$\pi^*(S_2-O_5)$	0.16199	14.07	0.38	0.066
INDA	$\pi(O_3-C_{18})$	0.99434	$\pi^*(N_7-C_{18})$	0.99177	0.26	1.4	22.2
	$\pi(O_3-C_{18})$	0.99434	$\pi^*(C_{19}-C_{20})$	0.01309	6.24	1.6	8.62
	$\pi(O_3-C_{18})$	0.99434	$\pi^*(N_7-H_{31})$	0.99330	0.95	1.41	6.86
	$\sigma(N_6-C_9)$	0.98630	$\sigma^*(C_{13}-H_{28})$	0.99085	6.51	1.43	0.034
	$\sigma(N_6-C_9)$	0.98630	$\sigma^*(C_{13}-H_{29})$	0.99366	3.32	1.63	0.029
	$\sigma(N_6-C_9)$	0.98630	$\sigma^*(C_{13}-H_{30})$	0.99236	2.25	1.31	0.023
	$n1(O_3)$	0.98816	$\pi^*(C_{18}-C_{19})$	0.03441	1.62	1.06	8.4
	$n1(O_4)$	0.99086	$\pi^*(S_2-O_5)$	0.15427	0.64	0.94	0.034
	$n1(O_4)$	0.99086	$\pi^*(S_2-C_{21})$	0.12058	0.51	1	0.03
	$n2(O_4)$	0.93109	$\pi^*(S_2-O_5)$	0.15427	2.4	0.32	0.036
	$n2(O_4)$	0.93109	$\pi^*(S_2-N_8)$	0.11259	1.53	0.35	0.03
	$n2(O_4)$	0.93109	$\pi^*(C_{20}-H_{36})$	0.01055	0.54	0.76	0.026
	$n2(O_3)$	1.86745	$\pi^*(C_{18}-C_{19})$	0.06564	12.29	1.09	0.045
	$n2(O_3)$	1.86745	$\pi^*(N_7-C_{18})$	0.07906	23.89	0.67	0.114
	$n3(O_4)$	0.92435	$\pi^*(S_2-O_5)$	0.15427	5.47	0.32	0.055
	$n3(O_4)$	0.92435	$\pi^*(S_2-N_8)$	0.11259	7.28	0.35	0.065
	$n1(O_5)$	0.98467	$\pi^*(S_2-O_4)$	0.06488	0.85	1	0.038
	$n1(O_5)$	0.98467	$\pi^*(S_2-O_5)$	0.15427	0.92	0.95	0.04
	$n1(O_5)$	0.98467	$\pi^*(S_2-N_8)$	0.11259	0.26	0.98	0.021
	$n3(Au_{41})$	0.86224	$\pi^*(S_2-O_5)$	0.15427	0.13	0.27	8.008

[a]E(2) means energy of hyperconjugative interactions.

[b]Energy difference between donor and acceptor I and J NBO orbitals.

[c]F(I, J) is the Fock matrix element between I and j NBO orbitals.

electronic structure and molecular properties. Natural population analysis (NPA) was used to understand the atomic charge distribution over the chemical bonding.[36] The plot of natural atomic charges is shown in Figure S1. The charge density of the atoms in the IND molecule is higher than the INDA molecule and the gold atom has a positive charge. This shows that the electrons move easily from the gold atom to the IND molecule. The electronegative sulfur atom shows the most positive charge on both INDA and IND molecule. This confirms the increase in the S—O bond length and the formation of C_{20}—H_{36}···O_4 hydrogen bonding. The chlorine atom shows positive charge on the IND molecule and negative charge on the INDA molecule. It also shows a longer C—Cl bond length, which is evidence of charge delocalization. The charge variation in oxygen, nitrogen, and the carbon atom (C_{23}) in the molecules strengthen the result. The carbon atoms in the secondary amide (C_{18}) and methyl group (C_{13}) have more positive and negative charge, respectively. This is due to the formation of intramolecular C_{22}—H_{37}···O_3 hydrogen bonding. Sulfamoyl nitrogen atom (N_8) and indole nitrogen atom (N_6) show more and less negative charge, respectively. It is due to the electron-withdrawing nature of the sulfamoylchlorobenzamide moiety and methylindoline moiety.

The second-order perturbation theory of the Fock matrix in the NBO analysis has given information about intramolecular charge transfer (ICT) or hyper conjugative interactions, electron donor orbital, acceptor orbital, and the interacting stabilization energies resulting from the second-order micro disturbances theory,[37,38] which are presented in Table 2. From the DFT calculations, strong intramolecular hyper conjugative interactions and ICT interactions are seen and confirmed here as seen in the optimized geometry. The intramolecular hyper conjugative interaction (C_{22}—H_{37}···O_3) of the IND and INDA molecule was formed by the core orbitals overlap between $\pi(O_3$—$C_{18})$ and $\pi^*(C_{19}$—$C_{20})$ which has resulted from intramolecular charge transfer (ICT) causing stabilization of the system. In IND molecule $\pi(O_3$—$C_{18})$ conjugate with anti-bonding orbital of $\pi^*(C_{19}$—$C_{20})$, $\pi^*(N_7$—$C_{18})$, and $\pi^*(N_7$—$H_{31})$ which leads to strong delocalization with energies 16.04, 22.12, 6.42 kcal/mol, respectively; around in chlorophenyl and indole ring through the bridge secondary amide. The same donations in the INDA molecule change to 6.24, 22.20, and 6.86 kcal/mol in the same order. These interactions are observed as an increase in electron density (ED) in the sp^2 hybridization orbital that weakens the respective bonds. Another important hyperconjugative interaction, the electron density transfer from one electron pair of the O_4 atom to the C_{20}—H_{36} anti-bonding orbital in the C_{20}—H_{36}···O_4 system are well-established in both IND and INDA molecule. In general, such interactions lead to a decrease in population (NPA) of C_{20}—H_{36} anti-bonding orbital, this increases the length of the C_{20}—H_{36} bond and decreases the length of S_2—O_4 and S_2—O_5 bonds, which is confirmed by optimized geometry and charge analysis. The NBO analysis of the both IND and INDA molecule clearly explains the evidence of the formation of strong ICT interaction between n(O3) and anti-bonding orbital of C_{18}—C_{19}, N_7—C_{18}. The stabilization energy $E(2)$ associated with conjugative interaction $\pi^*(C_{18}$—$C_{19})$ and $\pi^*(N_7$—$C_{18})$ is 17.06, and 23.89 kcal/mol, respectively for IND molecule and 12.29, and 23.89 kcal/mol, respectively for INDA molecule in the same order.NBO data show that the many other conjugative interactions in the IND and INDA molecule are $n1(C_{11}) \rightarrow \pi^*(C_{21}$—$C_{23}$, C_{23}—C_{24}, C_{21}—C_{23}, C_{23}—C_{24}, C_{21}—$C_{23})$, $n1(O_5) \rightarrow \pi^*$ (S_2—O_4, S_2—N_8, S_2—C_{21}, S_2—O_4, S_2—N_8), $n1(N_6) \rightarrow \pi^*(N_7$—$C_{18}$, N_7—H_{31}, C_9—C_{13}, C_9—H_{25}, C_{12}—$C_{15})$, $n1(N_7) \rightarrow \pi^*(O_3$—$C_{18}$, N_6—C_9, N_6—C_{12}, C_9—$C_{10})$, $n1(N_8) \rightarrow \pi^*(S_2$—$O_4$, S_2—O_5, S_2—$C_{21})$ with high stabilization energy (shown in Table 2). There are σ (N_6—C_9)/$\sigma^*(C_{13}$—$H_{28})$, $\sigma^*(C_{13}$—$H_{29})$, and $\sigma^*(C_{13}$—$H_{30})$ hyper conjugative interactions occur in both in the IND and INDA molecule. This interaction gives evidence of the existence of electronic effects such as back-donation and induction. The charge transfer from the Lewis valence orbital (donor) to the non-Lewis orbital (acceptor) confirms the decrease in its occupancy. This describes the electron delocalization. Also, the hybridization of the molecule rearranged according to the charge transfers. The chlorine atom and all hydrogen atom has s hybridization, a sulfur atom, and the 9th and 10th carbon atom have sp^3 hybridization and all other carbon atoms have sp^2 hybridization for IND and INDA molecule. The electron cloud movement from the donor to the acceptor causes the molecule to become highly polarized and the ICT is responsible for the biological activity of the IND and INDA molecules. The overall analysis of the NBO analysis shows that the conjugative and ICT interactions are dominant in the INDA molecule.

3.3 | Frontier molecular orbital and electronic spectra analysis

The energy separation between the highest occupied molecular orbital (HOMO) and the lowest unoccupied molecular orbital (LUMO) is known as the HOMO-LUMO energy gap. The HOMO-LUMO energy gap is otherwise known as the FMO's energy. The HOMO is associated with nucleophilicity and LUMO with the electrophilicity of the molecule. The frontier electron density predicts the most reactive site of the molecule as well as its chemical stability. In quantum chemistry, FMO's energy is an important parameter, which is the result of a significant degree of intramolecular charge transfer from the end-capping electron-donor groups (HOMO) to the efficient electron-acceptor groups (LUMO) through the conjugated path. In both IND and INDA molecule, the HOMO is located over the methylindoline and the LUMO is located over the sulfamoylchlorobenzamide. Both molecules have the same 'A' symmetry. The frontier molecular orbital transition implies an electron density transfer to methylindoline from sulfamoylchlorobenzamide in both IND and INDA molecule. The indapamide adsorbed on to gold nanoparticles affects the HOMO and LUMO distribution. The difference in energy between the FMOs of the IND and INDA molecules are 3.41 and 2.85 eV, respectively as shown in Figure 3A,B. This shows that the indapamide adsorbed on to gold nanoparticles leads to a decrement in the energy gap value. The narrow energy gap of the IND and INDA molecules enhances the molecular electrical transport properties and photostability, especially more in INDA molecule. As photostability increases its drug stability also increases. This means that the conjugative interaction between a lone pair electron in the gold nanoparticle and π-electron

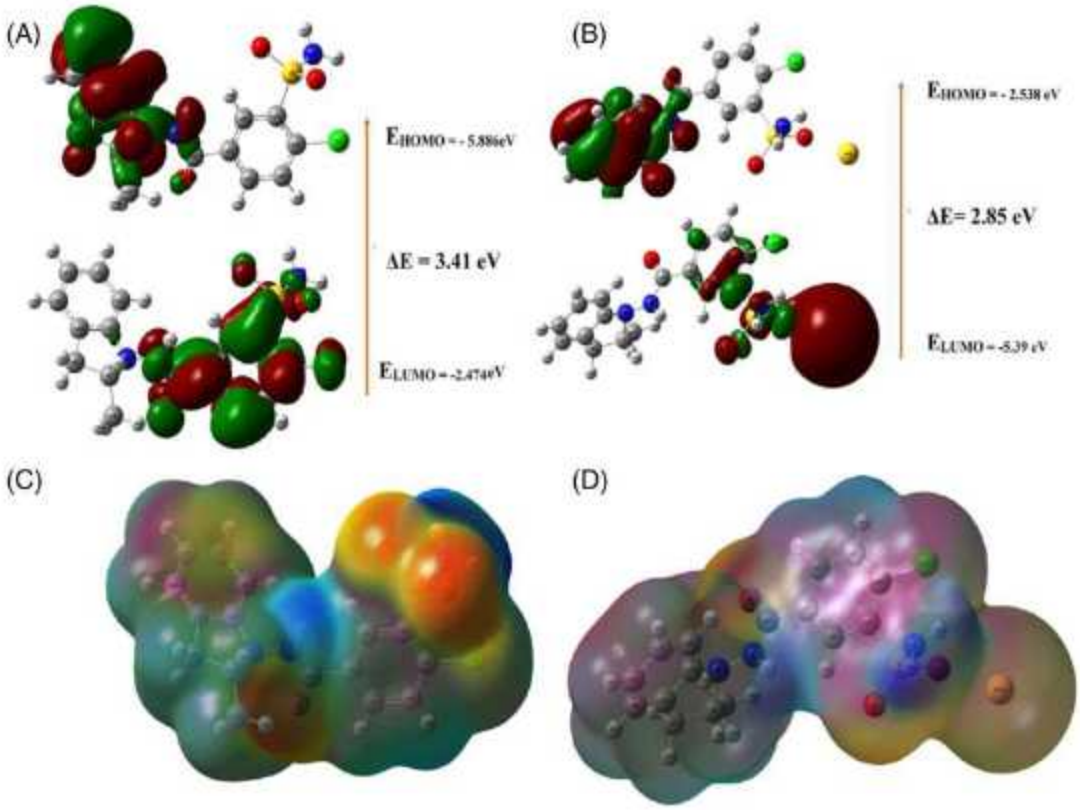


FIGURE 3 (A) Graphical representation of frontier molecular orbital of the IND molecule. (B) Graphical representation of frontier molecular orbital of the INDA molecule. (C) Molecular electrostatic potential plots of IND molecule and (D) molecular electrostatic potential plots of the INDA molecules

in the ring system increase high reactivity with low kinetic stability which leads to high stability in the INDA molecule than in the IND molecule.

Global chemical reactivity descriptors from FMO values such as ionization potential (A), electron affinity (I), electronegativity (χ), chemical potential (μ), electrophilicity index (ω), chemical hardness (η), and softness (S) is defined by Koopman's theorem[39] expressed by the relations $I = -E_{HOMO}$, $A = -E_{LUMO}$, $\eta = \frac{(I-A)}{2}$, $S = \frac{1}{\eta}$, $\mu = \frac{-(I+A)}{2}$, $\chi = \frac{(I+A)}{2}$, $\omega = \frac{\mu^2}{2\eta}$. The calculated values of I, A, χ, μ, η, S and ω are 5.89 eV, 2.47 eV, 4.18 eV, −4.18 eV, 1.71 eV, 0.59 $(eV)^{-1}$ and 5.12 eV, respectively for IND molecule and 5.39 eV, 2.54 eV, 3.97 eV, −3.97 eV, 1.43 eV, 0.70 $(eV)^{-1}$ and 5.51 eV, respectively for INDA molecule. The negative chemical potential and hardness of the IND and INDA molecules signify the resistance toward the deformation of the electron cloud of the chemical system under small perturbations encountered during the chemical process. In other words, the resistance to change the electronic distribution is low in IND and INDA molecule showing less hardness. The value of resistance and the electrophilicity index has confirmed these results. This is confirmed by the fact that when IND molecule are absorbed on to gold nanoparticles, the (INDA) electrophilicity index and chemical potential increase. Also, global chemical reactivity descriptors show that every group in the IND and INDA molecules are highly reactive, thereby the biological activity of drug-receptor (molecules interact with proteins in the cell) interaction being possible.

The condensed Fukui functions[40] are found by taking the finite difference approximations from population analysis of atoms in molecules, depending on the direction of the electron transfer. The Fukui indices are shown in Table S1. Parr and Yang et al,[41] showed that sites in chemical species with the largest values of kth Fukui function (f_k) on the atom site show high reactivity for corresponding attacks, electrophilic attack (f_k^-), nucleophilic attack (f_k^+), free radical attack(f_k^0). The sites for the nucleophilic attack of the IND and INDA molecules are suggested to be the C_{21},C_{19},C_{18}, and C_{23} atoms in the sulfamoylchlorobenzamide moiety and the results are graphically shown in LUMO in Figure 3A,B. Four carbon atoms being sites adapted for this type of attack it exists in a both great and very similar charge density. The carbon atoms are united to a sulfamoyl group, oxygen atom, and chlorine atom and this is the reason why they induce the formation of a carbocation, which disperses the charge by means of the resonance effect to obtain its stability. The C_9 and C_{21} atom, respectively are revealed to be the sites of electrophilic attack in IND and INDA molecules, according to the Fukui indices, and are represented in the HOMOplot in Figure 3A,B. The methyl group is connected to C_9 atom and the sulfamoyl group is connected to C_{21} atom. The presence of the methyl and sulfamoyl groups forms the electron donators by the effects of the resonance. The radical attack's possible sites are O_5 and O_4 connected to sulfur atom in the sulfamoyl group. The reactive site for the IND and INDA molecules are similar. Nevertheless, the intensity of reactivity is more in the INDA molecule.

The reactions of free radicals can be seen affected, and even controlled, by polar factors. Even though the free radicals are neutral, they present certain tendencies to gain or lose electrons. The reason why they exhibit the slight character of electrophilic or nucleophilic is due to the indapamide adsorption on to gold nanoparticles. In addition, it has increased the flow of electrons, that is, ICT. The literature review[42] shows that, the free radicals are unstable molecules that can damage the cancer cells in the body which means that the INDA molecule cause more damage to the cancer cells. The results of frontier molecular orbitals energy gap, global and local reactive descriptors of the INDA molecule projects that they have the highest cancer activity than the IND molecule.

Electrostatic potential maps or molecular electrostatic potential maps, also known as molecular electromagnetic surfaces, depict the charge distribution of molecules in three dimensions.[43] Molecular electrostatic potential (MEP) surfaces of IND and INDA molecule are shown in Figure 3C,D. According to MEP surfaces, the IND shows a more negative potential (red) value at the O_3, O_4, O_5, and N_8 atoms and the INDA shows more negative potential at O_3 and O_4 atoms for electrophilic attacks. The positive potential (blue) value of IND and INDA molecules are (H_{31}, H_{39}, H_{40}) and (H_{30}, H_{31}, H_{36}, H_{39}, H_{40}), respectively for nucleophilic attacks. The zero potential (yellow) shows that most of the atoms in the IND and INDA molecules are sites of radical attack, which is more in INDA molecule than IND molecule. The observed and calculated UV-vis spectra (DMSO solution) of the IND and INDA molecules are combined and analyzed in Figure 4A and Table 3. The observed and simulated UV-vis spectra of the IND molecules are noted as INDE and INDT, respectively and for INDA molecule they are noted as INDAE and INDAT, respectively in the above order, in Figure 4A. The IND and INDA molecules absorption bands are observed at 281 nm and (670, 621 nm), respectively with excitation energy values of 4.22 and 1.85, 1.99 eV, respectively. These peaks can be assigned to $\pi \rightarrow \pi^*$ and $n \rightarrow \sigma^*$ transitions, respectively.[44] These transitions were calculated for IND and INDA molecule at (235, 310, 366 nm) and 671 nm, respectively with excitation energy values of (2.81, 3.34, 3.78 eV) and 1.79 eV, respectively. Similar to the observed bands, the calculated bands can also be assigned to $\pi \rightarrow \pi^*$ and $n \rightarrow \sigma^*$ transitions. The absorption peaks of IND molecule are assigned to $\pi \rightarrow \pi^*$ transitions and arise due to the presence of conjugation interactions in the sulfamoylchlorobenzamide moiety. The absorption peaks of INDA molecule are assigned to $n \rightarrow \sigma^*$ transitions which arise due to the ICT interactions between the lone pair of electrons present in the electronegative atoms and σ electrons in the sulfamoylchlorobenzamide moiety. The $\pi \rightarrow \pi^*$ and $n \rightarrow \sigma^*$ transitions are responsible for biological activity of the molecule, the $n \rightarrow \sigma^*$ transition (ICT) being more responsible for the biological activity. The optical band gap was obtained from Tauc's equation[35] [$\alpha h\nu = A\,(h\nu - E_g)^n$] and graphical plot (Figure 5). The energy required for exciting electron from $\pi \rightarrow \pi^*$ (IND) and $n \rightarrow \sigma^*$ (INDA) transitions state is seen to be 3.63 eV (Figure 4C) and 2.80 eV (Figure 4D), respectively and it matches with the frontier molecular orbital energy gap. All of the above optical studies reveal that INDA possesses good optical behavior which has enhanced the bioactivity of the INDA molecule than IND.

3.4 | Vibrational spectral analysis

3.4.1 | IR and Raman spectra

The vibrational spectral analysis for the IND molecule, based on the FT-Raman, FT-IR, and the computed vibrational spectra were performed and the vibrational modes were assigned based on potential energy distribution (PED) analysis. The majority of the observed vibrational modes are coincident in both IR and Raman spectra, and therefore, the unit cell is probably non-centrosymmetric. The spectral assignments are tabulated in Table 4 and the compared graphical spectral assignments are shown in Figure 5.

Sulfamoyl group vibrations

The amino group and sulfonyl group together are known as the sulfamoyl or sulfonamide group. In sulfamoyl, the SO_2 symmetric and asymmetric stretching vibrations are expected in the regions 1125 to 1150 cm^{-1}, and 1295 to 1330 cm^{-1}, respectively, and the S=O stretching vibrations occur in the region 1225 to 980 cm^{-1}.[45] In IND, the observed bands at 1158 cm^{-1} in IR, 1299 cm^{-1}in IR (1301 cm^{-1}

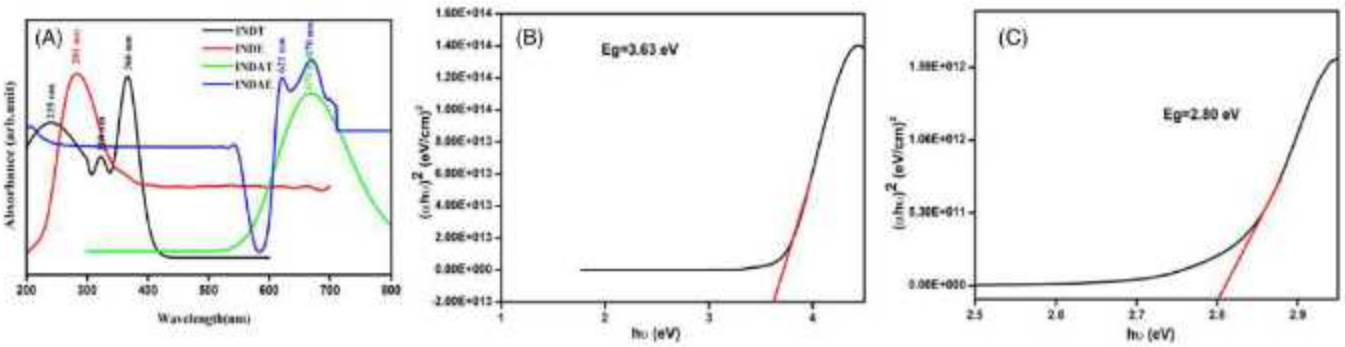


FIGURE 4 (A) The electronic transitions of simulated and observed UV–vis spectra of the IND and INDA molecule. (B) Tauc's plot of the IND molecule. (C) Tauc's plot of the INDA molecule

TABLE 3 Experimental absorptions (λ_{max}Expt),calculated absorptions (λ_{max}calc.), energy (E) and oscillator strength (*f*) of the IND and INDA molecule using TD-DFT method at the B3LYP/6–311++G(d,p) and B3LYP/LANL2DZ level of basis set

Molecules	Excitation	CI expansion co-efficient	λ_{max}calc. (nm)	*E* (eV)	λ_{max}Expt. (nm)	*E* (eV)	(*f*)	Contribution of orbital	Bands
IND (HOMO→95 and LUMO→96)	Excited state 1 95 → 96	Singlet-A	235	2.87	281	4.22	0.0073	π → π*	R-Bands (German: Radikalartig)
	Excited state 2 95 → 97	Singlet-A	310	3.34			0.0039	π → π*	R-Bands (German: Radikalartig)
	Excited state 3 95 → 98	Singlet-A	366	3.78			0.0054	π → π*	R-Bands (German: Radikalartig)
INDA (HOMO→95 and LUMO→94)	Excited state 1 95B → 94B	2.047-A	671	1.79	621	1.85	0.0005	n → σ*	R-Bands (German: Radikalartig)
	Excited state 2 93B → 94B	2.007-A			670	1.99	0.0087	n → σ*	R-Bands (German: Radikalartig)

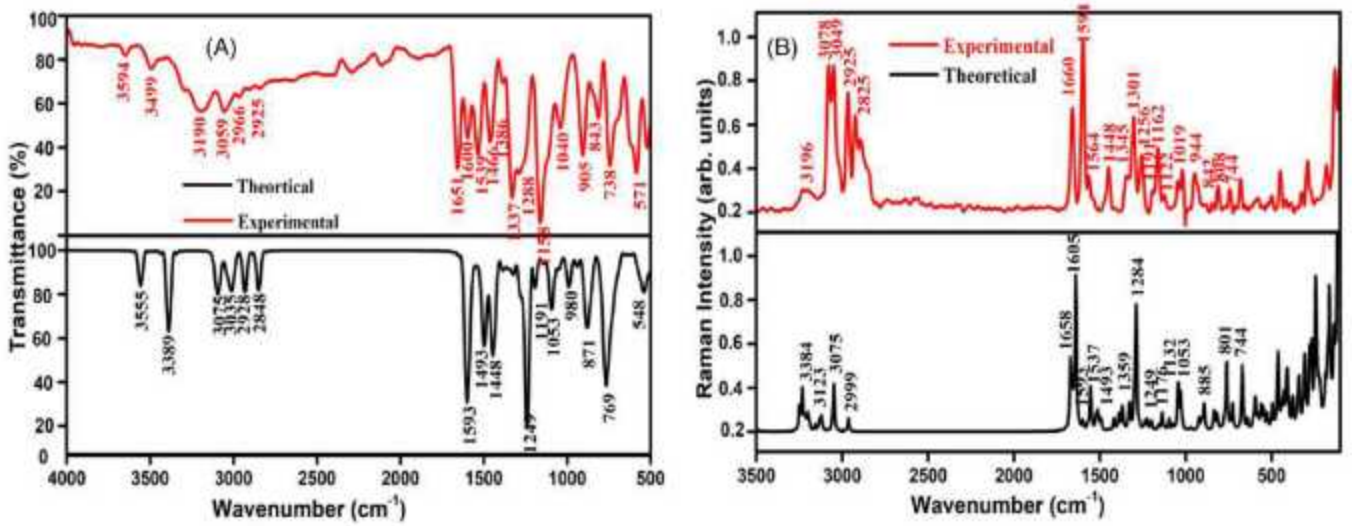


FIGURE 5 Comparison of observed and simulated (A) FT-IR spectra of the IND molecule. (B) FT-Raman spectra of the IND molecule

in Raman) and 889 cm^{-1} in Raman are assigned to SO_2 symmetric stretching, SO_2 asymmetric stretching and S=O stretching, respectively, which are in close agreement with the rule of Bellamy.[46] The observed red-shift in the SO_2 symmetric stretching vibrations and the blue-shift in S=O stretching confirms the formation of a strong intramolecular C_{20}—H_{36}···O_4 hydrogen bond. This intramolecular hydrogen bond increases the S—O bond length and OSO bond angle which bonds IND molecules more stable with chair conformation of the sulfamoyl chlorophenyl, which is essential in the stabilization of molecules of biological importance. The stretching frequencies of NH_2 group vibrations generally occur in the region 3500 and 3300 cm^{-1}.[46]The observed symmetric and asymmetric stretching vibrations are observed weak at 3594 cm^{-1} and 3499 cm^{-1}, respectively. The red-shift of wavenumber is due to the interaction between the sulfonyl functional group and chlorophenyl. The S—N stretching vibrations are generally observed in the region around 700 cm^{-1}.[47]The observed wavenumber is at 772 cm^{-1}, which strengthens the inference of ICT existing between the sulfonyl and amino group. The C—S stretching vibrations are generally observed in the region 850 to 570 cm^{-1}.[48] The observed weak Raman band at 944 cm^{-1}. The position of this band depends on the strength of hydrogen bonding; the blue-shift of the wavenumber evidenced by the stronger hydrogen bond. Also, this bond is the skeleton bond between the sulfamoyl group and chlorophenyl group. The blue-shift of the wavenumber may also be due to the ICT between the sulfamoyl group and chlorophenyl group. The spectral behavior of the sulfamoyl group is expected to be affected by the neighboring chlorophenyl ring system.

TABLE 4 Vibrational assignments for the IND molecule

Unscaled wavenumber	Scaled wavenumber	Experimental		Assignments with PED%
		IR	Raman	
3699	3555	3594w		$\nu_{asy}NH_2$ (100) sulfamoyl
3526	3389	3499w		$\nu_{sy}NH_2$ (100) sulfamoyl
3521	3384	3433w		νNH (100) amide
3249	3123	3190s	3196vw	ν_{sy}CH (100) phenyl
3200	3075		3078vs	ν_{asy}CH (99) indole
3190	3066	3059s		ν_{asy}CH (98) indole
3158	3035		3049vs	$\nu_{asy}CH_3$ (98) methyl
3120	2999	2966s		$\nu_{asy}CH_2$ (94) indole,
3047	2928	2925s	2925 s	$\nu_{sy}CH_2$ (64) indole $\nu_{sy}CH_3$ (30) methyl
2964	2848	2839s	2825 m	νCH (70) indole
2840	1658	1651vs	1660s	νC=O (88) amide
1670	1605	1600m		νC=C (68) indole δ_{sci} NH_2 (73)
1658	1593	1599m	1594vs	νC=C(82) indole
1640	1576		1564w	νC=C(80) phenyl
1600	1537	1539w		νC=C (72) phenyl
1554	1493	1466m		β NH (60) amide
1522	1463	1464m		δ_{sci} CH_3 (86)
1507	1448		1448w	δ_{sci} CH_2 (87) indole, δ_{sci} CH_3 (22) methyl
1491	1432	1399vs		β CH (61) indole
1443	1387	1386s		um CH_3(80)
1418	1362	1363vs		ν CC (62) indole
1414	1359		1345w	β CH (59) phenyl
1388	1334	1337vs		β CH (53) indole
1365	1311	1299w	1301 m	ν CC (68) phenyl, ν_{asy} SO_2 (82) sulfamoyl
1336	1284	1288vs		β CH (86) indole
1299	1249	1254w	1256w	β CH (68) phenyl
1239	1191		1191vw	t CH_2 (53) indole
1224	1176	1165vw	1162w	ν CC (56) indole
1200	1153	1158vs		β CH (68) indole, ν_{sym} SO_2 (52) sulfamoyl
1178	1132	1122w	1122vw	β CH (63) phenyl
1096	1053	1043m		ρNH_2 (61) sulfamoyl
1073	1031	1040m	1045vw	β NNC (45), CCN (28) indole, β CCC (15) phenyl
1043	1002		1019w	γ CH (52) phenyl,
1020	980		977vw	γ CH (56) indole
986	948		944w	γ CH (45) phenyl γ CH (63) indole, ν C–S (60) sulfamoyl
937	900		905m	ρ CH_2 (41) indole, ρ CH_3 (33) methyl, γ CH (20) indole
921	885		889vw	νS=O (47) sulfamoyl
906	871	905s		β NNC (49), β CCN (35) indole
891	856	843m	842vw	γ CH (37) phenyl, γ CH (18) indole
834	801	811m	808vw	νCCl (52) phenyl, β CCC (56) indole
801	769		772vw	ν CS (30) ν S–N (23) sulfamoyl
774	744	738m	744vw	γ CCN (16) indole, γ CH (31)phenyl

Abbreviations: ν, stretching; β, in-plane bending; γ, out-of-plane bending; τ, torsion; UM, umbrella mode.

Chlorophenyl ring vibrations

Ortho-, *Meta-* and *Para*-positions in phenyl hydrogen atoms are replaced with secondary amide's carbonyl group, a chlorine atom, and sulfamoyl group's sulfur atom, respectively. The aromatic C–Cl absorption bands occur in the region 830 to 560 cm^{-1}.[49,50] The medium C–Cl stretching Raman band is observed at 811 cm^{-1}. The

C—Cl stretching mode was decreased due to the mass of the chlorine atom in the *meta*-position in the phenyl ring. This tends to increase the C—Cl bond length. That is, this result confirms the optimized geometry result. Furthermore, according to Socrates' findings,[44] single and double bonded CC stretching is expected in the range 1380 to 1280 cm^{-1} and 1650 to 1430 cm^{-1}, respectively, when combined with the chlorophenyl with C=O group.[44] A semi-circular single and double bonded CC ring vibrations are observed at (1299, 1301) cm^{-1} and (1599, 1594, 1539, 1564) cm^{-1}, respectively owing to the charge delocalization in the ring. The C—H symmetric and asymmetric stretching vibrations of the phenyl ring are expected in the wide region of 3130 to 3000 cm^{-1}.[46,51]The intense band in IR at 3190 cm^{-1} and the very weak band in Raman at 3196 cm^{-1} are assigned as C—H symmetric stretching. Also, a very intense Raman and IR band at 3078 cm^{-1} and 3059 cm^{-1}, respectively is observed as C—H asymmetric stretching. The enhanced intensity clearly demonstrates the higher degree of the conjugation in the phenyl ring. The C—H in-plane and out-of-plane bending modes of tri-substituted phenyl ring occur at 1300 to 1000 cm^{-1} and 1000 to 750 cm^{-1}, respectively.[52,53] The C—H in-plane bending modes are observed at (1345, 1256, 1122) cm^{-1} as weak Raman bands and (1254, 1122) cm^{-1} as weak IR bands. And the C—H out-of-plane bending modes are observed at 1019, 944[1], 842, 744 cm^{-1}as Raman bands, and at 843 cm^{-1} as IR bands.

Secondary amide vibrations

The secondary amide consists of one amine and ketone group. It acts as the bridge between chlorophenyl and indole ring. Generally, the C=O stretching vibrations appear in the region 1630 to 1695 cm^{-1}.[54,55] In IND molecule C=O stretching vibration is observed at 1660 cm^{-1} as Raman band. The in-plane N—H bending vibrations appear in the region 1570 to 1515 cm^{-1}.[54] In IND molecule, the N—H in-plane bending vibration is observed at 1466 cm^{-1}. The N—H stretching vibration occurs at 3400 to 3000 cm^{-1}.[56] and is observed at 3433 cm^{-1}. All amides exhibit a band due to the C=O stretching vibration and secondary amides have the N—H stretching and deformation vibrations. Normally, in solid-phase, secondary amide exhibit increased frequency due to the strong electron-accepting property of the nitrogen atom. But here the in-plane bending modes are decreased, due to the interaction between the amide nitrogen and indole ring nitrogen.

Indole ring vibrations

Indole has a bicyclic structure, which is six-membered benzene ring fused to a five-membered nitrogen-containing pyrrole ring, which has useful biological properties.[56] The ring CC stretching vibrations of the heteroaromatic moiety like indole are expected in the region 1625 to 1300 cm^{-1},[56] which is its characteristic region. This characteristic region is observed at 1600, 1599, 1363, 1165 cm^{-1} as IR bands and at 1594, 1162 cm^{-1} as Raman bands. The variation of C—C stretching mode is due to the substitution around the ring. The C—H symmetric and asymmetric stretching vibrations are expected in the wide region of 3130 to 3000 cm^{-1}.[45] The CH asymmetric stretching vibrations are observed at 3078 cm^{-1} and 3059 cm^{-1}. The CH_2 symmetric and asymmetric stretching vibrations of the indole ring are expected in the region 2800 to 2900 cm^{-1}.[51] The CH_2 symmetric stretching vibrations are observed at 2925 cm^{-1} as strong IR and Raman bands. The CH_2 asymmetric vibration is observed at 2966 cm^{-1} as IR bands. The stretching mode of the CH_2 group is red shifted due to the steric hindrance between the methyl group and the indole group, which results in the indole ring envelope configuration. The CH in-plane and out of plane bending modes normally appear at 950 to 1225 cm^{-1} and 840 to 880 cm^{-1}, respectively.[51] The CH in-plane and out-of-plane bending modes are observed at 1399 cm^{-1} (IR),1337 cm^{-1} (IR), 1288 cm^{-1} (IR),1158 cm^{-1} (IR), and 977 cm^{-1} (Raman), 943 cm^{-1}(IR), 905 cm^{-1}(Raman), 843 cm^{-1} (IR),842 cm^{-1}(Raman), respectively. The slight shift was observed due to the substitution of secondary amide and methyl ring for hydrogen in the indole ring. It provides the evidence for the charge transfer interaction between the donor and acceptor groups through the π-system. The other bending modes are given in the Table 4.

Methyl vibrations

The symmetric and asymmetric CH stretching vibrations are expected in the range 2982 to 2962 cm^{-1} and 2882 to 2862 cm^{-1}, respectively.[56] The CH symmetric stretching mode is observed at 2925 cm^{-1} as a strong intense band as IR and medium intense Raman band at 2925 cm^{-1}. which is coupled with the indole symmetric stretching vibration. The CH asymmetric stretching mode is observed at 3049 cm^{-1}as a very strong intense Raman band. The shifting of symmetric and asymmetric CH stretching vibrations is due to the electronic effects owing to the methyl group attached to the indole ring. The CH_3 deformation vibrations are expected in the region 1375 to 1465 cm^{-1}.[57] The expected CH_3 deformation vibrations are observed at 1448 cm^{-1} as weak Raman band assigned to scissoring mode. An observed weak Raman band at 905 cm^{-1} assigned to the rocking mode. The reason for this shifting is the change in the sp^3 hybridization state of the C_{13} atom arising from the hyperconjugation effect of the methyl group, which results in the strengthening of the CH bond. This is clearly reflected in the optimized geometry (Table 1). The symmetric bending vibration (umbrella mode) of methyl group occurs in the range 1385 to 1375 cm^{-1}.[58] Leenaraj et al[59] has reported a similar vibration. It is observed at 1386 cm^{-1} as strong IR bands. The shifting of wavenumber may be due to the electronic charge back donated from the electronegative nitrogen atom to the σ^*(C—H) bonds, causing a weakening in the CH bonds. The structural and bond orbital analysis clearly shows the evidence for the charge transfer. The shifting of wavenumber confirms the electronic effects including back-donation and induction.

3.4.2 | SERS spectra

The absorption spectra and the band gap energy of gold nanoparticle (AuNPs) are affected by the shape and size of the nanoparticles. The gold colloid has a wine red color with absorption maxima and band

gap energy is 530 nm and 3.01 eV, respectively. The nanostructure and morphology of gold colloids analyzed by transmission electron microscope (TEM) are illustrated detailed in our earlier report.[27] The absorption maxima, the bandgap energy, and the TEM result have shown that the average particle size of the gold colloids is about 40 nm. After chemical interactions between IND and gold atoms, maximum absorption peaks of IND redshift from 329 to 670 nm (Figure 8), indicating that IND has been adsorbed on the nanoparticles.

The SERS spectrum (Figure 6) of INDA has been recorded and tabulated (Table 5). The SERS fingerprint pattern of the INDA has been performed under 10^{-3}, 10^{-4}, and 10^{-5} M concentrations (Figure 6). The vibrational analysis was performed and compared with the normal Raman spectrum. The vibrational modes were calculated using DFT method to determine the vibrational modes unambiguously. Observed intense band at 258 cm^{-1} and a shoulder at 249 cm^{-1} show the presence of metal absorbate interaction, which interacts through oxygen atom whereupon the kinetically favorable interaction is achieved. This interaction is also favored by the steric effect imposed by the sulfamoyl functional group to the metal. The interaction via the oxygen of the sulfamoyl group arises from the charge transfer between the low electronegative oxygen with the metal. Optimized geometry and NBO analysis reveal that there are two possible different electron-donor sites available for the interaction with gold surface: two oxygen atoms in the sulfamoyl functional group. From theoretical calculations, both binding sites appeared of about the same binding probability, but the stabilization energy of the Au NPs interacting with the O_4 oxygen atom in tetrahydrofuran ring is stronger than that of the O_5 oxygen atom in the sulfamoyl functional group (Table 2). The MEP contour map indicates that the highest electron density is located on the O_4 oxygen atom in the sulfamoyl functional group, thus the molecule is supposed to adsorb through an O_4 oxygen atom in the sulfamoyl functional group.

The SO_2 in-plane bending modes occur at 245 to 575 cm^{-1}.[60] There is no SO_2 in-plane bending mode contribution in the normal Raman. But it appears very intense in SERS spectrum at 345 cm^{-1} in 10^{-3}, 10^{-4} M, and 10^{-5} M concentrations, respectively, which predicts a flat orientation of the IND bridge with respect to the gold surface. This prediction was strengthened by the SO_2 asymmetric stretching and NH_2 torsion. The SO_2 asymmetric stretching and NH_2 torsion occur at 1360 to 1280 cm^{-1} and 415 to 290 cm^{-1}($-SO_2NH_2$), respectively.[60] The SO_2 asymmetric stretching is observed in Raman at 905 cm^{-1} and in SERS spectrum at 906 cm^{-1} in 10^{-3} concentration. The NH_2 torsion was observed at 313 and 298 cm^{-1} in the SERS spectrum of 10^{-3} concentration. But it is absent in normal Raman and other concentrations. This indicates the direct interaction of sulfur atom through the oxygen atom in the sulfamoyl moiety with the gold surface, which is well documented in the literature.[60,63] This is the reason why chair conformation of sulfamoylchlorobenzamide changes moderately when the IND molecule are adsorbed on to the gold nanoparticles. The CH in-plane and out of plane bending modes are equally enhanced in the four concentrations. The shifting[56] and enhancing of CH in-plane and out of the plane modes in the chlorophenyl ring suggests that the chlorophenyl bridge possesses an almost tilted orientation on the gold surface favored by π- orbital gold surface interaction. This predicts that the interaction of the IND molecule with the gold surface may occur not only through one atom or group in the IND molecule but also by the combined effect. This result was justified by the MEP analysis. Other wavenumbers justifying these results are listed in Table 5. From this spectral analysis, it is clear that the SERS spectrum is best seen at a concentration of 10^{-3} M.

3.5 | Prediction of biological activity

The theoretical and experimental studies have been carried out to check the cancer activity of IND and INDA molecule. The theoretical prediction was carried out using Molecular docking studies. Based on the theoretical studies, experimental studies, the MTT assay, and SERS studies were conducted.

3.5.1 | In-silico biological activity screening

1. Predicting the physicochemical properties of "drug-like" molecules

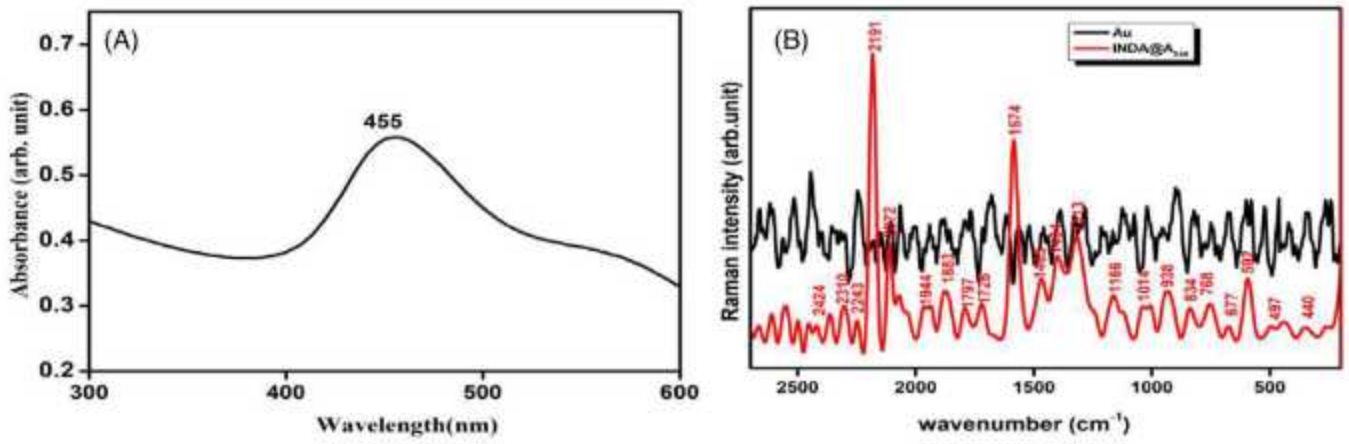


FIGURE 6 SERS of INDA atthree different concentrations (10-3, 10-4, 10-5 M) and calculated SERS spectra

TABLE 5 Selected experimental and theoretical SERS bands of IND

FT-Raman		SERS				
			Experimental wavenumber (cm^{-1})			Assignments
Theoretical wavenumber (cm^{-1})	Experimental wavenumber (cm^{-1})	Theoretical wavenumber (cm^{-1})	10^{-3} M	10^{-4} M	10^{-5} M	
2848	2825 m	2773	2707	2757	2758	ν CH (89) indole
1605	1660s	1672	1678	1672	1693	ν C=O (80)amide
		1658	1650	1650	1658	ν CC (76)indole
		1647	1649			ν CC (86) indole
1593	1594vs	1596	1587	1587	1586	ν CC (92) phenyl
1576	1564w	1574				νC=C(80) phenyl
		1507	1500			$\delta_{sci}CH_2$ (56),$\delta_{sci}CH_3$(45)indole
		1494	1497			β CH (72) phenyl β NH (30) amide
		1491		1472	1471	β CH (72) phenyl, β CH (58) indole
		1456				β CH (72) phenyl
1448	1448w	1442	1443			Um CH_3
		1413			1404	β CH (64) phenyl
		1389	1381	1399		β CH (49), ω CH_2 (34) indole
1359	1345w	1369	1371	1367		β CH (49) indole
1311	1301 m	1327		1326	1319	β NH (38) amide, β CH (36) indole
		1286	1262	1263		ν CC (48)
1249	1256w	1240	1240		1246	t CH_2 (50) indole β CH (28) phenyl
1191	1191vw	1193	1185			β CH (53) indole,
1176	1162w	1177	1163	1164	1155	β CH (68) phenyl
1132	1122vw	1119		1121	1118	β CH (62) indole, ω CH_3 (32) methyl
1053		1097	1086	1085		ρ NH_2 (50) sulfamoyl
		1073	1068			t CH_2 (38) indole
1031	1045vw	1042	1041	1039	1041	γ CH (28) phenyl
1002	1019w	1019			1004	γ CH (25) indole
980	977vw	978		997		γ CH (32) indole
948	944w	968	950			β CC (27) indole
		935	930	923	929	ρ CH_2 (34) indole ρ CH_3 (18) methyl
900	905vw	906	900			β NNC (16), ν_{asy} OSO sulfamoyl
885	889vw	893	899			β CH (29) phenyl, β NNC (15)
856	842vw	834	839	839	842	β CCC (27) indole
801	808vw	798				β CCC (56) indole
769	772vw	786	780			γ CH (26) indole
756		775	778			β CCC (31) phenyl
744	744vw	746	751		755	γ CH (15) indole
717		734		735		γ CH (28) phenyl, γ CNH (14)
699		682		672	680	β CCC (39) phenyl
571		595	594	594	595	β CCN (34) indole
540		560	558			γ NH (20)

(Continues)

TABLE 5 (Continued)

FT-Raman		SERS				
			Experimental wavenumber (cm^{-1})			Assignments
Theoretical wavenumber (cm^{-1})	Experimental wavenumber (cm^{-1})	Theoretical wavenumber (cm^{-1})	10^{-3} M	10^{-4} M	10^{-5} M	
526		541	532		539	β CCO (32)
475		494	498	489	497	γ NH (31), βCCN (21) indole
451		462	459			γ CH (25) phenyl
424		436	439	436	423	γ CH (33) indole, β SO (20) sulfamoyl
363		372	365			τ CCO (36)
336		339	333	347	345	τ CNNH (30)
298		310	313	313	312	δ_{sci} OSO (25), τ NH (18) sulfamoyl
293		293	298			τ NH_2 (23) sulfamoyl
257		261	259	258	258	AU-O
234		246	252	249	249	AU-O

Abbreviations: ν, stretching; β, in-plane bending; γ, out-of-plane bending; τ, torsion.

To predict the novelty of drug for oral absorption Lipinski rule was employed. According to rule 5[62,63] desirable properties for orally active drugs in humans are that the calculated logP (ClogP) value is above five, should have more than five hydrogen bond donors, ten hydrogen bond acceptors and molecular weight above is 500 amu. If any two of these properties are present, the compound is likely to experience oral absorption characteristics. In the IND molecule calculated logP value, hydrogen bond donors, hydrogen bond acceptors, and the molecular weight is 1.67, 2, 4, and 365.83 amu, respectively. The INDA molecule has calculated logP value, hydrogen bond donors, hydrogen bond acceptors, and the molecular weight is 0.00, 2, 4, and 562.80 amu, respectively. This only provides an alert for potential absorption or permeation difficulties. As stated by the Wessel and coworkers,[64] quantitative structure-property relationship (QSPR) study and human intestinal absorption (HIA), provides a quantitative estimate of a compound's absorption profile. The prediction of QSPR models could be carried out directly from the molecular structure. It has been calculated by some topological indices such as molecular descriptors. In IND molecules lipophilicity has been calculated as Log Po/w (iLOGP), Log Po/w (XLOGP3), Log Po/w (WLOGP), Log Po/w (MLOGP), Log Po/w (SILICOS-IT) and Consensus Log Po/w are 1.67, 2.87, 2.78, 2.27, 1.05, and 2.13, respectively. For INDA molecule the values are 0.00, 2.87, 2.78, 2.27, 1.05, and 1.79, respectively in the same order. The Water Solubility parameters of the IND molecule Log S (ESOL), Solubility, Class, Log S (Ali), Solubility, Log S (SILICOS-IT) and Solubility are −4.02, 3.48e-02 mg/mL; 9.50e-05 moL/L, moderately soluble, −4.65, 8.23e-03 mg/mL; 2.25e-05 moL/L, −5.09 and 2.97e-03 mg/mL; 8.11e-06 moL/L, respectively. And for INDA molecule, −5.23, 3.32e-03 mg/mL; 5.91e-06 moL/L, moderately soluble, −4.65, 1.27e-02 mg/mL; 2.25e-05 moL/L, −5.09 and 4.56e-03 mg/mL; 8.11e-06 moL/L, respectively in the same order. The Pharmacokinetics properties of IND molecule show that GI absorption is High, Log Kp (skin permeation) is −6.49 cm/s, and the other Pharmacokinetics parameters such as BBB permeant, P-gp substrate, a CYP1A2 inhibitor, CYP2C19 inhibitor, CYP2C9 inhibitor, a CYP2D6 inhibitor, CYP3A4 inhibitor are no. The Pharmacokinetics properties of INDA molecule show that GI absorption is High, Log Kp (skin permeation) is −7.70 cm/s, and the other pharmacokinetics parameters such as BBB permeant, a CYP1A2 inhibitor, CYP2C19 inhibitor, CYP2C9 inhibitor, a CYP2D6 inhibitor, CYP3A4 inhibitor are no contribution except P-gp substrate. These results show that the IND molecule show good result compared with INDA molecule. Druglikeness calculations show that IND molecule has not violated the rules but the INDA molecule has violated two rules. The bioavailability score for IND and INDA molecule is 0.55. The Medicinal Chemistry parameter, Leadlikeness has found to be violated in both IND and INDA molecule. PAINS and Brenk parameters have no alerts in both IND and INDA molecule. Synthetic accessibility of the IND and INDA molecule are 3.22 and 3.26, respectively. The result predicts comparing between IND and INDA molecule, IND molecule shows good agreement as far as drug-likeness is compared.

3.5.2 | Prediction of binding sites of lung cancer

Molecular docking has become an integral part of the drug discovery in *in-silico* biological activity screening, and its relatively low-cost implications. Its ease of use has fueled its growing popularity in academic communities.[65,66] It is used to investigate the preferred binding orientation, affinity, and activity of drug molecules and their protein targets. A molecular modeling study has been performed using AutoDock Tools for docking. The three-dimensional (3D) X-ray crystal structure of the cancer receptors were obtained from the Research Collaboratory for Structural Bioinformatics (RCSB) protein data bank, with a resolution

above 2.21 Å. LEGFR (L858R, T790M, V948R) in complex with N-{3-[(2-{[4-(4-methylpiperazin-1-yl)phenyl]amino}-7*H*-pyrrolo[2,3-days] pyrimidin-4-yl)oxy]phenyl}prop-2-enamide (5HG5)[67] protein receptors selected from the Protein Data Bank (RSCSB-PDB) to dock to IND and INDA molecules to locate the active site. The ligand PDB file was generated from the optimized molecular structure of the IND and INDA molecules. The AutoDock Tools graphical user interface [A, B-same as computation] was used to remove the ligand and water molecules present in the target proteins, which has also been used to add the polar hydrogen bond and Geisteger charges in the target proteins. The Lamarckian Genetic Algorithm (LGA) is used for molecular docking calculations in the AutoDock 4.0 software program.[68]

The docking parameters of IND molecule such as binding energy, inhibition constant, and intermolecular energy of the molecule with respect to the targeted proteins have been calculated to be −5.6 kcal/mol, 310.12 mM, and −5.02 kcal/mol, respectively. For INDA molecule they are −7.52 kcal/mol, 452.65 mM, and −6.23 kcal/mol, respectively in the same order. The INDA molecule shows less binding energy and intermolecular energy but the inhibition constant is shown high for both the IND and INDA molecule. The hydrogen bonds between 5HG5 and the IND molecule, O···H–N, O···H–N, N–H···O, and O···H–C are 2.37 Å (ASN 239), 1.92 Å (ASN700), 2.04 Å (GLN701), and 2.22 Å (LEU704), respectively. Also, the hydrogen bonds between 5HG5 and the INDA molecule, O···H–N, O···H–N, N–H···O and O···H–C are 1.92 Å (ARG748), 2.11 Å (MET766), 1.92 Å (VAL834), and 2.91 Å (VAL834), respectively (shown in Figure 7). The results reveal that both IND and INDA molecule show good binding affinity towards lung cancer activity, the INDA molecule exhibiting more binding affinity than IND molecule.

3.5.3 | Recognition of human lung cancer cells—in vitro analysis

In-vitro analysis of lung cancer cells using SERS and MTT assay was performed to examine the cytotoxic effect of mutations, IND, and INDA molecules. For SERS study within the cell, INDA molecule is taken up by the cell and delivered to the cytoplasmic area within 2 hours. From Figure 9A, the absorption peak is observed at 455 nm. Normally cytoplasmic peak appears at 300-700 nm.[69] After 3 hours this absorption peak disappears. This shows that the INDA molecule is slowly migrating to the nucleus. After 4 hours, nuclear accumulation is observed without cytoplasmic fluorescence, which justifies the SERS studies. The results obtained were compared with other similar studies reported in the literature[64,70] shown in the table. The nucleic acid exhibited phosphodioxy group vibration at 1091 cm^{-1} which confirms that the INDA molecule is taken inside the lung cancer cell line. The Raman intensity corresponding to nucleotides are identified at 768, 1313, 1574 cm^{-1}, corresponds to (thymine, cytosine, and uracil), (thymine, guanine, and adenine), and (guanine and adenine), respectively. In the nucleotides, Raman intensity at 771 cm^{-1} confirms the mixing of DNA and RNA which shows the apoptotic nature of the cell. The vibration of the sugar-phosphate o-p-o backbone is observed at 826 cm^{-1}. This confirms the structural framework of nucleic acids, including DNA and RNA. The shifting of lipid band is observed at 1423 cm^{-1}, which indicates the decrease of the lipid-to-protein ratio. The change of biochemical property of lipid-to-protein ratio shows the change of biocompatibility of lung cancer cell line.

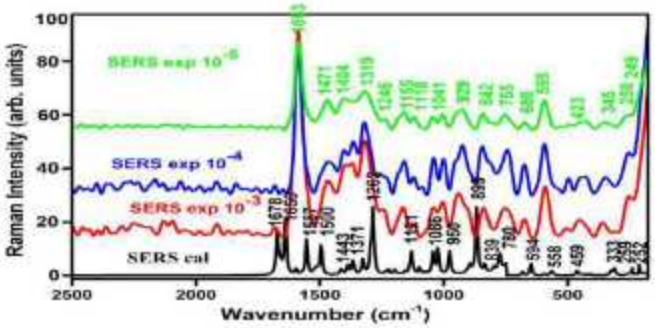


FIGURE 7 Pictorial representation of possible binding sites of (A) IND and (B) INDA molecules with the target protein

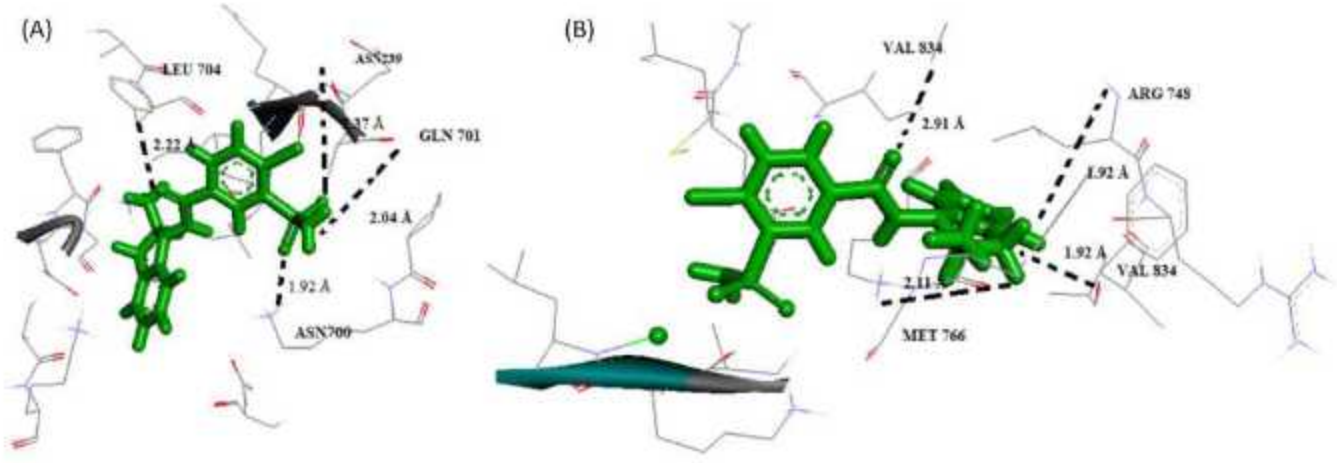


FIGURE 8 (A) UV–Vis spectra of the INDA molecule inside the A_{549} cell line. (B) SERS spectra analysis of INDA and AuNp inside A_{549}

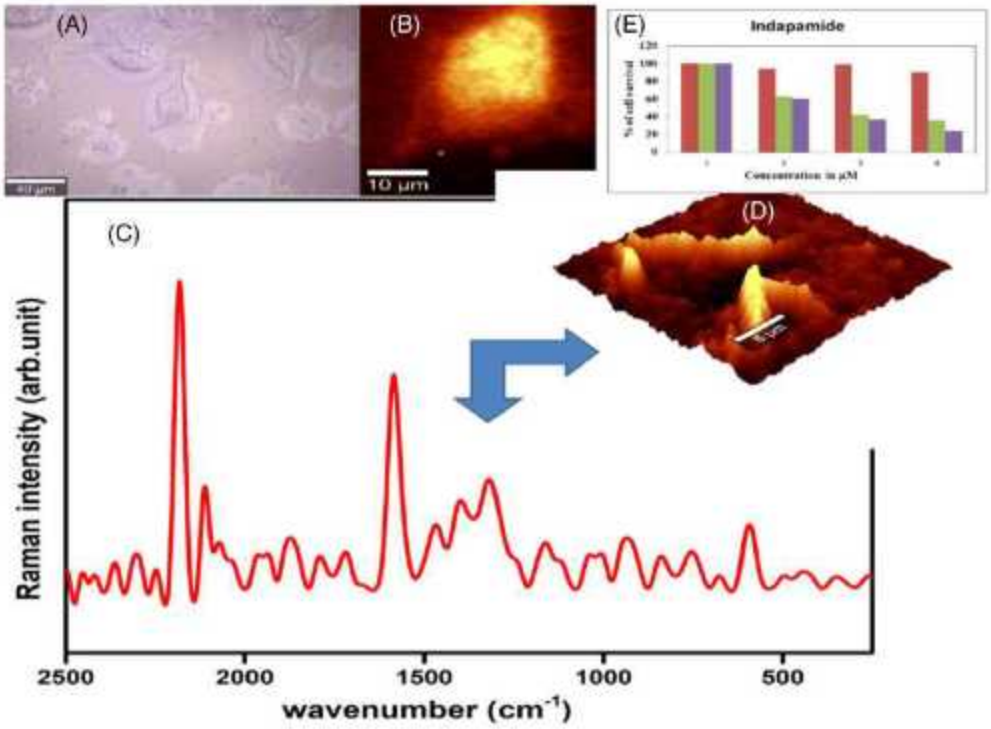


FIGURE 9 Raman imaging of cells: (A) Bright field images; (B) 2D image; (C) spectrum; (D) 3D Image, respectively; (E) Graphical representation of cytotoxic effect

The above-intended bands show that INDA interacts with apoptotic (cancer) cell. This will enable label-free monitoring and further enhance therapeutic use. SERS spectrum obtained from INDA within the lung cancer cell is associated with proteins, nucleic acids, lipids, and carbohydrates which are identified, and assigned; assignments are plotted in Figure 9B and Table 6. The references of intense bands are shown in the table.

We have explored the cellular internalization by Raman imaging analysis. For that, Bright field (Figure 9A) and Raman mapping for INDA localization has been observed within 1 and 3 hours of incubation of INDA in A_{549} cells. Raman spectral and imaging analysis from A_{549} cells showed an improved Raman signal. Raman imaging and corresponding spectral analysis of INDA demonstrated a time-dependent localization with an early distribution in the cytoplasm and later migration toward the nucleus. From the Raman images, it is clear that INDA has entered into A_{549} lung cancer cells. 2D SERS mapping (Figure 9B) shows the track of the spatial and temporal progress of the nanoparticle uptake in cancer cells at various time points.[70,71] Also, SERS maps were constructed to show drug internalization. The white light image of such an apoptotic A_{549} lung cancer cell is shown in Figure 9A. From the Figure 10D, it is clear that the cell has a size of 8 μm and is much smaller than the control cell. Therefore the cells are apoptotic. It has been further confirmed through the MTT viability assay.[72,73] MTT assay has been done in three concentrations of IND and INDA molecules. IND and INDA show cytotoxic effect and more cytotoxicity in 10 μM. The INDA molecule shows more cytotoxicity effect than IND molecule. But there is no cytotoxic effect for Au NPs alone. The above results show that Au NPs aids cellular uptake of the drug of interest and allow targeted drug delivery. The comparative results are delineated in the Table 7 and Figure 10E. From the above results, it is evident that INDA interacts with apoptotic cell (MTT assay) and can be effectively monitored through SERS, which enable label-free monitoring and further potentiate the therapeutic utility.

4 | CONCLUSION

Quantum chemical calculations and vibration spectral studies have been performed on IND and INDA molecules to identify their structural and bonding features responsible for their bioactivity. The conformational behavior of the IND and INDA molecule has been investigated by the hybrid DFT method B3LYP with LANL2DZ basis set. The conformational analysis shows that IND and INDA molecule has a complicated configuration formed by polar sulfamoylc hlorobenzamide moiety and a lipid-soluble methylindoline molety with the presence of C—H···O intramolecular hydrogen bonding. Moreover, the stabilized geometry confirms the steric interactions between axial substituents in both molecules. The NBO analysis corroborates these results. The stabilization energy has confirmed that hyperconjugative interactions are more pronounced in the INDA molecule than the IND molecule, thus leading to enhanced bioactivity of INDA molecule. The comparative study between normal Raman spectrums with the SERS spectrum along with the scaled DFT calculations predicts the tilted orientation. It confirms that the INDA molecule has high molecular electrical transport property, photostability, and high reactivity with low kinetic stability. In-silico biological activity screening confirms that the IND and INDA molecules can act as a good inhibitor against lung cancer. The current investigation reveals the potential of SERS based diagnostics and therapeutic efficiency of IND. Hence IND can be suggested as a good substitute to dyes in imaging, as conventional dyes are highly harmful to kidney patients. The strongest Raman

TABLE 6 Assignments of major surface enhanced Raman peaks inside the cell

Raman band (cm^{-1})	Assignment	Reference number
440	Phenylalanine	71
497	Proteins and lipids	71
592	Glycerol	71
677	Superposition of a strong tyrosine	72
768	Cytosine/uracil ring breathing (nucleotide) (thymine, cytosine and uracil)	71
834	Most probably due to single bond stretching vibrations for the amino acids and valine and polysaccharides	71
938	C—C stretch backbone	72
1014	ν (C—N)	72
1166	ν (C—C) skeletal of acyl backbone in lipid (transconformation)	72
1313	Thymine, guanine, and adenine, methylene twisting	72
1404	Tryptophan	71
1465	CH_2/CH_3 deformation of lipids & collagen CH_2 wagging, CH_2/ CH_3 deformation deoxyribose	71
1574	C=C olefinicstretch C=C olefinic stretch (protein assignment) (guanine and adenine)	71
1726	amide I	72
1797	Carbohydrates and lipids	71
1883	C=O (lipid)	72
1944	Ester group	72
2072	C—N stretch (one of three thiocyanate peaks)	72
2191	C=N	71
2243	Asymmetric stretching band of $CO^{-}{}_2$ 2 hydrates	71
2310	Asymmetric stretching band of $CO^{-}{}_2$ 2 hydrates	71
2424	CH stretch of lipids and proteins	72

TABLE 7 information about cytotoxic effect

Concentration (μg/mL)	Au	IND	INDA
0	100	100	100
10	94.20	63.33	60.20
100	99.30	42.17	36.90
1000	90.20	35.73	23.90

bands of INDA-A_{549} clearly show label-free methods for the detection of intracellular components. Therefore indapamide@AuNPs can act as a drug for cancer treatment as well as a biomarker. As an alternative optical tracking technology, SERS has attracted enormous attention for its advantages as high sensitivity, non-photo bleach property, and improved detection ability. Due to these advantages, early-stage cancer detection is possible. This technique may also be used as a substitute to conventional bronchoscopy and to carry out biopsies for histopathology investigation of lung malignancies.

ACKNOWLEDGEMENT

The author (SV) acknowledges Department of Physics, Mar Ivanios College, Thiruvananthapuram, Kerala for the computational facility using the Gaussian 09. DS also acknowledge the DST-FIST program (SR/FST/College-182/2013, November 2013 & FIST No. 393 dated September 25, 2014) to the Bishop Moore College.

CONFLICT OF INTEREST

The authors declare that they have no known competing financial interests or personal relationships that could have appeared to influence the work reported in this paper.

AUTHOR CONTRIBUTIONS

V. Shyni: Conceptualization, Methodology, Writing–original draft, D. R. Leenaraj: Conceptualization, Methodology, Reena Ittyachan: Data curation, Lynnette Joseph: Writing–review & editing, Supervision, D. Sajan: Conceptualization, Writing–original draft, Funding acquisition, Validation.

DATA AVAILABILITY STATEMENT

The data that support the findings of this study are available from the corresponding author upon reasonable request.

ORCID

D. Sajan https://orcid.org/0000-0002-0344-0744

REFERENCES

1. Weber A, Casini A, Heine A, et al. *Unexpected nanomolar inhibition of carbonic anhydrase by COX-2-selective celecoxib: new pharmacological opportunities due to related binding site recognition*. J Med Chem. 2004;47:550-557.
2. Supuran CT. *Carbonic anhydrases: novel therapeutic applications for inhibitors and activators*. Nat Rev Drug Discov. 2008;7:168-181.
3. Smith RE, Ashiya M. *Antihypertensive therapies*. Nat Rev Drug Discov. 2007;6:597-598.
4. Scozzafava A, Supuran C, Casini A. *Development of sulfonamide carbonic anhydrase inhibitors*. Carbon Anhydrase. 2004;14 67-147.
5. Supuran CT, Scozzafava A, Casini A. *Carbonic anhydrase inhibitors*. Med Res Rev. 2003;23:146-189.
6. Supuran CT. *Carbonic anhydrases as drug targets-an overview*. Curr Top Med Chem. 2007;7:825-833.
7. Scozzafava A, Owa T, Mastrolorenzo A, Supuran CT. *Anticancer and antiviral sulfonamides*. Curr Med Chem. 2003;10:925-953.
8. Supuran CT, Briganti F, Tilli S. *Carbonic anhydrase inhibitors: sulfonamides as antitumor agents*. Bioorg Med Chem. 2001;9:703-714.
9. Casini A, Scozzafava A, Supuran CT. *Sulfonamide derivatives with protease inhibitory action as anticancer, antiinflammatory and antiviral agents*. Expert Opin Ther Pat. 2002;12:1307-1327.
10. Supuran CT. *Indisulam-an anticancer sulfonamide in clinical development*. Expert Opin Investig Drugs. 2003;12:283-287.
11. Cecchi A, Hulikova A, Pastorek J. *Carbonic anhydrase inhibitors. Design of fluorescent sulfonamides as probes of tumor-associated carbonic*

anhydrase IX that inhibit isozyme IX-mediated acidification of hypoxic tumors. J Med Chem. 2005;48:4834-4841.
12. Clare BW, Supuran CT. *A perspective on quantitative structure–activity relationships and carbonic anhydrase inhibitors*. Expert Opin Drug Metab Toxicol. 2006;2:113.
13. Krishnamurthy VM, Kaufman GK, Urbach AR, et al. *Carbonic anhydrase as a model for biophysical and physical-organic studies of proteins and protein–ligand binding*. Chem Rev. 2008;108:946.
14. Kaushik N, Kaushik N, Attri P, et al. *Biomedical importance of indoles*. Molecules. 2013;18(6):6620-6662.
15. Sun S, Fu J. *Methyl-containing pharmaceuticals: methylation in drug design*. Bioorganic Med Chem Lett. 2018;28(20):3283-3289.
16. Supuran CT. *Structure-based drug discovery of carbonic anhydrase inhibitors*. J Enzyme Inhib Med Chem. 2012;27:759-772.
17. Uehara Y, Hirawa N, Takeda T, et al. *Possible linkage between renal injury and cardiac remodeling in Dahl salt-sensitive rats treated with the calcium channel antagonist benidipine*. Hypertens Res. 1995;18:245-253.
18. Batailllard A, Schiavi P, Sassard J. *Pharmacological properties of indapamide*. Clin Pharmacokinet. 1999;37(1):7-12.
19. Savale L. *Lung transplantation in pulmonary arterial hypertension*. ESC CardioMed. 2018;7:2520-2524.
20. Stuart Rich. *Pulmonary arterial hypertension*. Vickii Vigneswaran, Edward Garrity, *Lung Transportation*. London: Informa Health Care. 2010;243:65-74.
21. Acchiardo SR, Skoutakis VA. *Clinical efficacy, safety and pharmacokinetics of indapamide in renal impairment*. Am Heart J. 1983;106: 239-244.
22. Legorburu MJ, Alonso RM, Ortiz E, et al. *Quantitative determination of indapamide in pharmaceuticals and urine by high-performance liquid chromatography with Amperometric detection*. J Chromatogr Sci. 1999; 37(8):283-287.
23. Martinez FJ. *Pulmonary hypertension in idiopathic pulmonary fibrosis*. Robert P. Baughman, Roberto G. Carbone, Giovanni Bottino, *Pulmonary Arterial Hypertension and Interstitial Lung Diseases*. 2009;177-194.
24. Qi W-X, Shen Z, Lin F, et al. *Incidence and risk of hypertension with vandetanib in cancer patients: a systematic review and meta-analysis of clinical trials*. Br J Pharmacol. 2013;75(4):919-930.
25. Bondoc E, Laane J. *Far-infrared rotational–vibrational spectra of the ring-puckering vibration of 2,5-dihydrofuran*. J Mol Struct. 1998;470(1–2):237-240.
26. Salabat A, Mirhoseini F. *A novel and simple microemulsion method for synthesis of biocompatible functionalized gold nanoparticles*. J Mol Liq. 2018;268:849-853.
27. Shyni V, Leenaraj DR, Joseph L, et al. *Investigations of dianhydro-D-glucitol adsorbed on AuNPs surface: in silico and in vitro approach based on anticancer activity studies against A549 lung cancer cell lines*. J Mol Recognit. 2021;0952-3499:1099-1352.
28. Frisch MJ, Trucks GW, Schlegel HB, et al. *Gaussian 09: RevisionA 02*. Wallingford, CT, Gaussian Inc; Gaussian; 2009.
29. Becke AD. *Density-functional thermochemistry. III. The role of exact exchange*. J Chem Phys. 1993;98:5642-5648.
30. Becke AD. *Density-functional exchange-energy approximation with correct asymptotic behavior*. Phys Rev. 1988;38:3098-3100.
31. Lee C, Yang W, Parr RG. *Development of the Colle-Salvetti correlation-energy formula into a functional of the electron density*. Phys Rev B. 1988;37:785-789.
32. Wadt WR, Hay PJ. *Ab initio effective core potentials for molecular calculations. Potentials for the transition metal atoms Sc to Hg*. J Chem Phys. 1985;82:270.
33. Wadt WR, Hay PJ. *Ab initio effective core potentials for molecular calculations. Potentials for main group elements Na to Bi*. J Chem Phys. 1985;82:284.
34. Smrkolj M, Meden A. *Crystal structure of indapamide determined from powered diffraction data*. Pharmazie. 2006;61:999-1004.
35. Yadav LDS. *Ultraviolet (UV) and visible spectroscopy*. Org Spectro. 2005;7:51.
36. Reed AE, Weinstock RB, Weinhold F. *Natural population analysis*. J Chem Phys. 1985;83:735-746.
37. Weinhold F, Landis CR. *Natural bond orbitals and extensions of localized bonding concepts*. Chem Educ Res Pract Eur. 2001;2:91-104.
38. Foster JP, Weinhold F. *Natural hybrid orbitals*. J Am Chem Soc. 1980; 102:7211-7218.
39. Calais J-L. *Density-functional theory of atoms and molecules*. Int J Quantum Chem. 1989;47(1):101-101.
40. Yang W, Mortier WJ. *The use of global and local molecular parameters for the analysis of the gas-phase basicity of amines*. J Am Chem Soc. 1986;108:5708-5711.
41. Parr RG, Yang W. *Density-Functional Theory of Atoms and Molecules*. New York, NY: Oxford University Press; 1989.
42. Sailaja RP, Kalva S, Yerramilli A, Mamidi S. *Free radicals and tissue damage: role of antioxidants*. Free Radic Biol Med. 2011;1(4):2-7.
43. Muthu S, Renuga S. *Vibrational spectra and normal coordinate analysis of 2-hydroxy-3-(2-methoxyphenoxy) propyl carbamate*. Spectrochim Acta A Mol Biomol Spectrosc. 2014;132:313-325.
44. Mooney EF. *The infrared spectra of chloro- and bromobenzene derivatives-I*. Spectrochim Acta. 1963;19:877-887.
45. Bhatt R, Bhaumik I, Ganesamoorthy S, et al. *Urbach tail and bandgap analysis in near stoichiometric LiNbO3 crystals*. Phys Stat Solid A. 2012;209(1):176-180.
46. Coates J. *Interpretation of Infrared Spectra: A Practical Approach*. New York, NY: John Wiley & Sons Inc.; 2000.
47. Bellamy LJ. *The Infrared Spectra of Complex Molecules*. Vol 2. London, UK: Chapman and Hall; 1980.
48. Chivers T, Lau C. *Raman spectroscopic identification of the S4N-and S3-ions in blue solutions of sulfur in liquid ammonia*. Inorg Chem. 1982; 21:453.
49. Bloxham S, Eicher-Lorka O, Jakubėnas R, Niaura G. *Surface-enhanced Raman spectroscopy of ethanethiol adsorbed at copper electrode*. Chemija. 2002;13:185.
50. Mooney EF. *The infra-red spectra of chloro- and bromobenzene derivatives- II. Nitrobenzenes*. Spectrochim Acta. 1964;20:1021-1032.
51. Socrates G. *Infrared Characteristic Group Wavenumber*. New York, NY: John Wiley and Sons; 1980.
52. Roeges NPG. *A Guide to Complete Interpretation of Infrared Spectra of Organic Structures*. New York, NY: John Wiley & Sons Inc.; 1994.
53. Keresztury G, Chalmers JM. *Raman spectroscopy: theory*. In: Griffith PR, ed. *Hand Book of Vibrational Spectroscopy*. New York, NY: John Wiley & Sons Ltd; 2002.
54. Krishnakumar V, Prabavathi N, Muthunatesan S. *Density functional theory study of vibrational spectra, and assignment of fundamental vibrational modes of 1-bromo 4-fluoronaphthalene*. Spectrochim Acta A. 2008;70:991-996.
55. Renuga S, Muthu S. *Molecular structure, normal coordinate analysis, harmonic vibrational frequencies, NBO, HOMO–LUMO analysis and detonation properties of (S)-2-(2-oxopyrrolidin-1-yl) butanamide by density functional methods*. Spectrochim Acta A Mol Biomol Spectrosc. 2014; 118:702-715.
56. Smith B. *Infrared Spectral Interpretation: A Systematic Approach*. Washington, DC: CRC Press; 1999.
57. Colthup NB, Daly LH, Wiberley SE. *Introduction to Infrared and Raman Spectroscopy*. New York, NY: Academic Press; 1990.
58. Radwan MAA, Ragab EA, Sabry NM, El-Shenawy SM. *Synthesis and biological evaluation of new 3-substituted indole derivatives as potential anti-inflammatory and analgesic agents*. Bioorg Med Chem. 2007;15: 3832-3841.
59. Leenaraj DR, Manimaran D, Joe IH. *Molecular docking and structural analysis of non-opioid analgesic drug acemetacin with halogen substitution: a DFT approach*. J Mol Struct. 2016;1123:180-190.

60. Bürgi T. *Properties of the gold–Sulphur interface: from self-assembled monolayers to clusters*. Nanoscale. 2015;7(38):15553-15567.
61. Min BK, Alemozafar AR, Biener MM, et al. *Reaction of Au(111) with sulfur and oxygen: scanning tunneling microscopic study*. Top Catal. 2005;36(1–4):77-90.
62. Lipinski CA, Lombardo F, Dominy BW, Feeney PJ. *Experimental and computational approaches to estimate solubility and permeability in drug discovery and development settings*. Adv Drug Deliv Rev. 1997;23:3-25.
63. Blake JF. *Chemoinformatics–predicting the physicochemical properties of 'drug-like' molecules*. Curr Opin Biotechnol. 2000;**11**(1):104-107.
64. Smith R, Wright KL, Ashton L. *Raman spectroscopy: an evolving technique for live cell studies*. Analyst. 2016;141(12):3590-3600.
65. Kuruvilla TK, Prasana JC, Muthu S, George J. *Vibrational spectroscopic (FT-IR, FT-Raman) and quantum mechanical study of 4-(2-chlorophenyl)-2-ethyl-9-methyl-6H-thieno[3,2-f] [1,2,4]triazolo[4,3-a][1,4] diazepine*. J Mol Struct. 2018;**1157**:519-529.
66. Berry M, Fielding B, Gamieldien J. *Practical considerations in virtual screening and molecular docking EURASIP*. J Bioinform Syst Biol. 2015; 487-502. https://www.sciencedirect.com/science/article/pii B97801 28025086000272?via%3Dihub.
67. Gajiwala KS. EGFR (L858R, T790M, V948R) in complex with N-{3-[(2-{[4-(4- methylpiperazin-1-yl)phenyl]amino}-7H-pyrrolo[2,3-d] pyrimidin-4-yl)oxy]phenyl}prop-2-enamide PDB 2016.
68. Morris GM, Goodsell DS, Halliday RS, et al. *Automated docking using a Lamarckian genetic algorithm and an empirical binding free energy function*. J Comput Chem. 1998;19:1639-1662.
69. Chen Y, Zhang YX, Wu ZF, et al. *Biodegradable poly(ethylene glycol)-poly(ε-carprolactone) polymeric micelles with different tailored topological amphiphilies for doxorubicin (DOX) drug delivery*. RSC Adv. 2016;6 (63):58160-58172.
70. González-Solís JL, Luévano-Colmenero GH, Vargas-Mancilla J. *Surface enhanced Raman spectroscopy in breast cancer cells*. Laser Ther. 2013; 22(1):37-42.
71. Chen Y, Zhang YX, Wu ZF, et al. *Biodegradable poly(ethylene glycol)-poly(ε-carprolactone) polymeric micelles with different tailored topological amphiphilies for doxorubicin (DOX) drug delivery*. RSC Advances. 2016;6(63):58160–58172. http://dx.doi.org/10.1039/c6ra06040d.
72. Smith R, Wright KL, Ashton L. *Raman spectroscopy: an evolving technique for live cell studies*. The Analyst. 2016;141(12):3590–3600. http://dx.doi.org/10.1039/c6an00152a.
73. Mosmann T, Immunol J. *Rapid colorimetric assay for cellular growth and survival: application to proliferation and cytotoxicity assays*. J Immunol Methods. 1983;65:55-63.
74. Flahaut E, Durrieu MC, Remy-Zolghadri M, et al. *Investigation of the cytotoxicity of CCVD carbon nanotubes towards human umbilical vein endothelial cells*. Carbon. 2006;44:1093-1099.
75. Li J, Chen N, Liu S, et al. *Ag nanoparticles for the direct detection of Oxaprozin in the blood using surface-enhanced Raman spectroscopy*. ACS Appl Nano Mater. 2020;3(6):5928-5935.

SUPPORTING INFORMATION

Additional supporting information may be found online in the Supporting Information section at the end of this article.

How to cite this article: V. Shyni, D. R. Leenaraj, R. Ittyachan, L. Joseph, and D. Sajan, *Anticancer activity of indapamide adsorbed on gold nanoparticles: DFT, in-silico, and in-vitro analysis*, J Mol Recognit (2021), e2920. https://doi.org/10.1002/jmr.2920

Received: 22 June 2021 | Revised: 26 August 2021 | Accepted: 14 September 2021

DOI: 10.1002/jmr.2939

RESEARCH ARTICLE

Journal of Molecular Recognition WILEY

Spectroscopic studies, quantum chemical investigations, and in silico and in vitro scrutiny of the diuretic drug trichlormethiazide adsorbed on AuNPs

V. Shyni[1] | D. R. Leenaraj[2] | Reena Ittyachan[3] | G. J. Shyju[4] | Lynnette Joseph[1] | D. Sajan[1]

[1]Centre for Advanced Functional Materials, Department of Physics, Bishop Moore College, Mavelikara, India

[2]Department of Physics, Mar Ivanios College, Thiruvananthapuram, India

[3]Department of Physics, Sacred Heart College, Chalakudy, India

[4]Department of Physics, Christian College, Thiruvananthapuram, India

Correspondence
Lynnette Joseph and D. Sajan, Centre for Advanced Functional Materials, Department of Physics, Bishop Moore College, Mavelikara, Kerala 690110, India.
Email: lynnettejohn@gmail.com (L. J.) and drsajanbmc@gmail.com (D. S.)

Funding information
DST India

Abstract

Experimental and theoretical study was employed to study the adsorption of the diuretic drug, trichlormethiazide (TCM) molecule on AuNPs (TCMA). The stereo-electronic properties of the molecular structure of most stable conformers of TCM and TCMA were studied using DFT/B3LYP-6-311 + + G (d, p) together with LANL2DZ methodology. The Fourier transform Raman and Infrared spectra of TCM were recorded and analyzed. Quantum chemical calculations of TCM and TCMA molecules were used to evaluate the stability of the molecule, hyper-conjugative interactions, electron delocalization, and binding interactions. The calculated and experimentally observed vibrational frequencies of the molecule were assigned and compared. The shifting and intensity enhancement of the CCl_2 band manifests the back-donation and conjugation effect, which are the result of the presence of nitrogen atom adjoining the dichloromethyl groups and the oxygen in the sulfur dioxide group attached among the amino group and the chlorophenyl ring, respectively, which enhances bioactivity. Anticancer activity was examined based on molecular docking analysis, and it was identified that TCM and TCMA molecules act as good inhibitors against lung cancer. SERS analysis and MTT assay confirmed the molecular docking analysis results.

KEYWORDS
DFT, molecular docking, MTT assay, SERS

1 | INTRODUCTION

Lung cancer is one of the most crucial and deadly ones among most of the cancers reported in human beings. So measures for its remedy are very crucial. Also, the development and improvement of immune response along with treatment in lung cancer patients is a challenge faced in cancer treatment over the years.[2,3] This challenge paved the way toward the search for new promising lung cancer therapeutic agents. It has been identified that the derivatives of sulfonamide (electroncgative group), benzothiadiazine (fused ring), and dichloromethyl (electroncgative group) have multifarious pharmacological activities and have potential applications in the field of medicine.[4–8] In addition, sulfonamides are identified as the first major drug to be used, and they form an integral component of more than 30 drugs used in the clinical field;[9–23] Dichloromethyl groups have been reported to show significant antiviral activity.[7,8] The efficacies of benzothiadiazines in clinical applications such as schizophrenia, depression, Alzheimer's disease, Parkinson's disease, ADHD, and respiratory depression have also been recognized.[24–33]The synergistic combination of the medicinally important sulfonamide, benzothiadiazine, and dichloromethyl group in the trichlormethiazide molecule (TCM) and its possibility in fighting against lung cancer in any infectious (antimicrobial) situation thus became the subject of our present investigation. Furthermore, the TCM molecule shows a peculiar diuretic (a type of thiazide diuretic)

 © 2021 John Wiley & Sons Ltd.

activity.[34,35] Diuretics are drugs used for treating blood pressure fluctuations.[36,37] without causing any change in blood pressure in someone who does not have fluctuations in blood strain.[38] Blood pressure fluctuations in cancer patients are a high risk factor during treatment.[39] Qi et al, have reported that diuretics can be used for cancer therapy. Along with this, AuNPs are implemented for use as imaging/diagnostic equipment, radiosensitizer agents, drug and gene delivery systems, photothermal therapy, biosensors, and tissue engineering.[40–45] It is known that gold nanoparticles (AuNPs) have excellent biocompatible properties, making it a metallic surface suitable for drug distribution. The medicinal importance of TCM molecules and the biocompatibility of AuNPs offer better cancer therapy with fewer side effects.[46,47] This further motivated us to study TCM and the molecule adsorbed on AuNPs (TCMA) using theoretical studies along with an experimental approach.

Molecular structure and spectral investigations of molecules can provide in-depth knowledge of the relationship between molecular architecture and bioactivity.[48,49] The vibrational spectra of sulfonamides, benzothiadiazines, dichloromethyl, and its derivatives have been subjected to spectroscopic and quantum chemical investigations.[50–52]Nevertheless, this medicinal important derivative TCM and TCMA molecule has not yet been subjected to spectroscopic and quantum chemical investigations. Hence, the vibrational spectral investigation of TCM and TCMA molecule was performed aided with density functional theory (DFT) along with experimental spectral analysis. Global and local DFT reactivity descriptors of TCM and TCMA molecules were performed for predicting the possible reactive sites of the molecular systems and the overall stability of the system. Molecular docking study, a powerful computational tool for predicting binding mode and binding affinity in protein-ligand interactions, was used here to examine the lung cancer activity in TCM and TCMA molecules as a scaffold for in vitro learning.

MTT assay, being a sensitive and reliable indicator of cellular metabolic function, was performed on TCM and TCMA to assess the cell viability of the lung cancer cells in culture. Research extends to SERS technology for the analysis of lung cancer cells using gold colloidal nanoparticles. In addition to the abovementioned studies, analysis of optimized molecular geometry, frontier molecular orbital analysis (FMOs), molecular electrostatic potential (MEP) surface analysis, natural population analysis (NPA), and natural bond orbital (NBO) analysis of TCM and TCMA molecules were done. In a nutshell, the present study aims to investigate the molecular structure, electronic properties, vibrational spectra, in silico and in vitro analyses of TCM and TCMA molecules, with the hope that the results may be decisive in the diagnostic function of lung cancer.

2 | MATERIALS AND METHODS

2.1 | Preparation of gold colloids, cell culture, and protocol used for MTT assay

Trichlormethiazide (98%), gold (III) chloride trihydrate (99.99%), and trisodium citrate (99%) was purchased from Sigma-Aldrich and used without further refining. Double distilled water was used throughout the experiments. Procedures for the preparation of gold colloids, the cell culture of human lung cancer cell lines A549, and the protocol used for MTT assay are described in our previous report in the Journal of Molecular Recognition.[53]

2.2 | Characterization

The FT-IR spectrum of TCM was recorded with Perkin-Elmer spectrum one FT-IR spectrometer using the KBr pellet technique. The wavenumber range was 4000 to 400 cm^{-1} in transmission mode with 10 scans at an optical resolution of 2 cm^{-1}. The Raman spectrum was recorded using the BRUKER RFS 27: Stand-alone Fourier transform-Raman (FT-Raman) spectrometer. The spectral resolution of the Raman spectrum is 2 cm^{-1}, at room temperature, within the 3500 to 50 cm^{-1} range. SERS experiments had been executed by incubating TCM molecules into the citrate-stable spherical AuNPs (AuNPs; 40 nm) as SERS substrate, and spectra were measured using the WI-Techmon microscope (WI-Tec, Inc., Germany, alpha 300R). The laser beam was guided through a 20 × objective using a 600 g/mm grating and a Peltier-cooled CCD detector. Samples were excited using a 633 nm excitation wavelength laser with a power of 7 mW. The Stokes shifted Raman spectra were accumulated inside the 200 to 3000 cm^{-1} range with 1 cm^{-1} resolution. Prior to each measurement, calibration was performed using a silicon standard (520 cm^{-1}centered Raman peak). The UV-Vis spectrum of TCM and TCMA molecule in ethanol was recorded at room temperature within the 200 to 800 nm wavelength range, using excessive-decision transmission electron microscopy (Tecnai T30 G2 S-Twin, FEI Company). The pattern was located in a quartz cuvette (1 cm direction length). Samples for TEM characterization were prepared by placing a drop of gold colloidal solution on a carbon-coated copper grid and drying beneath the IR lamp.

A549 lung cancer cells were cultured in a four-well chamber slide, and 100 μL (9:1, Au NPs/TCM) of TCM were added to separate wells and incubated at a temperature of 37°C. Exactly 30 minutes later, the SERS spectrum was recorded. After examining the SERS spectra within the cells, SERS mapping was performed using two cells using a confocal Raman microscopy at 0.5 synchronous times, 150 × 150 points per line, and a 50 × 50 μm mapping area across the X and Y directions. The excitation and emission spectra were recorded on a SPEX Fluorolog F112X spectrofluorimeter. The MTT assay was recorded with a reference reading of 655 nm on a TECAN spectrophotometer.

2.3 | Quantum chemical calculations

DFT and time-dependent density functional theory (TD-DFT)[54] calculations were performed using the Gaussian '09 suite programs[55] using the long-range corrected CAM-B3LYP functional[56] along with the Pople's 6-311++G (d, p) split-valence basis set[57,58] together with LANL2DZ basis set, which is widely used to model the metal

atoms.[59–62] B3LYP is a hybrid functional combining the Hartree-Fock and Becke exact exchange functionals[57] with the Lee-Yang-Parr correlation functional (LYP).[58] TCM and TCMA molecules were optimized at the B3LYP level of theory in conjunction with the 6-31++G (d, p) together with LANL2DZ basis set, and the results were visualized using Gauss-View program.[63] The input files were designed using Avogadro software.[64] Frequency calculations were executed to ensure that there are no imaginary frequencies to confirm the minimal structure. Furthermore, the vibrational modes were identified by potential energy distribution (PED) by VEDA4 program.[65] The calculated Raman activities were converted to relative Raman intensities using the theory of Raman scattering.[66] An empirical uniform scaling factor was used to offset the systematic errors caused by basis set incompleteness, neglect of electron correlation, and vibrational anharmonicity.[67,68] Berny's optimization algorithm was used for the complete optimization of the molecular geometry of TCM and TCMA with redundant internal coordinates. Detailed quantum chemical computations (geometry optimization, vibrational wave number calculation based on NBO potential energy supply [PED]) and in silico studies (docking) are described in our previous report in the Journal of Molecular Recognition.[53]

3 | RESULT AND DISCUSSION

3.1 | Structural analysis

The stable structure of TCM and TCMA molecules along with the atom numbering scheme is shown in Figure 1. The convergence criteria used for geometrical optimization are maximum force, RMS force, maximum displacement, and RMS displacement. The calculated structural parameters were compared with crystallographic data (CCDC No: 7034137)[69] and are tabulated in Table S1. TCM is a chloro benzothiadiazine dioxide, hydrogenated at positions 16, 19, 13 (carbon) and 10, 11 (nitrogen) and substituted with an aminosulfonyl group at C_{17}, a chlorine at C_{20}, a dichloromethyl group at C_{13}, and with sulfur dioxide groups at positions 4 and 5. The chlorobenzothiadiazine dioxide ring and chlorophenyl ring are seen to adopt in-plane conformation with bond angles C_{15}—C_{19}—C_{20} and C_{14}—C_{16}—C_{17}. The corresponding theoretical and experimental bond angle values of C_{15}—C_{19}—C_{20} for TCM and TCMA molecules are 120.84° and 121.89°, respectively. The theoretical and experimental bond angle values of C_{14}—C_{16}—C_{17} for TCM and TCMA molecules are 18.92° and 119.46°, respectively. The values are slightly different from that of crystallographic data. These discrepancies arise due to the fact that theoretical results belong to the gaseous phase (isolated molecule), whereas the experimental results belong to the solid phase. However, thiadiazinane ring is seen to adopt an envelope conformation with bond angles C_{14}—S_4—N_{10} (97.34° for TCM, 97.16° for TCMA and 102.12° from crystallographic data) and N_{11}—C_{13}—N_{10} (112.48° for TCM, 112.48° for TCMA and 107.57° from experiment). The slight discrepancies rise up because of the fact that theoretical consequences belong to the gaseous phase (isolated molecule) while the experimental outcomes belong to the solid phase. The envelope conformation may be due to the steric hindrance between diazinane hydrogen (H_{22}) and dichloromethyl hydrogen (H_{25}). As a result of this conformation, intramolecular hydrogen bond is formed between sulfonyl oxygen and methene hydrogen $O_{7}\cdots H_{21}$ (2.53 Å for both TCM and TCMA molecules). All hydrogen atoms in the chloro benzothiadiazine dioxide ring are in equatorial positions around the plane of the ring, except H_{22} and H_{21}. The hydrogen atoms H_{22} and H_{21} are in axial position with the torsional angles H_{21}—C_{13}—N_{10}—H_{22} (−174.45° for TCM and −174.03° for TCMA). This is due to the intramolecular hydrogen bonding $H_{21}\cdots N_{10}$ (2.06 Å for both TCM and TCMA molecules) and $C_{13}\cdots H_{23}$ (2.14 Å for both TCM and TCMA molecule). Another interesting fact observed is that the dichloromethyl exhibits anti-periplanar conformation with methene of chloro benzothiadiazine dioxide ring with bond angle C_{12}—C_{18}—C_{11} (109.91° for TCM and 109.93° for TCMA). The opposite end of the title molecule possesses nearly trigonal bipyramidal conformation with respect to the aminosulfonyl group of chloro benzothiadiazine dioxide ring with bond angles H_{27}—N_{12}—H_{28} (117.95° for TCM and 118.47°

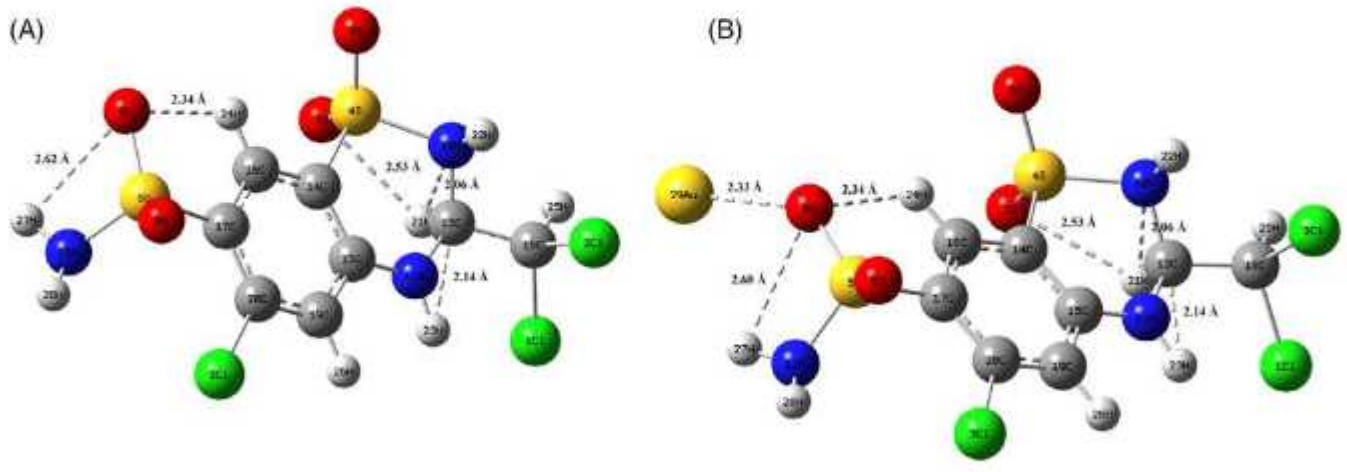


FIGURE 1 Optimized structure of (A) TCM and (B) TCMA using B3LYP functional and 6-31++G (d, p) together with LANL2DZ basis sets

for TCMA), C_{17}—S_5—O_9 (104.47° for TCM and 103.58° for TCMA), and C_{17}—S_5—O_8 (110.86° for TCM and 110.15° for TCMA). As a result of this trigonal bipyramidal conformation, a weak intramolecular hydrogen bond $O_9 \cdots H_{27}$ (2.62 Å for TCM and 2.60 Å for TCMA) has been formed in the sulfonamide. In addition, the steric hindrance has been observed between the electronegative chlorophenyl chlorine (Cl_{13}) and sulfonamide oxygen (O_8). TCM and TCMA exhibit almost the same conformation except for minute changes. This minute variation is due to the intermolecular hydrogen bonding ($O_9 \cdots Au_{29}$ [2.33 Å]) between TCM molecule oxygen (O_9) and AuNPs (Au_{29}), which is reflected by the bond angles as shown in Table S1. The table shows that the bond length of S_5—O_9 (1.63 Å for TCM and 1.68 Å for TCMA) is elongated in TCMA molecule than TCM molecule. The SO bond lengths S_4—O_6 (1.62 Å for TCM and TCMA molecules), S_4—O_7 (1.62 Å for TCM and TCMA molecules), S_5—O_8 (1.62 Å for TCM and TCMA molecules) are lesser than the S_5-O_9 (1.63 Å for TCM and 1.68 Å for TCMA). This is due to the strong and weak intramolecular hydrogen bonds $O_9 \cdots H_{24}$ (2.34 Å for TCM and TCMA molecules) and $O_9 \cdots H_{27}$ (2.62 Å for TCM and 2.60 Å for TCMA), respectively. The comparison of theoretical and experimental geometrical parameters using linear regression coefficient (R^2) calculations is graphically represented in Figure S1. The R^2 value shows the reliability of theoretical calculation; however, a slight deviation is observed. This deviation is due to the adsorption of TCM molecule to AuNPs through O_9 oxygen atom. Experimental geometric parameters deviate from theoretical geometric parameters due to intermolecular interactions existing within the molecule.

3.2 | Natural localized molecular orbitals (NLMOs) analysis

Natural localized molecular orbital (NLMO) analysis sternly appraises the potential for common hole/electron NPA patterns in vacant/occupied NBOs or other localized orbits. This has been analyzed in the hierarchy of natural atomic orbitals (NAOs) analysis (NAO), natural hybrid analysis (NHO), NPA,[20] and NBO analysis. The variation between the occupancy and energy of TCMA molecule and TCM molecule was analyzed based on the NAO analysis. This divulges that TCM molecule has less orbital invasion and orbital energy than TCMA molecule, which indicates that the delocalization of electrons is higher in TCMA molecule. Also, it reveals that TCM molecule has eight low-occupancy atoms (<1.9990e) (S_4, C_{14}, C_{15}, C_{16}, C_{17}, C_{18}, C_{19}, and C_{20}) and that population inversion occurs. Thus, it is evidenced that the occupancy order is inconsistent with its energy order, which occurs in the Rydberg-type orbitals of very low occupancy and near degeneracy energy. But in the TCMA molecule, it is seen that 55 electrons are in the effective core potential (ECP). It is direct evidence that the substitution effect increases delocalized electrons. Natural hybrid orbits (NHOs) are the result of an asymmetric orthogonalized hybrid orbit derived from the NAO concentrated on specific atoms through a uniform transition. The direction of each hybrid is specified in terms of the spherical polar (θ) and azimuthal (φ) angles from the nucleus as well as the deviation angle (dev.) from the line of centers between the bonded nuclei as shown in Table S2. The two CC bonds, C_{16}—C_{17} and C_{19}—C_{20} are more bent away from the line and are above 90° and 89°, respectively, in TCM molecule, which is due to intramolecular hydrogen bonding and the presence of a heavy chlorine atom. In TCMA molecule, two CC bonds, C_{14}—C_{15}, C_{16}—C_{17} are more bent away from the line and are above 90°, which is due to charge delocalization. Uniformly, the bonds S_4—O_7 and N_{10}—C_{13} in TCM molecule and C_{12}—C_{18}, S_4—C_{14}, S_5—C_{17}, C_{15}—C_{19} in TCMA molecule deviate less than 2°. This may be the obvious cause for the envelope conformation of the thiadiazinane ring in the chloro benzothiadiazine dioxide ring. The NHO analysis on TCMA molecule has evidence that there is a strong charge transfer between the AuNPs and TCM molecule.

The NPA of the electronic structures of TCM and TCMA molecules clearly describes the distribution of electrons in the various subshells of their atomic orbits. Figure S2 shows the accumulation of charges in the individual atom and the accumulation of electrons in the core, valence, and Rydberg subshells. The most electronegative charges for both molecules are −1.00481e and −1.07303 e and are found to be accumulated on N_{12} atom in TCM and TCMA molecules, respectively. In addition, the accumulated charge on the atoms follows the sequence $O_9 > O_8 > N_{10} > O_7 > O_6 > N_{11}$ with small variations in the sequence. From an electrostatic point of view of the molecule, these electronegative atoms tend to donate an electron. In contrast, the most electropositive atoms such as S_4 and S_5 have the tendency to accept an electron. The magnitude of charge accumulation is greater in TCMA molecule compared with that of the TCM molecule. This is due to the charge delocalization from AuNPs to TCM molecule. As a result, TCMA molecule tends to donate and receive electrons to a greater extent than TCM molecule. Further, from the NPA (Figure S3), it is observed that the electrons in TCM and TCMA molecules are distributed on the sub-shells as follows:

For TCM molecule,	
Core	79.98439 (99.9805% of 80)
Valence	111.34063 (99.4113% of 112)
Natural Minimal Basis	191.32503 (99.6485% of 192)
Natural Rydberg Basis	0.67497 (0.3515% of 192)
For TCMA molecule,	
Core	37.98869 (99.9702% of 38)
Valence	122.65236 (99.7174% of 123)
Natural Minimal Basis	270.64105 (99.8675% of 271)
Natural Rydberg Basis	0.35895 (0.1325% of 271)

The second-order perturbation theory analysis of the NBO-based Fock matrix of TCM and TCMA shows strong intramolecular hyperconjugative, charge delocalization interventions, which are presented in Table S3. The charge delocalization is formed due to the orbital overlap between the π(C—C) and π*(C—C) bond orbits, leading to relatively high stabilization energy on both molecules; the stabilization energy (28.54 and 2.64 kcal/mol for TCM, 34.94 and 1.38 kcal/mol for TCMA) in TCMA molecule being higher. This means that the intramolecular charge transfer (ICT) occurs between AuNPs and TCM molecule to attain system stability. The two conjugated π bonds of the

thiadiazinane ring clearly demonstrate a lesser degree of conjugation (Table S3), leading to de-aromatization. There occurs a strong delocalization of π-electrons in the chloro benzothiadiazine dioxide ring, which is reflected in the stabilization energy. A substantial amount of hyperconjugative interactions occurs from σ donor to σ* acceptor (Table S3) in the chloro benzothiadiazine dioxide ring in both TCM and TCMA molecules. A different level of π-electron delocalization is observed with higher energy in the thiadiazinane ring of TCM and TCMA molecule due to n_1 (N_{11}) to π*(C_{14}—C_{15}) in both TCM and TCMA molecules. The enhanced π*(C_{14}—C_{15}) results in an enormous stabilization of 49.57 kcal/mol in TCM molecule and 36.06 kcal/mol in TCMA molecule. It can be seen from the NPA analysis that charge acquisition is higher in O_9 in both molecules. The NBO analysis provides evidence of this. They are n_3 (O_8) → σ* (S_5—O_9) and n_3 (O_9) → σ*(S_5—O_8) in TCM molecule and n_3 (O_8) → σ*(S_5—O_9), n_6 (Au_{29}) → σ* (S_5-O_9) in TCMA molecule. This interaction proves that an ICT interaction from AuNPs to (S_5—O_9) is responsible for more charge on O_9 atom in TCMA molecule than TCM molecule. This may be due to the adsorption of TCM molecule to the AuNPs through O_9 atom in the S_5—O_9 bond. The hyperconjugative interaction between σ(S_5—O_9) to σ*(C_{17}—C_{20}) as shown in Table S3 for TCM and TCMA molecule makes chloro benzothiadiazine dioxide ring a highly chelating agent. Protonation or hydrogen bonding (O_7···H_{21}—C_{13}) at O_7 weakens the π system, and this eventually strengthens (C—C) as per the above charge-transfer scheme. Thus, (C—C) behaves as a protonation marker of the chloro benzothiadiazine dioxide ring.

3.3 | Frontier molecular orbital and electronic spectra analysis

The frontier molecular orbital (FMO) energies are major quantum mechanical descriptors that play an important role in regulating a wide range of chemical interactions. In the TCM molecule, the HOMO is located over the whole molecule except chlorine and sulfur atom, and the LUMO is located over the whole molecule except hydrogen atoms. In the TCMA molecule, the HOMO is located on all atoms except for electrochemical atoms in the chloro benzothiadiazine, and also on the AuNPs. The LUMO is located over the whole molecule except AuNPs. The positive and negative phase is represented in green and red color, respectively. The CI expansion coefficient reveals that the adsorption of gold nanoparticles affects the HOMO and LUMO distribution. The difference in frontier molecular orbital energies (FMOs) of TCM and TCMA molecules are 3.866 and 2.265 eV, respectively, as shown in Figure 2. Due to the aromatic system, both the molecules show small FMOs energy. The difference in FMOs energy of TCMA is small compared with TCM, indicating that charge transfer easily occurs in TCMA. It may be due to the enhanced molecular electrical transport properties and photostability of TCMA molecule as a consequence of its adsorption on gold nanoparticles. Enhanced photostability also enhances its drug stability as the dynamics of electrons in large hyperconjugated orbital systems increase. This alludes to that a lone pair of electron in a gold nanoparticle combined with a π-electron in a ring system to produce a high reactivity with low kinetic stability, resulting in higher drug stability in TCMA molecule than in TCM molecule. Also, a molecule with a small gap is more polarized and is known as a soft molecule. The low value of the energy gap is also due to electron-withdrawing groups that enter into conjugation. The optical band gap was obtained from Tauc's equation[71] [$\alpha h\nu = A\,(h\nu - E_g)^n$] and graphical plot as shown in Figure 3B,C. The energy required for exciting electron from n → π* transitions state[72] is 3.87 eV (TCM) and 2.27 eV (TCMA) (Figure 3B,C), and it matches with the frontier molecular orbital energy gap. The FMO energies and optical studies reveal that the eventual charge-transfer interaction is more in TCMA molecule than TCM molecule, which influences the biological activity and stability of the molecule; the reactivity and the biological activity of TCMA molecule are much more than TCM molecule, but the stability is low.

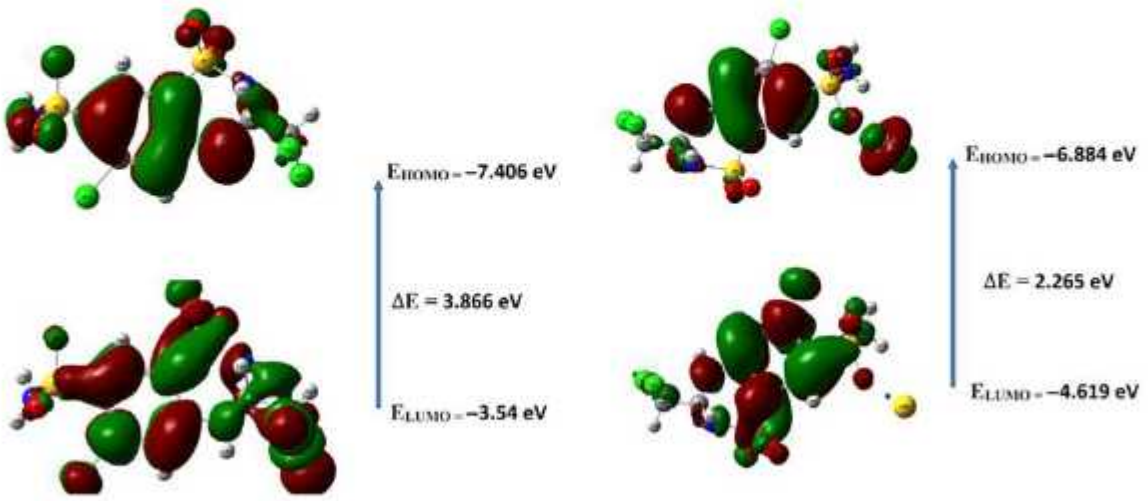


FIGURE 2 (A) Graphical representation of frontier molecular orbital of the TCM molecule (B) Graphical representation of frontier molecular orbital of the TCMA molecule

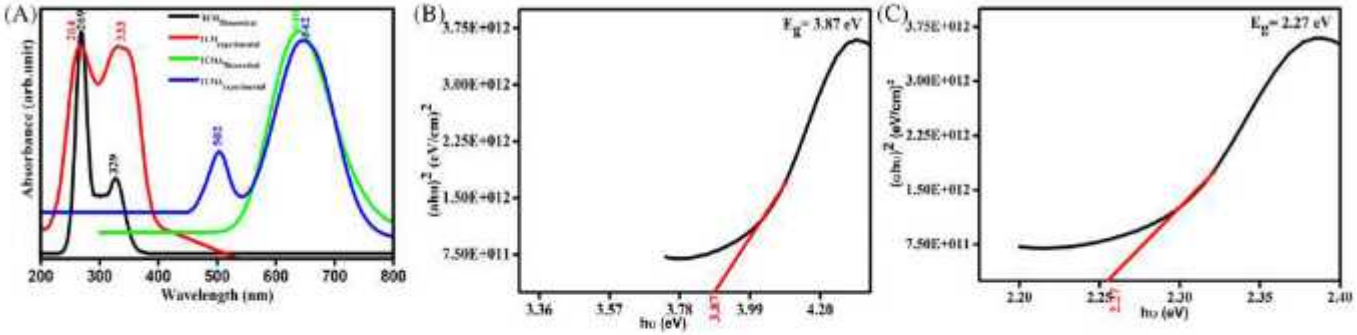


FIGURE 3 (A) The electronic transitions of simulated and observed UV-Vis spectra of the TCM and TCMA molecules (B) Tauc's plot of TCM molecule (C) Tauc's plot of TCMA molecule

In order to understand the nature of electronic transitions within TCM and TCMA molecules, TD-DFT calculations on electronic absorption spectra in methanol were performed. The percentages of major contributions for electronic transitions corresponding to the calculated wavelengths were determined with GaussSum 3.0.1 program package,[73] and the theoretical calculations were verified with experimental UV-Vis spectra. The calculated and experimental UV absorption maxima, theoretical electronic excitation energies, and oscillator strengths are detailed in Table 1. The experimental and theoretically predicted UV-visible spectra are visualized in Figure 3A. As can be seen from Table 1 and Figure 3A, the calculated absorption maxima values for the title compound are found to be 329 and 269 nm for TCM molecule and 640 nm for TCMA molecule. Oscillator strength *f* is a dimensionless quantity that describes the strength of an electronic transition. Transitions with extremely low or zero *f* values are forbidden. The oscillator strength for the transition at 269 nm in TCM molecule and 640 nm in TCMA molecule is higher in magnitude than the other transitions and its corresponding experimental value is observed at 333 and 264 nm in TCM molecule and 642 and 502 nm in TCMA molecule. The maximum absorptions are assigned to the transition from the HOMO to LUMO molecular orbital. This transition is predicted to be of $n \rightarrow \pi^*$ nature (Table 1). The absorption peaks arise due to the presence of conjugation interactions. The absorption peaks of TCMA molecule arise due to the electronic transitions from a lone pair of electrons present in the electronegative atoms to π electrons in the chloro benzothiadiazine moiety of the molecule. The wavelength, excitation energies, oscillator strength, and calculated counterparts with major contributions can be seen in Table 1.

By using these HOMO-LUMO energy values, the important properties like global hardness (η), global softness (σ), electronegativity (χ), chemical potential (μ), and electrophilicity index (ω) were calculated according to the molecular orbital (MO) theory done within the limitations of Koopmans theorem.[74] These electronic properties of the molecules are termed global reactivity descriptors.[75,76] The calculated values of I, A, χ, μ, η, S, and ω are 7.41 eV, 3.54 eV, 5.47 eV, −5.47 eV, 1.93 eV, 0.52(eV), −1, and 7.75 eV, respectively, for TCM molecule. For TCMA molecule these values are 6.88 eV, 4.62 eV, 5.75 eV, −5.75 eV, 1.13 eV, 0.88(eV), −1, and 14.60 eV, respectively, in the same order. The negative chemical potential (μ) of TCM and TCMA molecule reveals the stability of the molecule, TCMA molecule being more stable and hence more reactive than TCM. TCM molecule has a higher chemical hardness than TCMA molecule, and in terms of softness, it is the opposite, showing that the electronegativity and chemical stability of TCMA molecule is higher than that of TCM molecule. The electrophilicity index and ionization value of TCMA molecule are higher than that of TCM molecule. This divulges that ICT interaction between AuNPs and TCM molecules occurs through the oxygen atom in the aminosulfonyl. The FMOs energy value confirms that TCM molecule is chemisorbed on the gold surface through the lone-pair electrons on the oxygen atoms in the FMOs.[77] The frontier orbital density *f* is called the condensed Fukui functions.[71,72] It is found by taking the finite difference approximations from population analysis of atoms in molecules, depending on the direction of the electron transfer. The Fukui functions (f_k^+, f_k^-, f_k^0), local softness (S_k^+, S_k^-, S_k^0), and local electrophilicity indices (ω_k^+, ω_k^-, ω_k^0) calculated using Mulliken population analysis are termed as local reactivity descriptors and are tabulated in Table S4. The local nucleophilic and electrophilic reactivity descriptors such as nucleophilic attack (f_k^+) and electrophilic attack (f_k^-)[78] for TCM molecule are calculated in a slumping order as $C_{17} > C_{15} > C_{19}$ and $C_{11} > C_{13} > O_6 > O_9 > O_7 > O_8$, respectively. The potential for electrophilic attack due to adsorption of AuNPs can be seen to have spread to more atoms. Electrophilic attack (f_k^-) on TCM and TCMA molecules occurs on hydrogen atoms. Its intensity is different in TCM and TCMA molecules. Possible sites of radical attack (f_k^0) are C_{11} in TCM molecule and $Au_{29} > Cl_1$ in TCMA molecule. Au_{29} in TCMA molecule is the most likely to be radically attacked. All other reactive sites of TCM and TCMA molecules have a similar attack potential. However, the intensity of action is higher in TCMA molecule. Polar factors affect the reactions of free radicals. Although free radicals are neutral, they present some properties for gaining or losing electrons because they have some characteristic electrophilic or nucleophilic nature, that is, the absorption of gold nanoparticles in TCM molecule increases the flow of electrons, that is, ICT. According to Sailaja Rao et al,[79] free radicals are volatile molecules that destroy cancer cells in the body. This means that TCMA molecule can cause more damage to cancer cells.

TABLE 1 Experimental absorptions ($\lambda_{max\ Exot.}$), calculated absorptions ($\lambda_{max\ calc.}$), energy (E) and oscillator strength (f) of TCM and TCMA molecule using TD-DFT method at the B3LYP/6-311++G(d,p) and B3LYP/LANL2DZ level of basis set

Molecules	Excitation	CI expansion coefficient	λ_{max} calc. (nm)	λ_{max} expt. (nm)	E (eV)	(f)	Contribution of orbital	Bands[a]
TCM (HOMO → 71 and LUMO → 72)	Excited state 1 71 → 72 (77%) 70 → 74 (5%)	Singlet-A	329 269	325 264	4.5869	0.0935	n → π*	R-Bands (German: Radikalartig)
	Excited state 2 71 → 73 (76%) 71 → 72 (6%)	Singlet-A			4.8123	0.0023	n → π*	R-Bands (German: Radikalartig)
	Excited state 3 71 → 72 (78%) 71 → 75 (7%)	Singlet-A			5.1169	0.2611	n → π*	R-Bands (German: Radikalartig)
	Excited state 4 71 → 75 (30%) 71 → 74 (7%)	Singlet-A			5.2539	0.0234	n → π*	R-Bands (German: Radikalartig)
	Excited state 5 65 → 73 (21%) 66 → 73 (15%)	Singlet-A			5.3598	0.0094	n → π*	R-Bands (German: Radikalartig)
	Excited state 6 69 → 75 (18%) 65 → 73 (14%)	Singlet-A			5.4487	0.0095	n → π*	R-Bands (German: Radikalartig)
TCMA (HOMO → 80 and LUMO → 81)	Excited state 1 80B → 81B (76%) 79B → 81B (17%)	2.008-A	640	642 502	1.9454	0.306	n → π*	R-Bands (German: Radikalartig)
	Excited state 2 79B → 81B (78%) 76B → 81B (14%)	2.008-A			2.1003	0.0404	n → π*	R-Bands (German: Radikalartig)
	Excited state 3 77B → 81B (58%) 75B → 81B (17%)	2.006-A			2.1281	0.0302	n → π*	R-Bands (German: Radikalartig)
	Excited state 4 76B → 81B (63%) 78B → 81B (12%)	2.006-A			2.1331	0.0201	n → π*	R-Bands (German: Radikalartig)
	Excited state 5 75B → 81B (67%) 77B → 81B (24%)	2.007-A			2.2387	0.0112	n → π*	R-Bands (German: Radikalartig)
	Excited state 6 80A → 82A (37%) 80A → 81A (23%)	2.112-A			2.9036	0.2107	n → π*	R-Bands (German: Radikalartig)

[a]Reference in UV.[46]

3.4 | Vibrational spectral analysis

3.4.1 | IR and Raman spectral analysis

The vibrational analysis of the TCM molecule was performed on the basis of vibrations of the dichlormethyl, chloro benzothiadiazine dioxide ring, and sulfonamide. Table S5 gives detailed spectral assignments of the fundamental modes of TCM along with IR, Raman intensity, and percentage of PED. For visual comparison, the observed and simulated FT-IR and FT-Raman spectra are presented in Figure 4A,B, respectively. The calculated frequencies are seen to be slightly different from the experimental values. The reason for these discrepancies is that they were recorded using a solid phase sample during the experimental process, whereas DFT calculations were performed using an isolated gas-phase molecule.

Dichlormethyl

The anti-periplanar conformation dichlormethyl groups form one side of the TCM molecule. The CCl_2 asymmetric and symmetric stretching band appears in the wide region at 830 to 560 cm^{-1} and the anti-periplanar CCl_2 form absorbs near 649 cm^{-1}.[80] The observed band at 624 and 621 cm^{-1} in IR and Raman, respectively, are assigned to asymmetric stretching mode. The observed region confirms the anti-periplanar conformation. The CCl_2 in-plane bending and wagging vibrations appear normally in the regions at 290 to 210 and 420 to 300 cm^{-1}, respectively, as medium intense bands.[81,82] The observed medium band at 260 cm^{-1} and a weak band at 320 cm^{-1}, respectively, in Raman are assigned to CCl_2 in-plane bending and wagging vibrations, respectively. Electronic effects such as back-donation, mainly caused by the presence of nitrogen atom adjacent to dichlormethyl groups, shift the position of these wavenumbers and alter the intensity of CCl_2 stretching and bending modes. Similarly, the methine scissoring mode vibration is expected in the region ~1350 cm^{-1}.[80] The deformation modes of methine in the dichloromethyl group of TCM are found in the FT-Raman spectrum at 1342 cm^{-1} with a 12% contribution of PED for scissoring mode. As this vibration in these molecules results in no change or any appreciable change in dipole moment, it is often of very low contribution to the vibration and is absent in the IR spectrum.

Chloro benzothiadiazine dioxide ring

The chlorobenzothiadiazine dioxide ring is the backbone of the TCM molecule. The heavier mass of chlorine clearly makes the C—Cl stretching mode appear in the lower wavelength region. The aromatic C—Cl bands absorb in the region at 830 to 560 cm^{-1}.[83,84] Based on this, the very weak band observed at 687 cm^{-1} and 684 cm^{-1} in FT-IR and FT-Raman, respectively, was assigned to C—Cl stretching. The computed wavenumber of C—Cl stretching vibration coincides exactly with the experimental observation. The C—H stretching vibrations of the chorobenzothiadiazine dioxide ring are expected in the region at 3200 to 3000 cm^{-1}.[85,86] Observed Raman bands at 3228 cm^{-1}, 3198 cm^{-1}, and 3050 cm^{-1} are assigned to aromatic C—H stretching. This result exposes that the mode of C—H stretching is shifted to the upper wavenumber region, which may be due to induction of the thiazine group with the adjacent electronegative chlorine atom in the chlorophenyl ring. From the literature, it is seen that the vibrational band corresponding to the SO_2 symmetric stretching is reported at 1170 to 1120 cm^{-1}.[87] The $O_6—S_4—O_7$ symmetric stretching mode is observed at 1158 cm^{-1} in IR and 1164 cm^{-1} in Raman. The calculated frequencies and intensities are nearly consistent with the observed and previously reported values.[87] Thiazine compounds give rise to strong CN bands in the 1200 to 1160 cm^{-1} region.[88] But the CN stretching mode was observed as a medium IR band at 1071 cm^{-1} and a weak band at 951 cm^{-1}. The corresponding theoretical bands are observed at 1072 and 954 cm^{-1}. The theoretical wave number of CN stretching vibration coincides exactly with the experimental IR observation. The lowering of CN stretching band may be due to the electron release effect of the CN bond. In addition to the intermolecular effect, it can also cause ICT. This can increase the bioactivity of TCM molecule. The in-plane and out-of-plane deformation CH bands are

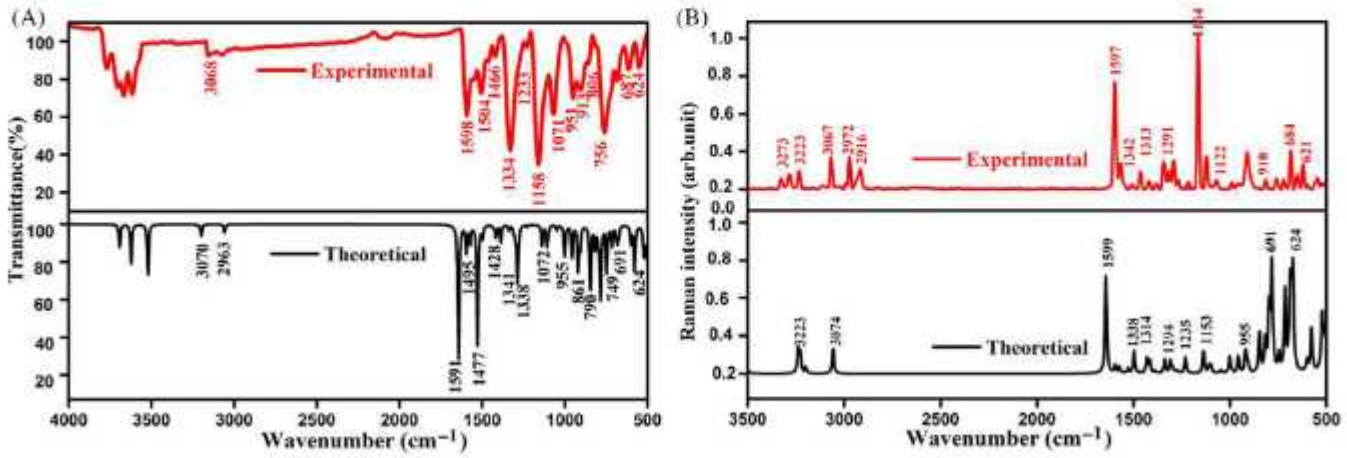


FIGURE 4 Comparison of observed and simulated (A) FT-IR spectra and (B) FT-Raman spectra of TCM molecule

expected in the regions 1425 to 1265 cm^{-1} and 1000 to 850 cm^{-1}. Two IR bands at 1428 and 1233 cm^{-1} are assigned to CH in-plane deformation. The three IR bands (at 1334, 913, 863 cm^{-1}) and two Raman bands (at 1342, 910 cm^{-1}) are assigned to CH out-of-plane deformation. The corresponding computational CH in-plane and out-of-plane deformation are observed at 1428 and 1235 cm^{-1}, and 1342, 1338, 925, and 861 cm^{-1}, respectively. The computational wave number of CH stretching vibration coincides precisely with the experimental IR wavenumbers. The CH in-plane and out-of-plane bending modes appeared simultaneously in both IR and Raman spectra, which may provide evidence for ICT interaction. A protonated amine group (—NH) has characteristic absorption bands within the range of 1660 to1485 cm^{-1}.[89] A strong IR band at 1466 and 1477 cm^{-1} in the computational prediction are attributed to the in-plane bending of NH. The activation and shifting of this band is a strong evidence for the presence of C_{13}—H_{21}···N_{10} hydrogen bonds in the molecule. The CS rocking and CH wagging vibrations are expected in the region 1190 to 1120 cm^{-1} and 1375 to 1225 cm^{-1}, respectively. The corresponding Raman bands are observed at 1122 and 1313 cm^{-1}, respectively, in the above order. The shifting of the wavenumber may be due to the interaction of the lone-pair atoms with the nucleophilic atoms of the chloro benzothiadiazine dioxide ring. The ring puckering and ring torsional vibrations are clearly manifested in the range of 800 to 120 cm^{-1}, which are well supported by calculations.

Sulfonamide

The vibrational bands corresponding to the NH_2 symmetric and asymmetric stretching mode are reported in the range of 3450 to 3250 cm^{-1} and 3550 to 3330 cm^{-1},[87] respectively. The NH_2 symmetric stretching mode is observed at 3068 cm^{-1} in the IR band and 3067 cm^{-1} in the Raman band, and the NH_2 asymmetric stretching mode is observed at 2972 cm^{-1} in Raman. The lowering of the NH_2 symmetric and asymmetric stretching mode vibration wavenumber is a result of the conjugation due to the SO_2 group. The SO_2 symmetric stretching mode has been reported with the vibration bands being in the range of 1200 to 1100 cm^{-1}.[87] In TCM, this mode is observed at 1158 cm^{-1} in IR and 1164 cm^{-1} in Raman, which is in good agreement with the earlier literature. The SO_2 out-of-plane mode is observed at 556 cm^{-1} and the CS—NH_2 scissoring vibration is observed at 1504 cm^{-1} in IR and at 1495 cm^{-1} in the computational prediction, which is influenced by the conjugation effect of oxygen in the sulfur dioxide group attached between the amino group and the chlorophenyl ring.

3.4.2 | SERS spectral analysis

The shape and size of AuNPs were identified from the absorption spectra, band gap energy, and transmission electron microscope (TEM) analysis. The color of the prepared AuNPs is wine red color. The bandgap energy and absorption maxima are found to be 3.2 eV and 532 nm, respectively, and from this, it is recognized that the AuNPs are spherical in shape with an average particle size of 40 nm. This is further confirmed by TEM analysis. The detailed explanation and figures are described in the previous paper in the Journal of Molecular Recognition.[53] The absorption spectrum is observed to be redshifted from 329 nm to 670 nm, which shows that the title molecule TCM is transformed to TCMA molecule, indicating that the TCM molecule has been adsorbed onto the nanoparticle surface. The oscillator strength (Table 1) of the TCMA molecule is greater than the TCM molecule. This reveals that the probability of absorption of electromagnetic radiation in transitions between energy levels is greater in TCMA molecule due to the effect of adsorption on AuNPs. The SERS spectrum of TCMA molecule (Figure 5) was recorded, and assignments are tabulated in Table 2. The SERS fingerprint pattern of TCMA was implemented at concentrations of 10^{-3}, 10^{-4}, and 10^{-5} M (Figure 5). The observed SERS spectrum is interpreted on the basis of different adsorption sites, geometries, and adsorbate conformation/orientation. The SERS spectrum was analyzed by comparing theoretical and experimental data with normal Raman spectral data. The SERS signal is mainly contributed by the analyte located in hot spots, where the fluorescence signal is significantly quenched. Therefore, the number of hot spots, analyte molecules, and their locations within these plasmonic structures directly determine the strength of the SERS signal.[90] The intense absorption bands are observed at 245 cm^{-1} for 10^{-3} M, 10^{-4} M concentrations and at 251 cm^{-1} for 10^{-5} M concentration, which indicates the presence of a metal-adsorbing reaction, which reveals that the metal adsorption bond reacts with the oxygen atom and achieves a dynamically favorable interaction. The steric effect imposed by the amino sulfonyl group on the metal also supports this interaction. The oxygen-related interaction of the amino sulfonyl group is derived from the charge transfer between the low electronegative oxygen with the metal. This interaction is more pronounced in the oxygen atom O_9 attached to the intramolecular S_5—O_9···Au_{29} hydrogen bonding compared with other oxygen atoms. These results are consistent with the results of optimized geometry and NBO analysis. The Fukui function indicates that the highest electron density is located on the O_9 oxygen atom of the

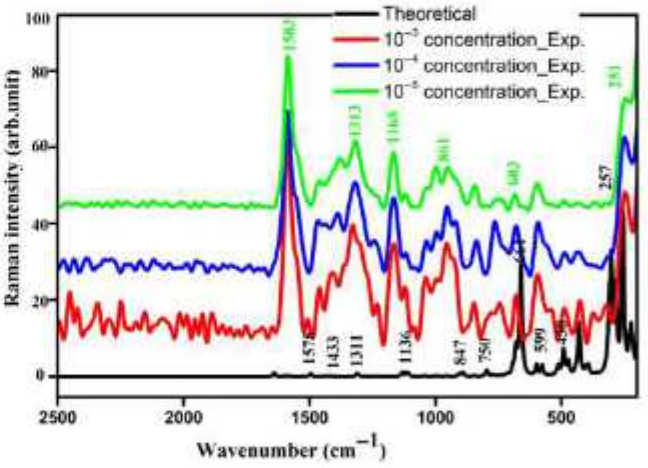


FIGURE 5 SERS of TCMA at three different concentrations (10^{-3}, 10^{-4}, 10^{-5} M) and calculated SERS spectra

TABLE 2 Selected experimental and theoretical SERS bands of TCMA

FT-Raman		SERS				
			Experimental wavenumber (cm^{-1})			
Theoretical wavenumber (cm^{-1})	Experimental wavenumber (cm^{-1})	Theoretical wavenumber (cm^{-1})	10^{-3} M	10^{-4} M	10^{-5} M	Assignments
1645	1591	1575	1586	1583	1583	ν C═C (95) ring
1545	1494	1495	1507			τ C19—H26 (85), τ C16—H24(46) ring
1492	1443	1433	1470	1451		ν C—C (80) ring
1354	1309	1311	1319	1319	1313	ρ C19—H26 (81), ρ C16—H24 (32) ring
1278	1235	1232	1225			νasy N10—S4—O6 (62), νasy O9—S5—O8 (50) ring
1183	1144	1136	1175	1168	1168	νsym C15—N11—C13 (46), νsym O9—S5—O8 (55) ring
995	963	957	955	955		ρ O8—S5—O9 (43) ring
870	841	847	842	836	861	β CC (83) ring, β C17—S5 (43) ring, β C19—H26 (52), β C16—H24 (38)
771	746	750	748	760		ω C19—H26 (59),ω C16—H24 (20) ring
665	643	661	678	685		δsci O8—S5—O9 (28) sul
617	597	599	590	597	603	γ C19—H26 (42), γ C16—H24 (12), γ C17—S5 (43) ring
448	433	430	433	433		ν Cl1—C18—Cl2(26) meth
262	253	257	245	245	251	ν Au29—O9 (92), ν Au29—O8 (20)

Note: ν, stretching; ν_{sym}, symmetric stretching; ν_{asym}, asymmetric stretching; β, in-plane bending; δ_{sci}, scissoring; ρ, rocking; ω, wagging; t, twisting; γ, out-of-plane bending; sul, sulfonamide; ring, chloro benzothiadiazine dioxide ring; meth, dichlormethyl.

amino sulfonyl group, which reveals that the molecule is adsorbed through the O_9 oxygen atom in the amino sulfonyl group.

The aromatic C═C stretching bands normally appear at 1600 to 1450 cm^{-1}.[87] In TCM molecule, it is observed at 1575 cm^{-1} theoretically, at 1586 cm^{-1} for concentrations 10^{-3} M, and at 1583 cm^{-1} of concentrations 10^{-4} and 10^{-5} M concentrations. Simultaneous activation of the C═C stretching mode in the SERS spectra provides evidence for the charge-transfer interaction between the donor and acceptor groups through the π system. This confirms that TCM molecule is adsorbed on the AuNPs through chemisorption. The frequencies of the asymmetric and symmetric SO_2 (O_9—S_5—O_8) stretching vibrations in TCMA are lower than in TCM, as shown in Table 2. This variation and intramolecular S_5—O_9···Au_{29} hydrogen bonding are due to the charge-transfer interaction between TCM molecule and AuNPs via oxygen atom. The halogen-substituted phenyl ring CH in-plane and out-of-plane bending modes are expected in the range of 1425 to 850 cm^{-1} and 635 to 620 cm^{-1}, respectively.[87] The CH in-plane bending modes are observed at 847 cm^{-1} (theoretical), 842 cm^{-1} (10^{-3} M), 836 cm^{-1}(10^{-4} M), and 861 cm^{-1} (10^{-5} M). The CH out-of-plane bending modes are observed at 599 cm^{-1} (theoretical), 590 cm^{-1} (10^{-3} M), 597 cm^{-1} (10^{-4} M), and 603 cm^{-1} (10^{-5} M). From Figure 5, the in-plane bending mode is seen to be more enhanced than out-of-plane bending mode. According to the surface selection rule,[88] when a molecule is adsorbed in perpendicular orientation to the metal surface, its in-plane bending mode is more enhanced than out-of-plane bending mode. In the present case, this has happened. This leads to evidence for a perpendicular orientation of TCM on the gold surface. So TCM molecules are probably perpendicular on the AuNPs surface with perpendicular orientation through the lone pair of electrons on oxygen atom in the amino sulfonyl group. The other supportive assignments are given in Table 2.

3.5 | Prediction of biological activity

Theoretical and experimental studies have been conducted to understand the structural function of TCM and TCMA molecules. The literature review shows that TCM molecule is used as a diuretic in the treatment of edema (including those associated with cardiac arrest) and in pulmonary hypertension in patients with chronic obstructive pulmonary disease (COPD).[89] Hence analytical scrutiny (in silico and the in vitro) was performed with respect to surgical COPD type diseases (lung cancer) using the diuretic drug (TCM) and the diuretic drug adsorbed with AuNPs (TCMA). The in silico study was carried out using molecular docking. Based on the in silico studies, we progressed to the in vitro studies. The MTT assay and SERS studies were conducted under in vitro studies.

3.5.1 | In silico biological activity screening

Predicting the physicochemical properties of "drug-like" molecules

The conventional benchmark Rule of Five (RO5) is known as the Lipinski rule.[91] The RO5 has gained popularity as a "good rule of thumb". The RO5 rule defines drug candidate with desirable physicochemical properties to have molecular weight (MW) < 500 Da, log

$P < 5$, number of hydrogen bond donor (HBD) < 5, and number of hydrogen bond acceptors (HBA) < 10; but this prediction is not specific to the central nervous system (CNS) drugs. The RO5 rule was analyzed with the help of Molsoft drug-likeness and molecular property prediction online software.[92] The physicochemical properties such as the MW, log P, HBD, HBA are 378.90, 0.18, 4, and 5, respectively, in TCM molecule and 575.87, 0.71, 4, and 6, respectively in TCMA molecule in the same order. If any two laws are molecularly obeyed, it is likely to experience verbal assimilation features.[53] The analyzed results obey the Lipinski rule and so predict the novelty of the drug. TCM molecule has not violated Ghose filter properties (160 < MW < 480, 0.4 < WlogP<5.6, 40 < MR < 130, 20 < atoms<70) but TCMA molecule violated one property. TCM and TCMA molecules obey the Veber (GSK) filter properties (Rotatable bonds<10, TPSA < 140). TCM and TCMA molecules obey the Egan (Pharmacia) filter properties (WlogP < 5.88, TPSA < 131.6) and Muegge (Bayer) filter properties (200 < MW < 600, −2 < XlogoP<5, TPSA < 150, No. of rings < 7, no. of hetero atoms>1, no. of rotatable bonds < 15, HBA < 10, HBD < 5). The bioavailability score is 0.55 for TCM and TCMA molecules. These drug-likeness properties show TCM and TCMA molecule lies in the drug range. Also, the drug-likeness and blood-brain barrier (BBB) scores are predicted with the help of the Molsoft drug-likeness and molecular property prediction online software. The drug-likeness score of TCM and TCMA molecule is 0.73, that is, it lies in the drug range. The BBB score of TCM and TCMA molecule is 2.38 and 2.37, respectively. This means TCM and TCMA molecule protects the brain from toxic side effects. The physicochemical, lipophilicity, and water solubility properties of TCM and TCMA molecules are in good agreement with the Lipinski rule, which supports the drug-likeness results.

Prediction of binding sites of lung cancer

Molecular docking is a molecular modeling technique that is used to predict how a protein (enzyme) interacts with small molecules (ligands).[93] The molecular docking approach was used to model the interaction between the molecule and selected proteins at the atomic level, and to characterize the behavior of small molecules in the binding site of target proteins as well as to elucidate fundamental biochemical processes. Also, a molecular modeling study was performed using auto-dock tools for analyzing the preferred binding orientation, affinity, and activity of drug molecules and their protein targets. Protein selected for docking to TCM and TCMA molecules were taken from protein database (PDB) to detect protein receptor active site. MAPK13 complex with an inhibitor of non-small cell lung cancer (PDB id: 4eyj)[94] receptor was used for docking with both molecules. The lung cancer protein (4eyj) was selected following the literature survey. Also, the minimum resolution (2.10 Å) and the domain completeness of the PDB structure (XRD) have been checked and availability was confirmed. The optimized molecular structure was converted to the PDB file and was used as a ligand. Rigid protein and flexible ligand dockings were carried out using the AutoDock 4.2 program package.[95] The Lamarckian genetic algorithm (LGA) was used for molecular docking calculations. The following protocol was adopted: trials of 100 dockings, energy evaluations of 25 000 000, population size of 200, mutation rate of 0.02, crossover rate of 0.8, and elitism value of 1. The coordinates of the binding site for both TCM and TCMA molecules are given below.

Grid map x-dimension: 76.0 Angstroms
Grid map y-dimension: 76.0 Angstroms
Grid map z-dimension: 76.0 Angstroms
Maximum coordinates: (71.894, 68.861, 64.739)
Minimum coordinates: (−4.056, −7.089, −11
Box_min: −42.179 -8.890 -52.493
Box_max: 21.984 41.002 14.518
Cube_min: −43.604 −17.450 −52.493
Cube_max: 23.408 49.562 14.518

The RMSD value for both TCM and TCMA in molecular docking is 1.00, which validates that the docking results are good.[96] The docking parameters of TCM molecule such as binding energy, inhibition constant, and intermolecular energy of the molecule with respect to the targeted proteins are −5.34 kcal/mol, 310.12 mM, and −5.33 kcal/mol, respectively. For TCMA molecule the values are −7.53 kcal/mol, 584.56 mM, and −7.51 kcal/mol, respectively, in the same order. TCMA molecule shows more negative binding energy, intermolecular energy, and high inhibition constant. The hydrogen bonds between the ligand (TCM molecule) and MAPK13 complex with an inhibitor (4eyj) are at S_5—O_9···O, S_5—O_9···N, S_5—O_8···O, and S_5—O_8···N with amino acids ASP A227, ARG A186, ARG A 186, and LEU A 195, respectively with distances 1.26, 2.35, 2.13, and 1.75 Å, respectively. The hydrogen bonds between the ligand (TCMA molecule) and MAPK13 complex with an inhibitor (4eyj) are at S_5—O_9···O, S_5—O_9···N, S_5—O_8···O, and S_5—O_8···N (1.05, 2.21, 1.95 and 1.52 Å, respectively) with amino acids LEU A 3, ILE A 4, ARG A 5, and LYS A 6 in the same order. The ligands TCM, TCMA molecules, and MAPK13 complex with an inhibitor (4eyj) displayed four hydrogen bonds with key binding site residues. The key binding site residues of TCM molecule are ASP A227, ARG A186, ARG A 186, and LEU A 195. LEU A 3, ILE A 4, ARG A 5, and LYS A 6 are the key binding sites of TCMA molecule. The highly active site predicted by docking is O_8 and O_9 atoms in both TCM and TCMA molecules. From the spectroscopic studies also it was confirmed that O_8 and O_9 are the most active sites of the TCM and TCMA molecules. The functional H bond acceptor and donor group from protein major binding sites of proteins are shown in Figure 6. The overall results reveal that both TCM and TCMA molecules show good binding affinity toward lung cancer activity through the O_8 and O_9 atoms in sulphonamide, but the TCMA molecule exhibits more binding affinity than TCM molecule. That is, TCMA molecule is a better ligand than the TCM molecule.

3.5.2 | Recognition of human lung cancer cells—in vitro analysis

Based on the results of the docking study, in vitro analysis of lung cancer cells was performed using the SERS and MTT assay to test the cytotoxic effect of TCM and TCMA molecules. For intracellular SERS

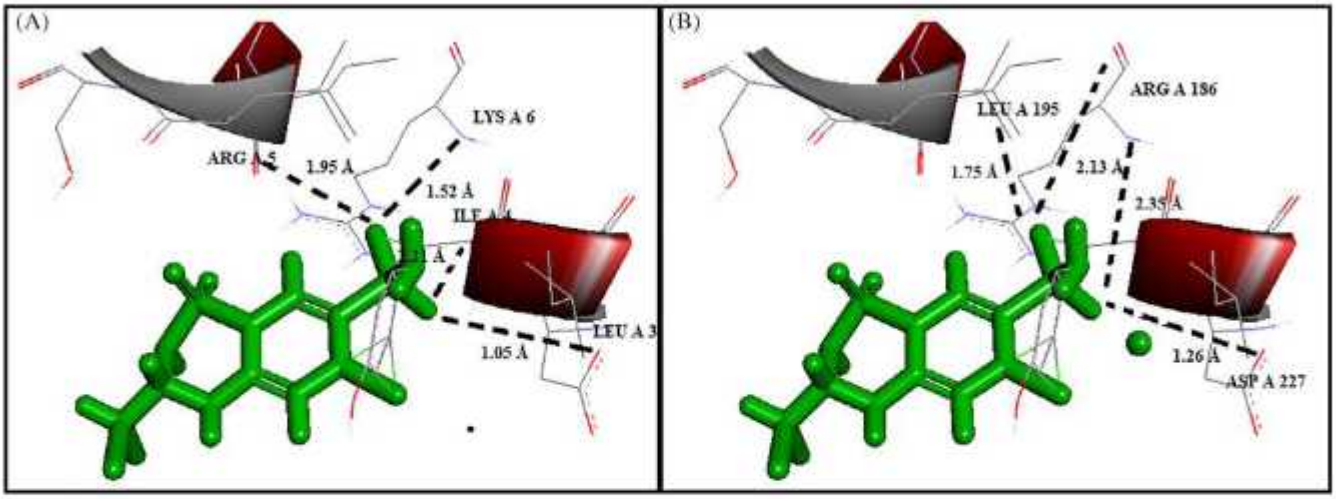


FIGURE 6 Pictorial representation of possible binding sites of (A) the TCM molecule and (B) the TCMA molecule with the target proteins

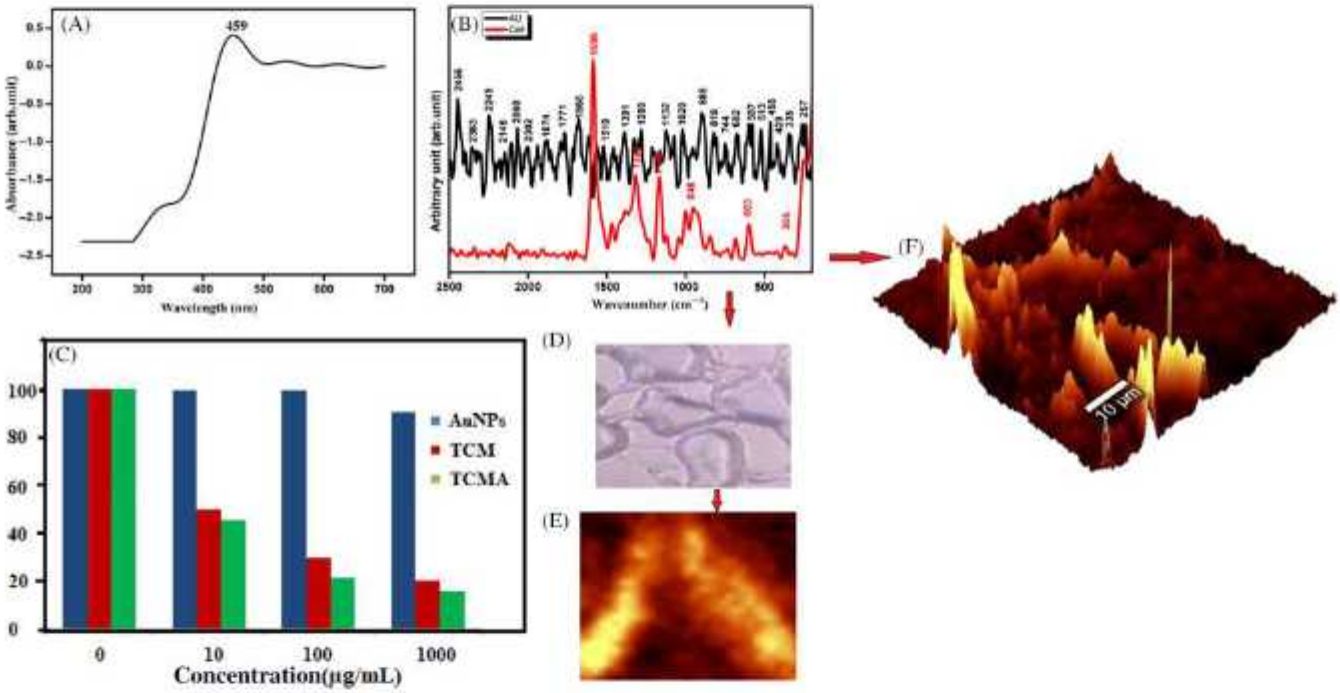


FIGURE 7 (A) UV-Vis spectra of the TCMA molecule inside the A549 cell line (B) SERS spectra analysis of TCMA and AuNPs inside A549 (C) Graphical representation of cytotoxic effect and Raman imaging of cells: (D) Bright field images (E) 2D image (F) 3D image

study, TCMA molecule was taken up into cell A549. Two hours later, when the absorption spectrum was examined, a cytoplasmic region absorption peak of 459 nm was observed, as shown in Figure 7A. This absorption peak confirmed that the molecule is in the cytoplasmic area. Normally cytoplasmic peak appears at 300 to 700 nm.[97] After another 1 hour (3 hours), when the absorption spectrum was examined again, it was seen that the absorption peak disappeared. This evidences that TCMA molecule is slowly moving toward the nucleus. After 4 hours, nuclear accumulation without cytoplasmic fluorescence was observed, which justifies the SERS studies. The results obtained were compared with other similar studies reported in the literature and are shown in Table S6.

The SERS spectra were collected from the different sections of the cell and then averaged. Our experiments show that the 40 nm AuNPs do not influence the viability of the cells and also provide a strong SERS factor. The strong and intense bands are presented in Table S6 and are graphically shown in Figure 7B. A broad and intense band is observed at 1595 cm^{-1}. According to Zhang et al,[98] this vibration is assigned to the phenylalanine, acetoacetate, riboflavin, which confirms changes in the nucleic acid and lipid. Raman bands

corresponding to nucleotides are identified at 697 cm^{-1} (thymine, cytosine, and uracil), 1168 cm^{-1} (thymine, guanine, and adenine), and a broadened band at 1595 cm^{-1} (guanine and adenine).[97,98] The 697 cm^{-1} band confirms the mixing of DNA and RNA. The presence of nucleic acids inside the cell line was detected by the spectral line observed at 848 cm^{-1}, which is assigned to the vibration of the sugar-phosphate o-p-o backbone. The sugar-phosphate backbone forms the structural framework of nucleic acids, including DNA and RNA. A reduction in the relative intensity of the lipid band at 1326 cm^{-1}[97,98] indicates the decrease of the lipid-to-protein ratio. The above assignments show biochemical changes in the nucleus and indicate that TCMA interacts with apoptotic (cancer) cells. This will enable label-free monitoring and further strengthen therapeutic use. The SERS spectrum derived from TCMA within lung cancer cells, related to proteins, nucleic acids, lipids, and carbohydrates, are identified.

The SERS imaging of single live cells can accurately quantify the cellular biomarker expression difference from the SERS intensity ratio and is hence employed for cancer cell screening.[97] Raman imaging analysis was performed for confirming cellular internalization. To that end, the bright field for TCMA localization (Figure 7D) and Raman mapping was observed in A549 cells for 1 to 3 hours after TCMA incubation. Then, 2D SERS mapping (Figure 7E) was used to determine the location and temporal progression of nanoparticle acquisition in cancer cells[99] at different time points. In addition, 3D SERS maps (Figure 7F) were also constructed to show the internalization of the drug. Raman spectral and imaging analysis from A549 cells shows an enhanced Raman signal. Raman imaging and spectral analysis of TCMA demonstrate time-dependent localization using an early distribution of the cytoplasm and subsequent migration to the nucleus. It is clear from the Raman images that TCMA has entered the A549 lung cancer cells. A white light image of such an apoptotic A549 lung cancer cell is shown in Figure 7D. Image form showed that the cell is 10 μm in size and is much smaller than the control cell.[100] So, the cells are apoptotic. The MTT ability assay confirmed the above-stated result. The MTT test was performed on three concentrations of TCM and TCMA molecules. TCM and TCMA show cytotoxic effects with more cytotoxicity in 1000 μM in TCMA. But there is no cytotoxic effect for AuNPs alone. The above results show that AuNPs aids cellular uptake of the drug of interest and allow targeted drug delivery. The comparative results are delineated in Table S7 and Figure 7C. It is further evident that TCMA interacts with apoptotic cell (MTT assay) and can be used for effective monitoring through SERS, which enable label-free monitoring and further potentiate its therapeutic utility.

4 | CONCLUSION

The molecular structures of TCM and TCMA were analyzed by comparing the reported experimental single crystal X-ray diffraction and the computational studies. TCM and TCMA have almost the same conformation except for minute changes due to the intermolecular hydrogen bonding ($O_9\cdots Au_{29}$ [2.33 Å]) between TCM molecule oxygen (O_9) and AuNPs (Au_{29}). The variation between the occupancy and energy of TCMA and TCM molecule showed that TCMA molecule has less orbital invasion and orbital energy than TCMA molecule. The NHO analysis on TCMA molecule has evidence that there is a strong charge transfer between the AuNPs and TCM molecule. Accumulation of charge on the atoms was analyzed by NPA analysis, which confirmed that the accumulation of charge is greater in the O_9 atoms. The NBO analysis interactions proved the adsorption of TCM molecule to the AuNPs through the O_9 atom of the S_5—O_9 bond. The theoretical and experimental energy gap of TCMA molecule is found to be lower than TCM molecule due to electron-withdrawing groups that enhance conjugation and result in higher drug stability in TCMA molecule than in TCM molecule. The global and local reactivity descriptors and electronic spectra analysis revealed that TCMA molecule can cause more damage to cancer cells. Experimentally observed and theoretically calculated vibrational frequencies were compared and assigned on the basis of PED calculations. Electronic effects such as back-donation, mainly caused by the presence of a nitrogen atom adjacent to the dichlormethyl group, shifted the position and altered the intensity of CCl_2 stretching and bending modes. The shifting of NH in-plane bending mode is a strong evidence for the presence of C_{13}-$H_{21}\cdots N_{10}$ hydrogen bonds. The IR and Raman spectral assignments were performed supported by quantum chemical calculations. The complementary experimental and theoretical analysis of Raman and SERS spectra revealed that TCM molecule is predominantly adsorbed perpendicular to the gold surface through the O_9 oxygen atom in the amino sulfonyl group. The intramolecular S_5—$O_9\cdots Au_{29}$ hydrogen bonding resulted from the charge-transfer interaction between TCM molecule and AuNPs via an oxygen atom. Molecular docking analysis revealed that TCM and TCMA molecules can act as a good inhibitor against lung cancer. The MTT assay and SERS study inside the cell supported the molecular docking results. MTT assays have predicted positive drug resistance with high accuracy and drug sensitivity for TCM and TCMA molecules. Also, the cellular uptake of AuNPs shows nontoxicity. In addition, TCMA molecule shows higher activity than TCM molecule. In such cases, AuNPs can be used as carriers of TCM drug molecules. Raman imaging and spectral analysis of TCMA demonstrate time-dependent localization using an early distribution of the cytoplasm and subsequent migration to the nucleus. The results confirmed that TCMA interacts with apoptotic cell (MTT assay) and can be used for effective monitoring through SERS, which enable label-free monitoring and further potentiates its therapeutic utility.

ACKNOWLEDGEMENTS

The author (SV) acknowledges the Department of Physics, Mar Ivanios College, Thiruvananthapuram, Kerala for the computational facility using the Gaussian 09. The author DS acknowledges the facilities offered by the DST-FIST programme (SR/FST/College-182/2013, November 2013 & FIST No.393 dated 25-09-2014) of Bishop Moore College, Mavelikara, Kerala.

CONFLICT OF INTEREST

The authors declare no conflicts of interest.

AUTHOR CONTRIBUTIONS

V. Shyni: Conceptualization, methodology, writing–original draft. **D. R. Leenaraj**: Conceptualization, methodology. **Reena Ittyachan**: Data curation. **G. J. Shyju**: Data curation. **Lynnette Joseph**: Writing–review and editing, supervision. **D. Sajan**: Conceptualization, writing–original draft, Funding acquisition, validation.

ETHICS STATEMENT

The submission of this work is according to the ethics followed by the journal.

CONSENT TO PARTICIPATE

All the co-authors consent to participate and are aware of and approve of the submission.

CONSENT TO PUBLISH

All the co-authors consent to publish. All authors approved the version to be published. All authors agree to be accountable for all aspects of the work in ensuring that questions related to the accuracy or integrity of any part of the work are appropriately investigated and resolved.

DATA AVAILABILITY STATEMENT

All data generated or analyzed during this study are included in this article and its supplementary information file.

ORCID

Lynnette Joseph https://orcid.org/0000-0003-4528-680X
D. Sajan https://orcid.org/0000-0002-0344-0744

REFERENCES

1. Siegel RL, Miller KD, Fuchs HE, Jemal A. Cancer statistics, 2021. *CA Cancer J Clin*. 2021;71(1):7-33.
2. Rabaan AA, Al-Ahmed SH, Sah R, et al. SARS-CoV-2/COVID-19 and advances in developing potential therapeutics and vaccines to counter this emerging pandemic. *Ann Clin Microbiol Antimicrob*. 2020;19(1):40.
3. Hegde PS, Chen DS. Top 10 challenges in cancer immunotherapy. *Immunity*. 2020;52(1):17-35.
4. Wallace RJ, Jones DB, Wiss K. Sulfonamide activity against *Mycobacterium fortuitum* and *Mycobacterium chelonei*. *Clin Infect Dis*. 1981;3(5):898-904.
5. Buckheit RW Jr, Fliakas-Boltz V, Decker WD, et al. Biological and biochemical anti-HIV activity of the benzothiadiazine class of non-nucleoside reverse transcriptase inhibitors. *Antiviral Res*. 1994;25(1):43-56.
6. Novello FC, Sprague JM. Benzothiadiazine dioxides as novel diuretics. *J. Am. Chem Soc*. 1957;79(8):2028-2029.
7. Wright JM, Schwartz J, Vartiainen T, et al. 3-Chloro-4-(dichloromethyl)-5-hydroxy-2(5H)-furanone (MX) and mutagenic activity in Massachusetts drinking water. *Environ Health Perspect*. 2002;110(2):157-164.
8. Velihina YS, Pil'o SG, Zyabrev VS, Brovarets VS. 2-(Dichloromethyl) pyrazolo[1,5-a][1,3,5] triazines: synthesis and anticancer activity. *Biopolym Cell*. 2019;36(1):60-73.
9. Hansch C, Sammes PG, Taylor JB. The rational design, mechanistic study and therapeutic application of chemical compounds. *Curr Top Med Chem*. 1990;103(3):341-341.
10. Kanda Y, Kawanishi Y, Oda K, et al. Synthesis and structure-activity relationships of potent and orally active sulfonamide ETB selective antagonists. *Bioorg Med Chem*. 2001;9(4):897-907.
11. Stokes SS, Albert R, Buurman ET, et al. Inhibitors of the acetyltransferase domain of N-acetylglucosamine-1-phosphate-uridylyltransferase/glucosamine-1-phosphate acetyltransferase (GlmU). Part 2: optimization of physical properties leading to antibacterial aryl sulphonamides. *Bioorg. Med. Chem. Lett*. 2012;22(23):7019-7023.
12. Chibale K, Haupt H, Kendrick H, et al. Antiprotozoal and cytotoxicity evaluation of sulfonamide and urea analogues of quinacrine. *Bioorg Med Chem Lett*. 2001;11(19):2655-2657.
13. Rahavi EI, Camoutsis C, Zoumpoulakis P, et al. Sulfonamide-1,-2,4-triazole derivatives as antifungal and antibacterial agents: synthesis, biological evaluation, lipophilicity, and conformational studies. *Bioorg Med Chem*. 2008;16(3):1150-1161.
14. Kennedy JF, Thorley M, Kleeman A, Engel J, Kutscher B, Reichert D. *Pharmaceutical Substances*. 3rd ed. Stuttgart, Stuttgart: Thieme; 1999.
15. Serradeil-Le GC. An overview of SR121463, a selective non-peptide vasopressin V2 receptor antagonist. *Cardiovasc Drug Rev*. 2001;19(3):201-214.
16. Natarajan A, Guo Y, Harbinski F, et al. Novel arylsulfoanilide−oxindole hybrid as an anticancer agent that inhibits translation initiation. *J Med Chem*. 2004;47(21):4979-4982.
17. Vullo D, De Luca V, Scozzafava A, et al. The extremo-α-carbonic anhydrase from the thermophilic bacterium *Sulfurihydrogenibium azorense* is highly inhibited by sulphonamides. *Bioorg. Med. Chem*. 2013;21(15):4521-4525.
18. Wilson CO, Gisvold O, Block JH. In: Block J, Beale JM, eds. *Wilson and Gisvold's Textbook of Organic Medicinal and Pharmaceutical Chemistry*. 11th ed. Philadelphia, PA: Lippincott Williams and Wilkins; 2004.
19. Levin JI, Chen JM, Du MT, et al. Anthranilate sulfonamide hydroxamate TACE inhibitors. Part 2: SAR of the acetylenic P1' group. *Bioorg. Med. Chem Lett*. 2002;12(8):1199-1202.
20. Kim DK, Lee JY, Lee N, et al. Synthesis and phosphodiesterase inhibitory activity of new sildenafil analogues containing a carboxylic acid group in the 5′-sulfonamide moiety of a phenyl ring. *Bioorg. Med. Chem*. 2001;9(11):3013-3021.
21. Hu B, Ellingboe J, Han S, et al. Novel (4-piperidin-1-yl)-phenyl sulfonamides as potent and selective human beta3 agonists. *Bioorg. Med. Chem*. 2001;9(8):2045-2059.
22. Ma T, Fuld AD, Rigas JR, et al. Phase I trial and in vitro studies combining ABT-751 with carboplatin in previously treated non-small cell lung cancer patients. *J. Antimicrob. Chemother*. 2012;58(4):321-329.
23. Roush WR, Gwaltney SL, Cheng J, Scheidt KA, McKerrowJ H, Hansell E. Vinyl sulfonate esters and vinyl sulfonamides: potent, irreversible inhibitors of cysteine proteases. *J Am Chem Soc*. 1998;120(42):10994-10995.
24. Grove SJA, Jamieson C, Maclean JKF, Morrow JA, Rankovic Z. Positive allosteric modulators of the α-amino-3-hydroxy-5-methyl-4-isoxazolepropionic acid (AMPA) receptor. *J Med Chem*. 2010;53(20):7271-7279.
25. Ward SE, Bax BD, Harries M. Challenges for and current status of research into positive modulators of AMPA receptors. *Br J Pharmacol*. 2010;160(2):181-190.
26. Phillips D, Sonnenberg J, Arai AC, et al. 5′-alkyl-benzothiadiazides: a new subgroup of AMPA receptor modulators with improved affinity. *Bioorg Med Chem*. 2002;10(5):1229-1248.
27. Braghiroli D, Puia G, Cannazza G, et al. Synthesis of 3,4-dihydro-2*H*-1,2,4-benzo- thiadiazine 1,1-dioxide derivatives as potential allosteric modulators of AMPA/kainate receptors. *J Med Chem*. 2002;45(12):2355-2357.
28. Pirotte B, Podona T, Diouf O, et al. 4H-1,2,4-pyridothiadiazine 1,1-dioxides and 2,3-dihydro-4H-1,2,4-pyridothiadiazine

1,1-dioxides chemically related to diazoxide and cyclothiazide as powerful positive allosteric modulators of (R/S)-2-amino-3-(3-hydroxy-5-methylisoxazol-4-yl) propionic acid receptors: design, synthesis, pharmacology, and structure−activity relationships. *J. Med. Chem.* 1998;41(16):2946-2959.
29. Graindorge E, Francotte P, Boverie S, Tullio P, Pirotte B. New trends in the development of positive allosteric modulators of AMPA receptors. *Curr MedChem.* 2004;4(2):95-103.
30. Hashimoto K, Okamura N, Shimizu E, Iyo M. Glutamate hypothesis of schizophrenia and approach for possible therapeutic drugs. *Curr Med Chem.* 2004;4(2):147-154.
31. Black MD. Therapeutic potential of positive AMPA modulators and their relationship to AMPA receptor subunits. A review of preclinical data. *Psychopharmacology.* 2005;179(1):154-163.
32. Francotte P, de Tullio P, Goffin E, et al. Design, synthesis, and pharmacology of novel 7-substituted 3,4-dihydro-2H-1,2,4-benzothiadiazine 1,1-dioxides as positive allosteric modulators of AMPA receptors. *Eur. J. Med. Chem.* 2007;50(13):3153-3157.
33. Dintilhac G, Arslan D, Dilly S, et al. New substituted aryl esters and aryl amides of 3,4-dihydro-2H-1,2,4-benzothiadiazine 1,1-dioxides as positive allosteric modulators of AMPA receptors. *Med. Chem. Commun.* 2011;2(6):509.
34. Rankin GO. Trichlormethiazide. *xPharm: The Comprehensive Pharmacology*; Netherland: Elsevier; 2008:1-6.
35. Trichlormethiazide. *Reactions Weekly.* 1990;(292):8. http://dx.doi.org/10.2165/00128415-199002920-00036
36. Karadsheh F, Weir MR. Thiazide and thiazide-like diuretics: an opportunity to reduce blood pressure in patients with advanced kidney disease. *Curr Hypertens Rep.* 2012;14(5):416-420.
37. Uzu T, Harada T, Namba T, Yamamoto R, et al. Thiazide diuretics enhance nocturnal blood pressure fall and reduce proteinuria in immunoglobulin A nephropathy treated with angiotensin II modulators. *J. Hypertens.* 2005;23(4):861-865.
38. Kahonen M, Mäkynen H, Arvola P, Wuorela H, Pörsti I. Arterial function after trichlormethiazide therapy in spontaneously hypertensive rats. *J. Pharmacol. Exp.* 1995;272(3):1223-1230.
39. Mouhayar E, Salahudeen A. Hypertension in cancer patients. *Tex Heart Inst J.* 2011;38(3):263.
40. Heo DN, Yang DH, Moon HJ, Lee JB, et al. Gold nanoparticles surface-functionalized with paclitaxel drug and biotin receptor as theranostic agents for cancer therapy. *Biomaterials.* 2012;33(3):856-866.
41. Popovtzer A, Mizrachi A, Motiei M, Bragilovski D, et al. Actively targeted gold nanoparticles as novel radiosensitizer agents: an in vivo head and neck cancer model. *Nanoscale.* 2016;8(5):2678-2685.
42. Wang H, Thorling CA, Liang X, Bridle KR, et al. Diagnostic imaging and therapeutic application of nanoparticles targeting the liver. *J. Mater. Chem. B.* 2015;3(6):939-958.
43. Bhattacharyya J, Bellucci JJ, Weitzhandler I, McDaniel JR, et al. A paclitaxel-loaded recombinant polypeptide nanoparticle outperforms Abraxane in multiple murine cancer models. *Nat Commun.* 2015;6(1):1-12.
44. Rossi A, Donati S, Fontana L, Porcaro F, et al. Negatively charged gold nanoparticles as a dexamethasone carrier: stability in biological media and bioactivity assessment in vitro. *RSC Adv.* 2016;6(101):99016-99022.
45. Wang Z, Sun J, Qiu Y, Li W, et al. Specific photothermal therapy to the tumors with high EphB4 receptor expression. *Biomaterials.* 2015;68:32-41.
46. Klots TD, Collier WB. Vibrational assignment and analysis for 2,3-dihydrofuran and 2,5-dihydrofuran. *Spectrochim Acta.* 1994;50(10):1725-1748.
47. Bondoc E, Laane J. Far-infrared rotational–vibrational spectra of the ring-puckering vibration of 2,5-dihydrofuran. *J Mol Struct.* 1998;470(1-2):237-240.
48. Fortunato B. The vibrational spectrum and assignment of 2, 5-dihydrofuran. *Gazz Chim Ital.* 1976;106:799.
49. Takawaga K, Hildebrandt RL. Masthead. *J. Am Chem Soc.* 1984;106(20):0002-7863.
50. Ibrahim AA, Adam FA, Allam AM. Study of charge transfer complexes of chlorothiazide. *Energy Environ.* 2021;2(1):75-90.
51. Pringouri K. New derivatives of 1,2,4-benzothiadiazines and their coordination chemistry. *Electron Libr.* 2018;75:60.
52. Li C, Yang Y, Ma C, Liu Y. Effect of amino group on the excited-state intramolecular proton transfer (ESIPT) mechanisms of 2-(2′-hydroxyphenyl)benzoxazole and its amino derivatives. *RSC Advances.* 2016;6:(6):5134-5140. http://dx.doi.org/10.1039/c5ra23261a
53. Shyni V, Leenaraj DR, Lynnette J, Sajan D. Investigations of Dianhydro-D-glucitol adsorbed on AuNPs surface: in silico and in vitro approach based on anticancer activity studies against A549 lung cancer cell lines. *J Mol Recognit.* 2021;34(9):1099-1352.
54. Bauernschmitt R, Ahlrichs R. Treatment of electronic excitations within the adiabatic approximation of time dependent density functional theory. *Chem Phys Lett.* 1996;256(25):454-464.
55. Frisch MJ, Trucks GW, Schlegel HB, et al. *Gaussian09, Rev. A.02.* Wallingford, CT: Gaussian. Inc; 2009.
56. Beegum S, Mary YS, Mary YS, Thomas R, et al. Exploring the detailed spectroscopic characteristics, chemical and biological activity of two cyanopyrazine-2-carboxamide derivatives using experimental and theoretical tools. *Spectrochim Acta A Mol Biomol Spectrosc.* 2020;224(12):117414.
57. Becke AD. Density-functional thermochemistry. III. The role of exact exchange. *J Chem Phys.* 1993;98(7):5648-5652.
58. Lee C, Yang W, Parr RG. Development of the Colle-Salvetti correlation-energy formula into a functional of the electron density. *Phys Rev B.* 1998;37(2):785-789.
59. Yang Y, Weaver MN, Merz KM. Assessment of the "6-31+G** + LANL2DZ" mixed basis set coupled with density functional theory methods and the effective core potential: prediction of heats of formation and ionization potentials for first-row-transition-metal complexes. *J Phys Chem A.* 2009;113(36):9843-9851.
60. Hay PJ, Wadt WR. Ab initio effective core potentials for molecular calculations. Potentials for the transition metal atoms Sc to Hg. *J Chem Phys.* 1985;82(4):270-283.
61. Wadt WR, Hay PJ. Ab initio effective core potentials for molecular calculations. Potentials for main group elements Na to Bi. *J Chem Phys.* 1985;82(6):284-298.
62. Hay PJ, Wadt WR. Ab initio effective core potentials for molecular calculations. Potentials for K to Au including the outermost core orbitals. *J Chem Phys.* 1985;82(2):299-310.
63. Dennington R II, Keith T, Eppinnett K, et al. Gauss View, Version 3.0, Semichem, Inc., Shawnee Mission, KS; 2000.
64. Hanwell MD, Curtis DE, Lonie DC, Vandermeersch T, Zurek E, Hutchison GR. Avogadro: an advanced semantic chemical editor, visualization, and analysis platform. *J. Cheminform.* 2012;4(1):17.
65. Jamroz MH. Vibrational energy distribution analysis (VEDA): scopes and limitations. *Spectrochim Acta, Part A.* 2013;114(63):220-230.
66. Keresztury G. Raman spectroscopy: theory. In: Chalmers JM, Griffiths PR, eds. *Handbook of Vibrational Spectroscopy.* Vol 1. Chichester, England: John Wiley & Sons; 2001:71-87.
67. Scott AP, Radom L. Harmonic vibrational frequencies: an evaluation of Hartree−Fock, Møller−Plesset, quadratic configuration interaction, density functional theory, and semiempirical scale factors. *J Phys Chem.* 1996;100(20):16502-16513.
68. Foresman JB, Frisch A. *Exploring Chemistry with Electronic Structure Methods.* 2nd ed. Pittsburgh, PA: Gaussian Inc.; 1996.

69. Fernandes P, Leech CK, Johnston A, et al. (S)-Trichlormethiazide. *Acta Crystallogr Sect E*. 2007;63(9):o3685.
70. Reed AE, Weinstock RB, Weinhold F. Natural population analysis. *J Chem Phys*. 1985;83(2):735-746.
71. Bhatt R, Bhaumik I, Ganesamoorthy S, et al. Urbach tail and bandgap analysis in near stoichiometric $LiNbO_3$ crystals. *Phys Status Solidi Rapid Res Lett*. 2012;209(1):176-180.
72. Yadav LDS. *Organic Spectroscopy*. Netherlands: Springer; 2005.
73. O'boyle NM, Tenderholt AL, Langner KM. A library for package-independent computational chemistry algorithms. *J. Comput. Chem*. 2008;29(5):839-845.
74. Bendikov M, Wudl F, Perepichka DF. Tetrathiafulvalenes, oligoacenenes, and their buckminsterfullerene derivatives: the brick and mortar of organic electronics. *Chem Rev*. 2005;36(6):8.
75. Kuruvilla TK, Prasana JC, Muthu S, George J. Vibrational spectroscopic (FT-IR, FT-Raman) and quantum mechanical study of 4-(2-chlorophenyl)-2-ethyl-9-methyl-6H-thieno[3,2-f] [1,2,4] triazolo[4,3-a][1,4] diazepine. *J Mol Struct*. 2018;1157(1):519-529.
76. Mary YS, Miniyar PB, Mary YS, Resmi KS, et al. Synthesis and spectroscopic study of three new oxadiazole derivatives with detailed computational evaluation of their reactivity and pharmaceutical potential. *J Mol Struct*. 2018;1173(2):469-480.
77. Premkumar R, Hussain S, Mathavan T, Anitha K, Benial AMF. Surface-enhanced Raman scattering and quantum chemical studies of 2-trifluoroacetylpyrrole chemisorbed on colloidal silver and gold nanoparticles: a comparative study. *J Mol Liq*. 2019;290:111209.
78. Mary YS, Mary YS, Armaković S, Armaković SJ, et al. Stability and reactivity study of bio-molecules brucine and colchicine towards electrophile and nucleophile attacks: insight from DFT and MD simulations. *J Mol Liq*. 2021;335(1):116192.
79. Sailaja RP, Kalva S, Yerramilli A, Mamidi S. Free radicals and tissue damage: role of antioxidants. *Free Radic Res*. 2011;1(4):2-7.
80. Colthup NB, Daly LH, Wiberley SE. *Introduction to Infrared and Raman Spectroscopy*. New York: Academic Press; 1990.
81. Nagabalasubramanian PB, Periandy S, Mohan S, Govindarajan M. FTIR and FT Raman spectra, vibrational assignments, ab initio, DFT and normal coordinate analysis of alpha, alpha dichlorotoluene. *Spectrochim. Acta, Part A*. 2009;73(2):277-280.
82. Balachandran V, Lalitha S, Rajeswari S. Rotational isomers, density functional theory, vibrational spectroscopic studies, thermodynamic functions, NBO and HOMO-LUMO analyses of 2,6-Bis(chloromethyl) pyridine. *Spectrochim Acta Part A*. 2012;97(12):1023-1032.
83. Mooney EF. The infra-red spectra of chloro- and bromobenzene derivatives—II. Nitrobenzenes. *Spectrochim Acta*. 1964;20(6):1021-1032.
84. Mooney EF. The infrared spectra of chloro- and bromobenzene derivatives-I. *Spectrochim Acta*. 1963;19(6):877-887.
85. Coates J. *Interpretation of Infrared Spectra: a Practical Approach*. New York: John Wiley & Sons Inc.; 2000.
86. Roeges NPG. *A Guide to Complete Interpretation of Infrared Spectra of Organic Structures*. New York: John Wiley & Sons Inc; 1994.
87. Socrates G. *Infrared Characteristic Group Wavenumber*. New York: John Wiley and Sons; 1980.
88. Gao X, Davies JP, Weaver MJ. Test of surface selection rules for surface-enhanced Raman scattering: the orientation of adsorbed benzene and monosubstituted benzenes on gold. *J Phys Chem C*. 1990;94(7):6858-6864.
89. Takahashi Y, Nishida Y, Nakayama T, Asai S. Adverse effect profile of trichlormethiazide: a retrospective observational study. *Cardiovasc. Diabetol*. 2011;10(1):45.
90. Etchegoin PG, Le Ru EC. A perspective on single molecule SERS: current status and future challenges. *Phys Chem Chem Phys*. 2008;10(40):6079.
91. Benet LZ, Hosey CM, Ursu O, Oprea TI. BDDCS, the Rule of 5 and drugability. *Adv Drug Deliv Rev*. 2016;101(1):89-98.
92. RPRT. GAP Final Technical Report, 12-14-04, OSTI, 2004. info@molsoft.com.
93. McConkey BJ, Sobolev V, Edelman M. The performance of current methods in ligand-protein docking. *Curr Sci*. 2002;83(12):845-855.
94. Miller C. A., Brett T. J. *MAPK13 Complex with Inhibitor*. RCSB; 2012.
95. Morris GM, Huey R, Lindstrom W, et al. AutoDock4 and AutoDockTools4: automated docking with selective receptor flexibility. *J Comput Chem*. 2009;30(16):2785-2791.
96. Hevener KE, Zhao W, Ball DM, Babaoglu K, et al. Validation of molecular docking programs for virtual screening against dihydropteroate synthase. *J Chem Inf Model*. 2009;49(2):444-460.
97. Li L, Liao M, Chen Y, Shan B, Li M. Surface-enhanced Raman spectroscopy (SERS) nanoprobes for ratiometric detection of cancer cells. *J. Mater. Chem B*. 2019;7(5):815-822.
98. Zhang K, Liu X, Man B, et al. Label-free and stable serum analysis based on Ag-NPs/PSi surface-enhanced Raman scattering for noninvasive lung cancer detection. *Biomed Opt Express*. 2018;9(9):4345.
99. Smith R, Wright KL, Ashton L. Raman spectroscopy: an evolving technique for live cell studies. *Analyst*. 2016;141(12):3590-3600.
100. Mosmann T. Rapid colorimetric assay for cellular growth and survival: application to proliferation and cytotoxicity assays. *J Immunol Methods*. 1983;65(1-2):55-63.

SUPPORTING INFORMATION

Additional supporting information may be found in the online version of the article at the publisher's website.

How to cite this article: Shyni V, Leenaraj DR, Ittyachan R, Shyju GJ, Joseph L, Sajan D. Spectroscopic studies, quantum chemical investigations, and in silico and in vitro scrutiny of the diuretic drug trichlormethiazide adsorbed on AuNPs. *J Mol Recognit*. 2021;e2939. doi:10.1002/jmr.2939

A Review on Using Predictive Analytics to Determine the Severity of Anaphylaxis

P. U. Reesha[1(✉)] and Jisha Jose Panackal[2]

[1] Department of Computer Science, St. Joseph's College (Autonomous), Irinjalakuda, India
[2] Department of Computer Science, Sacred Heart College, Chalakudy, Thrissur, Kerala 680722, India

Abstract. Anaphylaxis is a severe, life-threatening allergic reaction that occurs suddenly after contact with an allergen. The studies about anaphylaxis are significant in identifying the severity of that reaction and planning, evaluating the new strategies that prevent this reaction. It will also help in providing a guide to the treatment of patients who have just suffered an anaphylactic reaction. Electronic Medical Records (EMR) are one of the most efficient sources for the analysis of the severity of anaphylaxis. To review a large amount of information, researchers use efficient classifiers in text classification and compare different document representations.

In addition to classical machine learning algorithms, the recent studies use a Convolutional Neural Network (CNN) to classify the datasets. This study closely examines the possibility of applying predictive analysis for determining the severity of anaphylaxis. It also mentions the scope of using Recurrent Neural Network (RNN) for validation on clinical notes and patient history. This model could be applied to improve allergy care in healthcare settings and could be assessed in other patient safety domains, potentially enabling real-time event surveillance and guidance for medical errors and system improvement.

Keywords: Anaphylaxis · Artificial intelligence · Health care · Neural networks · Predictive analysis

1 Introduction

Hospital safety event reporting systems will help for the detection of patient safety signals in health care. Safety reports contain a large amount of data, but still lacking are processes to analyse them in a manner that allows for timely feedback to health care professionals or actions to prevent similar future events. An artificial intelligence method, a hierarchical attention-based deep neural network (DNN), can automatically reads the free-text description of hospital safety reports and identifies cases describing allergic reactions.

This paper illustrates the possibility of improving allergy care in the healthcare sector, assessing the patient safety domains through predictive analysis. This paper provides a brief study of various literatures and gives some conclusions based on certain parameters.

© The Author(s), under exclusive license to Springer Nature Switzerland AG 2022
A. Abraham et al. (Eds.): SoCPaR 2021, LNNS 417, pp. 473–483, 2022.
https://doi.org/10.1007/978-3-030-96302-6_44

The rest of the paper organizes as Sect. 2 provides the basic understandings regarding the practical implications of Predictive Analysis in Health Care. Section 3 explores various studies related to the disease Anaphylaxis and disease prediction. Next, Sect. 4 illustrates the scope of several techniques to improve allergy care in healthcare settings. And Sect. 5 conclude the paper with some future research directions.

2 Predictive Analysis

Predictive analytics helps to understand possible future occurrences by analysing the past. Predictive analytics encompasses a variety of techniques like machine learning, predictive modelling and data mining and uses both historical and current statistics to predict future outcomes. There are two types of predictive models. They are Classification models, that predict class membership, and Regression models that predict a number. These models are then made up of algorithms. The algorithms perform the data mining and statistical analysis, determining trends and patterns in data.

Predictive analytics software solutions will have built in algorithms that can be used to make predictive models. The algorithms are defined as 'classifiers', identifying which set of categories data belongs to. The most widely used predictive models are: Decision trees, Regression (linear and logistic), Neural networks. Other classifiers include time series algorithms, clustering algorithms, outlier detection algorithms, Ensemble models, Factor analysis, Naive Bayes and Support vector machines. Each classifier approaches data in a different way, therefore to get the results as needed, choose the right classifiers and models.

Machine learning is a sub field of AI. Machine learning is also often referred to as predictive analytics, or predictive modelling. At its most basic, machine learning uses programmed algorithms that receive and analyse input data to predict output values within an acceptable range. As new data is fed to these algorithms, they learn and optimise their operations to improve performance, developing 'intelligence' over time. There are four types of machine learning algorithms: supervised, semi-supervised, unsupervised and reinforcement. Classification, Regression and forecasting are different types of supervised learning. Clustering and dimension reduction are the types of unsupervised learning.

Various methods have been proposed for automatically extracting useful information from hospital safety reports and diagnosing of diseases. Machine Learning and Deep Learning Methods are used for accurate diagnosis while the Rule-based methods are used for auxiliary diagnosis. This review focuses on papers, which describes Rule-Based Methods, Machine Learning (ML) Methods, and Deep Learning (DL) Methods. Machine learning methods are further categorized into Support Vector Machine Methods (SVM), Bayes Methods, and Decision Tree Methods (DT). Deep learning methods are categorized into Convolutional Neural Networks (CNN), Recurrent Neural Networks (RNN), Deep Belief Network (DBN) and Auto encoders (AE) methods [15].

3 Literature Review

Anaphylaxis is a severe, life threatening allergic reaction. It's immediate reaction like urticaria and angioedema [14]. The reaction may be mild & localized one, e.g. allergic

conjunctivitis or it may be severe generalized reaction, e.g. anaphylactic shock. Anaphylaxis is not common, but prevalence and incidence figures in general population are unavailable because it is not a reportable disease. The diagnosis must be made on the basis of clinical findings and treatment initiated with the greatest urgency because the mortality rate approaches 10% in anaphylactic shock.

Min Chen et al. [1] proposed new method as multimodal disease risk prediction (MDRP) for predicting the chronic diseases. In that machine learning algorithm such as k-nearest neighbour, naive Bayesian and decision tree algorithms and deep learning algorithm convolutional neural network used to predict the diseases risk. MDRP algorithm process the datasets into two parts as training set and testing set which is train and test the data respectively for better prediction of diseases with good accuracy. The predicting accuracy of proposed algorithm is 94.8% with the high speed of predicting the diseases. Here the difficulty is to determine window size of data and it can't handle the sequential data by using CNN.

R.Tamilarasi et al. [2] proposed a system for predicting heart diseases by the help of data mining techniques. In medical science large amount data is generated from patient clinical reports and patient symptoms. Data mining is used to handle that large amount of data with the help of classification and clustering. In their study they use various attributes and decision trees method for predicting diseases. For predicting the diseases they uses data mining algorithms like decision tree algorithm, naive bayes algorithm, neural network algorithm, k- nearest neighbor algorithm with the classification of diseases. Proposed system accuracy is 85%.The disadvantages of data mining techniques like they are lazy still remaining.

Darcy A. Davis et al. [3] proposed the method for predicting the diseases which is based on patient medical history. They propose a CARE, collaborative Assessment and Recommendation Engine which depends on the medical history of patient. They use the IDC-9-CM codes to predict the diseases risks. This method is used for predicting the chronic diseases. In that they also describe a Iterative version of CARE, as ICARE which is incorporates ensembles concepts, but those approach did not have positive capacity of prediction. CARE system can do the prediction based on the vector similarity, inverse frequency and clustering with the medical data of patients. In that IDC-9-CM is the 3-digit code, which represents the small group of similar or related diseases of patients. CARE framework is used explore the border history of diseases suggestions related to previous unconsidered concerns about the prevention. But CARE system generates prediction on only feature visits of patients based on medical history.

Feixiang Huang et al. [4] developed a system for predicting the diseases by using data mining techniques with the healthcare information. For that they apply data mining process which predicts the hypertension of patient by using the patient medical records. For that prediction data mining techniques are used such as naive Bayesian and RJ-48 classifiers. In that WEKA data mining tool is used to generate those data mining techniques. Confusion matrix is used to represent the performance of naive Bayesian algorithm. Accuracy of proposed system is 83.5%.

Abhishek Rairikar et al. [5] proposed prediction model for predicting the heart diseases with the data mining techniques. In that they use more number of patients attributes, such as gender, blood pressure, cholesterol like other some attributes for predicting the

heart diseases. In this system three different data mining classification techniques such as K-nearest neighbour, decision tree and Naive Bayes are used to analyse the datasets. K-nearest neighbour classification and regression methods are used to pattern reorganization and decision tree are used to build the good decision. The functions are only locally approximated and also in that need to determine values of parameters of previous neighbour using KNN.

Saurabh Pandey et al. [6] developed efficient way to predicting the diabetes of patient by using the bio medical signal data with the help of artificial intelligence techniques. This system gives brief overview of diagnosis of diabetes using patient medical bio signal data. In that they use the artificial intelligence approach like ANN, Fuzzy for fixing the wide variety of issues in different application of area. For the simulation result they use the algorithm which is developed by using MATLAB for detection of diabetes.

For that datasets are used with the number of input value which is selected by using regression analysis. In that they use the 768 input samples in diabetes datasets. After that gives the value of regression coefficient which shows the output dependency of every input sample that gives the prediction of diseases. The accurate representation of the statistical properties of real time data which does not possible here to predict diseases.

Dr. B.Srinivasan et al. [7] studied the data mining techniques for efficiently predicting the diseases in healthcare sectors. They introduce the data mining knowledge discovery for converting the low level data to high level data knowledge. In that they studied various data mining technique like as, Bayesian classifiers, decision tree, support vector machine and artificial neural networks for predicting diseases. They discussed about various diseases like Eye diseases, Cancer, Heart diseases, Diabetics, etc. Data mining based prediction systems reduce the cost and human effects but they are time consuming and lazy learning methods.

Parithosh Khubchandani et al. [8] proposed a system based on artificial intelligence and probabilistic model for medical prediction. In that they present the new approach suitable for medical prediction which is based on the probabilistic modelling. When the information is large and complex the system uses this approach. Knowledge based approach cannot handle the large or complex data, so probabilistic approach is used for medical prediction. The statistical approach associates a probability for each output of medical data for which Bayes theorem is used for prediction. By using this system physicians can focus on important activities of patients. Some result of this technique take more time for evaluation and some computations are complex that is effects on the other factors of prediction.

Smita.T et al. [9] developed an efficient algorithm for predicting the diseases with the help of multidimensional data. Main objectives of this system are create an easy, fast, effective approach for diseases prediction. They introduced new hybrid algorithm for diseases identification and prediction by using data mining techniques. New algorithm is diseases identification and prediction (DIP) it is combination of decision tree and association rule. They use data mining approach for extracting the information which is previously not known.

It also used for analysing the information for prediction. This research work is based on different data mining approach on the multidirectional data analysis. For that they uses the common data mining models for prediction, such as Association rule, decision tree,

clustering, classification rule and various statistical data mining tools. For DIP decision tree and Association rule which construct the Apriori principle. Apply the statistical mining techniques in cluster analysis for extracting the data. DIP predicts the diseases only on multidimensional data. The result is represented in graphical format.

Anandanadarajah Nishanth et al. [10] proposed a new method for early detection of the chronic kidney diseases by identifying the important features from the datasets. Chronic kidney diseases (CKD) are the not know those medical tests of patients are taken for the other purposes that is useful for the diseases. In this paper they use the different techniques for the detection like CSP and LDA. CPA is the Common Spatial Pattern and the LDA is the Linear Discriminant Analysis which is identifies the important attributes and detects the chronic kidney diseases. In this paper classification methods is used for the identifying the attributes of diseases. This analysis contains the albumin, haemoglobin, specific gravity, haemoglobin, with the serum like important features for early detection of kidney diseases. With the Linear Discriminant Analysis get the 98% accuracy of chronic kidney diseases.

Fatma Taher et al. [11] proposed a system for detecting the lung cancer by using artificial neural network and fuzzy clustering method. Lung cancer is the common cause of death of people among the world because its symptoms are appears at only advanced stage. There are many techniques such as x-ray, CT scan, MRI is available for diagnosis of lung cancer but they are very expensive and time consuming. These systems solve the problem effectively with the help of artificial network and fuzzy clustering. For that they use a segmentation process which detects the lung cancer early stage.

In that two segmentation techniques are used that is Hopfield Neural Network (HNN) and Fuzzy C-Mean (FCM). Hopfield Neural Network (HNN) is one of the artificial neural network, which is used for image segmentation. Those propose the segmentation process for both black and white and colour images. This algorithm contains a predefined number of inputs and gives the clusters of outputs. For input they can takes the number of image dataset of diseases and applies the both algorithm and gives the prediction on that image data. But this system is gives the result only on image datasets which requires more numbers of image datasets.

A team of researchers set out to develop a deep learning tool [13] that could identify allergic reactions in the free-text narrative of hospital patient safety reports. The findings show the potential for deep learning to perceive allergies and probably enhance affected person safety. The deep learning model was able to reduce the number of cases to review during the actual case detection from a massive data set and overcame the low sensitivity associated with using the keyword search approach.

The group made sure to expand the deep learning model so that its predictions could be interpretable to providers. After its far advanced and training, the model could detect true allergic reactions more efficiently than manual review, facilitating viable real-time applications to enhance allergy documentation and medical follow-up. After refining the deep learning model, the tool will have critical implications for allergic reaction identification and patient safety measures with the use of automated surveillance.

Isabel Segura-Bedmar and team proposed that their experiments show that the most classifiers and representations are effective (F1 above 90%). Logistic Regression, Linear SVM, Multilayer Perceptron and Random Forest achieve an F1 around 95%, however

linear methods have considerably lower training times. CNN provides slightly better performance (F1 = 95.6%) [12].

Numerous research works have been carried out for the prediction of the diseases based on the symptoms shown by an individual using machine learning algorithms. Sreevalli et al. [17] used the random forest machine-learning algorithm to predict the disease based on the symptoms. The system resulted in low time consumption and minimal cost for the prediction of diseases. The algorithm resulted in an accuracy of 84.2%.

A variety of ML techniques such as artificial neural networks (ANNs), bayesian networks (BNs), support vector machines (SVMs) and decision trees (DTs) have been widely applied in cancer research for the development of predictive models, resulting in effective and accurate decision making [18].

Karayilan et al. [19] proposed a heart disease prediction system that uses the artificial neural network back propagation algorithm. 13 clinical features were used as input for the neural network and then the neural network was trained with the back propagation algorithm to absence or presence of heart disease with an accuracy of 95%.

Various machine learning algorithms were streamlined for the effective prediction of a chronic disease outbreak by Chen et al. [20]. A new convolutional neural network-based multimodal disease risk prediction (CNN-MDRP) was structured. The algorithm reached an accuracy of around 94.8%.

Chae et al. [21] used 4 different deep learning models namely deep neural networks (DNN), long short term memory (LSTM), ordinary least squares (OLS), an autoregressive integrated moving average (ARIMA) for monitoring 80 infectious diseases in 6 groups. Of all the models used, DNN and LSTM models had a better performance. The DNN model performed better in terms of average performance and the LSTM model gave close predictions when occurrences were large.

Haq et al. [22] used a database that contained information about patients having any heart disease. They extracted features using three selection algorithms which are relief, minimum redundancy, and maximum relevance (mRMR), and least absolute shrinkage and selection operator which was cross-verified by the K-fold method. The extracted features were sent to 6 different machine learning algorithms and then it was classified based on the presence or absence of heart disease.

An effective heart disease prediction system was developed by Mohan et al. [23]. They achieved an accuracy level of 88.4% through the prediction model for heart disease with the hybrid random forest with a linear model (HRFLM).

Maniruzzaman et al. [24] classified the diabetes disease using ML algorithms. Logistic regression (LR) was used to identify the risk factors for diabetes disease. The overall accuracy of the ML-based system was 90.62%.

Khourdifi et al. [25] achieved the highest accuracy of 99.7% using the KNN model for the prediction and classification of heart diseases.

Sriram et al. [26] used the Random Forest model and achieved an accuracy of 90.26%.

The SVM model proved to have a higher accuracy of 79.13% as compared to the other methods used by Mir et al. [27].

Rinkal Keniya suggested weighted KNN model proved to have a higher accuracy of 93.5% as compared to the other methods [16].

Recurrent networks belong to the category of artificial neural networks. Unlike feed forward neural networks, the connections in nodes create a directed graph which displays a time sequence for temporal dynamic behaviour. The accurately mining of EHR records is very challenging because of various factors including incomplete prescription, free text writing, and disease variability. A RNN based long short term memory (LSTM) architecture has been proposed for predicting the risk of heart failure from EHR [28].

Deep-Diagnosis [29] was introduced by Shi et al. to address these challenges. The proposed method was constructed using RNN-based prediction diagnosis algorithm by mining pediatric EHR data. The patients' symptoms and their relationship have been identified using the proposed bidirectional Recurrent Neural Network. A pediatric dataset composed of 81476 records were used to train and test the model which achieved 80.912 of precision.

Luo [30] has been used RNN based Long-Short Term Memory (LSTM) model for classifying relations in EHRs data. The model was evaluated on relation classification challenge database i2b2/VA. The proposed model achieved f-measure of 0.61, 0.80, and 0.68 for classifying medical problem-treatment, medical problem-test, and medical problem-medical problem relations.

The challenge of adverse medical detection (ADEs) has been solved using the proposed recurrent neural network based on context attention embedding (CA-RNN) [31]. The proposed method was evaluated on 8845 cardiovascular medical records and achieved 0.929 and 0.561 of recall and precision for AME of Ischemia.

Table 1. Comparison of the methodologies discussed in literature survey

Author	Methods used	Accuracy	Objective
[1] Min Chen et al.	MDRP-KNN, Naïve Bayesian, Decision tree, CNN	94.8%	For predicting the chronic diseases
[2] R.Tamilarasi et al.	Decision tree, Naïve Bayesian, KNN	NA	Predicting heart diseases
[3] Darcy A. Davis et al.	CARE	NA	Predicting the chronic diseases
[4] Feixiang Huang et al.	WEKA-naive Bayesian and RJ-48 classifiers	83.5%	Predicts the hypertension of patient
[5] Abhishek Rairikar et al.	K-nearest neighbour, decision tree and Naive Bayes	NA	Predicting the heart diseases
[6] Saurabh Pandey et al.	ANN, Fuzzy	NA	Predicting the diabetes of patient
[7] Dr. B.Srinivasan et al.	Bayesian classifiers, decision tree, support vector machine, ANN	NA	Predicting the diseases in healthcare sectors

(*continued*)

Table 1. (*continued*)

Author	Methods used	Accuracy	Objective
[8] Parithosh Khubchandani et al.	Probabilistic model -Bayes theorem	NA	For medical prediction
[9] Smita.T et al.	Diseases identification and prediction (DIP)-Association rule, decision tree, clustering, classification rule and various statistical data mining tools	NA	Predicts the diseases only on multidimensional data
[10] Anandanadarajah Nishanth et al.	CSP and LDA	98%	Early detection of the chronic kidney diseases
[11] Fatma Taher et al.	ANN and fuzzy clustering		Detecting the lung cancer
[12] IsabelSegura-Bedmar	Logistic Regression, Linear SVM, Multilayer Perceptron and Random Forest, CNN	95.6%	
[17] Sreevalli et al.	Random forest	84.2%	Prediction of diseases
[20] Karayilan et al.	Back propagation algorithm	95%	Heart disease prediction system
[32] Chen et al.	MDRP-CNN	94.8%	Effective prediction of a chronic disease
[21] Chae et al.	DNN,LSTM,OLS,ARIMA	NA	For monitoring 80 infectious diseases in 6 groups
[22] Haq et al.	Mrmr, and least absolute shrinkage and selection operator	NA	Heart disease prediction
[23] Mohan et al.	Hybrid random forest with a linear model (HRFLM)	88.4%	Heart disease prediction system
[24] Maniruzzaman et al.	Logistic regression (LR)	90.62%	Identify the risk factors for diabetes
[25] Khourdifi et al.	KNN	99.7%	For the prediction and classification of heart diseases
[26] Sriram et al.	Random Forest model	90.26%	Heart disease prediction
[27] Mir et al.	SVM model	79.13%	Heart disease prediction
[16] Rinkal Keniya	Weighted KNN	93.5%	Heart disease prediction
[28] Jin et al.	LSTM-RNN	64.83%	Heart disease prediction
[29] Shi et al.	BiRNN	80.91%	8 Paediatric diseases
[30] Luo	LSTM-RNN	80%	Chronic kidney diseases
[31] Chu et al.	CA-RNN	96.2%	Cardiovascular

4 Results and Discussion

Different machine learning models were used to examine the prediction of disease for available input dataset. Here different ML models for the prediction are discussed. Out of that models deep learning models acquired highest accuracy. As shown in Table1 (NA-Not Available), among all the models, the highest accuracy is for the CNN and KNN models. KNN is proved to be the most accurate model as compared to the other ML algorithms.

A lot of work has been done for automatic extraction of useful information from electronic health records, clinical notes and discharge summaries. The physician uses features extracted information as an input for the automatic diagnosis of disease. Knowledge bases initially performed this extraction. In the present era, various rule-based learning, machine learning, and deep learning concepts are used for the extraction and diagnosis of diseases. There are several challenges associated with this automatic extraction including missing values, incomplete information, and data abundance. Recent research for the automatic diagnosis of various diseases from electronic medical records is reviewed here. Rule-Based Methods, Machine Learning Methods, and Deep Learning Methods were discussed here. These categories are further divided into sub-categories based on the proposed algorithm.

5 Conclusion and Future Research Directions

From the review done, concluding that disease prediction was done with models such as machine learning, Data Mining using various algorithms like logistic regression, decision tree and so on. Previously existing techniques do the prediction on diseases but cannot predict the subtypes of diseases. Those systems also can't find the diseases which are caused by occurrences of any previous diseases. That fails to do predictions of all possible conditions of patients.

Existing system predicts the particular diseases with the help of data mining techniques which are ambiguous. In the existing systems the datasets size is small, for the patients and diseases are present some specific conditions and the characteristics are selected from experience. So such a pre-selected characteristics are not satisfying the changes in the diseases and its influence factors. Those systems have a lower accuracy of diseases predictions. So by enhancing deep learning network models, the prediction of severity of anaphylaxis may be more accurate since it also considers previous data and produces more accurate results by refining previous data and current data.

References

1. Chen, M., Hwang, K., Hao, Y., Fellow, Wang, L., Wang, L.: By using machine learning algorithm predicting the diseases with big data technology from the healthcare communities. IEEE (2016)
2. Tamilarasi, R., Porkodi, R.: A study and analysis of disease prediction techniques in data mining for healthcare. Int. J. Emerg. Res. Manag. Technol. (IJERMT) **4**(3) (2015). ISSN 2278-9359

3. Davis, D.A., Blumm, N., Chawla, N.V.: Predicting individual disease risk based on medical history. ACM (2008)
4. Huang, F., Chan, C.-C., Wang, S.: Predicting disease by using data mining based on healthcare information system. In: IEEE International Conference on Granular Computing (2012)
5. Rairikar, A., Sabale, V., Kulkarni, V., Kale, H.: Heart disease prediction using data mining techniques. In: International Conference on Intelligent Computing and Control (I2C2) (2017)
6. Pandey, S., Tripathi, M.M.: Diagnosis of diabetes using artificial intelligence techniques by using bio medical signal data. Int. J. Res. Dev. Appl. Sci. Eng. (IJRDASE), ISSN 2454-6844 (2017)
7. Srinivasan, B., Pavya, K.: A study for prediction in healthcare sector using data mining techniques. Int. Res. J. Eng. Technol. (IRJET) **03**(03) (2016)
8. Khubchandani, P., Lala, S., Jha, K., Saindane, P., Bijani, R.: Medical diseases prediction using artificial intelligence techniques. Int. J. Eng. Sci. Comput. (IJESC) (2017)
9. Smitha, T., Sundaram, V.: An efficient algorithm for disease prediction with multi dimensional data. Int. J. Comput. Appl. (0975-8887) **63**(9), 1–4 (2013)
10. Nishanth, A., Thiruvaran, T.: Identify the important attributes of chronic kidney diseases for early detection. IEEE (2017)
11. Taher, F., Al-Ahmad, H., Werghi, N., Sammouda, R.: Lung cancer detection by using artificial neural network and fuzzy clustering methods. IEEE (2011)
12. Segura-Bedmar, I., Colón-Ruíz, C., Tejedor-Alonso, M., Moro-Moro, M.: Predicting of anaphylaxis in big data EMR by exploring machine learning approaches. J. Biomed. Inf. **87**, 50–59 (2018)
13. Yang, J., et al.: Development and validation of a deep learning model for detection of allergic reactions using safety event reports across hospitals. JAMA Netw. Open **3**(11), e2022836 (2020)
14. Mahmood, A.H.: Anaphylaxis, Researchgate, June 2021
15. Cardona, V., et al.: World allergy organization anaphylaxis guidance 2020. World Allergy Organ. J. **13**(10), 100472 (2020). https://doi.org/10.1016/j.waojou.2020.100472
16. Keniya, R., et al.: Disease prediction from various symptoms using machine learning. SSRN (2020)
17. Sreevalli, R.D.H.D.P., Asia, K.P.M.: Prediction of diseases using random forest classification algorithm
18. Langbehn, D.R., Brinkman, R.R., Falush, D., Paulsen, J.S., Hayden, M.: An international Huntington's disease collaborative group, a new model for prediction of the age of onset and penetrance for huntington's disease based on cag length. Clin. Genet. **65**(4), 267 (2004)
19. Kourou, K., Exarchos, T.P., Exarchos, K.P., Karamouzis, M.V., Fotiadis, D.I.: Machine learning applications in cancer prognosis and prediction. Comput. Struct. Biotechnol. J. **13**, 8 (2015)
20. Karayılan, T., Kiliç, Ö.: International Conference on Computer Science and Engineering (UBMK), pp. 719–723. IEEE (2017)
21. Chae, S., Kwon, S., Lee, D.: Predicting infectious disease using deep learning and big data. Int. J. Environ. Res. Public Health **15**(8), 1596 (2018)
22. Haq, A., Li, J., Memon, M., Nazir, S., Sun, R.: A hybrid intelligent system framework for the prediction of heart disease using machine learning algorithms. Mobile Inf. Syst. **2018**, 1–21 (2018). https://doi.org/10.1155/2018/3860146
23. Mohan, S., Thirumalai, C., Srivastava, G.: Effective heart disease prediction using hybrid machine learning techniques. IEEE Access **7**, 81542 (2019)
24. Maniruzzaman, M., Rahman, M.J., Ahammed, B., Abedin, M.M.: Classification and prediction of diabetes disease using machine learning paradigm. Health Inf. Sci. Syst. **8**(1), 1–14 (2020). https://doi.org/10.1007/s13755-019-0095-z

25. Khourdifi, Y., Bahaj, M.: Heart disease prediction and classification using machine learning algorithms optimized by particle swarm optimization and ant colony optimization. Int. J. Intell. Eng. Syst. **12**(1), 242 (2019)
26. Sriram, T.V., Rao, M.V., Narayana, G.S., Kaladhar, D., Vital, T.P.R.: Intelligent Parkinson disease prediction using machine learning algorithms. Int. J. Eng. Innov. Technol. (IJEIT) **3**(3), 1568 (2013)
27. Mir, A., Dhage, S.N.: 2018 Fourth International Conference on Computing Communication Control and Automation (ICCUBEA), pp. 1–6. IEEE (2018)
28. Jin, B., Che, C., Liu, Z., Zhang, S., Yin, X., Wei, X.: 'Predicting the risk of heart failure with EHR sequential data modeling.' IEEE Access **6**, 9256–9261 (2018)
29. Shi, J., Fan, X., Wu, J., Chen, J., Chen, W.: DeepDiagnosis: DNN-based diagnosis prediction from pediatric big healthcare data. In: Proceedings of 6th International Conference on Advances Cloud Big Data (CBD), pp. 287–292 (2018)
30. Luo, Y.: Recurrent neural networks for classifying relations in clinical notes. J. Biomed. Informat. **72**, 85–95 (2017)
31. Chu, J., Dong, W., He, K., Duan, H., Huang, Z.: Using neural attention networks to detect adverse medical events from electronic health records. J. Biomed. Informat. **87**, 118–130 (2018)
32. Chen, M., Hao, Y., Hwang, K., Wang, L., Wang, L.: Disease prediction by machine learning over big data from healthcare communities. IEEE Access **5**, 8869 (2017)

Colloids and Surfaces A: Physicochemical and Engineering Aspects 646 (2022) 128255

Contents lists available at ScienceDirect

Colloids and Surfaces A: Physicochemical and Engineering Aspects

journal homepage: www.elsevier.com/locate/colsurfa

Density functional theoretical study, spectroscopic characterization and molecular docking of the diuretic drug, spironolactone, adsorbed on AuNPs surface and in-vitro studies based on anticancer activity studies against A549 lung cancer cell line

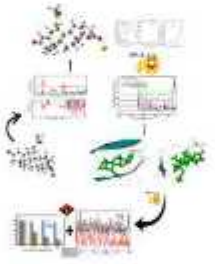
V. Shyni [a], D.R. Leenaraj [b], Reena Ittyachan [c], Rejeena V. Rajan [d], G.J. Shyju [e], Lynnette Joseph [a,*], D. Sajan [a]

[a] Centre for Advanced Functional Materials, Department of Physics, Bishop Moore College, Mavelikara, Kerala 690110, India
[b] Department of Physics, Mar Ivanios College, Thiruvananthapuram 695015, Kerala, India
[c] Department of Physics, Sacred Heart College, Chalakudy, Kerala, 680307, India
[d] St. Cyril's College, Department of Physics, Vadakkedathukavu P.O., Kilivayal, Adoor, Pathanamthitta 691529, India
[e] Department of Physics, Christian College, Kattakada, 695571 Thiruvananthapuram, Kerala, India

HIGHLIGHTS

- DFT calculations have been performed on the diuretic drug Spironolactone and Spironolactone adsorbed on gold nanoparticles.
- The IR, Raman, UV-Vis and SERS spectra of both the molecules were recorded to support the theoretical calculations.
- NBO, NHO, natural population analyses and HOMO–LUMO energy gap reveals the charge transfer interactions within the molecules.
- The in-silico and in-in-vitro results indicate that molecules interact with carcinoma type proteins.

GRAPHICAL ABSTRACT



ARTICLE INFO

Keywords:
DFT
SERS
MTT assay
Molecular docking

ABSTRACT

In this study, the geometry, intramolecular charge transfer interactions, and harmonic vibrational frequencies of the diuretic drug, Spironolactone (SPL) and SPL adsorbed on gold nanoparticle (SPLA molecule) were investigated with the help of density functional theory method. Both molecules were found to be stabilized by intramolecular hydrogen bonds C_7-H_{37}. O_{27} and C_{16}-H_{47}. O_2, as well as intramolecular charge transfer interactions. These interactions were quantitatively confirmed using natural localized molecular orbitals (NLMOs) analysis. The frontier molecular orbital analysis provided a comparative picture of the reactivity, showing a low value of the energy gap, revealing electron transport in the molecule. The most reactive sites of the molecules were predicted by the molecular electrostatic potential map analysis together with the study of local and global reactivity descriptors. FT-IR and Raman spectral analysis confirmed the existence of significant hydrogen bonding, and charge delocalization in the molecules. Molecular docking performed for the biological activity

* Corresponding author.
E-mail addresses: drlynnette@bishopmoorecollege.org (L. Joseph), drsajanbmc@gmail.com (D. Sajan).

https://doi.org/10.1016/j.colsurfa.2022.128255
Received 18 September 2021; Received in revised form 1 December 2021; Accepted 3 January 2022
Available online 6 January 2022
0927-7757/© 2022 Elsevier B.V. All rights reserved.

screening of both molecules along with the SERS and MTT assay (in vitro) analysis confirmed their cancer activity. All the comparative results lead to the conclusion that SPLA possess enhanced therapeutic activity than SPL and hence can be used for effective label-free monitoring of cells in-vitro.

1. Introduction

Spironolactone (SPL) is a synthetic steroidal diuretic used to treat edema, cirrhosis of the liver, hypokalemia and hypertension [1,2]. It has been reported that diuretics [3], can be effectively used to overcome the high-risk factor of blood pressure fluctuations involved in cancer treatment. SPL exhibits itself as a combination of a human xenobiotic metabolite cyclic ketone cyclohexanone ring [4], a solubility enhanced unit-decahydro derivative of naphthalene decahydro naphthalene ring [5], a volatile organic unit-cycloalkane cyclopentane ring [6], a promising bioactive dihydrofuran ring [7], an S-methyl ethanethioate and two methyl groups. These combinations are found to enrich its biological properties and physicochemical activities due to various reasons [8]. Cyclopentane ring and dihydrofuran ring have been reported to act as effective core scaffolds in highly successful medicinal chemistry research [9]. In addition, solubility properties and dissolution rate of a solid drug are also important parameters for determining oral bioavailability [10]. SPL exhibit low aqueous solubility along with a slow dissolution rate, resulting in variable and incomplete oral bioavailability [11,12].

Previous studies reveal that the biocompatibility of gold nanoparticles (AuNPs) makes them potential biomarkers in cancer therapy with fewer side effects [7–9]. In the present work, we perform a combined density functional theory based and experimental approach to study of the molecular system of SPL and SPLA (SPL adsorbed on AuNPs), to bring out the underlying charge transfer, electronic and vibrational properties and thereby to throw light into the potential of SPLA in effective drug delivery. Literature review reveals that SPL or SPLA have not been subjected to spectroscopic or quantum chemical investigations so far. It is well established that experimental studies on the vibrational spectra of molecular systems aided with quantum chemical calculations, provide in-depth knowledge of the molecular architecture and bioactivity relationship [13,14]. Prediction of potential reactive sites of molecular systems and its overall stability, can be done using the DFT calculated global and local reactivity descriptors. Molecular docking is effectively used to predict the binding orientation of ligands to protein molecules, thereby predicting the affinity and activity of the former molecule. MTT assay testing [15] and intracellular Surface Enhanced Raman Scattering (SERS) [16] studies provide sensitive and reliable indication of cellular metabolic functions, with drug molecules in cells. Taking into consideration of these facts, in the present investigation, the vibrational and electronic properties of SPL and its relationship between its structure and biological activity is performed based on Density Functional Theory (DFT) along with FT-IR, Raman, Surface Enhanced Raman Scattering (SERS) and UV-Vis spectroscopic techniques. Evaluation of the viability of cells in culture for SPL and SPLA is performed using MTT assay and intra cellular SERS in human lung cancer A549 cell line and the molecular docking study of SPL and SPLA has been done as a scaffold for in-vitro learning. Research extends to frontier molecular orbital (FMOs) analysis to quantify the molecular reactivity of SPL and SPLA through reactivity descriptors, as well as the application of SERS technology for the analysis of cancer cells.

2. Materials and methods

2.1. Preparation of gold colloids, Cell Culture and Protocol used for MTT assay

Spironolactone (98%) (SPL), Gold (III) chloride trihydrate (99.99%), and trisodium citrate (99%) were purchased from Sigma–Aldrich and was used without further refinement. Colloidal gold nanoparticles (AuNPs) were prepared by modifying the reported method of citrate thermal reduction. 1 mLof 1 wt% Gold (III) chloride aqueous solution was added to 1.5 mL of 38.8 mM sodium citrate aqueous solution drop-by-drop into 90 mL boiling water under stirring. After 10 min the solution turned ruby red, after which it was stirred and cooled in ambient temperature still under stirring [17]. MTT assay and intra cellular SERS study were done with the human lung cancer cell lines A549, following the protocol detailed in our earlier report [18].

2.1.1. Spectroscopic measurements

The FT-IR spectrum of SPL and SPLA were recorded with a Perkin-Elmer Spectrum One FT-IR spectrometer using the KBr pellet technique in the wavenumber range of 4000–400 cm^{-1} with an optical resolution of 2 cm^{-1}. A BRUKER RFS 27: A Standalone Fourier Transform-Raman (FT-Raman) spectrometer was used to record the Raman spectrum at room temperature with a spectral resolution of 2 cm^{-1} in the range 3500–50 cm^{-1}. The absorption spectra of SPL and SPLA were recorded using Shimadzu 2600, UV–Vis spectrophotometer in the region 200–800 nm in DMSO solvent. High Resolution Transmission electron microscopy (Tecnai T30 G2 S-Twin, FEI Company) was employed for particle size measurements. A drop of gold colloidal solution was placed on carbon coated copper grid and was dried under IR lamp to prepare the sample for TEM measurement.

For SERS recording, SPL was incubated with citrate stabilized spherical AuNPs (40 nm) as SERS substrate. The spectra were measured by a WI-Tec Raman microscope (WI-Tec, Inc., Germany, alpha 300R) in the range 200 – 3000 cm^{-1} with 1 cm^{-1} resolution and an integration time of 0.5 s and 20 accumulations. A 633 nm wavelength laser with 7 mW power was used to excite the sample. SERS mapping was performed using two cells by confocal Raman microscopy using 0.5 s integration time, 150 × 150 as points per line, and 50 × 50 μm mapping area along the X and Y directions. A SPEX Fluorolog F112X spectrofluorimeter was used to measure the excitation and emission spectrum. The MTT assay was documented at 490 nm on a TECAN spectrophotometer with a 655 nm reference reading in Dimethyl Sulfoxide solvent.

2.2. Computational details

The structural optimization, and the vibrational spectral and electronic properties studies of SPLA and SPLA were done by Gaussian '09 program software [19] using B3LYP functional 20, 21] with LANL2DZ (where LANL stands for Los Alamos National Laboratory) basis set. The calculations using LANL2DZ pseudopotentials accurately define the attachment of noble metal atoms in single particle or cluster, to molecular systems [20–22]. Berny's optimization algorithm was employed to fully optimize the molecular geometries of SPL and SPLA, using redundant internal coordinates. Both optimized structures were confirmed to be minimum energy conformations and were determined by minimizing the energy with respect to all geometrical parameters without imposing molecular symmetry constraints [18]. Natural localized molecular orbitals (NLMOs) analysis rigorously assesses the potential for the common hole/electron NPA patterns in vacant/occupied NBOs or other localized orbits. This has been analyzed in the hierarchy order of atomic orbital analysis (AO), natural hybrid analysis (NHO), natural atomic orbital analysis (NAO), natural population analysis (NPA), and natural bond orbital analysis (NBO). NBO 3.1 package [23] implemented in Gaussian 09 version has been utilized for natural localized molecular orbitals analysis. In order to correct the overestimations arising from the basis set truncation effect, neglect of

electron correlations and anharmonicity characters of the vibrational modes, the calculated wavenumbers were scaled using a single scaling factor of 0.970 [24]. Electronic Absorption spectra of SPL and SPLA molecule were calculated using TD-DFT using the B3LYP/6–31 + +G (d, p) along with the LANL2DZ basis set in the presence of solvent DMSO by placing the solute in a cavity via a set of overlapping spheres within the solvent reaction field (Polarizable Continuum Model) [25]. The time-dependent density functional theory (TD-DFT) calculations were performed through which the accurate description of electronically excited states is possible [26]. The global reactivity descriptors [18] associated with reactivity and stability of molecules, i.e. the ionization potential (I), electron affinity (A), chemical hardness (η), softness (S), electronegativity (χ), chemical potential (μ) and the electrophilicity index (ω) were obtained from the Frontier Molecular Orbital (FMO) energy calculations as follows: $I = -E_{HOMO}$, $A = -E_{LUMO}$, $\eta = ((I-A))/2$, $S = 1/\eta$, $\mu = (-(I+A))/2$, $\chi = ((I+A))/2$, $\omega = \mu^2/2\eta$, where E_{HOMO} and E_{LUMO} refers to the energies of the Highest Occupied Molecular Orbital (HOMO) and Lowest Unoccupied Molecular Orbital (LUMO) respectively. Potential Energy Distribution (PED) analysis was employed using the VEDA 4 program [27] for the detailed assignment of the various vibrational modes and the observed and simulated spectra were compared.

Molecular docking has become a vital part of drug discovery in *in-silico* biological activity screening. Owing to its relatively low cost and ease of use, its growing popularity is accelerating among academic communities.[28] In the present study, molecular modelling using Auto Dock tools [29] was used. The SPL and SPLA ligand file was generated by converting the optimized molecular structure into the PDB file. Proteins for docking were selected from the protein database (PDB) for SPL and SPLA molecules to detect protein receptor active sites. YEATS2 YEATS bound to H3K27ac peptide [30] receptor (PDB ID: 5XNV) was used for docking both the molecules. The three-dimensional (3D) coordinates of the protein file were downloaded from the Research Collaborator for Structural Bioinformatics (RCSB) protein data bank, with a resolution of 2.696 Å. The steps involved in protein preparation included removal of all water molecules, addition of valence hydrogen atoms and Coulomb charges and removal of previously docked inhibitor. Affinity grids centred on the active site were created using Auto Grid 4.2 program with 126 × 126 × 126 grid size and with a spacing of 0.42 Å. The rigid protein and flexible ligand docking scheme was employed. The Lamarckian Genetic Algorithm (LGA) was used for molecular docking calculations in the Auto Dock 4.0 software program interfaced with the MGL Tools-1.5.4 package. Trials of 100 dockings, energy evaluations of 25000000, population size of 200, a mutation rate of 0.02, a cross-over rate of 0.8, and an elitism value of 1, was the protocol followed. The binding free energy predicted by docking conformations were sorted to evaluate the docking results.

3. Results and discussion

3.1. Structural analysis

The optimized stable conformers of SPL and SPLA molecules are dispensed in Table 1. The stable structure of both SPL and SPLA molecules and the atom numbering scheme used are shown in Fig. 1. The comparison of geometrical parameters of theoretical (gas phase) and reported (solid phase) crystallographic data (CCDC No: 1103845) [31] using calculations of the linear regression coefficient (R^2) is graphically represented in Fig. 2. The reliability of theoretical calculation is evident from the R^2 value except for slight discrepancies in aromatic C-H bond lengths, which is due to the fact that the gas phase geometry optimization done on a single molecule account little for the intermolecular effects in the real system.

(a) Optimized geometry of SPL molecule

The fused rings (cyclohexanone, decahydronaphthalene and cyclopentane) in SPL molecule are slightly distorted from the steroid conformation, as evidenced by the dihedral angle C_3-C_4-C_5-C_6 (173.10 for SPL and 171.98 from crystallographic data) and C_2-C_1-C_{10}-C_9 (165.27 for SPL, 160.50 from crystallographic data) (Table 1). When we examine each ring separately, we see that each of them are in a different conformation. In the case of the cyclohexanone ring, it is in the sofa conformation. The value of the angle of endocyclic torsion (C_1-C_2-C_3-C_4 and C_4-C_5-C_{10}-C_1) supports this result. Taking into account of cyclohexane ring, it exhibits a chair conformation, while the cyclopentane ring exhibits envelope conformation as seen from Table 1. The S-methyl ethanethioate, attached to the carbon atom in the decahydronaphthalene ring, has attained Z-confirmation with the torsional angle 174.37° (C_7-S_{29}-C_{23}-C_{24}) together with C_7-$H_{\cdots}O_{27}$ intramolecular hydrogen bonding. Perpendicularity of S-methyl ethanethioate with decahydronaphthalene ring is confirmed by the bond angle C_8-C_7-S_{29} and C_6-C_7-S_{29} which are 109.39° and 112.49°, respectively. The Z-confirmation is confirmed by the bond angles C_7-S_{29}-C_{23}, C_{24}-C_{23}-S_{29} and C_7-S_{29}-C_{23} which are 99.86°, 113.12° and 99.86°, respectively.

(b) *Optimized geometry of SPLA molecule*

The SPLA molecule has more or less the same conformation as SPL molecule with a minor variation of bond angle and torsional angle, due to O_{25}-Au_{62} bond. The lengthening of the C_{22} =O_{25} bond shreds of evidence of back donation of electrons from Au *d* orbital to the π * orbital of C_{22} =O_{25}. The ring angles at the point of substitution of the benzene ring are smaller than 120° and slightly larger than 120° at the ortho and meta positions, which results in a slight distortion in the symmetry of the ring. This reveals the adsorption of SPL on the AuNP surface through the oxygen atom in the dihydrofuran due to synergic bonding, $O_{25}Au_{62}$. The interesting structural feature of both SPL and SPLA molecules is that an

Table 1
Optimized geometrical parameters of SPL and SPLA along with corresponding experimental data obtained by XRD.

Bond length (Å)				Bond Angle (°)				Torsional Angle (°)			
Parameter	DFT		[a] Exp.	Parameter	DFT		[a] Exp.		DFT		[a] Exp.
	SPL	SPLA			SPL	SPLA			SPL	SPLA	
C_{22}-O_{25}	1.23	1.24	1.19	C_8-C_7-S_{29}	112.49	112.49	111.05	C_1-C_2-C_3-C_4	-32.09	-38.43	37.19
C_{23} =O_{27}	1.24	1.24	1.18	C_6-C_7-S_{29}	109.39	109.39	110.67	C_1-C_{10}-C_9-C_4	-17.52	-38.43	37.19
C_7-H_{37}	1.09	1.09	0.85	C_7-S_{29}-C_{23}	99.86	99.76	100.21	C_2-C_1-C_{10}-C_9	165.27	165.27	160.50
C_{24}-H_{39}	1.10	1.10	0.85	C_{24}-C_{23}-S_{29}	113.12	113.02	112.64	C_7-S_{29}-C_{23}-O_{27}	-4.45	-5.07	-4.67
C_{22}-O_{26}	1.39	1.36	1.30	C_7-$H_{\cdots}O_{27}$	121.75	121.75	123.09	S_{29}-C_{23}-C_{24}-H_{60}	23.47	23.47	-22.12
C_{17}-O_{26}	1.50	1.51	1.47	C_{20}-C_{17}-O_{26}	102.82	102.20	102.95	C_3-C_4-C_5-C_6	173.10	-165.94	171.98
$H_{\cdots}O_{26}$	2.46	2.50	2.68	C_{17}-O_{26}-C_{22}	111.97	111.32	112.95	C_{17}-C_{20}-C_{21}-C_{22}	-24.52	-29.25	4.40
$H_{\cdots}O_{27}$	2.26	2.25	2.31	C_{17}-C_{20}-C_{21}	104.92	103.12	104.79	C_{21}-C_{22}-C_{26}-C_{17}	-3.21	-2.43	-2.58
$O_{25}Au_{62}$	–	2.59	–	C_{12}-C_{17}-C_{16}	103.71	104.01	102.65	C_7-S_{29}-C_{23}-C_{24}	174.37	173.52	174.54

[a] taken from Ref [22]

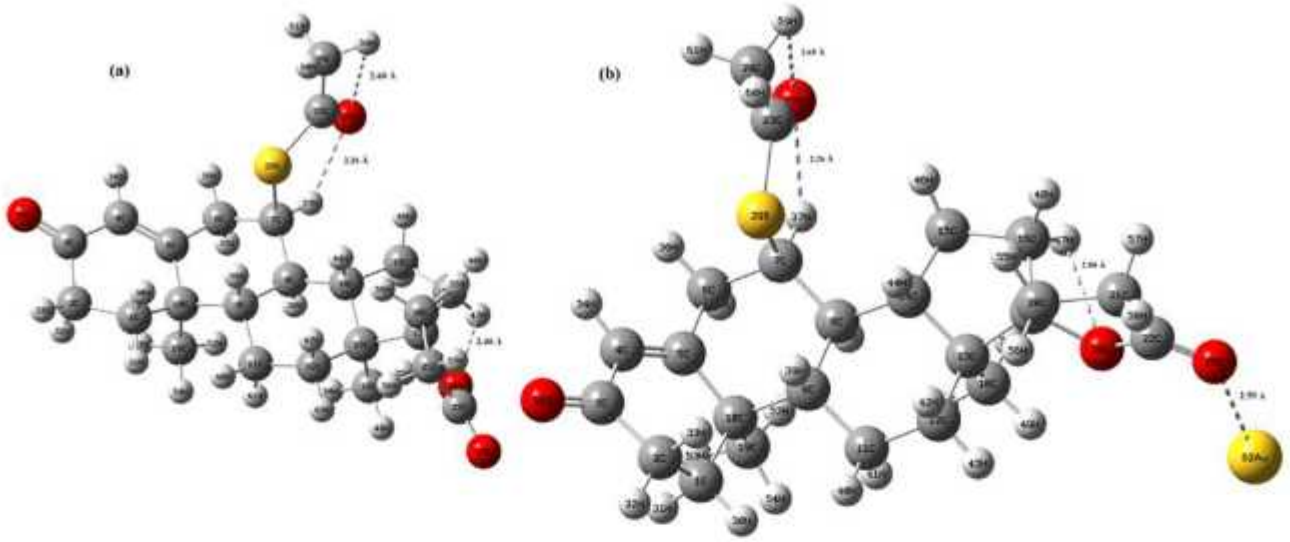


Fig. 1. Optimized structure of (a) SPL and (b) SPLA using B3LYP functional together with the 6–31 + +G (d,p) and LANL2DZ basis sets, respectively.

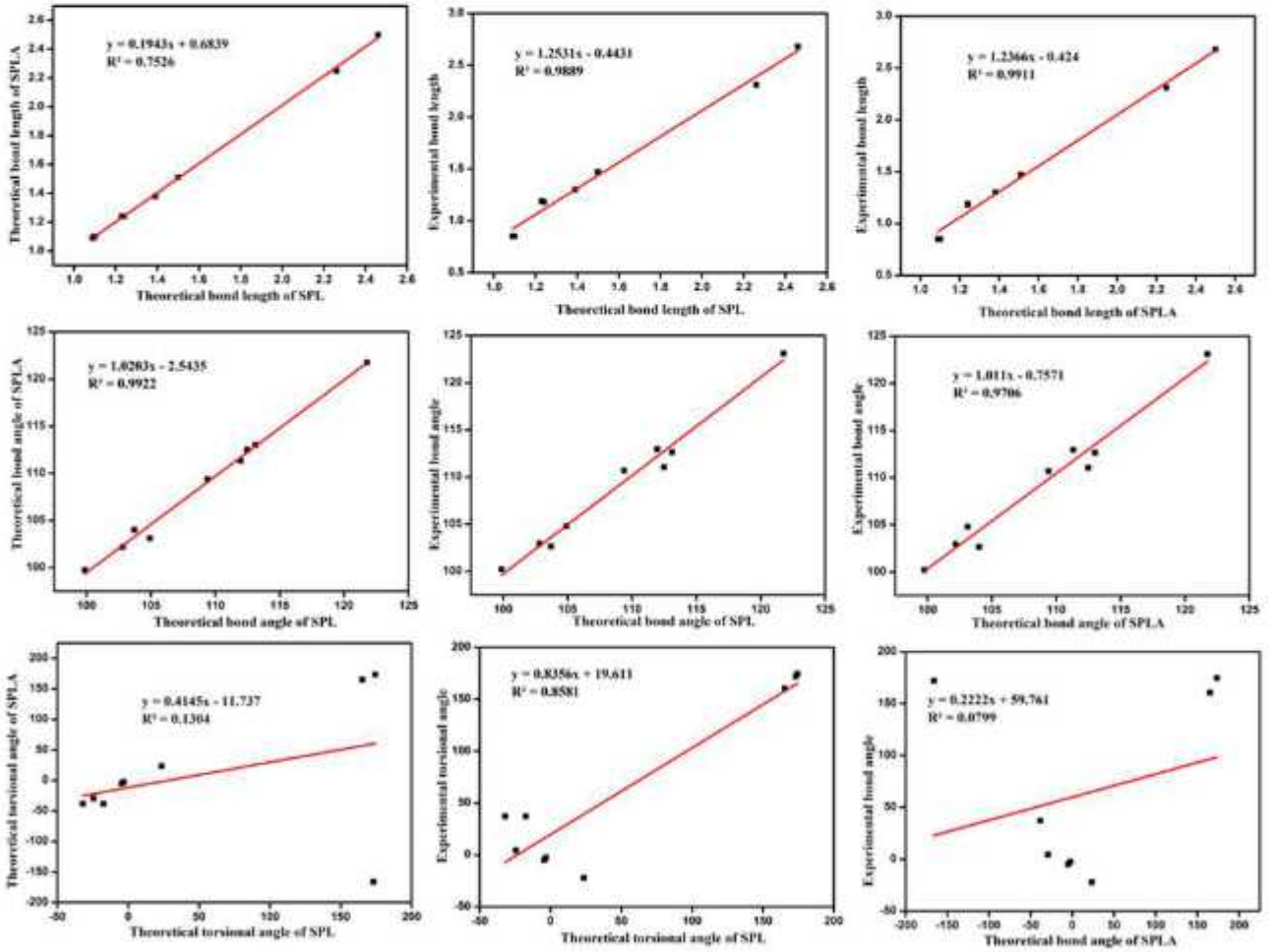


Fig. 2. Linear regression coefficient (R2); (a) correlation between the bond length of theoretical SPL and theoretical SPLA (b) correlation between the bond length of experimental and theoretical SPL (c) correlation between the bond length of experimental and theoretical SPLA (d) correlation between the bond angle of theoretical SPL and SPLA (e) correlation between the bond angle of experimental and theoretical SPL (f) correlation between the bond angle of experimental and theoretical SPLA (g) correlation between the torsional angle theoretical SPL and SPLA (h) correlation between the torsional angle experimental and theoretical SPL (i) correlation between the torsional angle experimental and theoretical SPLA.

attraction of the oxygen atom of S-methyl ethanethioate (O_{27}) with aromatic decahydronaphthalene hydrogen H_{37} is observed at a non-bonded distance of 2.26 Å which can be due to the anomeric effect through which the decahydronaphthalene ring is stabilized by the electronegative O_{27} attachment at H_{37}. [32].

The hydrogen bond angle (θ) of C_7-$H_{37}O_{27}$ is 121.78° in SPL and 121.75° in SPLA; naturally higher θ values show stronger hydrogen bond strength. Another intramolecular hydrogen bond $H_{59}O_{27}$ (2.60 Å) is formed due to steric interference between the carbonyl group and the methyl group in the S-methyl ethanethioate group in both the molecules. The dihydrofuran ring oxygen atom forms another intramolecular hydrogen bonding (C_{16}-$H_{47}O_{26}$) with cyclopentane in both the molecules. The shortening of the length of the C_{22}-O_{26} bond length (1.39 Å in SPL and 1.38 Å in SPLA) and the lengthening of the C_{17}-O_{26} bond (1.50 Å in SPL and 1.51 Å in SPLA) [32,33] confirms the intermolecular hydrogen bonding $H_{47}O_{26}$ (2.46 Å for SPL and 2.50 Å for SPLA).

3.2. Natural localised molecular orbitals (NLMOs) Analysis

Natural Hybrid Orbital directionality and "bond bending" (deviations from line of nuclear centres) of Hydrogen bonded Natural Bond Orbitals of SPL and SPLA molecule are furnished in Table 2. Atomic orbital analysis reveals that the orbital occupancy and orbital energy in the SPL molecule are less than that of the SPLA molecule, which shows that the delocalization of electrons is more in SPLA molecule. The atomic orbital analysis is extended to natural atomic orbital analysis. Natural atomic orbital analysis of SPL molecule reveals that it has four low-occupancy atoms (C_4, C_5, C_{13} and C_{17}) and that population inversion occurs. It is seen that the occupancy order is inconsistent with its energy order, and it is more evident in the Rydberg-type orbitals of very low occupancy and near degeneracy energy. In the SPLA molecule, it is seen that there are 35 electrons in the effective core potential (ECP). Natural hybrid orbits (NHOs) are due to an asymmetric orthogonalized hybrid orbit; resulting from the natural atomic orbitals (NAO) concentrated on specific atoms via a uniform transition. Tale 2 shows the direction of each hybrid orbital, specified in terms of the spherical polar (θ) and azimuthal (φ) angles from the nucleus and the deviation angle (dev) from the line of centres between the bonded nuclei. The Carbon hybrid orbital of the C=O is bent more away from the line of C_{22} =O_{23} and C_{23} =O_{27} centres above 80. This deviation may be due to the steric repulsion and hydrogen bonding C_7- H_{37} O_{27} respectively, attaining Z confirmation. It is seen that the bending of the C_{23}-S_{29} bond is lowered by 7.1° as a result of the methyl group attachment, which is electron-donating.

In NPA, all carbon atoms are negatively charged except C_3, C_5, C_{17}, C_{22} and C_{23}, but C_{22} is more positive than other positive carbon atoms in SPL and SPLA molecule it is bonded with two oxygen atoms (Fig. S1). This unearthing suggests that these oxygen atoms are at sites most suitable for protonation. The C_{10} and C_{13} carbon atoms have a lower negative charge compared to the other negative carbon atoms, and it may be due to the presence of the methyl group. Among the hydrogen atoms, the H_{37} atom possesses the most positive charge, which confirms the existence of the C_7-$H_{37}O_{27}$ hydrogen bonding. Fig. S1 represents the atomic charges of the active site in SPL and SPLA. All atoms of SPL molecules have a larger magnitude of charge compared to the respective ones of SPLA, which reveals that the adsorption of AuNPs affects the charge density of the SPL molecule. NBO analysis shows that orbital overlap between n (O) and σ * (C–H) causes intramolecular hydrogen bonding of C_{16}-H_{47} O_{26} and C_7-H_{37} O_{27}, and as a consequence of this, the H-bonded systems stabilize. As a result of this hydrogen bonding interaction, the electron density (ED) of the C–H antibonding orbital increases, weakening the C–H bond, thereby increasing the strength of the intramolecular O·H hydrogen bonds. The occupation numbers of the NBOs that interact with energies are given in Table 3. The extent of charge transfers from lone pairs of n(O_{26}) and n(O_{27}) into the antibonds σ * (C_{16} -H_{47}) and σ * (C_7 – C_{37}), respectively, is significantly decreased in SPLA, which provides corroborated on the elongation of both bonds. The energy of interaction E (2) associated with $n_2(O_{27}) \rightarrow \sigma^*$ (C_7 - H_{37}) and $n_2(O_{26}) \rightarrow \sigma^*$ (C_{16} - C_{47}) are obtained as 18.96 and 12.3 kcal / mol, respectively, for the SPL molecule and 19.63 and 13.3 kcal / mol, respectively, for SPLA molecule, which shows that the extent of intermolecular hydrogen bonding is increased in SPLA. Furthermore, the analysis of the donor-acceptor stabilization energy E (2) analysis clearly manifests the intramolecular hydrogen bond between the AuNPs and SPL molecule. The higher stabilization energy associated with the hyperconjugative interaction $n_5(Au_{62}) \rightarrow \sigma^*$ (O_{26} – C_{17}) as well as $n_6(Au_{62}) \rightarrow \sigma^*$ (O_{23} – C_{22}) evidence the delocalization of charge.

3.3. UV-Vis spectral analysis and electronic properties

In quantum chemistry, frontier molecular orbital (FMOs) energy plays a crucial role in chemical stability and are important indicators of the effect of adsorption on a metal. In the SPL molecule, the HOMO is located over the junction between the dihydrofuran ring and cyclopentane and the LUMO is located over the dihydrofuran ring, a major portion of the cyclopentane ring and a small portion of the thioacetic acid. In the SPLA molecule, the HOMO is concentrated over the dihydrofuran ring, as well as AuNPs and the LUMO, over the cyclohexanone

Table 2
NHO directionality and "bond bending" (deviations from line of nuclear centres) of H-bonded NBOs of SPL and SPLA molecule.

Molecule	NBO	Line of centres		Hybrid 1			Hybrid 2		
		θ	φ	θ	φ	Dev	θ	φ	Dev
SPL	π (C_4 - C_5)	69.1	181.2	149.7	131.6	90.2	147.1	129.3	90.8
	σ (C_7 - C_8)	91.6	229.7	96.8	229.2	5.2	90.9	49.8	2.6
	σ (C_{13} - C_{14})	89.8	49	87.3	45.1	4.6	90	230.2	1.1
	σ (C_{13} - C_{17})	103.7	148.8	105.3	152.9	4.3	78.3	325.5	3.6
	π (C_{22} - O_{23})	83.8	215.6	92.8	126.7	89.2	92.5	124.8	89
	π (C_{23} - O_{27})	19.8	134.8	74.5	5.9	87.3	79.6	4.9	87.5
	σ (C_{23} - S_{29})	107.2	279.7	100.2	278.1	7.1	69.7	100.6	3.2
SPLA	σ (C_5 – O_{28})	90.7	172	57.7	251.6	81.6	57.1	272.1	81.1
	π (C_{23} – O_{27})	90.7	172	98.5	160.2	14.1	98.1	3.3	14.3
	π (C_{22} - O_{23})	116.3	6.4	54.1	74.3	89.2	53.5	76.8	88.7
	π (C_{23} - O_{27})	21.6	215.9	107.6	194.7	87.4	113.7	194.1	86.5
	σ (C_8 – C_9)	72.6	50.3	68.3	42.7	8.3	102.9	237.6	8.4
	σ (C_{20} - C_{17})	127.7	106	125.7	97.4	7.2	51.7	287.3	1.1
	π (C_{17} - C_{20})	59.7	184.5	135.5	240.7	91.4	130.2	242.1	91.5
	σ * (C_5 - O_{28})	90.7	172	57.7	251.6	81.6	57.1	272.1	81.1
	π * (C_{17} - O_{26})	21.6	215.9	107.6	194.7	87.4	113.7	194.1	86.5

θ – Polar angle.
φ – Azimuthal angle

Table 3
Second-order perturbation theory analysis of Fock matrix in NBO basis of SPL and SPLA molecule.

Molecule	Donor (i)		Acceptor (j)		E (2)[a] kcal/mol	E (j)-E (i)[b] (a.u.)	F (i,j)[c] (a.u.)
	NBO	Occupancy	NBO	Occupancy			
SPL	σ (C_7 - H_{37})	1.97445	σ * (C_7 - S_{29})	0.05099	0.55	0.6	0.016
	σ (C_2 - H_{32})	1.95905	π * (C_3 - O_{26})	0.1582	6.57	0.51	0.053
	σ (C_4 - H_{34})	1.9758	σ * (C_5 - C_{10})	0.03994	6.79	0.9	0.07
	σ (C_{24} - H_{61})	1.96339	π * (C_{23} - O_{27})	0.22223	6.45	0.5	0.053
	n2(O_{25})	1.84114	σ * (C_{21} - C_{23})	0.06709	16.75	0.61	0.092
	n2(O_{25})	1.84114	σ * (C_{22} - O_{26})	0.10969	31.71	0.58	0.122
	n2(O_{27})	1.97371	σ * (C_7 - H_{37})	0.02333	16.96	0.71	0.024
	n2(O_{26})	1.96701	σ * (C_{18} - C_{47})	1.97703	12.3	0.67	0.037
SPLA	σ (C_7 - H_{37})	0.98097	σ * (C_7 - S_{29})	0.01134	17.94	0.44	0.113
	σ (C_2 - H_{32})	0.98869	π * (C_3 - O_{26})	0.11616	8.82	0.62	0.094
	σ (C4 - H34)	0.98719	σ * (C5 - C10)	0.02029	7.98	0.69	0.095
	σ (C_{24} - H_{61})	0.98685	π * (C_{23} - O_{27})	0.02461	14.63	0.58	0.117
	n2(O_{26})	0.99024	σ * (C_{18} - C_{47})	0.01692	8.16	0.61	0.091
	n2(O_{27})	0.98099	σ * (C_{22} - C_{24})	0.04665	14.65	0.65	0.09
	n2(O_{27})	1.82782	σ * (C_{23} - S_{29})	0.14254	33.14	0.4	0.104
	n2(O_{28})	0.98617	σ * (C_2 - H_{32})	0.00907	19.63	0.58	0.117
	n2(O_{26})	0.98761	σ * (C_{17} – C_{18})	0.01887	13.3	0.67	0.037
	n5(Au_{62})	0.99894	σ * (O_{28} – C_{17})	0.11992	23.18	0.23	0.009
	n6(Au_{62})	0.99217	π * (O_{25} – C_{22})	0.01335	20.05	0.36	0.006

[a] E(2) means energy of hyperconjugative interactions.
[b] Energy difference between donor and acceptor i and j NBO orbitals.
[c] F(i, j) is the Fock matrix element between i and j NBO orbitals.

ring. This reveals that the adsorption of gold nanoparticles disturbs the HOMO and LUMO distribution. The energy difference between the frontier molecular orbitals (FMO's) of SPL and SPLA molecules is 4.88 eV and 2.35 eV respectively as shown in Fig. 3(a) and (b). The significant decreases of the HOMO–LUMO energy gap is attributed to the mixing of the O-lone pairs of the heterocycle with carbon π-orbitals thereby increasing the aromaticity of the system [34,35]. However, when the two molecules were compared, it was found that the SPLA molecule possesses a smaller FMO energy difference. The low energy gap of SPL and SPLA molecules improves the molecular electrical transport properties and photostability, especially in SPLA molecules. Photostability enhances its drug stability owing to the fact that the greater the mobility of the electrons in large hyperconjugated orbital systems, the greater the distribution of the energy throughout the molecule, stabilizing it. From the frontier molecular orbital energy gap of SPLA molecule shows that the combination of a lone pair of electrons in gold nanoparticles and the σ-electron in the ring system further lowers the FMO energy gap. The mixing of AuNP d electrons into the ring system, increases the delocalization of electron density in the ring system. Literature survey reveals that the increased extent of electron delocalization in a molecular system leads to increased stabilization, which increases the reactivity of the system [36]. The highest occupied molecular orbital (HOMO)-lowest unoccupied molecular orbital (LUMO) energy separation has been used as a simple indicator of kinetic stability. A lower HOMO-LUMO gap implies lower kinetic stability and high chemical reactivity, because it is energetically favorable to add electrons to a relatively low-lying LUMO, to extract electrons from a relatively high-lying HOMO, and so to form the activated complex of any potential reaction [37]. Kinetic stability refers to reactivity or the ability of the metal complex to undergo ligand substitution reactions. Lower kinetic stability implies higher extent to which the drug substance retains, the same properties and characteristics that it possessed at the time of its manufacture, within specified limits and throughout its period of storage and use.

According to the Koopmans theorem, global reactivity descriptors [38] the calculated values of I, A, χ, μ, η, S and ω are 6.879 eV, 1.996 eV, 4.438 eV, 4.438 eV, 2.441 eV, 0.410 (eV) ^{1} and 4.030 eV respectively for SPL molecule. For SPLA molecule these values are 5.119 eV, 2.765 eV, 3.942 eV, − 3.942 eV, − 3.942 eV, 0.850 (eV) ^{1}, and 6.60 eV, respectively in the same order. Both molecules possess a negative chemical potential (μ), which reflects their stability, SPLA molecule being more stable. SPL molecule has higher chemical hardness than SPLA molecule. This shows that the chemical stability and electronegativity of SPLA molecule are higher than that of SPL molecule. SPLA molecule shows more electrophilicity index and ionization potential value than the SPL molecule. This confirms that intramolecular charge transfer (ICT) interaction occurs between AuNPs and SPL molecules through an oxygen atom in a dihydrofuran ring. This is also evident from the natural localized molecular orbital analyses. Furthermore, the FMOs value confirms that SPL molecule is chemisorbed on the AuNP surface through the lone pair electrons on the oxygen atoms [39].

The electron density-based local reactivity descriptors, the Fukui functions (f_k^+, f_k^-, f_k^0), local softness (S_k^+, S_k^-, S_k^0) and local electrophilicity indices (ω_k^+, ω_k^-, ω_k^0) were calculated for the SPL and SPLA molecules using Mulliken population analysis [39] (Table S1). For SPL molecule, the highest value for local nucleophilic reactivity descriptors at C_{22}, C_3 and C_{23} indicates that these sites are more susceptible to electrophilic attack, but in SPLA molecule it is found that C_{22} and C_{24} has higher affinity, the situation changing due to the adsorption on AuNPs. This is pictorially shown in Fig. 3. The common electrophilic attack sites in SPL and SPLA molecules are located at C_{18} and C_{19} in the methyl group, the methyl groups being electron donors further favoured by the resonance effects. The possible sites of radical attack are at O_{25} and O_{26} in the hydrofuran ring of both SPL and SPLA molecules. The Au_{62} in the SPLA molecule is more prone to radical attack than O_{25} and O_{26}. All other reactive sites for SPL and SPLA are almost similar, with the intensity of reactivity being higher in the SPLA molecule. The polar factors can affect the reactivity of free radicals. The free radicals, though neutral, exhibit some sort of electrophilic or nucleophilic character because the adsorption of SPL on gold nanoparticles increases the flow of electrons or ICT. According to Rao *et.al.*, [40] free radicals, being unstable, can damage the cancer cells in the body. This means that SPLA molecule causes more destruction to cancer cells. From the FMO analyses and molecular reactivity descriptor analysis of SPL and SPLA molecules, it is excavated that SPLA molecules have higher cancer activity than SPL molecules. The Molecular Electrostatic Potential (MEP) surfaces of SPL and SPLA pictorially (Fig. 3(c) and (d)) strengthen the FMOs, global and local reactive descriptor analysis results, wherein the electrophilic attacks, nucleophilic attacks, and radical attack are represented as red, green, and yellow, respectively.

The electron density-based local reactivity descriptors, the Fukui

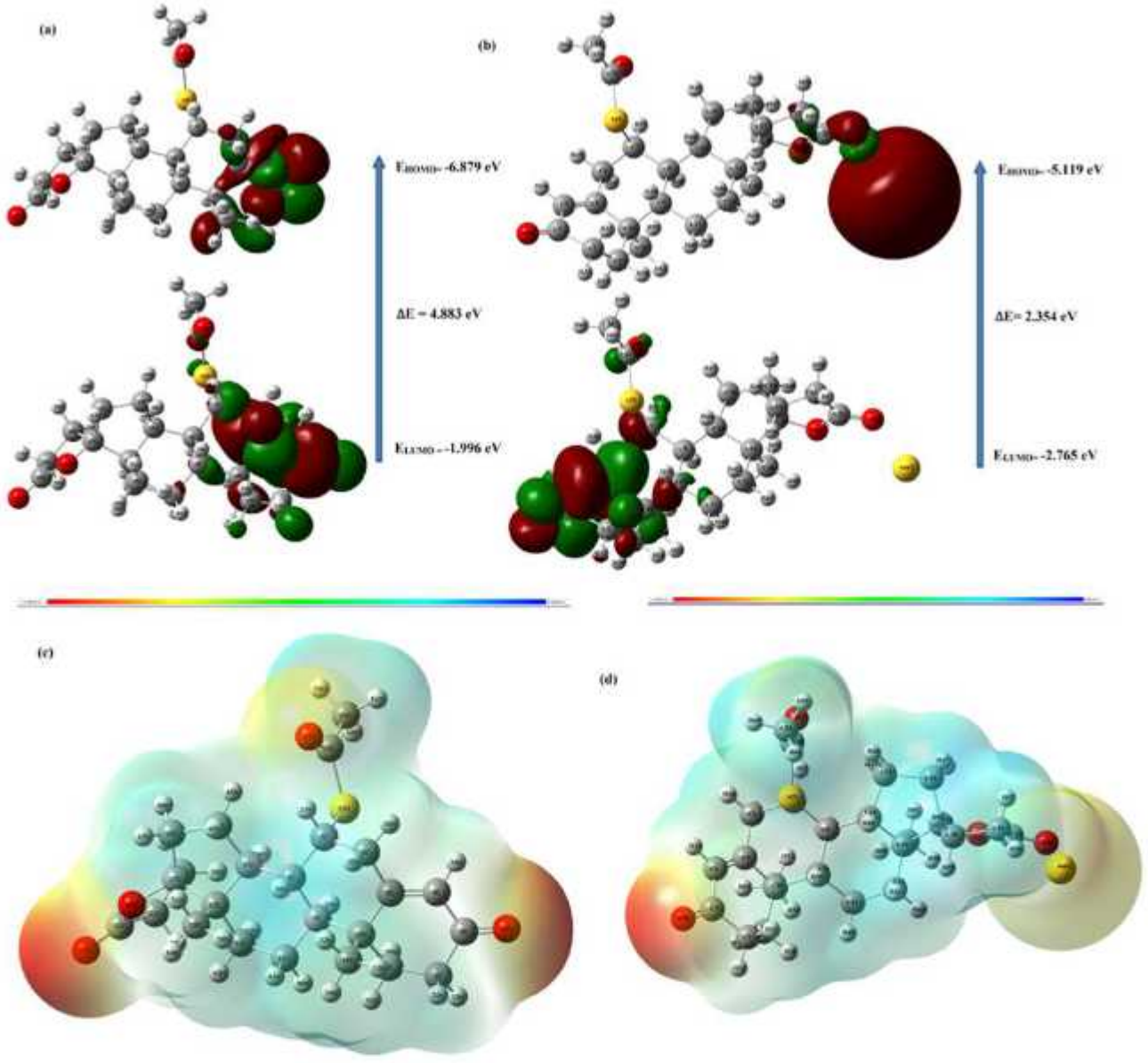


Fig. 3. (a) The frontier molecular orbital diagrams of SPL molecule (b) The frontier molecular orbital diagrams of SPLA molecule. (c) Molecular electrostatic potential plots of SPL molecule and (d) Molecular electrostatic potential plots of SPLA molecules.

functions (f_k^+, f_k^-, f_k^0), local softness (S_k^+, S_k^-, S_k^0) and local electrophilicity indices (ω_k^+, ω_k^-, ω_k^0) were calculated for the SPL and SPLA molecules using Mulliken population analysis [39] (Table S1). For SPL molecule, the highest value for local nucleophilic reactivity descriptors at C_{13}, S_{29}, C_{18}, C_{19} and C_{22} indicates that these sites are more susceptible to electrophilic attack, but in SPLA molecule it is found that C_5, C_{18}, C_{19} and C_{24} has higher affinity, the situation changing due to the adsorption on AuNPs. This is pictorially shown in Fig. 3. The common electrophilic attack sites in SPL and SPLA molecules are located at C_{18} and C_{19} in the methyl group, the methyl groups being electron donors further favoured by the resonance effects. The possible sites of radical attack are at O_{25} and O_{26} in the hydrofuran ring of both SPL and SPLA molecules. The Au_{62} in the SPLA molecule is more prone to radical attack than O_{25} and O_{26}. All other reactive sites for SPL and SPLA are similar, with the intensity of reactivity being higher in the SPLA molecule. The polar factors can affect the reactivity of free radicals. The free radicals, though neutral, exhibit some sort of electrophilic or nucleophilic character because the adsorption of SPL on gold nanoparticles increases the flow of electrons or ICT. According to Rao *et al.* [40], free radicals, being unstable, can damage the cancer cells in the body. This means that SPLA molecule causes more destruction to cancer cells. From the FMO analyses and molecular reactivity descriptor analysis of SPL and SPLA molecules, it is excavated that SPLA molecules have higher cancer activity than SPL molecules. The Molecular Electrostatic Potential (MEP) surfaces of SPL and SPLA pictorially (Fig. 3(c) and (d)) strengthen the FMOs, global and local reactive descriptor analysis results, wherein the electrophilic attacks, nucleophilic attacks, and radical attack are represented as red, green, and yellow, respectively.

The electron density-based local reactivity descriptors, the Fukui functions (f_k^+, f_k^-, f_k^0), local softness (S_k^+, S_k^-, S_k^0) and local electrophilicity indices (ω_k^+, ω_k^-, ω_k^0) were calculated for the SPL and SPLA molecules using Mulliken population analysis [39] (Table S1). For SPL molecule, the highest value for local nucleophilic reactivity descriptors at C_{22}, C_3 and C_{23} indicates that these sites are more susceptible to electrophilic attack, but in SPLA molecule it is found that C_{22} and C_{24} has higher affinity, the situation changing due to the adsorption on AuNPs. This is pictorially shown in Fig. 3. The common electrophilic attack sites in SPL and SPLA molecules are located at C_{18} and C_{19} in the methyl group, the

methyl groups being electron donors further favoured by the resonance effects. The possible sites of radical attack are at O_{25} and O_{26} in the hydrofuran ring of both SPL and SPLA molecules. The Au_{62} in the SPLA molecule is more prone to radical attack than O_{25} and O_{26}. All other reactive sites for SPL and SPLA are similar, with the intensity of reactivity being higher in the SPLA molecule. The polar factors can affect the reactivity of free radicals. The free radicals, though neutral, exhibit some sort of electrophilic or nucleophilic character because the adsorption of SPL on gold nanoparticles increases the flow of electrons or ICT. According to Rao *et al.*,[40] free radicals, being unstable, can damage the cancer cells in the body. This means that SPLA molecule causes more destruction to cancer cells. From the FMO analyses and molecular reactivity descriptor analysis of SPL and SPLA molecules, it is excavated that SPLA molecules have higher cancer activity than SPL molecules. The Molecular Electrostatic Potential (MEP) surfaces of SPL and SPLA pictorially (Fig. 3(c) and (d)) strengthen the FMOs, global and local reactive descriptor analysis results, wherein the electrophilic attacks, nucleophilic attacks, and radical attack are represented as red, green, and yellow, respectively.

To understand electronic transitions of SPL and SPLA molecules, time-dependent DFT (TD-DFT) calculations were performed using DMSO as solvent and results are tabulated in Table 4 and Fig. 4(a). The calculated oscillator strength *(f)* for SPL and SPLA molecules shows highest value corresponding to the wavelength 262 nm and 674 nm, respectively. The experimental absorption bands are observed at 258 nm and 641 nm, respectively, in the same order. The absorption band of the SPL molecule are assigned to the R-bands which originate from an $n \rightarrow \pi^*$ [41]. The absorption peaks of SPLA molecule are due to the charge transfer interaction between a lone pair of electrons present in the AuNP to σ^* electrons in the dihydrofuran moiety of the molecule. These $n \rightarrow \sigma^*$ transitions are also responsible for the enhanced chemical activity of the molecule as seen from the low value of HOMO-LUMO gap. The optical band gap has been obtained from Tauc's equation [30] and the graphical plot (Fig. 4(b) and (c)). The energy required for exciting electrons from in both the molecules are found at 4.51 eV (Fig. 4(b)) and 1.74 eV (Fig. 4(c)), respectively which is consistent with the calculated frontier molecular orbital energy gap. The optical and electronic studies support that SPLA has enhanced chemical activity than SPL.

3.4. Vibrational spectral analysis

3.4.1. IR and Raman spectral analysis

The observed and simulated FT-IR and FT-Raman spectra of SPL molecule are shown in Fig. 5 and are tabulated in Table 5.

3.4.1.1. Cyclohexanone ring. The CH_2 asymmetric and symmetric stretching vibrations of cyclohexanone ring generally appear in the region 2940–2915 cm^{-1} and 2870–2840 cm^{-1}, respectively. [42] These modes are observed separately both in IR and Raman as intense bands at 2948 cm^{-1}, 2946 cm^{-1}, 2891 cm-1, and 2870 cm-1, respectively. The up-shifting of H_{31}-C_1-H_{30} and H_{33}-C_2-H_{32} stretching vibrational modes is attributed to the steric hindrance between the aromatic decahydronaphthalene rings and the cyclohexanone ring. This has been confirmed in the optimized geometry as a reduction of the endocyclic torsion angles, C_1-C_2-C_3-C_4 and C_4-C_5-C_{10}-C_1 to 32.0883° and − 17.5157°, respectively, (with respect to standard CCCC torsion angles) which resulting in the chair conformation. The CH_2 scissoring and wagging vibrations are observed as coupled vibrations at 1430 cm^{-1} in Raman spectra. Also, coupled twisting and wagging vibrations are observed at 1343 cm^{-1}. The rocking vibration is observed 1069 cm^{-1} in IR spectra. According to Sajan, D. *et al.*,[43] the lowering of bending vibration is due to the association in the solution phase. Also, the CCC bend of the cyclohexanone ring in the SPL molecule is observed in IR at 721 cm^{-1} which are mixed with the bridge and decahydronaphthalene ring bending vibrations. In addition, the CCC bend is observed at a lower wavenumber, i.e. 520 cm^{-1} in IR in the cyclohexanone ring. In the SPL molecule, due to the mixing of cyclohexanone vibrations with that of decahydronaphthalene rings and bridges, it is difficult to identify the spectral separation between cyclohexanone and decahydronaphthalene rings.

3.4.1.2. Decahydronaphthalene Ring. Decahydronaphthalene C–H stretching vibrations is singularly observed in the IR spectrum at 3077 cm^{-1} and the corresponding Raman band is observed at 3038 cm^{-1} as expected. [42,43] The C–H out-of-plane bending vibrations due to the fused naphthalene ring occur at 815 cm^{-1} and 856 cm^{-1}, while the C–H out-of-plane bending vibration due to the adjacent cyclopentane and S-methyl ethanethioate are observed at 752 cm^{-1}. Decahydronaphthalene ring stretching vibrations usually occur in the region 1640–1400 cm^{-1}. In the SPL molecule, IR and Raman bands are observed at 1616 cm^{-1}. The CC marker stretching band vibrations in the IR spectrum are observed at 1595 cm^{-1} which is found to be coupled with the C═O stretching band.

3.4.1.3. Cyclopentane. The cyclopentane asymmetric CH_2 stretching mode is likely to be observed in the range 2960–2950 cm^{-1} [42] and is observed at 2948 cm^{-1} and 2946 cm^{-1} in the Raman and IR spectrum, respectively. The reason behind the blue-shifting lies in the fact that these two CH_2 act as the hyper conjugative interactive path between dihydrofuran ring and the *s*-methyl ethanethioate. Due to this interaction, a C_{16}-H⁄⁄O_{26} hydrogen bond is formed. The CC stretching band and ring breathing vibration band appear at (1100 cm^{-1}, 800 cm^{-1}) and 866 cm^{-1}, respectively in Raman. These bands are seen at 889 cm^{-1} and 856 cm^{-1} in IR spectra in the same order. The lowering of the ring breathing band occurs due to the mixing of CC stretching vibration. The puckering modes of cyclopentane ring generally appear in the range 1000–960 cm^{-1} [42,43] which are observed at 985 and 989 cm^{-1} in IR and Raman spectrum, respectively. The puckering mode of the cyclopentane confirms the conformation change that has been explained in the structural geometry and charge delocalization. In the envelope conformation of cyclopentane, there should be five infrared-active frequencies in the 1300–700 cm^{-1} region, four CH_2 and one C-C vibration. [44] From the IR spectra, it is observed that four CH_2 vibrations are observed at 1013 cm^{-1}, 951 cm^{-1}, 911 cm^{-1} and 1156 cm^{-1}. Along

Table 4
Maximum of the absorption (λmaxExpt and λ_{max}calc.), and oscillator strength (*f*) of the SPL and SPLA molecule using TD-DFT method at the B3LYP/6–311 + +G(d,p) and B3LYP/LANL2DZ level of basis set.

Molecule	Excitation	CI expansion co-efficient	λ_{max} calc. (nm)	λ_{max} Expt. (nm)	E (eV)	Oscillator strength (*f*)	Contribution of orbital	Assignment [28]
SPL	Excited state 3		262	258			$n \rightarrow \pi^*$	R-Bands
	110 → 113	0.38625						
	111 → 113	0.58556			4.7246	0.0164		
SPLA	Excited state 1		677	641			$n \rightarrow \sigma^*$	B-Bands
	115 → 116	0.17940						
	116 → 116	0.39602						
	104 → 116	0.87171						
	117 → 116	0.17770			1.8306	0.0012		

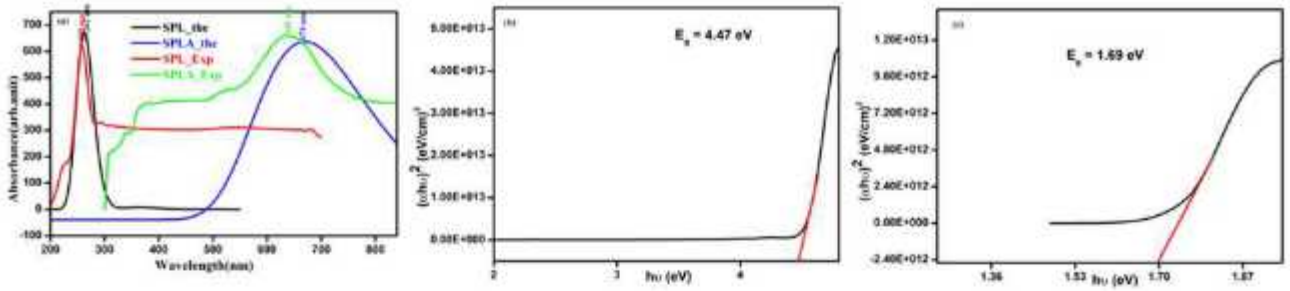


Fig. 4. (a) The electronic transitions of simulated and observed UV–vis spectra of the SPL and SPLA molecule (b) Tauc's plot of SPL molecule (c) Tauc's plot of SPLA molecule.

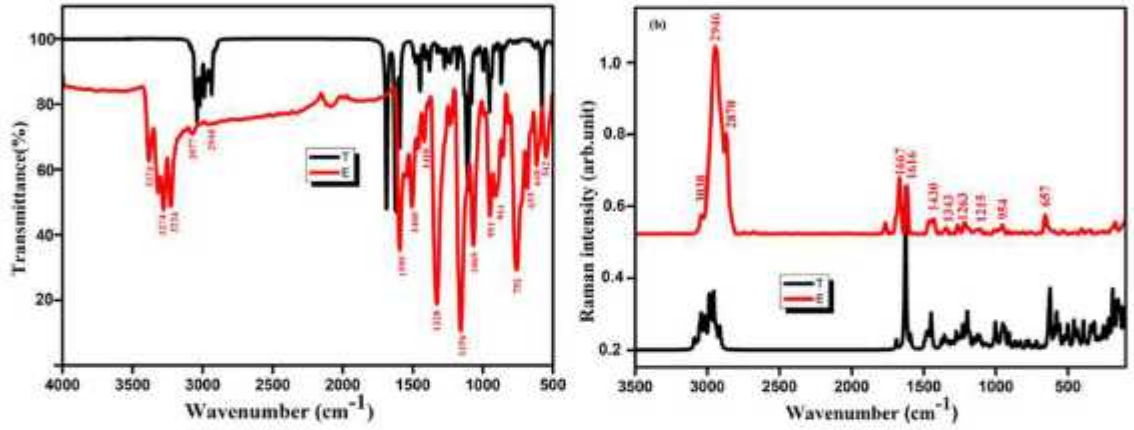


Fig. 5. Comparison of observed and simulated (a) FT-IR spectra and (b) FT-Raman spectra of the SPL molecule.

with CH_2 stretching, there is a CC stretching IR band observed at 889 cm^{-1}, which confirms the envelope conformation of cyclopentane.

3.4.1.4. Dihydrofuran. The CH_2 asymmetric stretching vibrations are observed in IR and Raman at 2948 cm^{-1} and 2946 cm^{-1} respectively and the symmetric stretching vibrations are observed at 2891 cm^{-1} and 2870 cm^{-1} respectively. The lowering of stretching frequency is due to the electronic effects caused the presence of the oxygen atom and carbonyl group, ie, the induction effect. [44] The C-O-C in-plane bending and C═O stretching bands are observed at 542 cm^{-1} (IR) and 1687 cm^{-1}(IR), 1667 cm^{-1} (Raman), respectively. The up-shift of in-plane bending mode is due to hydrogen bonding and charge delocalization in the system.

3.4.1.5. S-methyl ethanethioate. The C-S stretching vibration in the S-methyl ethanethiol usually appears at 626–628 cm^{-1} and it is observed at 657 cm^{-1} in Raman spectra. The up-shift of CS stretching is attributed to the perpendicularity of *S*-methyl ethanethioate. The out-of-plane bending mode of S-(C═O)-CH_3 are normally expected in the range 1680–1640 cm^{-1} and it is observed at 1687 cm^{-1} in IR spectra and 1667 cm^{-1} in Raman spectra. The in-plane bending mode of S-(C═O) normally appear in the range 430–460 cm^{-1} [43] and it is observed at 520 cm^{-1}. The up-shifting of the in-plane bending mode of *S*-(C═O) is due to the methyl substitution in the carbonyl group.

3.4.1.6. Methyl group. The methyl group is connected in the *cis* form at the two sides of the decahydronaphthalene ring. The C–H stretching modes of CH_3 are expected in the region 3038–2870 cm^{-1}. [45] It is observed at 2948 cm^{-1} and 2946 cm^{-1} in IR and Raman bands, respectively for meth1 (C_{18}, H_{49}, H_{50}, H_{51}) and meth2 (C_{19}, H_{52}, H_{53}, H_{54}). The methyl symmetric stretching wavenumber is affected by the hyperconjugation and induction of the methyl group in the aromatic ring (decahydronaphthalene). The methyl deformation vibration is expected in the region 1470–1350 cm^{-1}.[46] The in-plane bending of meth1 and meth 2 are observed at 1460 cm^{-1}(IR) and 1430 cm^{-1} (Raman), respectively. Also, the butterfly mode of meth1 and meth2 are observed at 1418 cm^{-1}.

3.4.2. SERS spectral analysis

The UV-Vis spectra, Tauc's plot and transmission electron microscope (TEM) image of the AuNP colloids prepared are explained in our earlier report [14]. The absorption maxima, bandgap energy, and TEM have confirmed that the particles are spherical with an average particle size of 40 nm. The prepared gold colloids showed a wine red colour with absorption maxima and bandgap energy of 530 nm and 3.08 eV respectively. After the chemical interactions between SPL and AuNPs (ie, in SPLA), the absorption spectrum was redshifted from 329 nm to 670 nm which indicated that the SPL molecule has been adsorbed onto the gold nanoparticles.

The SERS fingerprint pattern analysis of SPLA was performed under 10^{-3}, 10^{-4} and 10^{-5} M concentrations (Fig. 6). Table 6 shows the important assignments of the SERS spectrum of SPLA molecule. The SERS spectrum was analyzed by comparing theoretical and experimental data with the normal Raman spectral data. Observed intense band at 250 cm^{-1} in 10^{-3} M and 248 cm^{-1} in 10^{-4} and 10^{-5} M showed the presence of metal absorbate interaction, through oxygen atom thereby achieving a kinetically favourable interaction. This interaction is further favoured by the steric interaction imposed by the dihydrofuran ring on the metal and the charge transfer between the low electronegative oxygen with the metal. Optimized geometry and NBO analysis also support that the electron-donor site oxygen atom (O_3) interacts with the AuNPs. The MEP map and Fukui function calculations indicates that the electron density is highest on the O_3 oxygen atom in the dihydrofuran ring, revealing that SPL is supposed to be adsorbed through the O_3

Table 5
Vibrational assignments for the SPL molecule at the B3LYP//6–311 + +G(d,p) level of theory.

Unscaled wavenumber	Scaled wavenumber	Experimental		Assignments with PED%
		IR	Raman	
3195	3090	3077		ν C_9-H_{39}(99), C_8-H_{38}(56), C_{14}-H_{44}(33), C_7-H_{37}(21) nap
3138	3035		3036	ν C_9-H_{39} (89), C8-H_{38} (56), C_{14}-H_{44} (33), C_7-H_{37} (21) nap. ν CH_3meth1, meth2
3047	2947	2946	2946	$\nu_{asym}H_{31}$-C_1-H_{30} (76) cyclo, $\nu_{asym}H_{32}$-C_2-H_{32} (66) cyclo, $\nu_{asym}H_{45}$-C_{13}-H_{46} (52) pent, H_{47}-C_{16}-H_{48} (34) pent, H_{57}-C_{21}-H_{58}(53), H_{53}-C_{20}-H_{54} (26) dihy, ν CH_2 (42) S-meth, ν CH_3meth1, meth2
3001	2903	2891	2870	$\nu_{sym}H_{31}$-C_1-H_{30} (86) cyclo, $\nu_{sym}H_{32}$-C_2-H_{32} (72) cyclo, ν C_9-H_{39} (82), C_8-H_{38} (76) nap, H_{57}- C_{21}-H_{58}(43), H_{55}-C_{20}-H_{56} (12) dihy
1745	1688	1687	1667	ν C_{22}—O_{23} (80) dihy, C_7-S_{29}-(C_{22}—O_{27})-CH_3 (25) S-meth
1671	1616	1616	1616	ν C_{22}—O_{27} (75) s-meth, ring streching nap
1645	1591	1595		ν C_{22}—O_{28} (67) cyclo, ν CC nap
1546	1495	1507		δ_{sci} H_{41}-C_{11}-H_{40} (56) nap
1514	1464	1460		βC_9-H_{39}(80), C_8-H_{38}(32), C_{14}-H_{44}(26), C_7-H_{37} (68) nap, dihy(32), meth 2 (18)
1492	1443		1430	βC_8-H_{38}(84), C_8-H_{38}(23), C_{14}-H_{44}(42), C_7-H_{37} (34) nap, δ_{sci}H31-C1-H30 (86) cyclo, ω H33-C2-H32 (72) cyclo β CH_2s-meth,meth1
1455	1406	1416		BM meth 1&2
1427	1381	1383		BM s-meth
1386	1341		1343	γ CH_2 nap (32), cyclo (22) ωH31-C1-H30 (56) cyclo, t H33-C2-H32 (32) cyclo
1371	1326	1328		γ CH_2 nap (26), cypen (22), dihy (18).
1302	1260	1266	1263	t H_{40}-C_{11}-H_{41} (52), ω H_{42}-C_{12}-H_{43} (48) nap
1271	1230	1233		t H_{31}-C_1-H_{30} (36) cyclo, ω H_{33}-C_6-H_{36} (23) nap
1254	1213	1218	1215	t H_{47}-C_{16}-H_{48}(28) cyclo, H_{45}-C_{13}-H_{46} (50) cyclo, H_{57}-C_{21}-H_{58} (12) dihy
1227	1187	1186		t H_{40}-C_{11}-H_{41} (28 0 nap
1192	1153	1156		ν H_{45}-C_{13}-H_{46} (52) pent, H_{47}-C_{16}-H_{48} (34) pent
1101	1065	1069		βH_{31}-C_1-H_{30} (46), H_{32}-C_2-H_{32} (22) cyclo
1048	1014	1013		ν H_{45}-C_{13}-H_{46} (52) pent, H_{47}-C_{16}-H_{48} (34) pent
1018	985	989		Ring puckering pent,
985	953	951	954	ν H_{43}-C_{13}-H_{46} (21) pent, H_{47}-C_{16}-H_{48} (14) pent
940	909	911		ν H_{43}-C_{13}-H_{46} (18) pent, H_{47}-C_{16}-H_{48} (32) pent
936	906	889		ν C_{13}-C_{16}(26), ν C_{16}-C_{17} (20), ν C_{17}-C_{13} (15), ν C_{13}-C_{14}(24), ν C_{14}-C_{15}(16) pent
870	842	856		γ C_9-H_{39}(72), C_8-H_{38}(42), nap ring breathing (pent)
856	828	815		γ C_9-H_{39}(72), C_8-H_{38}(42), nap
771	746	752		γ C_{14}-H_{44}(12), C_7-H_{37} (15) nap
747	723	721		β C_8-C_{10}-C_1 (53), β C_4-C_5-C_{10} (36) cyclo
703	680	682		
				ν C_7-S_{29} (20) S-meth, β C_4-C_5-C_{10} (11 cyclo
665	643	653	657	ν C_7-S_{29} (39), ν S-(C═O) (40) S-meth
646	624	618		ρ H_{31}-C_1-H_{30} (64), H_{32}-C_2-H_{32} (22) cyclo
550	532	542		β C_{22}-O_{28}-C_{17} (31) dihy
539	522	520		β C_4-C_5-C_6 (58), β C_5-C_6-C_1 (32) cyclo, β S-(C═O) (23) S-meth
76	73		73	δ_{sci} CCC nap

ν→ stretching, ν_{sym}→Symmetricstreching, ν_{asym}→ Asymmetric stretching, β→ in-plane bending, δ_{sci}→ Scissoring, ρ→ rocking, ω→ wagging, t→ twisting, γ→out-of-plane bending, nap→decahydronaphthalene, S-meth→S-methyl-ethanethioate, dihy→dihydrofuran, cyclo→Cyclohexanone, pent→cyclopentane.

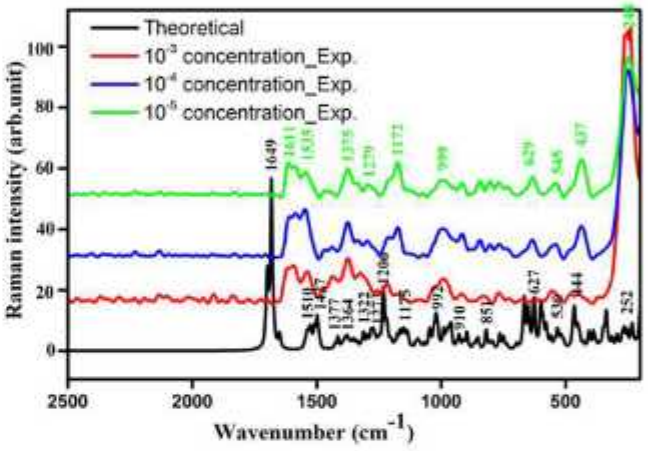


Fig. 6. SERS of SPLA at three different concentrations (10^{-3}, 10^{-4}, 10^{-5} M) and calculated SERS spectra.

oxygen atom in the dihydrofuran ring.

The in-plane bending modes associated with CCC and CCO are expected in the region 851–627 cm^{-1} and 630–520 cm^{-1}, respectively [44]. The bands are observed at (830 cm^{-1}(10^{-3} M), 629 cm^{-1}(10^{-4} M), 626 cm^{-1}(10^{-5} M)) and (526 cm^{-1}(10^{-4} M), 437 cm^{-1}(10^{-4} M and 10^{-5} M)), respectively in the same order. The out-of-plane bending modes associated with CCC and CCO are expected in the region 992–1002 cm^{-1} and 430–390 cm^{-1}, respectively [43]. These modes are observed at (992 cm^{-1}(10^{-3} M) and 999 cm^{-1} (10^{-5} M)) and (471 cm^{-1}(10^{-3} M)) respectively. According to the surface selection rule,[47,48] the in-plane and out-of-plane bending modes of a molecule will be equally enhanced, when it is adsorbed in tilted orientation to the metal surface. In SPLA, it is observed that the intensity of in-plane and out-of-plane bending modes associated with both CCC and CCO are enhanced together. This leads to the evidence that a tilted orientation exists for SPLA on the gold surface, and this tilted orientation is probably through the lone pair electrons on the oxygen atom in the dihydrofuran ring as evident from the tentative and supportive assignments, given in Table 6.

3.5. Prediction of biological activity

Literature review shows that the SPL molecule is used as a diuretic, [49] as well as to reduce the risk of pulmonary hypertension in patients with chronic obstructive pulmonary disease (COPD) [50]. Hence, we proceeded for analytical scrutiny (*in-silico* and the in-vitro) of the

Table 6
Selected experimental and Theoretical SERS bands of SPL.

FT-Raman		SERS				Assignments
Theoretical Wavenumber (cm^{-1})	Experimental Wavenumber (cm^{-1})	Theoretical Wavenumber (cm^{-1})	Experimental Wavenumber (cm^{-1})			
			10^{-3} M	10^{-4} M	10^{-5} M	
1688	1667	1649		1611	1616	ν C=O (36) hex
		1550	1586			ν_{sym} CH_2 (18) nap, (26) meth 2
		1542	1542			ν_{sym} CH_2 (33) meth 2, (56) pent
		1532			1535	ν_{sym} CH_2 (24) pent
		1510		1514		ν CH_2 (36) dec
1443	1430	1427	1431			BM S-meth
		1377		1377	1375	β CH (23) dec, (32) hex
		1364	1369			t CH_2 dec
1341	1343	1322	1326			β CH dihy
1260	1263	1273			1279	ρ CH_2 (24), hex
1213	1215	1206	1208			t CH_2 (26), ω CH_2 (12) hex, dec
		1175		1173	1172	t CH_2 (32) dec
953	954	992	992		999	γ CCC (26), CH (12) dihy
		910	904	915		ν SCO (24) S-meth
		851	830			β CCC (32) dec,(18) dihy
		749	756			ring deformation dihy
643	657	627		629	626	β CCC (12) pent, (31) hex, (26) dec, (36) dihy
		544	552		545	γ CH (32) hex
		530		526		ρ CH_2 (50) dihy
						β CCO (18) dihy
		470	471			γ CCO(39) S-meth
						ring deformation dec
		444		437	437	β CCO (42) dihy
		252	250	248	248	Au-O

ν→ stretching, ν_{sym}→Symmetricstreching, ν_{asym}→ Asymmetric stretching, β→ in-plane bending, δ_{sci}→ Scissoring, ρ→ rocking, ω→ wagging, t→ twisting, γ→out-of-plane bending, nap→decahydronaphthalene, S-meth→S-methylethanethioate, dihy→dihydrofuran, cyclo→Cyclohexanone, pent→ cyclopentane.

suitability of using the diuretic drug (SPL) and the drug adsorbed with Au NPs (SPLA), for surgical COPD type diseases (lung cancer). The *in-silico* study was carried out using Molecular docking and based on the *in-silico* studies we progressed to the in-vitro studies including the MTT assay and SERS studies.

3.5.1. In-silico biological activity screening

3.5.1.1. Predicting the physicochemical properties of 'drug-like molecules. The Lipinski rule [51] was used to predict the novelty of the drug; benchmark rule of five (RO5) defines a drug candidate with the desirable physicochemical property. If the molecule obeys any two of the rules, then it is likely to have oral absorption characteristics. As per the Lipinski rule, we analysed logP value, hydrogen bond donors, hydrogen bond acceptors and the molecular weight with the help of molsoft drug-likeness and molecular property prediction online software. The drug-likeness score is 1.35 for both SPL and SPLA molecule, i.e, it lies in the drugs range. Concerning M. Gupta *et al.* [52] the Blood-Brain Barrier (BBB) Score of the SPL and SPLA molecules lies in the medium range, 3.22 and 3.57respectively predicting that they protect the brain from the deadly side effects of drugs and exogenous molecules. The MW of SPL molecule is within the desired limit and that for SPLA molecule is not within the limit. The number of HBA and HBD of both SPL and SPLA molecules are 5 and 0 respectively. The MolLogP, MolLogS, MolPSA, MolVol and pKa of most Basic/Acidic group of SPL molecule are 2.40, − 4.04 (in Log (moles/L)) 38.06 (in mg/L), 47.39 A2, 488.63 A3, and < 0. / 18.90 respectively. For SPLA molecule they are 2.40, − 4.04 (in Log (moles/L)), 56.08 (in mg/L), 47.39 A2, 490.84 A3 and < 0. / 18.90 respectively in the same order. The bioactivity score of SPL against regular human receptors, ion channels, kinases, nuclear receptor-ligands, proteases and enzymes are − 0.52, − 0.35, − 0.51, − 0.02 and 0.03 respectively which are in the same order for SPLA also. The above mentioned Physicochemical, Lipophilicity and Water Solubility Properties of the SPL and SPLA molecules are in good agreement with the Lipinski rule. As far as drug-likeness is concerned, the SPL molecule does not violate Lipinski, Ghose, Veber, Egan and Muegge rules. But Lipinski, Ghose and Muegge rules are violated in the SPLA molecule. The bioavailability Score for both SPL and SPLA molecules is 0.55.

3.5.1.2. Prediction of binding sites of lung cancer. The values of the docking parameters of SPL molecule, the binding energy, inhibition constant and intermolecular energy of the molecule concerning the targeted proteins were found to be − 6.4 kcal/mol, 230.15 mM and − 5.83 kcal/mol respectively and for SPLA molecule these values were − 8.02 kcal/mol, 543.01 mM and − 7.03 kcal/mol respectively. The SPLA molecule shows less binding energy and intermolecular energy but the inhibition constant is seen to be high for both the SPL and SPLA molecules. The hydrogen bonds between the ligand (SPL molecule) and the amino acid HIS A330 in the protein (5xnv) are O_{25}-$C_{22}O$ and O_{26}-$C_{17}O$ (2.0345 Å and 1.8346 Å respectively). The hydrogen bonds between the ligand (SPLA molecule) and the amino acid LYS 294 in the protein (5xnv) are O_{25}-$C_{22}O$ and O_{26}-$C_{17}O$ (2.5623 Å and 2.0165 Å respectively). These interactions are pictorially shown in Fig. 7. The overall results establish that both SPL and SPLA molecules show good binding affinity towards lung cancer activity through O_{25} and O_{26} atoms respectively, the SPLA exhibiting more binding affinity than SPL molecule.

3.5.1.3. Recognition of Human Lung Cancer Cells -in vitro analysis. In order to examine the cytotoxic effect of SPL and SPLA molecules, SERS and MTT assay were performed. For the intracellular SERS study, the SPLA molecule was taken into the A549 cell. Two hours later, the absorption peak at 449 nm was observed in the spectrum, as shown in Fig. 8(a). This evidences that the molecule has reached the cytoplasmic area, as cytoplasmic peak appears at 300–700 nm [53]. After another hour (three hours), when the absorption spectrum was examined again and was seen that the absorption peak had disappeared. This is evidence

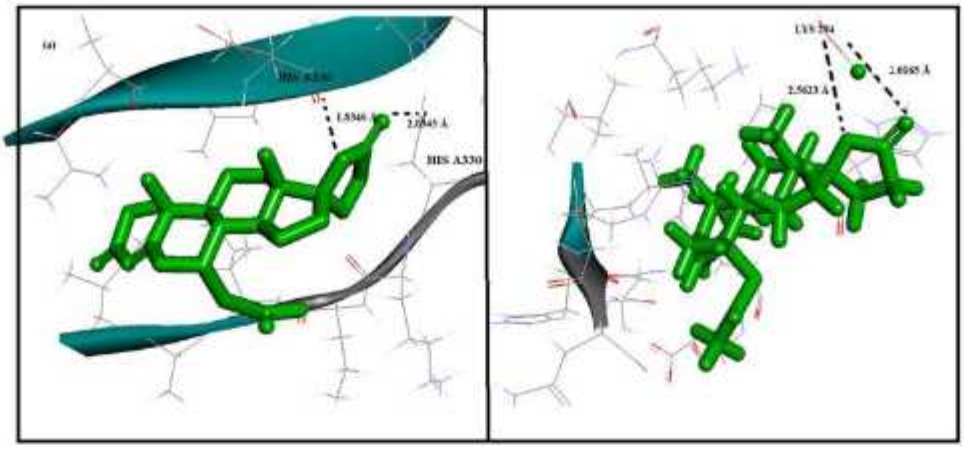


Fig. 7. Pictorial representation of possible binding sites of (a) SPL molecule and (b) SPLA molecule with the target proteins.

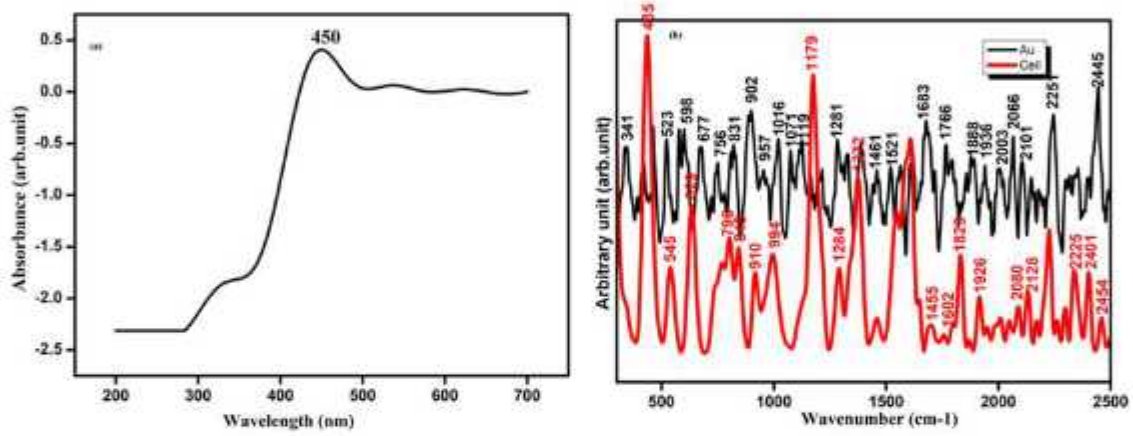


Fig. 8. (a) UV-Vis spectra of SPLA molecule inside the A549 cell line(b) SERS spectra analysis of SPLA and AuNP inside A549.

that the SPLA molecule slowly moved into the nucleus. The results obtained from SERS studies were compared with other similar studies and are shown in Table 7. The SERS studies are further justified through the fact that nuclear accumulation without cytoplasmic fluorescence was observed after 4 h.

From the SERS intensity ratio, it is possible to accurately quantify the cellular biomarker expression difference. Hence SERS imaging of single live cells is employed for cancer cell screening [54]. A broad and intense Raman band is observed at 1091 cm^{-1} corresponding to phosphodioxy group in the cell line,[55] which confirms changes in the nucleic acid. Raman bands corresponding to nucleotides are identified at 796 cm^{-1} for thymine, cytosine and uracil), and at 1284 cm^{-1} for thymine, guanine and adenine. A broadened band at 1552 cm^{-1} was observed corresponding to guanine and adenine. [55,56] Mixing of DNA and RNA is confirmed through the 796 cm^{-1}. The spectral line observed at 849 cm^{-1} detected the presence of nucleic acids inside the cell line. This corresponds to the vibration of the sugar-phosphate O-P-O backbone. The decrease of lipid-to-protein ratio is evident from the decrease in relative intensity of the lipid band at 1455 cm^{-1} [57,58]. The above assignments indicate the biochemical changes happened in the nucleus and thus indicate that SPLA interacts with apoptotic (cancer) cells. This will enable label-free monitoring and will further potentiate its therapeutic utility. SERS spectrum obtained from SPLA within the lung cancer cell which are associated with proteins, nucleic acids, lipids, and carbohydrates are identified, and assigned (Fig. 8(b) and Table 7).

Cellular internalization was performed through Raman imaging analysis. Bright field (Fig. 9(b)) and Raman mapping for SPLA localization were observed within 1–3 h of incubation of SPLA in A549 cells using a microscope. Raman spectral and imaging analysis from A549 cells showed an enhanced Raman signal. A time-dependent localization showing an early distribution within the cytoplasm and subsequent migration to the nucleus was evident from Raman imaging of SPLA, which shows that SPLA has entered the A549 lung cancer cells. In order to monitor the spatial and temporal progress of the uptake of nanoparticles in cancer cells, 2D SERS mapping (Fig. 9(a)) was employed [59]. SERS maps, a white light image of such an apoptotic A549 lung cancer cell was constructed to show the internalization of the drug. Fig. 9(a) and (c), shows that the cell has a size of 10 μm and is much smaller than the control cell, [60] showing that the cells are apoptotic. MTT viability assay was performed to confirm this. The standard deviation of the cytotoxicity assay was calculated and the results are furnished in Table 8. The MTT assay was performed on three concentrations of SPL and SPLA molecules. SPL and SPLA show cytotoxic effects, with more cytotoxicity in 1000 μM. The SPLA molecule shows more cytotoxicity effect than SPL molecule, but no cytotoxic effect for AuNPs alone. The above results show that cellular uptake of SPL is aided by AuNPs aids and hence allow targeted drug delivery. The comparative results are shown in Table 8 and Fig. 9(e).

4. Conclusion

The structural and bonding features responsible for the bioactivity of SPL and SPLA molecules were identified using quantum chemical calculations and vibrational spectral studies. The geometry of both the

Table 7
Assignments of major Surface-Enhanced Raman peaks inside the cell.

Raman band	nucleic acid	proteins	carbohydrates	lipids
435	Tyr	S-C str.		
545		Fe-O, P: S-S str.		
629		(C-C twist)		
796	T, U, C (ring br, RNA)			
849	O-P-O (asym. str.)	Tyr (ring br.)		
910		Lys (C-C, C-N str.)		
994		β-helix, C-C str.		=CHbend
1091	PO_2 str.	nar. (C-C str.)	C-O, C-C str.	Chain C-C str.
1179		C-C / C-N str.	C-C str.	
1284	T, A	Amide III, α- and β-helix structures		=CH bend
1372	adenine, guanine			
1455	G, A	CH_3def, collagen	CH_2def	CH_2def, phospholipids
1552		Amide II (CN str.)		
1602	G, A	Trp, (C=C ring str.)		
1829	T G, C (ring br.)	Amide I		C=C str.
1926		AA: ν(C=O)		
2080	C-N stretch (one of three thiocyanate peaks)		Trp: skeletal mode	
2128		C=N		Phospholipid
2225			Asymmetric stretching band of CO_2 2 hydrates	
2454		CH stretch of lipids and proteins		

abbreviation used: T - thymine; G - guanine; A- adenine; U-uracyl C-cytosine; Phe- phenylalanine; Tyr-tyrosine; Met-methionine; Cys-cystine; Trp-tryptophan; Lys-lysine; str-stretch; def- deformation; PO_2-phosphodioxy; nar- unspecified non-aromatic side-chains; br- breathing mode; sym-Symmetri; asym-asymmetric; bk – backbone

molecules was optimized, using the hybrid DFT method B3LYP with LANL2DZ basis set respectively, which showed that the rings are in non-planar conformation, which are affected by steric repulsion. The strength of the C-H···O intramolecular hydrogen bonding is seen to be very low in the SPL molecule compared with the SPLA molecule. The lengthening of C_{22}-O_{25} bond in SPLA molecule evidences back donation of an electron from Au NPs to the SPL molecule. Atomic orbital analysis has evidence that the localized electron effect is more prominent in SPLA molecules. NHO is bent more in SPLA than in SPL molecule as it lies in the strong charge transfer path towards the AuNPs in the former case. The NPA analysis reveals that SPL molecule has a greater charge than the SPLA molecule for all atoms which means the adsorption of AuNPs affects the charge density of the SPL molecule. Also, the donor-acceptor stabilization energy E (2) analysis established the intramolecular interaction between the Au NPs and SPL molecules. The FMOs analysis trots out that both molecules have small FMOs energy due to the larger aromatic system. SPLA molecule exhibited a smaller FMO energy gap, which may be due to the absorption of the gold nanoparticle. The global and local reactive descriptors divulge that ICT interaction occurs between AuNPs and SPL molecules through an oxygen atom in the dihydrofuran ring. The optical studies show that SPLA possesses good optical behaviour than SPL and hence better bioactivity than SPL. The molecular docking results indicate that SPL and SPLA molecules are effective drugs for interacting with carcinoma type proteins. The intense Raman bands of SPLA inside A549 noticeably provide label-free methods for the detection of intracellular components. Therefore, SPLA can be used as a biomarker as well as in the treatment of cancer.

CRediT authorship contribution statement

V. Shyni: Conceptualization, Methodology, Investigation, Writing – original draft. **D.R. Leenaraj:** Investigation, Data curation, Validation. **Ittyachan Reena:** Data curation, Validation. **Rejeena V. Rajan:** Data curation, Validation. **G. J. Shyju:** Data curation, Validation. **Lynnette Joseph:** Direction, Supervision, Writing – review & editing. **D. Sajan:** Funding acquisition, Resources, Writing – review & editing.

Declaration of Competing Interest

The authors declare that they have no known competing financial interests or personal relationships that could have appeared to influence the work reported in this paper.

Table 8
Information about cytotoxic effect.

concentration (μg/mL)	Au	SPL	SPLA
0	100	100	100
10	94.20	52.84	50.12
100	99.30	32.68	29.36
1000	90.20	23.22	19.01

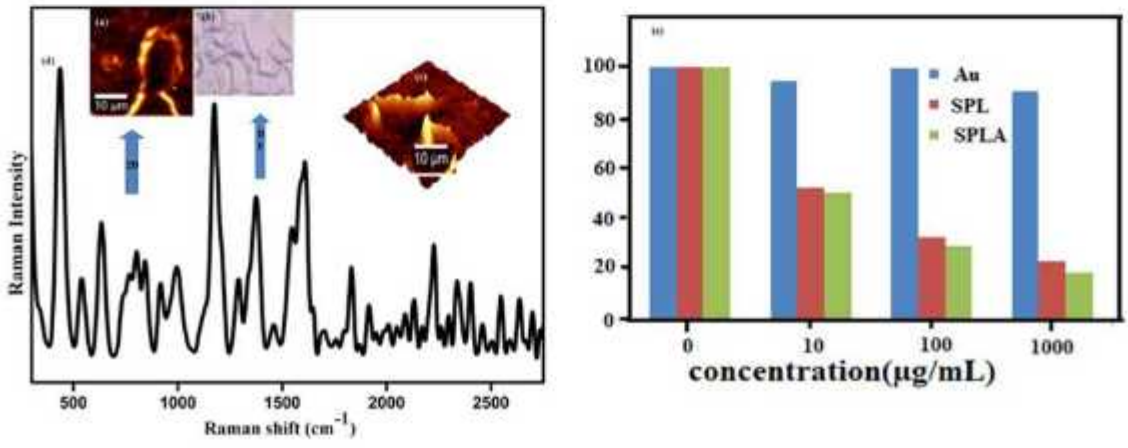


Fig. 9. Raman imaging of cells: (a) 2D image (b) Bright field images (c) 3D image (d) spectrum (e) Graphical representation of cytotoxic effect.

Appendix A. Supporting information

Supplementary data associated with this article can be found in the online version at doi:10.1016/j.colsurfa.2022.128255.

References

[1] W.-X. Qi, A.-N. He, Z. Shen, Y. Yao, Incidence and risk of hypertension with a novel multi-targeted kinase inhibitor axitinib in cancer patients: a systematic review and meta-analysis, Br. J. Clin. Pharmacol. 76 (2013) 348–357.

[2] N. Chanda, P. Kan, L.D. Watkinson, R. Shukla, A. Zambre, T.L. Carmack, H. Engelbrecht, J.R. Lever, K. Katti, G.M. Fent, S.W. Casteel, C. Jeffrey Smith, W. H. Miller, S. Jurisson, E. Boote, J.D. Robertson, C. Cutler, M. Dobrovolskaia, R. Kannan, K.V. Katti, Radioactive gold nanoparticles in cancer therapy: therapeutic efficacy studies of GA-198AuNP nanoconstruct in prostate tumor-bearing mice, Nanomedicine 6 (2017) 753–774.

[3] J.I.N. Zhang, C.Q. Lan, M. Post, B. Simard, Y. Deslandes, T.H. Hsieh, Design of nanoparticles as drug carriers for cancer therapy, Cancer Genom. Proteom. 3 (2006) 147–157.

[4] J. Gao, S. Bai, Q. Gao, Y. Liu, Q. Yang, Acid controlled diastereoselectivity in asymmetric aldol reaction of cycloketones with aldehydes using enamine-based organocatalysts, Chem. Comm. 47 (2011) 6716.

[5] P.N. Honkhambe, N.S. Bhairamadgi, M.V. Biyani, P.P. Wadgaonkar, M. M. Salunkhe, Synthesis and characterization of new aromatic polyesters containing cardo decahydronaphthalene groups, Eur. Polym. J. 46 (2010) 709–718.

[6] G. Wypych, Handbook of Foaming and Blowing Agents, Chemical origin of blowing agents, 3, Elsevier, 2017, p. 26.

[7] R. Abonia, R.K. Laali, Ionic liquid-mediated synthesis and functionalization of heterocyclic compounds, Adv. Heterocycl. Chem. 12 (2019) 333–431.

[8] B. Pitt, P. Zannad, W.J. Remme, R. Cody, A. Castaigne, A. Perez, J. Palensky, J. Wittes, The effect of spironolactone on morbidity and mortality in patients with severe heart failure, N. Engl. J. Med. 3411 (1999) 709–717.

[9] Heasley Brian, Recent developments in the stereocontrolled synthesis of highly substituted cyclopentane core structures: from drug discovery research to natural product synthesis, Curr. Org. Chem. 18 (2014) 641–686.

[10] S. Morissette, High-throughput crystallization: polymorphs, salts, co-crystals and solvates of pharmaceutical solids, Adv. Drug Deliv. Rev. 56 (2004) 275–300.

[11] C. Leuner, Improving drug solubility for oral delivery using solid dispersions, Eur. J. Pharm. Biopharm. 50 (2000) 47–60.

[12] G. Levy, Availability of spironolactone given by mouth, Lancet 280 (1962) 723–724.

[13] R.L. Takawaga, R. Hildebrandt, Masthead, J. Am. Chem. Soc. 106 (1984) 20.

[14] T.D. Klots, W.B. Collier, Vibrational assignment and analysis for 2,3-dihydrofuran and 2,5-dihydrofuran, Spectrochim. Acta A Mol. Biomol. Spectrosc. 50 (1994) 1725–1748.

[15] J. Van Meerloo, G.J. Kaspers, J. Cloos, Cell sensitivity assays: the MTT assay, Methods Mol. Biol. 731 (2011) 237–245.

[16] Wenjun Fang, Hongwei Duan, Intracellular and cellular detection by SERS-active plasmonic nanostructures, ChemBioChem 20 (2019) 2432–2441.

[17] Y. Yang, M. Nogami, J. Shi, H. Chen, G. Ma, S. Tang, Enhancement of third-order optical nonlinearities in 3-dimensional films of dielectric Shell capped au composite nanoparticles, J. Phys. Chem. B. 109 (2005) 4865–4871.

[18] V. Shyni, D.R. Leenaraj, Joseph Lynnette, D. Sajan, Investigations of Dianhydro-D-glucitol adsorbed on AuNPs surface: In silico and in vitro approach based on anticancer activity studies against A549 lung cancer cell lines, J. Mol. Recognit. 0952–3499 (2021) 1099–1352.

[19] M.J. Frisch, G.W. Trucks, H.B. Schlegel, G.E. Scuseria, M.A. Robb, J.R. Cheeseman, G. Scalmani, V. Barone, B. Mennucci, G.A. Petersson, H. Nakatsuji, M. Caricato, X. Li, H.P. Hratchian, A.F. Izmaylov, J. Bloino, G. Zheng, J.L. Sonnenberg, M. Hada, M. Ehara, K. Toyota, R. Fukuda, J. Hasegawa, M. Ishida, T. Nakajima, Y. Honda, O. Kitao, H. Nakai, T. Vreven, J.A. Montgomery Jr., J.E. Peralta, F. Ogliaro, M. Bearpark, J.J. Heyd, E. Brothers, K.N. Kudin, V.N. Staroverov, R. Kobayashi, J. Normand, K. Raghavachari, A. Rendell, J.C. Burant, S.S. Iyengar, J. Tomasi, M. Cossi, N. Rega, J.M. Millam, M. Klene, J.E. Knox, J.B. Cross, V. Bakken, C. Adamo, J. Jaramillo, R. Gomperts, R.E. Stratmann, O. Yazyev, A.J. Austin, R. Cammi, C. Pomelli, J.W. Ochterski, R.L. Martin, K. Morokuma, V.G. Zakrzewski, G.A. Voth, P. Salvador, J.J. Dannenberg, S. Dapprich, A.D. Daniels, O. Farkas, J.B. Foresman, J. V. Ortiz, J. Cioslowski D.J. Fox, Gaussian 09, Revision A.02, Gaussian, Inc., Wallingford CT, 2009.

[20] S. Thomas, N. Biswas, V.V. Malkar, T. Mukherjee, S. Kapoor, Studies on adsorption of carnosine on silver nanoparticles by SERS, Chem. Phys. Lett. 491 (2010) 59–64.

[21] P.S. Legge, G.L. Nyberg, J.B. Peel, DFT calculations for Cu-, Ag-, and aucontaining molecules, J. Phys. Chem. A 105 (2001) 7905–7916.

[22] N. Maiti, S. Thomas, J.A. Jacob, R. Chadha, T. Mukherjee, S. Kapoor, DFT and surface-enhanced Raman scattering study of tryptophanesilver complex, J. Colloid Interface Sci. 380 (2012) 141–149.

[23] NBO Version 3.1, E. D. Glendening, A. E. Reed, J. E. Carpenter, and F. Weinhold

[24] Tong-Hyok Cha, Scale factors of Gaussian type orbitals optimized in molecule's local environments, Chem. Phy. Lett. 765 (2021) 138–285.

[25] S. Miertuš, E. Scrocco, J. Tomasi, Electrostatic interaction of a solute with a continuum. A direct utilization of ab initio molecular potentials for the prevision of solvent effects, Chem. Phys. 55 (1981) 117–129.

[26] D. Escudero, A. Laurent, D. Jacquemin, Time-Dependent Density Functional Theory: A Tool to Explore Excited States, in: J. Leszczynski, A. Kaczmarek-Kedziera, T. Puzyn, G. Papadopoulos M., H. Reis, M. K. Shukla (Eds.), Handbook of Computational Chemistry, Springer, 2017.

[27] Michal. H. Jamroz, Vibrational Energy Distribution Analysis VEDA 4, Warsaw, 2004–2010.

[28] M. Berry, B. Fielding, J. Gamieldien, Practical considerations in virtual screening and molecular docking, J. Bioinform Comput. Biol. 52 (2015) 487–502.

[29] G.M. Morris, R. Huey, W. Lindstrom, M.F. Sanner, R.K. Belew, D.S. Goodsell, A. J. Olson, Autodock4 and AutoDockTools4: automated docking with selective receptor flexibility, J. Comput. Chem. 30 (16) (2009) 2785–2791, 2009 Dec.

[30] W. Mi, H. Guan, J. Lyu, D. Zhao, Y. Xi, S. Jiang, P.H. Andrews, X. Wang, M. Gagea, H. Wen, L. Tora, YEATS2 links histone acetylation to tumorigenesis of non-small cell lung cancer, Nat. Commun. 8 (2017) 01173–01174.

[31] V. Agafonov, B. Legendre, N. Rodier, A new crystalline modification of spironolactone, Acta Crystallogr., C: Cryst. Struct. Commun. 45 (1989) 1661–1663.

[32] C.O. Della Védova, R.M. Romano, H. Oberhammer, Gas electron diffraction analysis on S-methyl thioacetate, CH3C (O) SCH3, J. Org. Chem. 69 (2004) 5395–5398.

[33] S. Arnott, S.D. Dover, A.J. Wonacott, Least-squares refinement of the crystal and molecular structures of DNA and RNA from X-ray data and standard bond lengths and angles, Acta Crystallogr. B. Struct. Sci. Cryst. Eng. Mater. 25 (1969) 2192–2206.

[34] Ramachandran Rakhi, Cherumuttathu H. Suresh, A DFT study on dihydropyrazine annulated linear polyacenes: aromaticity, stability and HOMO–LUMO energy modulation, Phys. Chem. Chem. Phys. 18 (2016) 24631–24641, https://doi.org/10.1039/C6CP03723B.

[35] L. Reuter, A. Lüchow, Real space electron delocalization, resonance, and aromaticity in chemistry, Nat. Commun. 12 (2021) 4820, https://doi.org/10.1038/s41467-021-25091-8.

[36] Paul von Ragué Schleyer, Mariappan Manoharan, Haijun Jiao, Frank Stahl, The acenes: is there a relationship between aromatic stabilization and reactivity? Org. Lett. 3 (23) (2001) 3643–3646.

[37] J.I. Aihara, Reduced HOMO–LUMO gap as an index of kinetic stability for polycyclic aromatic hydrocarbons, J. Phys. Chem. A 103 (1999) 7487–7495, https://doi.org/10.1021/jp990092i.

[38] M. Bendikov, F. Wudl, D.F. Perepichka, Tetrathiafulvalenes, oligoacenenes, and their buckminsterfullerene derivatives, J. Chemin.-. Model 36 (2005) 8.

[39] R. Premkumar, S. Hussain, T. Mathavan, K. Anitha, A.M.F. Benial, Surface-enhanced Raman scattering and quantum chemical studies of 2-trifluoroacetyl-pyrrole chemisorbed on colloidal silver and gold nanoparticles: a comparative study, J. Mol. Liq. 290 (2019), 111209.

[40] P.S. Rao, S. Kalva, A. Yerramilli, S. Mamidi, Free radicals and tissue damage: role of antioxidants, Free Radic. Biol. Med. 1 (2011) 2–7.

[41] D.S. Yadav, Organic Spectroscopy, Springer, Netherlands, 2005.

[42] G. Socrates, Infrared and Raman Characteristic Group Frequencies, John Wiley & Sons Ltd, England, 1980.

[43] D. Sajan, K. Udaya Lakshmi, Y. Erdogdu, I. Hubert Joe, Molecular structure and vibrational spectra of 2,6-bis(benzylidene)cyclohexanone: a density functional theoretical study, Spectrochim. Acta A Mol. Biomol. Spectrosc. 78 (2011) 113–121.

[44] D.L. Vein, N.B. Colthup, W.G. Fateley, J.G. Grasselli, The Handbook of Infrared and Raman Characteristic Frequencies of Organic Molecules, Academic Press, New York, 1991.

[45] H.A. Szymanski, Cyclohexane Deriv. Interpret. Infrared Spectra 15 (1964) 229–293.

[46] R. Bhatt, I. Bhaumik, S. Ganesamoorthy, A.K. Karnal, M.K. Swami, H.S. Patel, P. K. Gupta, Urbach tail and bandgap analysis in nearly stoichiometric LiNbO3 crystals, Phys. Status Solidi B Basic Res 209 (2011) 176–180.

[47] M. Rumi, G. Zerbi, Conformational dependence of vibrational and molecular nonlinear optical properties in substituted benzenes: the role of π-electron conjugation and back-donation, J. Mol. Struct. 509 (1999) 11–28.

[48] M. Gussoni, C. Castiglioni, M.N. Ramos, M. Rui, G. Zerbi, Infrared intensities: from intensity parameters to an overall understanding of the spectrum, J. Mol. Struct. 224 (1990) 445–470.

[49] David Murdoch, Gerald Forrest, David Davies, Gordon McInnes, A comparison of the potassium and magnesium-sparing properties of amiloride and spironolactone in diuretic-treated normal subjects, Br. J. Clin. Pharmac. 35 (1993) 373–378.

[50] Broaddus V.C., Mason R.J., Ernst J. D., eds. Murray and Nadel's Textbook of Respiratory, Medicine. 6th ed. Philadelphia 44 (2016) 105.

[51] C.A. Lipinski, F. Lombardo, W.B. Dominy, P.J. Feeney, Experimental and computational approaches to estimate solubility and permeability in drug discovery and development settings, Adv. Drug Deliv. Rev. 23 (1997) 3–25.

[52] M. Gupta, H.J. Lee, C.J. Barden, D.F. Weaver, The Blood-Brain Barrier (BBB) score, J. Med. Chem. 62 (2019) 9824–9836.

[53] W. Mi, H. Guan, J. Lyu, D. Zhao, Y. Xi, S. Jiang, P.H. Andrews, X. Wang, M. Gagea, H. Wen, L. Tora, YEATS2 links histone acetylation to tumorigenesis of non-small cell lung cancer, Nat. Commun. 8 (2017) 01173–01174.

[54] L. Li, M. Liao, Y. Chen, B. Shan, M. Li, Surface-enhanced Raman spectroscopy (SERS) nanoprobes for ratiometric detection of cancer cells, J. Mater. Chem. B 7 (2019) 815–822.

[55] Z. Wang, S. Zong, H. Chen, H. Wu, Y. Cui, Silica coated gold nano aggregates prepared by reverse microemulsion method: Dual-mode probes for multiplex immunoassay using SERS and fluorescence, Talanta 86 (2011) 170–177.

[56] W. Fang, Z. Wang, S. Zong, H. Chen, D. Zhu, Y. Zhong, Y. Cui, pH-controllable drug carrier with SERS activity for targeting cancer cells, Biosens. Bioelectron. 57 (2014) 10–15.

[57] R.E. Hester, Biological applications of Raman spectroscopy Vols 1 & 2, FEBS Lett. 230 (1988), 222–222.

[58] F.R. Dollish, W.G. Fateley, F.F. Bentley, Characteristic Raman frequencies of organic compounds, Anal. Chim. Acta 75 (1975) 492.
[59] R. Smith, K.L. Wright, L. Ashton, Raman spectroscopy: an evolving technique for live cell studies, Analyst 12 (2016) 3590–3600.
[60] T. Mosmann, Rapid colourimetric assay for cellular growth and survival: application to proliferation and cytotoxicity assays, J. Immunol. Methods 65 (1983) 55–63.